Synthesis and Mesomorphism of an Homologous Series of Ionic Polycatenar Liquid Crystals based on the N-Phenylpyridinium Moiety

Jordan Herod

Chemistry, University of York.

Abstract

An homologous series of ionic polycatenar liquid crystals based on the *N*-phenylpyridinium motif was prepared with triflate, triflimide, octylsulfate and dodecylsulfate anions. Triflate and the alkylsulfate salts gave rise to a SmA phase in short-chain homologues due to an increase in the core volume by the associated anion; observation of a SmA phase is extremely rare in polycatenar mesogens. It was also found that the columnar mesophases of longer-chain homologues was stabilised significantly compared to the SmA phase (70 °C with a triflate anion) and that this observation is characteristic of all ionic polycatenar materials studied within this thesis. The triflimide salts behaved differently and all homologues formed a columnar rectangular mesophase.

The effect of added solvent on the mesomorphism of the *N*-phenylpyridinium ions was investigated and it was found that a range of mesophases were induced. It was postulated that small, polar, aprotic solvents such as DMSO associated at the polar core of the cation, increasing the effective core volume and leading to the induction of a lamellar phase when the dry material was columnar. In contrast, long-chain alcohols and linear alkanes were regarded as concentrating in the apolar terminal chains to increase the effective chain volume, so promoting mesophases with curvature (cubic and columnar). Preferential solvent location can readily be rationalised on the basis of the amphiphilic nature of the *N*-phenylpyridinium salts.

Finally, a series of phenylpyridine complexes of silver(I) were prepared and their mesomorphism was compared both with the *N*-phenylpyridinium salts and with the stilbazole complexes of silver(I). Once the difference in size and shape of the ligands was accounted parallels were observed between the two families of complexes, but comparison with the *N*-phenylpyridinium salts revealed both the strong influence in the way in which the anion is accommodated and also the formally ionic nature of the materials.

Contents

Abbreviations

LC   Liquid crystal

ILC   Ionic liquid crystal

Crys   Crystal

Iso   Isotropic

N   Nematic

Sm   Smectic (*i.e.* SmA = smectic A)

Col_h Columnar hexagonal

Col_r Columnar rectangular

Cub   Cubic

L   Lamellar

T   Tetragonal

H   Lyotropic Hexagonal

V   Lyotropic Cubic Bicontinuous

I   Lyotropic Micellar Cubic

M   Chromonic Hexagonal

n   Director

cmc   Critical micelle concentration

CPP   Critical packing parameters

POM   Polarising Optical Microscopy

DSC   Differential Scanning Calorimetry

ΔH Transition enthalpy

ΔS Transition entropy

T Temperature

°C   Degrees Celcius

Δ	Heat
G	Gibbs free energy
T_g	Glass transition
C_p	Specific heat capacity
XRD	X-Ray Diffraction
SAXS	Small angle X-ray scattering
λ	Wavelength
d	Separation of lattice planes
θ	Angle of incidence of X-rays
fwhm	Full width half maximum
NMR	Nuclear Magnetic Resonance
s	singlet
d	doublet
t	triplet
m	multiplet
r.t.	room temperature
mol	mole
ml	millilitre
dm	decimetre
mg	milligram
a	Lattice parameter of the Col_h mesophase
n_e	Extraordinary refractive index
n_o	Ordinary refractive index
Δn	Birefringence
α	Polarisability

DMSO   Dimethylsulfoxide

DMF   Dimethylformamide

THF   Tetrahydrofuran

MeCN   Acetonitrile

MeOH   Methanol

EtOH   Ethanol

PrOH   1-Propanol

BuOH   1-Butanol

dppf   diphenylphosphinoferrocene

SPhos   2-Dicyclohexylphosphino-2',6'-dimethoxybiphenyl

CHN   Carbon, nitrogen and hydrogen elemental analysis

n   Number of carbon atoms in an aliphatic chain

R_{eff} Effective volume

Å   Angstrom

Acknowledgements

Declaration

I declare that this thesis is a presentation of original work and I am the sole author. This work has not previously been presented for an award at this, or any other, University. All sources are acknowledged as References.

Chapter One: Introduction

1. General introduction to liquid crystals

Liquid-crystal phases exist between the highly ordered crystalline phase and disordered isotropic-liquid phase. The first liquid-crystalline compound was discovered by Reinitzer[1] in 1888 who noticed that cholesteryl benzoate (Figure 1.1) displayed two melting temperatures. First, was melting of the crystal into an opaque fluid and second was the transition of this turbid fluid into a clear liquid. The first melting point was actually a crystal to liquid crystal transition and the second was the transition from a liquid crystal phase to the isotropic liquid.
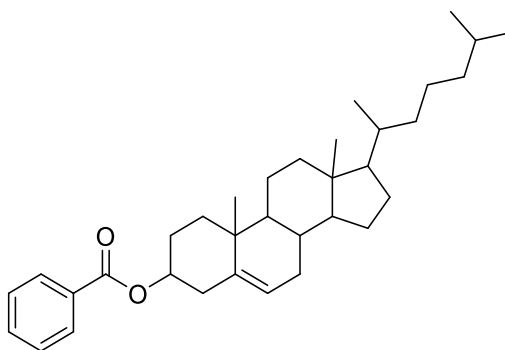
Figure 1.1. Structure of cholesteryl benzoate.

2. Thermotropic liquid crystals

Cholesteryl benzoate is an example of a thermotropic liquid crystal, in which the liquid-crystalline state is brought about by changing the temperature of the material to affect phase transitions. Thermotropic liquid crystals have been known since the late 1800's but it wasn't until the 1970's that research in this field really gained momentum after the realisation that liquid-crystalline phases could be employed in display devices. Early work concentrated on the synthesis of rod-shaped molecules (much like the structure of cholesteryl benzoate) with at least one flexible aliphatic chain attached to one end of the core; these compounds were termed calamitic liquid crystals.

2.1. Mesophases formed by calamitic compounds

Calamitic materials predominantly form nematic and/or smectic liquid-crystal phases (mesophases). The nematic phase is the most disordered liquid-crystal phase and molecules in this mesophase possess only orientational order in that their molecular long axes align in roughly the same direction and this is indicated by a director, **n** (Figure 1.2). Smectic phases, on the other hand, display additional order in that the constituent molecules also possess partial positional order

achieved by self-organisation into diffuse layers. A number of smectic phases have been identified and it is their differing degrees of positional order that sets them apart from one another.

Smectic A (SmA) and smectic C (SmC) phases are the most common of this type. The SmA phase is the most disordered smectic phase and molecules self-organise into diffuse layers with their long axes, on average, 90° to the layer normal as shown in Figure 1.2. In reality, the layers are not as well-defined as those depicted in Figure 1.2 and are best described by a sinusoidal density wave with density maxima defining the layers. The SmC phase displays additional order in that the molecules are tilted within the layers; the director, **n**, is thus at an angle <90° to the layer normal.

N   **SmA**   **SmC**
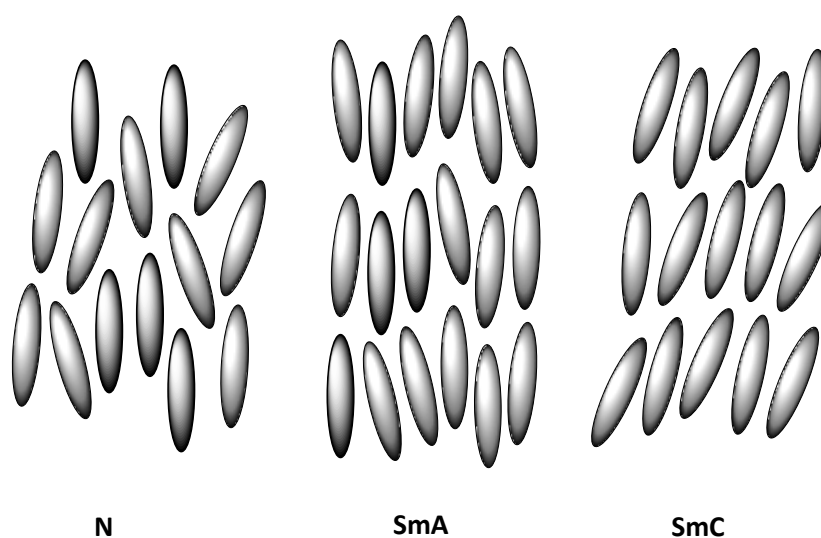
Figure 1.2. Structure of some common liquid-crystal phases formed by calamitic compounds.

2.2. Mesophases formed by discotic compounds

Disc-shaped molecules are another anisometric molecular shape that can self-organise into liquid-crystal phases and these are known as discotic mesogens. The mesophases formed by disc-like molecules organise into columnar aggregates that pack typically on a two-dimensional lattice. The columns can arrange in a nematic fashion with only one-dimensional order in that the columnar long axes point along a common direction; this results in the formation of the columnar nematic phase. More commonly, however, is for the columns to pack on a two-dimensional lattice in either hexagonal or rectangular symmetries to form columnar hexagonal (Col_h) or columnar rectangular (Col_r) mesophases, respectively. Col_r phases possess lower symmetry than do Col_h phases as molecules within the columns are tilted, which in turn reveals two lattice parameters, *a* and *b*, as opposed to the single lattice parameter, *a*, associated with a Col_h phase. Col_r phases belong typically to one of two space groups, namely *c2mm* or *p2gg* as depicted in Figure 1.3.[2] In extremely rare

cases, disc-like molecules can form the discotic nematic phase that does not involve the formation of columnar aggregates. In this mesophase, the molecular short axes orient along a common direction, **n**, to form a one-dimensionally ordered mesophase. Figure 1.3 shows a schematic of the different mesophases formed by discotic mesogens.

| Col$_h$ | Col$_r$ | Columnar nematic | Discotic nematic |

| Col$_h$ *p6mm* | Col$_r$ *p2gg* | Col$_r$ *c2mm* |
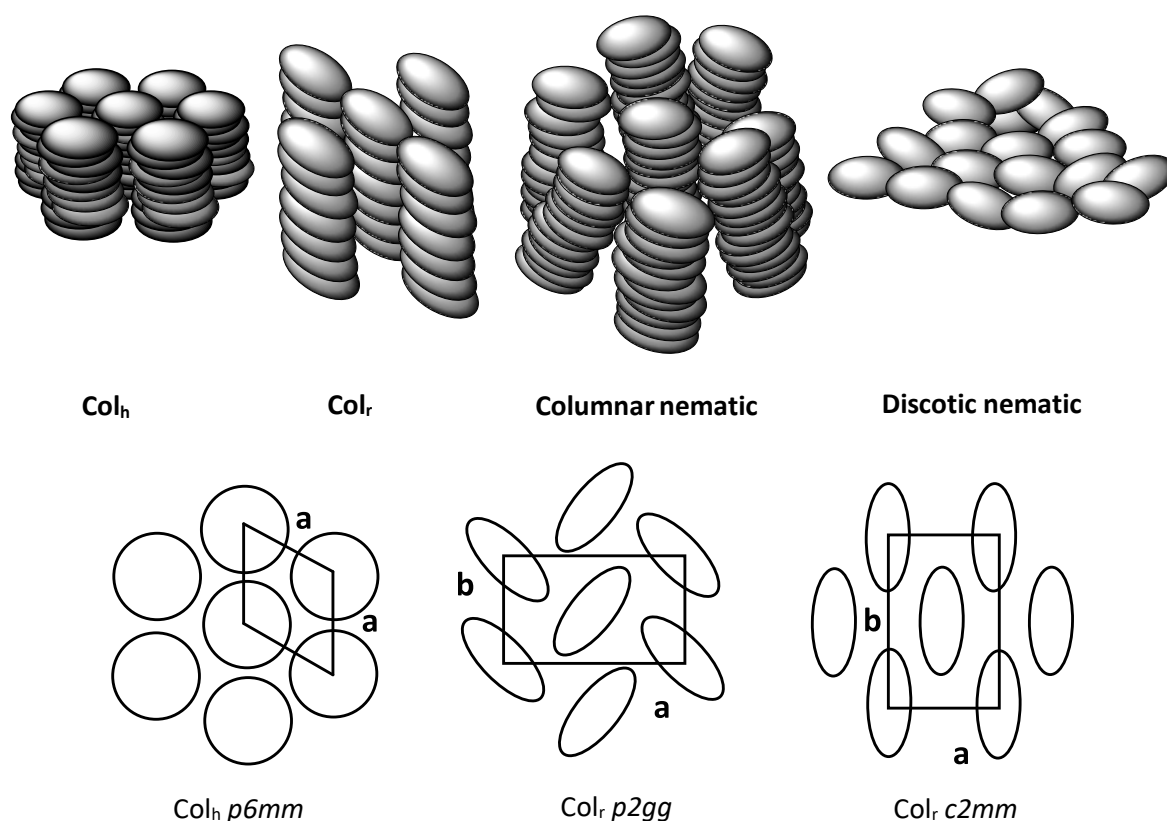
Figure 1.3. Structure of some common columnar mesophases formed by discotic compounds (top), the columnar *a* parameter of the Col$_h$ phase, the *p2gg* Col$_r$ phase and the *c2mm* Col$_r$ phase (bottom).

3.   Characterisation of liquid crystal phases

Mesophase identification is achieved through a combination of polarised optical microscopy and small-angle X-ray diffraction in combinateion with differential scanning calorimetry (DSC), which provides information on the enthalpy and entropy changes involved in phase transitions.

3.1. Polarised light microscopy

Liquid-crystal phases are anisotropic and, therefore, exhibit birefringence in that they possess at least two refractive indices. This property can alter the polarisation state of plane-polarised light as it passes through the material, hence mesophases display vibrant optical textures when viewed down a microscope equipped with crossed polarisers. For calamitic molecules, two different directions of polarisability exist, α_1 and α_2, which gives rise to two refractive indices called the

ordinary refractive index, n_o, and the extraordinary refractive index, n_e, as shown in Figure 1.4. If restricted rotation occurs about the short axis of the molecule then a third direction of polarisability occurs that produces a third refractive index; this can give rise to *biaxial* mesophases. Birefringence, Δn, is given by the difference between n_e and n_o as shown by the following equation:

$$\Delta n = n_e - n_o$$
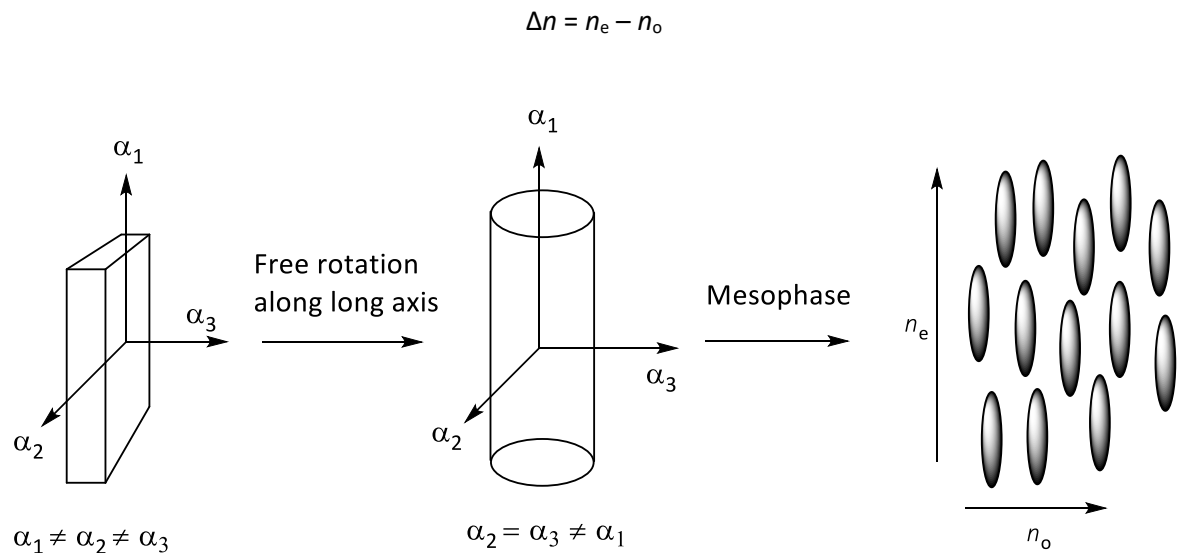
Figure 1.4. Relationship between polarisability, refractive indices and birefringence.

Different liquid-crystal phases display their own characteristic texture that allows identification of the mesophase; however, discrimination between the different optical textures requires practice and dedication. To perform microscopy experiments, a small amount of sample is placed on a microscope slide and covered with a glass coverslip. The sample is then heated using a hotstage that can easily be used in conjunction with a microscope equipped with crossed polarisers. As the sample is heated, the transition into the liquid-crystal phase (melting) is easily observed and a texture characteristic of the mesophase is observed. Mesophase-to-mesophase transitions (where present) can often be observed easily using polarising microscopy due to the different optical textures associated with each liquid-crystal phase; however, this isn't always the case as some liquid crystal textures appear remarkably similar to the untrained eye. The liquid crystal-to-isotropic liquid transition (clearing point) is easily identified from the loss of birefringence as the sample appears dark in the isotropic-liquid phase. Liquid-crystalline textures are best assigned on cooling from the isotropic liquid so that they do not contain defects from the preceding crystal or liquid-crystal phase. This is said to be the *natural* texture of the mesophase, where a texture on heating from the crystalline state is known as a *paramorphotic* texture.
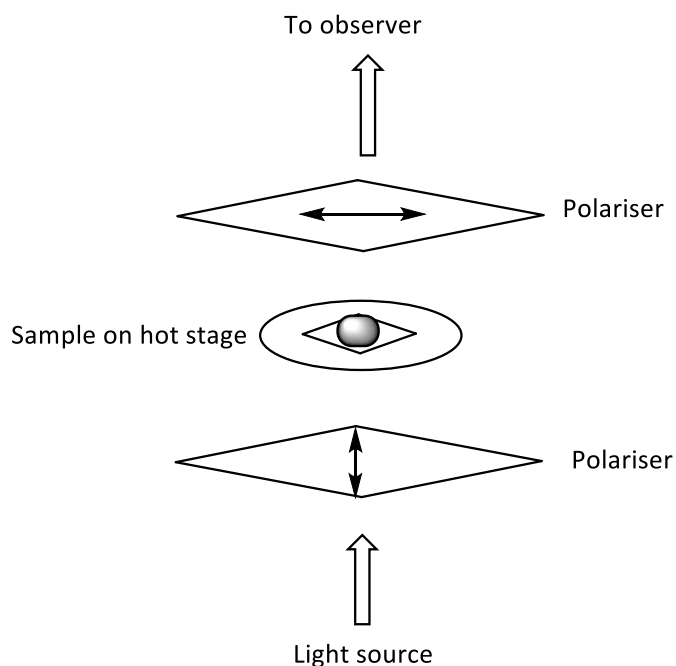
Figure 1.5. Schematic of the experimental setup of a polarising microscope.

As a rough guide, nematic phases give a schlieren texture that is characterised by the appearance of 2- and 4-point brushes (Figure 1.6 (**a**)). SmA phases produce a clear focal conic texture with fan-like regions and crosses of optical extinction known as ellipse and hyperbola; the SmA phase can also produce dark regions of optical extinction due to homeotropic alignment of the molecules that precludes birefringence (Figure 1.6 (**c**)). The SmC phase, however, forms broken focal-conic defects that appear more blurry than do the focal-conic defects seen in the SmA phase as shown in Figure 1.6 (**b**) and this occurs due to tilting of the molecules; the SmC phase can also give rise to a schlieren texture akin to that of the nematic phase but with only 4-point brushes. Columnar textures, on the other hand, can exhibit platelet textures with additional spine-like defects that appear as sharp, bright lines. Cubic mesophases, however, are quite different and are not birefringent appearing dark when viewed down the polarising microscope due to their three-dimensional structures of cubic symmetry. Cubic phases can be readily differentiated from the isotropic-liquid phase as a reduction in viscosity is typically observed on the transition into the isotropic liquid. It is often possible to differentiate a cubic mesophase even from a viscous isotropic liquid phase on the polarising microscope as air bubbles within the mesophase are incredibly difficult to deform when touched.

2-point brushes   4-point brushes   Broken focal-conics

(b)

Focal-conic   Homeotropic   **(c)**   Spine-like defect   **(d)**
defect   alignment
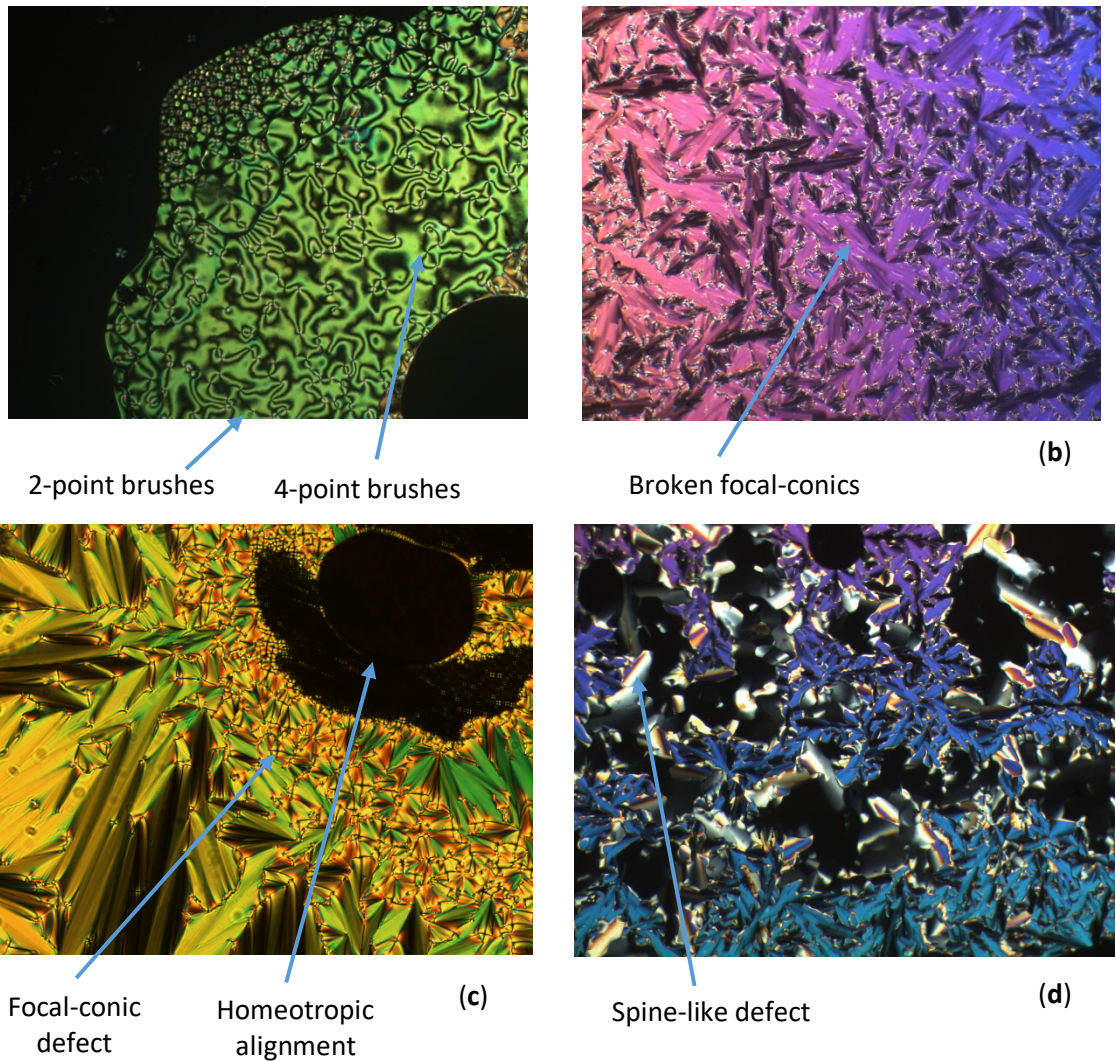
Figure 1.6. Optical textures of (**a**) the schlieren texture of the nematic phase, (**b**) the broken focal-conic texture of the SmC phase, (**c**) the focal-conic texture of the SmA phase and (**d**) a Col$_h$ phase. Textures are at x10 magnification.

3.2. Differential scanning calorimetry (DSC)

Differential scanning calorimetry, DSC, is a calorimetric technique used to identify phase transitions, which can be extremely useful if mesophase-to-mesophase transitions are not observed down the polarising microscope. It must be noted that DSC does not provide information concerning the nature of the liquid-crystal phase – it can only provide information on the phase transition itself. The point is to match every event in DSC with every event in microscopy and vice versa; however, some transitions are more easily detected by one method over the other and so it is important to use the two in tandem. Other than the temperature at which the phase transition occurs, DSC can provide information on the enthalpy (ΔH) and entropy (ΔS) changes involved. The magnitude of the enthalpy change is related to the change in molecular order on changing phase.

DSC experiments are performed by weighing out a small amount of sample (usually 1-2 mg) into an aluminium crucible, which is then sealed using an aluminium lid and the sample placed in the DSC furnace. The sample pan along with a reference pan are then heated at the same rate and kept at the same temperature with respect to one another, which is achieved through computer control. As the sample melts (an endothermic process), more energy must be supplied to the sample pan to keep it at the same temperature as the reference pan. This is recorded by the computer as differential power input (measured in mW) *vs* temperature (*T*). During an exothermic phase transition, the reverse is true, and, for example, a crystallisation process requires less heat energy be supplied to the sample pan than the reference pan. The area under the peak is proportional to the enthalpy change of the transition and can be calculated from the following expression:

$$\Delta H = \int_{T_1}^{T_2} C_p dT$$

Where C_p is the specific heat capacity and *T* is the temperature.

ΔG is assumed to be 0 at a phase transition and the system is said to be at equilibrium, therefore ΔS can be calculated from the following expression:

$$\Delta S = \Delta H / T$$

Figure 1.7 shows a schematic of a DSC instrument.
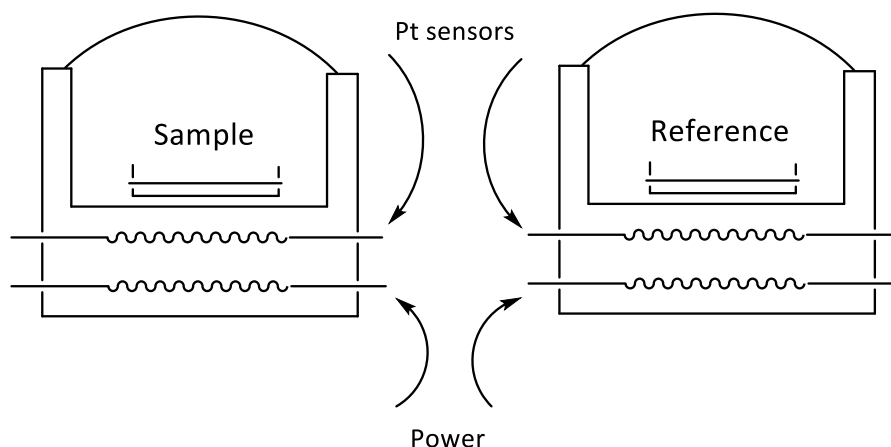
Figure 1.7. Schematic representation of a DSC.

Liquid crystal phase transitions can be either first or second-order and relate to the Gibbs free energy (*G*) change at the transition. Therefore, energy is defined as:

$$G = H - TS$$

The first derivative of G with respect to T gives the negative entropy, $-S$:

$$\mathrm{d}G/\mathrm{d}T = -S$$

In the case of a first-order transition, a plot of the $-S$ vs T shows a discontinuity at the phase transition as shown in Figure 1.8 (**a**), whereas at a second-order transition there is a simple change in gradient as seen in Figure 1.8 (**b**). As such, first-order transitions appear as peaks in a DSC thermogram and second-order transitions appear as a change in the baseline (Figure 1.8 (**c**)).

(**a**)   (**b**)

(**c**)
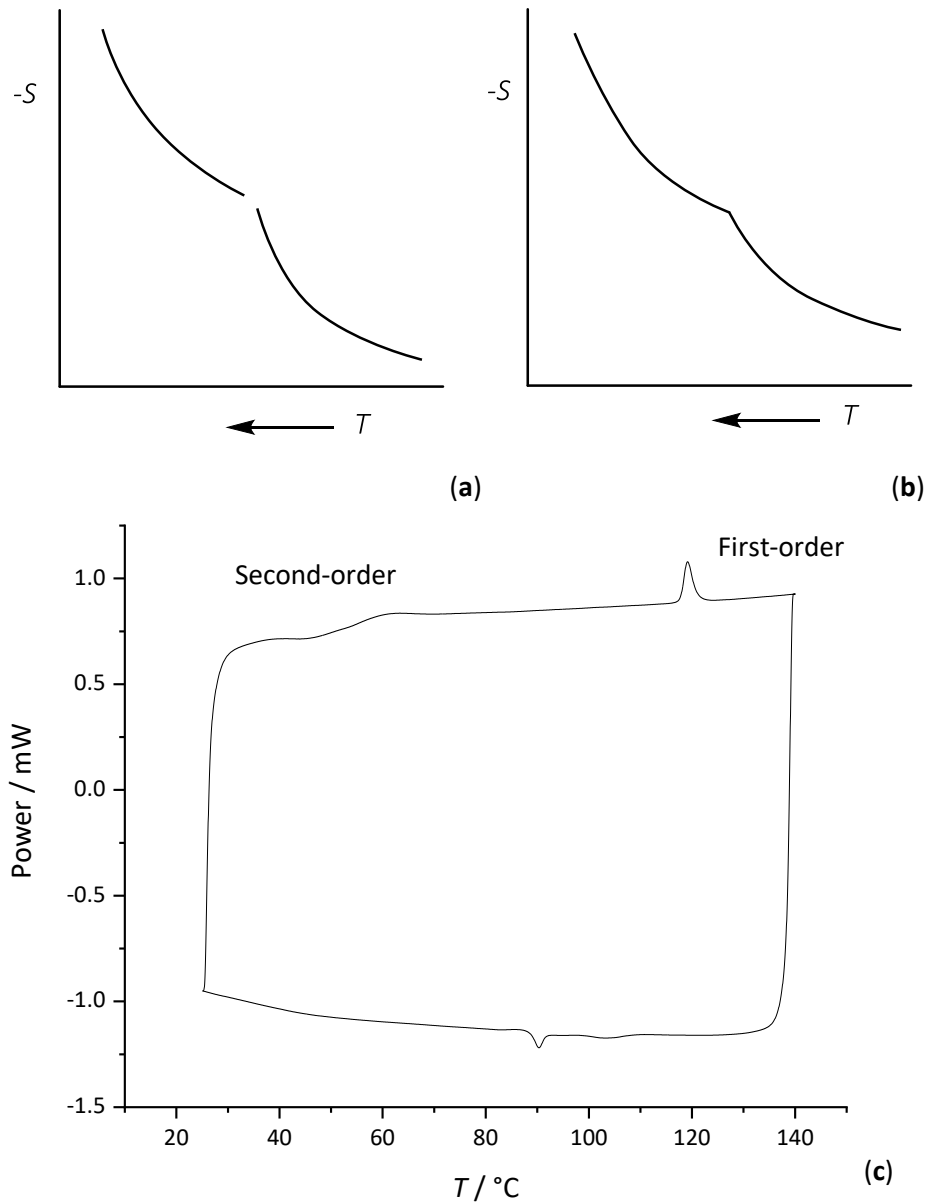
Figure 1.8. Plots of T vs $-S$ for (**a**) a first-order transition (**b**) a second-order transition and (**c**) a DSC trace showing a second-order and first-order phase transitions.

20

3.3. Small-angle X-ray diffraction

Liquid-crystal phases are periodic over the length scale of Å and, therefore, can be probed by X-rays to provide information on the structure of the mesophase.

$$2d\sin\theta = n\lambda$$

Where θ represents the angle of incidence
n can be any integer
λ represents the wavelength of X-rays
d represents the separation of the lattice planes

Typically, powder-diffraction experiments are performed by which a small amount of sample (in the solid state) is added to a glass capillary tube and X-ray diffraction patterns collected as a function of temperature. The crystalline phase is characterised by the appearance of several sharp diffraction peaks in both the small and wide-angle regions of the diffraction pattern. However, in the liquid-crystal phase, the wide-angle region displays usually a single diffuse peak that represents the average side-to-side separation of molecules in the mesophase, often thought of as a signal arising from the molten nature of the aliphatic chains. However, higher ordered mesophases with additional short-range correlations show more than one reflection in the wide-angle region and the smectic B phase, for example, displays multiple wide-angle peaks arising from the hexagonal packing of the rod-like molecules. The small-angle region, on the other hand, is characterised by sharper reflections where the number and d-spacing help to identify the mesophase. Figure 1.9 shows a schematic of the experimental setup employed to collect X-ray diffraction patterns of liquid crystal phases.
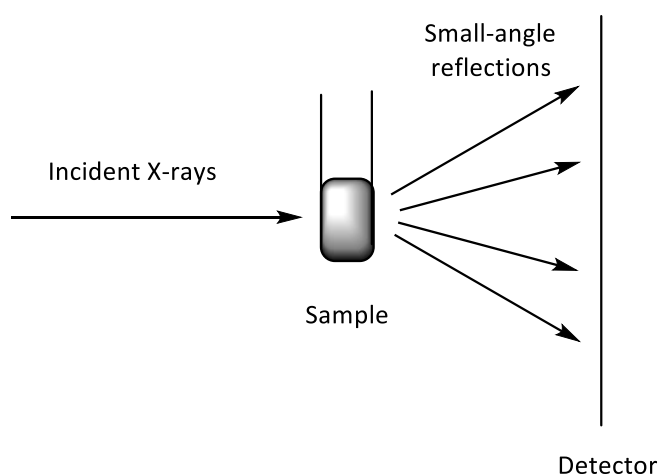
Figure 1.9. Schematic diagram of the experimental setup of a small-angle X-ray diffraction experiment.

Non-aligned diffraction patterns of a nematic mesophase show a single, broad reflection in the small-angle regime that approximates the total length of the rod-shaped molecules and a diffuse

scattering in the wide-angle region from their average side-to-side separation. Smectic phases, on the other hand, show sharper Bragg scattering in the small-angle region due to ordering of the molecules into diffuse layers and this signal corresponds to the layer periodicity (d_{001}) as seen in Figure 1.10 (**a**). The layer spacing of a SmA phase is typically similar to the molecular length, but sometimes slightly smaller due to chain interdigitation or chain folding. Columnar mesophases, on the other hand, show at least two reflections in the small-angle region due to the two-dimentional order of these mesophases (other than the columnar nematic and discotic nematic mesophases). The relative ratio between these small-angle signals indicates the symmetry of the columnar phase and hexagonal columnar mesophases, for example, show always a ratio of 1 : 1/√3 : 1/√4 in the separation spacing of the small-angle reflections and these are the d_{10}, d_{11} and d_{20} reflections (Figure 1.10 (**b**) and (**d**)).
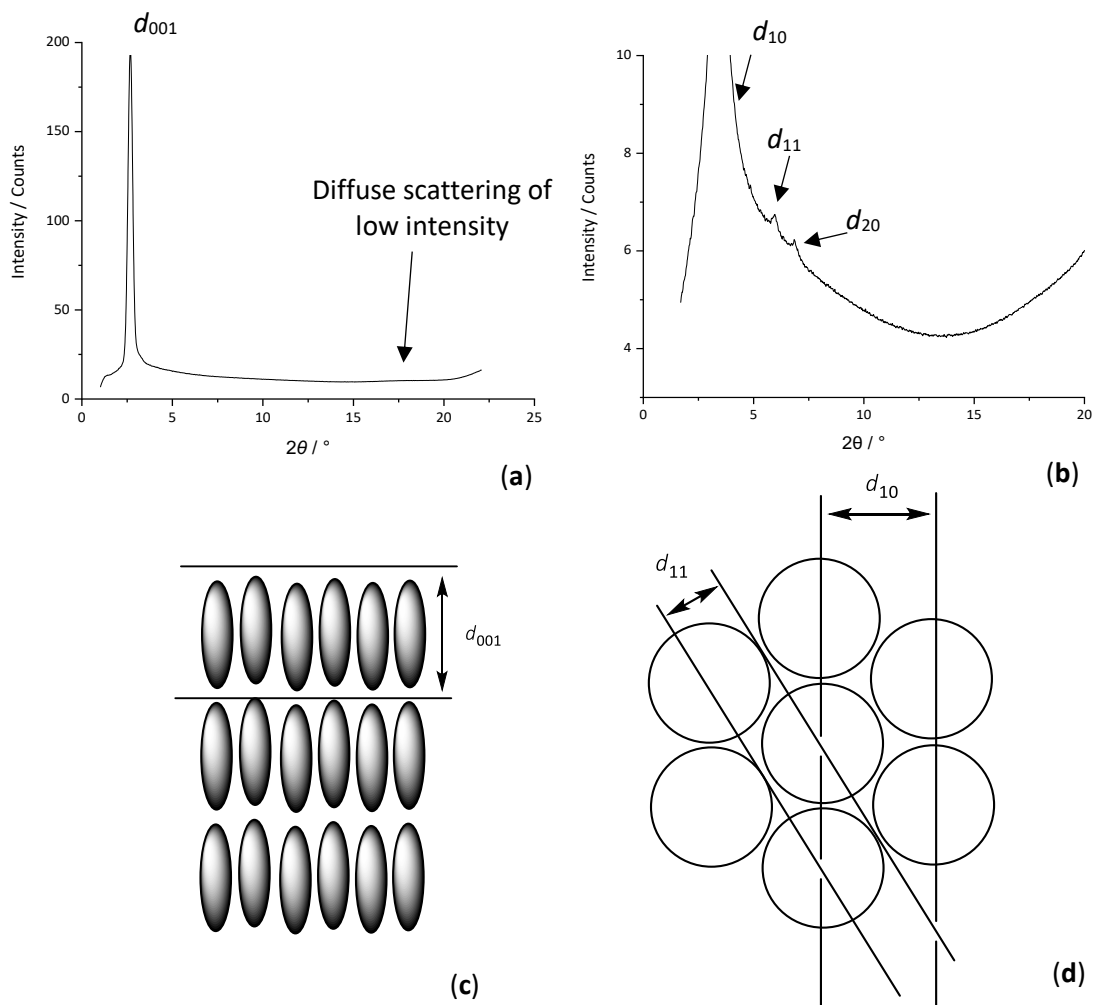
Figure 1.10. (**a**) SAXS pattern of a SmA phase and (**b**) SAXS pattern of a Col$_h$ phase zoomed in to show the two low intensity reflections in the small-angle region (**c**) origin of the d_{001} reflection in smectic mesophases and (**d**) origin of the d_{10} and d_{11} reflections of the Col$_h$ phase.

4. Lyotropic liquid crystals

A second class of liquid-crystalline behaviour is that displayed by lyotropic liquid crystals, where the ordered crystalline state is destroyed by the addition of solvent to generate a liquid-crystal phase. Three major types of lyotropic behaviour exist that are: surfactant,[3] polymeric[4] and chromonic.[5,6] However, this section will consider only the mesophases generated from surfactants; polymeric and chromonic lyotropic liquid crystal phases are discussed in Chapter Four where they are more relevant.

Surfactants are a type of amphiphile and they possess two mutually incompatible chemical units, a common example being a hydrocarbon chain and a charged (or polar) unit at opposite ends of the molecule (sodium dodecylsulfate, for example, as shown in Figure 1.11 (**a**)). At a certain concentration in water, surfactants self-assemble into structures known as micelles as this lowers the free energy of the system.[3] At a low concentration in water the surfactant molecules are distributed randomly in solution and only above a certain concentration, the critical micelle concentration (cmc), do micellar aggregates form. Micelle formation is driven by the hydrophobic effect where the chains are confined to the centre of the aggregates and the hydrophilic units are located on the periphery where interactions with water are favourable. Although the hydrophobic effect has both enthalpic and entropic contributions, the overall driving force behind it is said to be entropic as the formation of micelles liberates solvent molecules that would otherwise be interacting unfavourably with the aliphatic chains. This in turn unfreezes the alkyl chains of the surfactant and the entropy of the system as a whole increases.

The formation of micelles generates an interface between the hydrophilic and hydrophobic parts of the surfactant and the curvature present at this interface determines the shape of the micelle formed.[7] The critical packing parameters, CPP, which depend on the nature of the surfactant, dictate the curvature present at the hydrophilic-hydrophobic interface as depicted in Figure 1.11 (**b**). The CPP = $v/l_{max}a$, where l_{max} is the length of the hydrophobic chain, a is the area occupied by the hydrophilic head group and v is the volume occupied by the hydrophobic chain; Table 1.1 shows how the CPP influences micellar shape. Surfactants with large head groups and small aliphatic chains form spherical micelles, whereas those with head groups and chains that occupy similar volumes form micelles with a planar interface (discs, for example). Then, as the volume of the aliphatic chains increases and exceeds the volume occupied by the polar unit, curvature is re-established but of the reverse sense, where the head groups are confined in the centre of the aggregates and the aliphatic chains project away from the aggregate to form water-in-oil type

micelles. The same geometric arguments dictate the shape of inverse micelles such that inverse cylinders and inverse spherical micelles can also form.
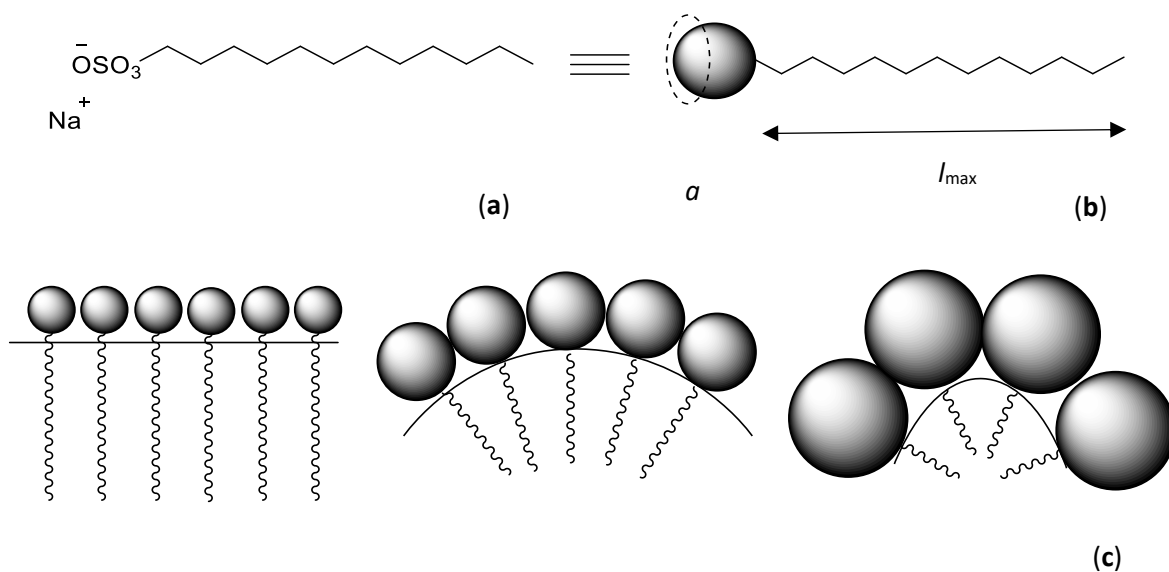
Figure 1.11. (**a**) Structure of sodium dodecylsulfate, (**b**) schematic representation of a surfactant where the sphere represents the hydrophilic unit and (**c**) how the relative volume of the hydrophilic and hydrophobic parts influence curvature at the hydrophilic-hydrophobic interface.

Table 1.1. How the critical packing parameters control micellar shape.

CPP	Shape of surfactant	Shape of micelle
$\dfrac{v}{l_{max}a} < \dfrac{1}{3}$		Spherical
$\dfrac{1}{3} < \dfrac{v}{l_{max}a} < \dfrac{1}{2}$		Cylindrical
$\dfrac{v}{l_{max}a} \approx 1$		Layers (discs)
$\dfrac{v}{l_{max}a} > 1$		Inverse
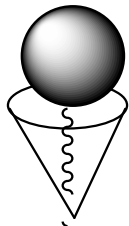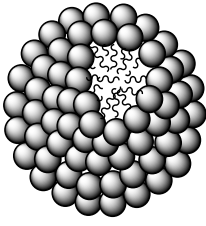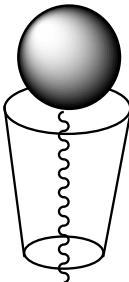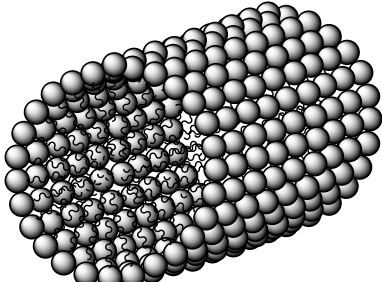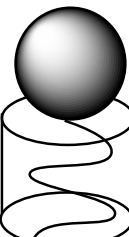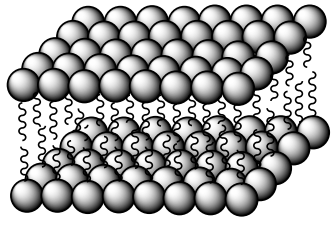
Eventually, the concentration of micelles in solution becomes so high that they must organise, and it is the resulting supramolecular assemblies formed that are the lyotropic liquid-crystal phases. The hypothetical phase diagram of a surfactant in water is shown in Figure 1.12 and shows how the curvature present at the hydrophilic-hydrophobic interface is modified on increasing surfactant

concentration. It must be stressed that no single surfactant forms every mesophase shown in Figure 1.12, nor are the phase transitions ever vertical with temperature in reality. However, it does show the richness of architectures that can be formed.
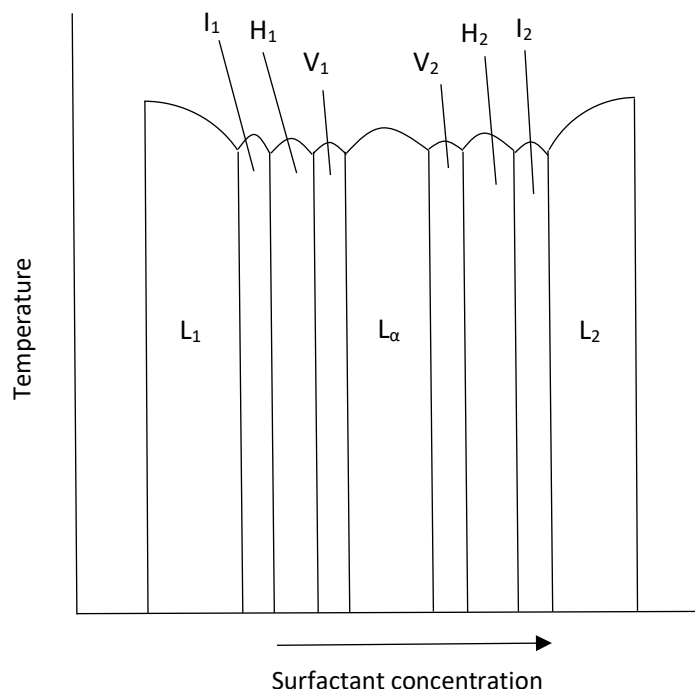
Figure 1.12. Hypothetical phase diagram of a surfactant in water.

Spherical micelles with large curvature of the oil-in-water type form at low surfactant concentrations and characterise the micellar cubic phase, known as I_1. Then, increasing surfactant concentration lends a transition to cylindrical micelles with less curvature, thus forming the hexagonal columnar phase (H_1) as shown in Figure 1.13. A transition then occurs to the bicontinuous cubic phase (V_1), with small curvature at the hydrophilic-hydrophobic interface that is characterised by the formation of continuous aggregates of interconnected rods[8] (Figure 1.14 (**a**) and (**b**)) or infinite periodic minimal surfaces[9] (Figure 1.14 (**c**)).The infinite periodic minimal surfaces model divides space into two parts that is commensurate with an interface between two incompatible units as is the case with the self-organisation of surfactants into micelles. Different shaped surfaces are possible depending on the space group of the bicontinuous cubic phase, the most common being $Im\bar{3}m$ and $Ia\bar{3}d$. The interconnected rod model of the direct cubic bicontinuous phase assumes that the hydrophilic head groups of the surfactant self-assemble to form the connected rods, with the aliphatic chains propagating out to fill the space between the rods; the inverse description is the case for the V_2 phase.
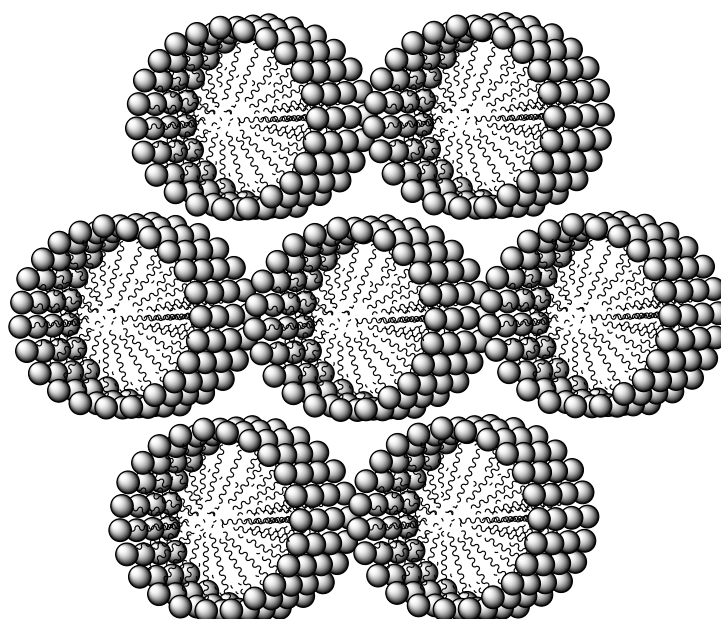
Figure 1.13. Structure of the H_1 phase.

(**a**) (**b**) (**c**)
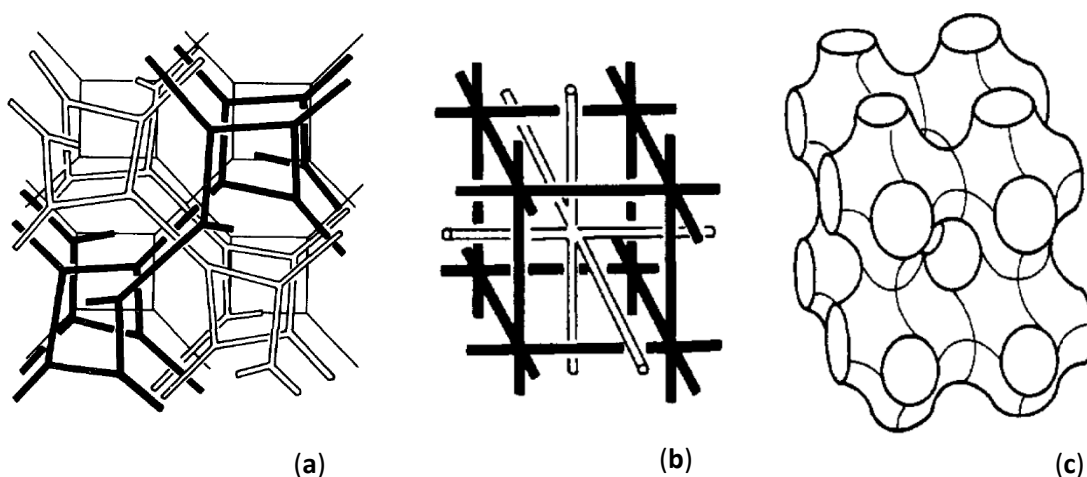
Figure 1.14. Interconnected rod models of (**a**) the bicontinuous cubic phase of the $Ia\overline{3}d$ space group and (**b**) the $Im\overline{3}m$ space group. The infinite periodic minimal surface model (**c**) of the $Im\overline{3}m$ space group.

Planar micelles with zero curvature at the hydrophobic-hydrophilic interface are next to form and this results in the formation of the lamellar phase (L_α). Further increasing the concentration of surfactant generates curvature once more, but of the reversed sense where the volume occupied by the hydrophibic chains is greater than that of the hydrophilic head group. A phase transition into the inverse cubic bicontinuous phase (V_2) occurs, followed by the inverse hexagonal columnar phase (H_2) and finally the inverse micellar cubic phase (I_2).

4.1. The thermotropic-lyotropic analogy

A geometric approach to the structure of liquid-crystalline phases in which the principles discussed above that direct lyotropic phase formation were applied to thermotropic materials by Tschierske[10] and Goodby.[11] Thus, Tschierske and co-workers found a change in mesomorphism from SmA to Col_h and to inverse micellar cubic (I_2) could be achieved by increasing the number of semi-perfluorinated chains attached to a series of pentaerythritol tetrabenzoates (Figure 1.15 I). The presence of semi-perfluorinated chains generates an interface between the largely aromatic core and the fluorinated periphery. Increasing the number of perfluoroalkyl chains increases the curvature generated at this interface, thus leading to a transition from SmA-to-Col_h and to a micellar cubic mesophase, each phase occurring in a different compound. Similarly, Goodby and co-workers demonstrated that a SmA-to-Col_h transition can be brought about by changing the relative volume of the polar and non-polar parts of the molecule in a series of substituted polyols as shown in Figure 1.15 (**a**) and (**b**). This was achieved by synthesising different molecular variants with a different number, and therefore, volume, of aliphatic chains. Results from both studies show how a different mesophase can be achieved by modifying the relative volumes of the incompatible parts of the molecule, conforming to the same arguments as those that explain the lyotropic liquid crystal phases formed by surfactants.
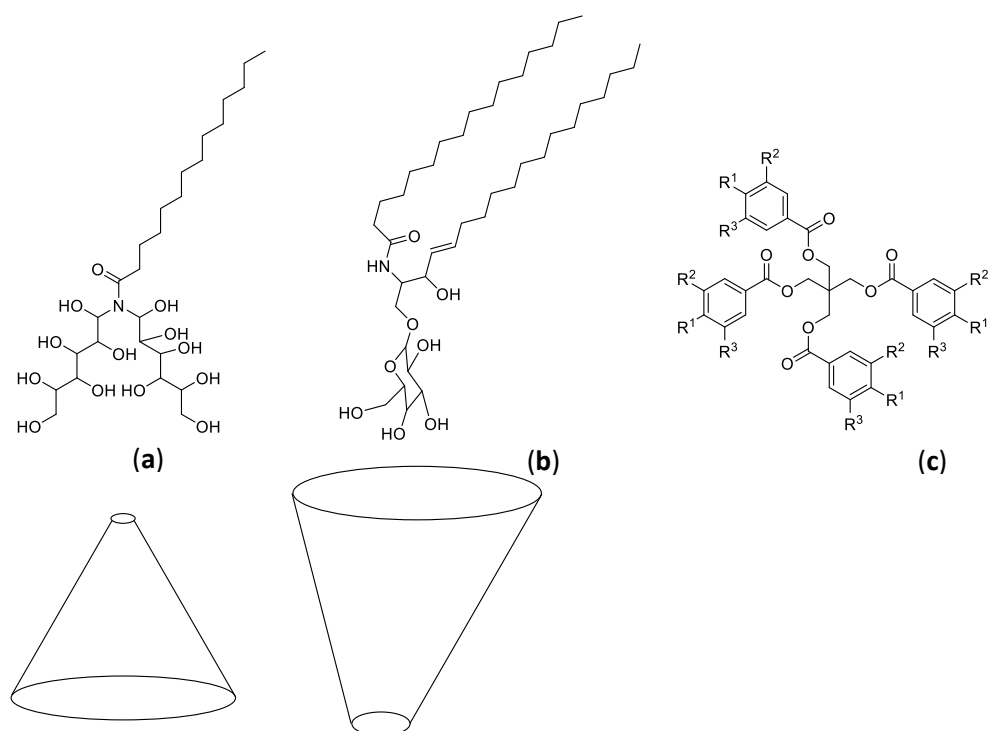
Figure 1.15. Carbohydrate liquid crystals studied by Goodby *et al.* (**a**) and (**b**) and the pentaerythritol tetrabenzoates studied by Tchierske *et al*. (**c**) where R^1, R^2 and R^3 are either H or perfluorocarbon chains to modify interfacial curvature.

5. Polycatenar liquid crystals

Polycatenar liquid crystals are a class of thermotropic liquid crystals that can form mesophases characteristic of both rods and discs, sometimes within a single homologous series. They possess a long, rigid, often aromatic core to which three or more terminal chains are attached to the terminal phenyl rings. Typical structures are shown in Figure 1.16 and they are named tricatenar, tetracatenar and so forth according to the total number of terminal chains attached. Their nomenclature further describes the substitution pattern of the terminal chains, so that, for example, a 2(*mp*)+2(*mp*) compound represents a symmetrically substituted tetracatenar liquid crystal with the terminal chains attached to the *meta* and *para* positions of the terminal aromatic rings. All contain at least one chain in a *meta* position, which is often destabilising, either reducing transition temperatures or supressing mesomorphism altogether. However, in the presence of a longer aromatic core as is the case in polycatenar liquid crystals, the added *meta* chains are reasonably well tolerated.

Hexacatenar: 3(*mpm*)+3(*mpm*)

Pentacatenar: 3(*mpm*)+2(*mp*)

Tetracatenar: 2(*mp*)+2(*mp*)

Tetracatenar: 3(*mpm*)+1(*p*)

Tricatanar: 2(*mp*)+1(*p*)
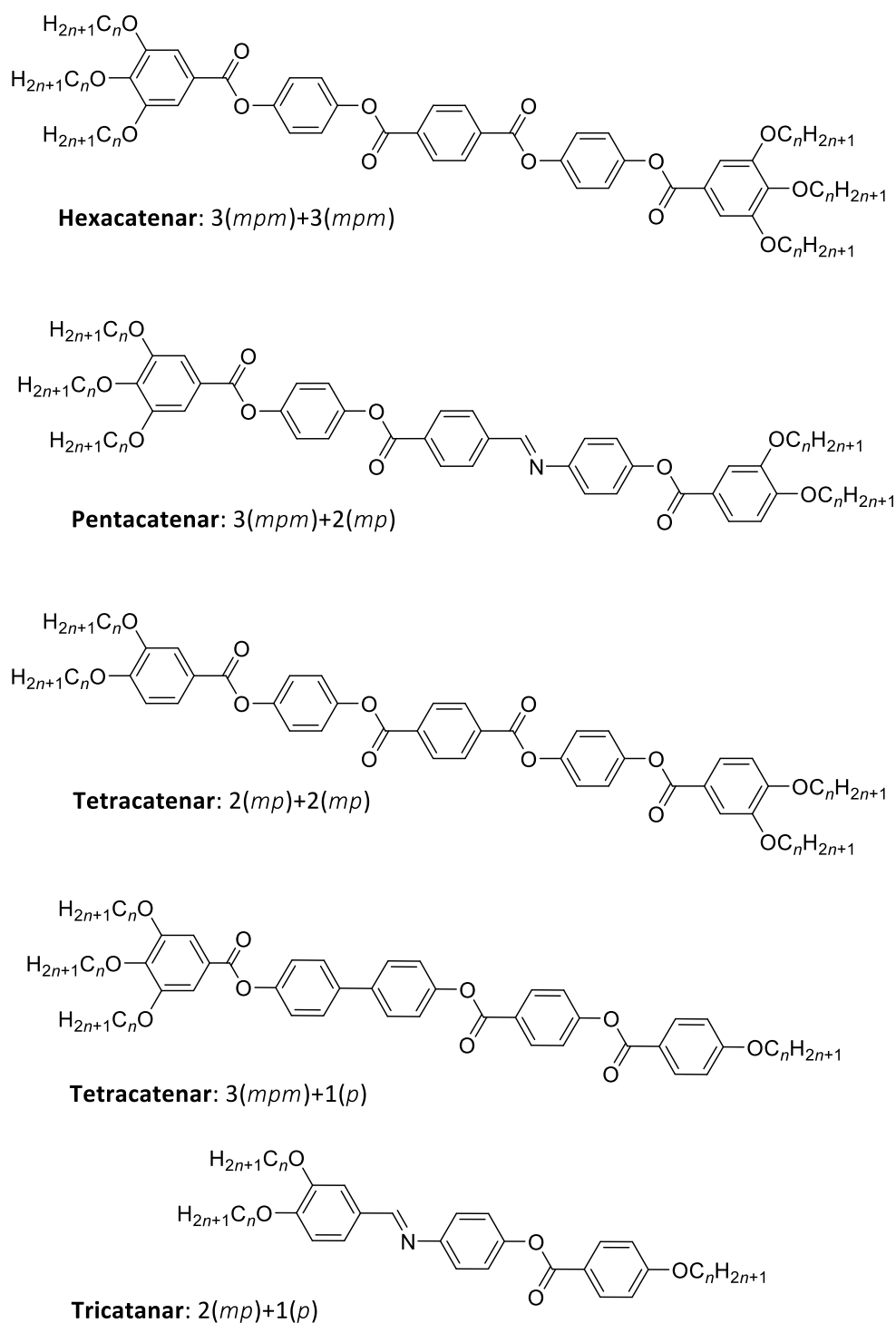
Figure 1.16. A few examples of polycatenar liquid crystals to show the different number and substitution patterns of the terminal chains.

Tricatenar liquid crystals of the 2(*mp*)+1(*p*) type tend to form mesophases characteristic of rods, that is nematic and/or smectic mesophases and this is well understood as their structure resembles closely that of a calamitic compound. 3(*mpm*) tricatenar compounds, on the other hand, have been shown to form cubic mesophases.[12]

30

Tetracatenar liquid crystals, on the other hand, display arguably the richest mesomorphism and their phase behaviour changes typically from nematic and/or SmC mesophases at short terminal chain lengths to columnar mesomophases at long terminal chain lengths, sometimes *via* the formation of an intermediate cubic phase. This behaviour stimulated a significant amount of interest in the field of polycatenar liquid crystals to try and understand exactly why the phase behaviour changes in this way on increasing chain length. As such, a large number of tetracatenar liquid crystals have been prepared and a few examples along with their mesomorphism are presented in Figures 1.17 and 1.18.
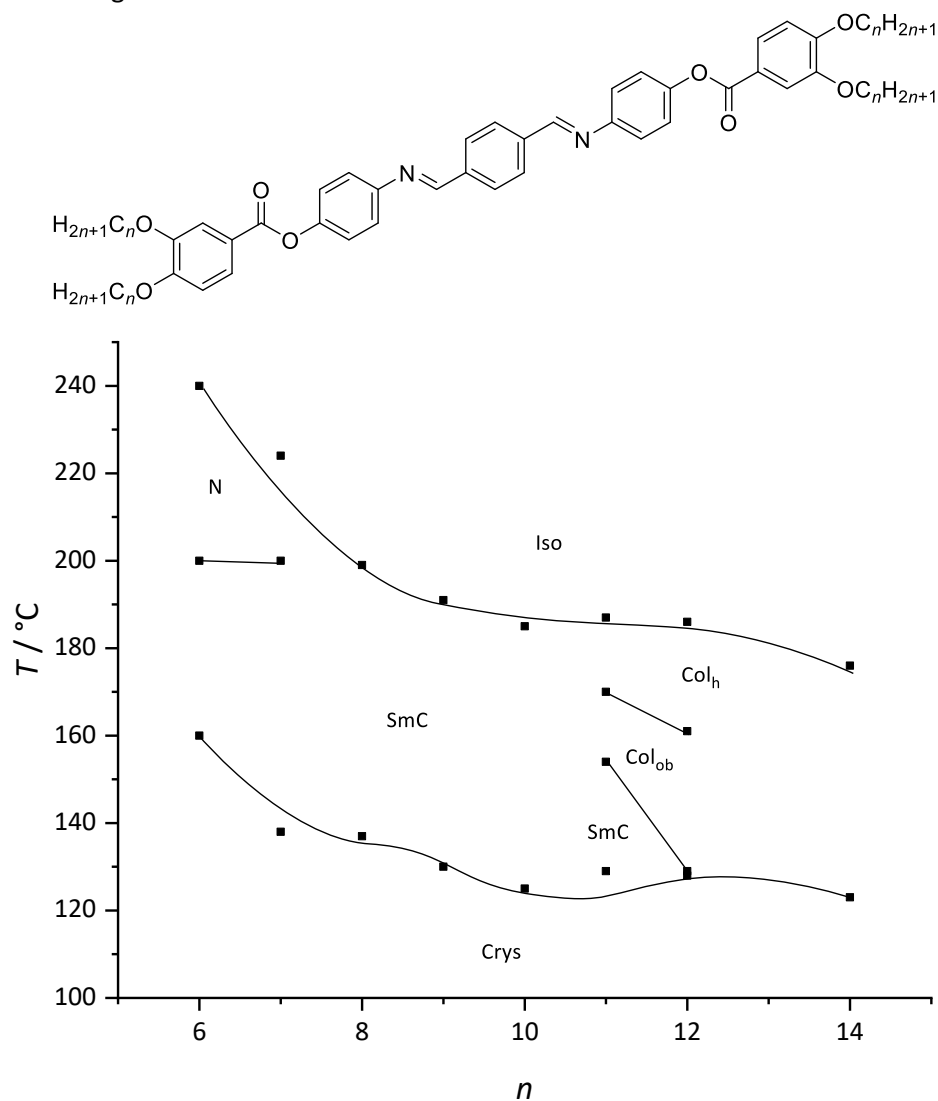
Figure 1.17. Structure and phase diagram of an homologous series of tetracatenar liquid crystals reported by Destrade *et al.*[13]
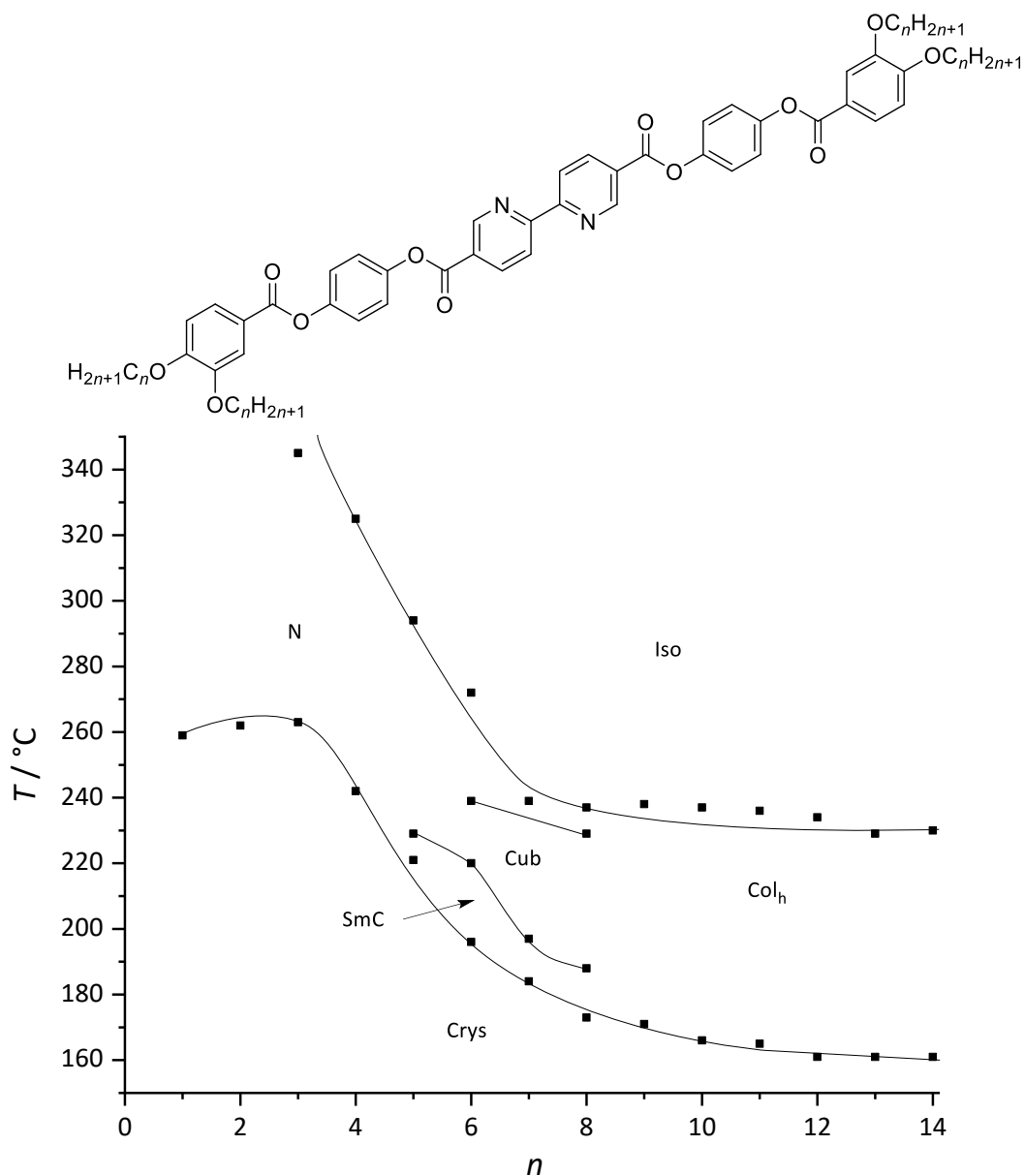
Figure 1.18. Structure and phase diagram of the tetracatenar 2,2'-bipyridines studied by Rowe and Bruce.[14]

Malthête *et al.*[15] originally proposed an initial model of the Col_h phase formed by tetracatenar liquid crystals that was akin to a two-dimensional layered structure as shown in Figure 1.19. In essence, an inner shell of molecules exist that pack in a more conventional discotic-like fashion and around this are arranged a curved layer of molecules to form a disc-like aggregate that can self-assemble in a hexagonal array.
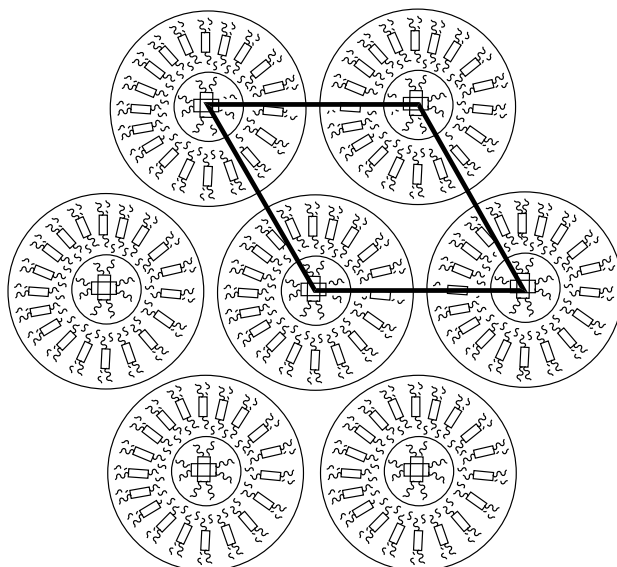
Figure 1.19. Initial structure of the columnar hexagonal phase formed by tetracatenar liquid crystals proposed by Malthête *et al.*[15]

The mesomorphism of pentacatenar and hexacatenar compounds is dominated by the formation of columnar hexagonal mesophases, with a few pentacatenar compounds also forming a cubic phase (Figures 1.20 and 1.21).

n = 7: Crys 80 °C Col$_{ob}$ 82 °C Iso
n = 12: Crys 70 °C Col$_{ob}$ 82 °C Col$_h$ 92 °C Iso
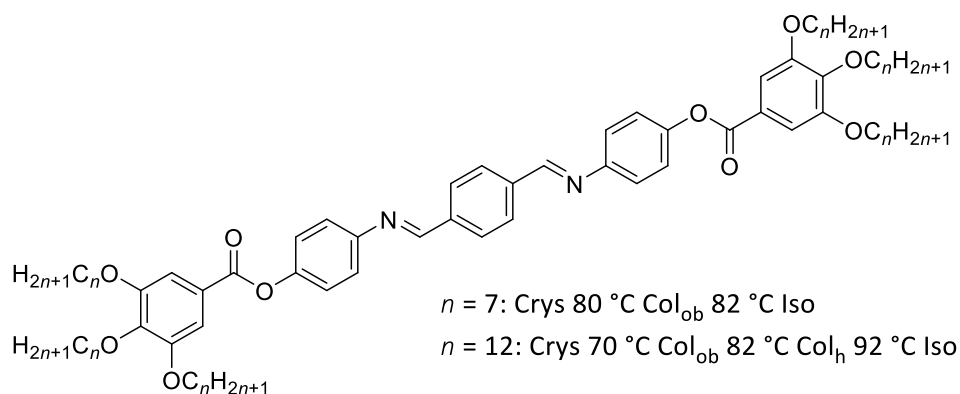
Figure 1.20. Structure and mesomorphism of a series of hexacatenar liquid crystals studied by Malthête *et al.*[16]

33

Crys 75 °C Col$_h$ 132 °C Iso
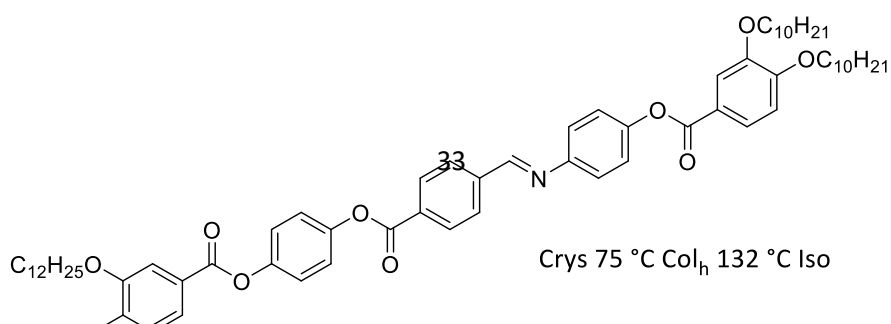
Figure 1.21. Structure and mesomorphism of a 3(*mpm*)+2(*mp*) pentacatenar liquid crystal.[12]

5.1. Discussion of general mesomorphic trends in tetracatenar liquid crystals

The behaviour of 2(*mp*)+2(*mp*) tetracatenar liquid crystals is most interesting as their mesomorphism changes from nematic and/or smectic C at short terminal chain lengths to columnar at long terminal chain lengths, sometimes even passing through an intermediate cubic phase.[17] Thus, at short terminal chain lengths, mesophases characteristic of rods are formed, whereas at long terminal chain lengths those characteristic of discs are observed. This behaviour is why tetracatenar materials have been studied rigorously, as the change in the nature of the mesophase is achieved simply by varying the length of the terminal chains (and in some cases even by changing the temperature of a single compound).

Tetracatenar liquid crystals tend to form a nematic phase at very short chain lengths as the terminal chains are not sufficiently long to cause segregation between the aromatic and aliphatic parts of the molecule. On increasing the chain length, the next mesophase observed is the SmC phase where segregation of the aliphatic and aromatic parts of the molecule now occurs due to the efficient space-filling that self-organisation into layers achieves. Interesting is that the only lamellar phase formed by tetracatenar materials is the SmC phase and this can be explained by the steric requirements that the four terminal chains impart.[17] Introducing the extra chains of a tetracatenar liquid crystal results in a discrepancy between the cross-sectional area of the terminal chains projected onto the core and the cross-sectional area of the core itself (Figure 1.22). As such, the mesogens must tilt to self-organise into layers, thus the SmC phase forms instead of the SmA phase.
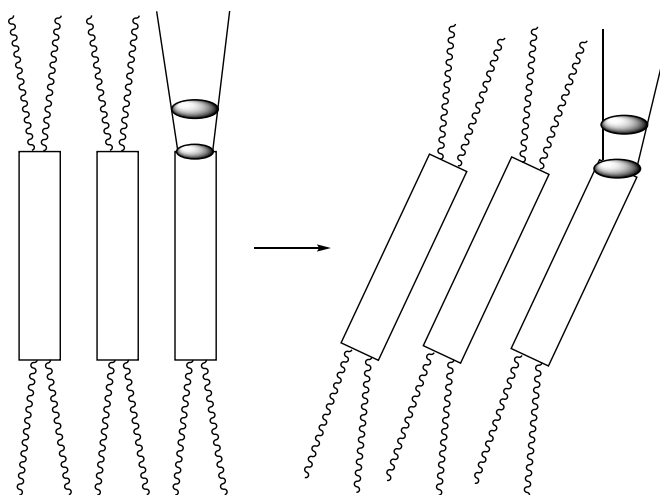
Figure 1.22. Schematic to show the origin of the tilt in the lamellar phases formed by tetracatenar liquid crystals.

Increasing the terminal chain length is accompanied by a transition into a columnar phase, sometimes *via* an intermediate cubic phase. Focussing on the transition into a columnar phase (as not all tetracatenar liquid crystals display a cubic phase), the mode of packing and mechanism for the transition into this phase must be addressed. In a paper published by Guillon, Skoulios and Malthête[18] concerning the structure of Col$_h$ phases formed by hexacatenar compounds, the authors found that the cross-section of a column contained three hexacatenar molecules where the chains propagated out from the cores to fill space efficiently as represented by Figure 1.23 (**c**). They also discovered that excluded volume effects were quite important at the anchoring point of the chains onto the terminal phenyl rings, such that the terminal rings of the core must bend outwards to generate the extended interface between the aromatic and aliphatic parts of the molecule (Figure 1.23 (**c**).

Guillon and co-workers[19] then investigated the SmC-to-Col$_h$ phase transition exhibited by the tetracatenar liquid crystal presented in Figure 1.23 (**b**). They concluded that the structure of the Col$_h$ phase was analogous to that proposed previously for hexacatenar materials, except that typically four molecules constituted the cross-section of the column rather than three in the case of hexacatenar compounds, thus departing from the original model proposed earlier in Figure 1.19. This is due to the lower number of alkyl chains present in tetracatenar compounds, so that more molecules were required to achieve the necessary density of alkyl chains to fill space efficiently. X-Ray diffraction data also showed that the cross-section of a column (the *a* parameter of the Col$_h$ phase) was equivalent to the all *trans* molecular length of the tetracatenar molecule, thus the molecules were likely positioned perpendicular to the propagation axis of a column.
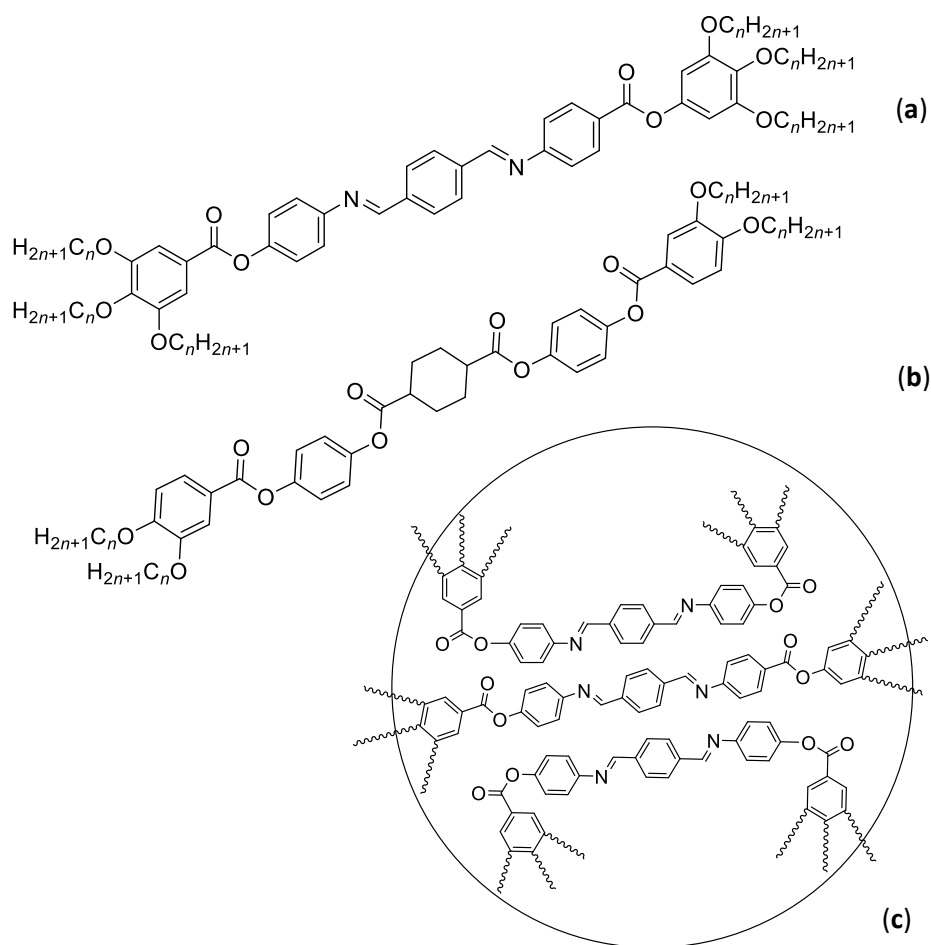
Figure 1.23. Structure of (**a**) the hexacatenar materials[18] and (**b**) tetracatenar materials[19] studied by Guillion and co-workers to determine the structure of the columnar mesophases formed by polycatenar liquid crystals. Arrangement of (**c**) the hexacatenar compounds in the cross-section of a column proposed by Guillon.[18]

In order to explain the transition from the SmC phase to the Col_h phase it was proposed that the tilt angle initially increases until the extra terminal chain volume can no longer be accommodated by additional tilting. The layers then begin to undulate and eventually these undulations become so great that discrete packets of molecules can be identified that represent the cross-section of a column, marking the transition into the Col_h phase (Figure 1.24). It was from these studies that an analogy was drawn between the structure of the columnar mesophases formed by polycatenar liquid crystals and the two-dimensional ribbon phases formed by the alkali metal soaps and polar calamitic mesogens.[20] Studies performed by Smirnova and co-workers also support this mechanism for the transition from SmC-to-columnar self-organisation in a series of laterally substituted tetracatenar mesogens.[21] It is therefore important to stress that the columnar mesophases formed by polycatenar liquid crystals are quite different in terms of the organisation present within the columns to the columnar mesophases formed by conventionally discotic mesogens. Thus, in

polycatenar systems, the columns are not constructed from single molecules stacked on top of one another, rather the columns are akin to ribbons that arrange on a two-dimensional hexagonal or rectangular lattice.

SmC   Undulating SmC   Columnar
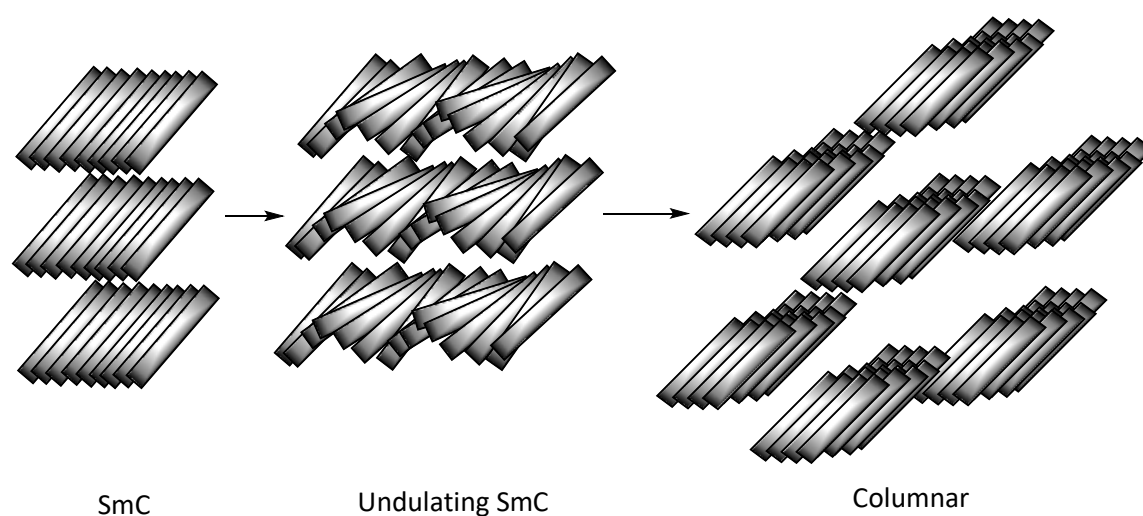
Figure 1.24. Schematic to show the transition from SmC to columnar self-organisation on increasing terminal chain length.

Bruce *et al.*[22] found that in the Col_h phases formed by a series of hexacatenar palladium complexes (Figure 1.25) the *a* parameter was significantly smaller than the all-*trans* molecular length. This observation therefore suggested a system in which the molecules cannot lie perpendicular to the propagation axis of a column as proposed earlier by Guillon.[19] However, the columns must project a circular cross-section when viewed down the propagation axis for the *p6mm* symmetry of the hexagonal phase to be satisfied and so the authors proposed a revised model by which the molecules tilt within the column to achieve this as depicted in Figure 1.25 (**b**). Different compounds can then tilt to different extents to project a circular cross-section, and, therefore, self-organise into the Col_h phase. It is the efficient space-filling of the Col_h phase that drives its formation and is the reason why different polycatenar molecules tilt to different extents to self-assemble into a hexagonal mode of packing. As such, the revised model takes into account different extents of tilting, with one extreme being the tetracatenar compounds studied by Guillion[19] that lie at 90° to the columnar long axis and the dithiolium compounds studied by Antzner *et al.*[23] that lie at the other extreme where molecules are almost parallel to the propagation axis.
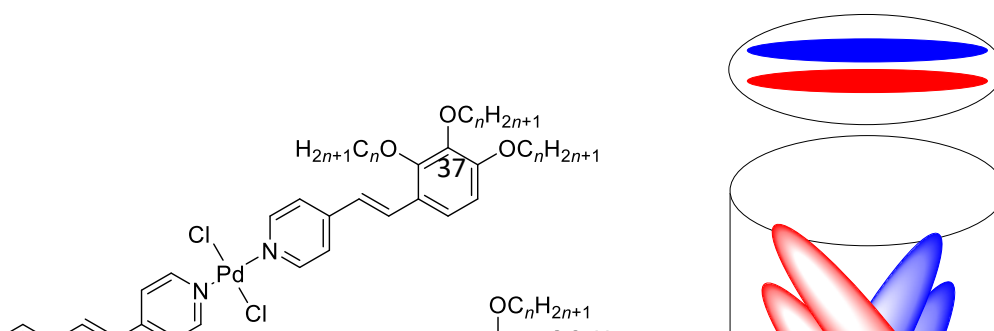
(a)

(b)

Figure 1.25. Two isomeric hexacatenar palladium stilbazole complexes studied by Bruce *et al.*[22] (**a**) and a generalised model for the arrangement of polycatenar liquid crystals within a column showing tilting of the mesogens (**b**).

5.2. Cubic phases formed by polycatenar liquid crystals

In the lyotropic liquid crystal phases formed by surfactants, a cubic phase can in principle form between any pair of mesophases as evidenced from the form of the hypothetical phase diagram presented in Figure 1.12. Staying with the analogy to lyotropic mesophases, the cubic phases formed by polycatenar liquid crystals are, therefore, analogues of the inverse cubic bicontinuous (V_2) phases as they typically appear above a lamellar phase and below a columnar phase that is the analogue of an H_2 hexagonal phase. However, the formation of cubic phases by polycatenar liquid crystals is rather delicate, as sometimes the transition from SmC to columnar self-organisation takes place directly. For example, the 2,2'-bipyridinines presented in Figure 1.18 demonstrate well the change from SmC to Col_h mesomorphism *via* an intermediate cubic phase, whereas the tetracatenar stilbazole complexes of Pd(II) shown in Figure 1.26 (**a**) move directly from SmC to Col_h self-organisation (no cubic phase is formed).

In considering the review published by Diele[24] on the formation of cubic mesophases by thermotropic materials, a large number of compounds forming this phase have the ability to form specific intermolecular interactions in addition to possessing interfacial curvature at the aromatic-aliphatic interface. Indeed, the polycatenar liquid crystals known to form a cubic phase also possess some kind of intermolecular interaction in addition to van der Waals forces. These are dipole-dipole in the case of the 2,2'-bipyridines[14] and electrostatic in the case of the stilbazole complexes of

silver(I)[25] presented in Figure 1.26 (**b**). Bruce and co-workers conducted a systematic study in trying to structurally replicate the ionic silver(I) salts by a series of neutral monoacetylide complexes of Pt(II) that also possessed stilbazole ligands and a single lateral chain that mimicked the counter-ion.[26] Interestingly, these neutral analogues formed only SmC and nematic mesophases and the cubic phase was totally absent. This supported the proposal of the need for specific intermolecular attractions in addition to the necessary interfacial curvature for the cubic phases to form. Although good evidence exists for the need of specific intermolecular interactions to stabilise the bicontinuous cubic phases formed by polycatenar liquid crystals, their stabilisation is still not completely understood.
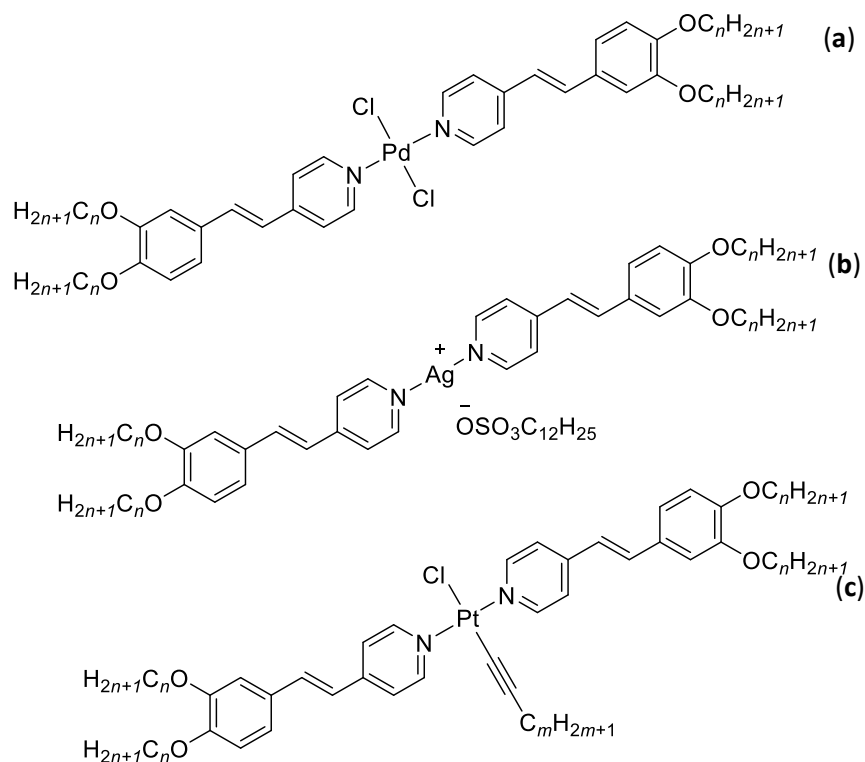
Figure **1.26.** Structure of (**a**) the tetracatenar stilbazole complexes of Pd(II),[27] (**b**) the stilbazole complexes of silver(I) dodecylsulfate[25] and (**c**) and the monoacetylide complexes of Pt(II).[26]

6. Ionic liquid crystals

Ionic liquid crystals (ILCs) differ from neutral thermotropic liquid crystals as the constituent components of the mesophase are anions and cations, with the species giving rise to mesomorphism usually being the cation. Often pyrdinium,[31,32] 4,4'-bipyridinium (viologen),[33,34] imidazolium[35] and guanidinium[36] moieties are employed as the ionic units in ILCs due to their ease of preparation and functionalisation (Figure 1.27). Anions vary but typically include halides, triflate, sulfate, tetrafluoroborate, isocyanate and, more recently, triflimide. The anion is usually smaller than the cation so as not to significantly disrupt self-organisation into liquid-crystal phases. However, varying the anion can actually be employed as a method of modifying the mesomorphism of ILCs.

ILCs are an interesting area of materials chemistry, as they combine the properties inherent to ionic liquids (good solvents with low volatility) and liquid crystals (anisotropic self-organisation). A recent review published by Goossens *et al*.[37] provides a good overview of ILCs and their applications up to and including 2015. Many of the ILCs studied to that date are typically rod-like, disc-like or wedge-shaped and a few examples of these compounds are presented in Figure 1.27. The most common mesophase formed by calamitic ILCs is the SmA phase, as electrostatic attractions between anions and cations stabilise the formation of layers. Discotic and wedge-shaped ILCs tend to form columnar mesophases with electrostatic attractions driving the formation of columnar aggregates. An important application of the wedge-shaped imidazolium based ILCs shown in Figure 1.27 (**b**) studied by Kato *et al*.[29,38] has been the development of devices with anisotropic conductivity and mass transport. This has been achieved due to segregation of the ionic and aliphatic parts of the molecule to give rise to Col_h mesophases. The columns can be aligned macroscopically parallel to a glass substrate that has been treated by mechanical shearing or perpendicular when the substrate is functionalised with amine groups. Bruce, Slattery and co-workers[28] have also demonstrated that ILCs can act as solvents to influence the stereochemistry of the Diels Alder reaction.
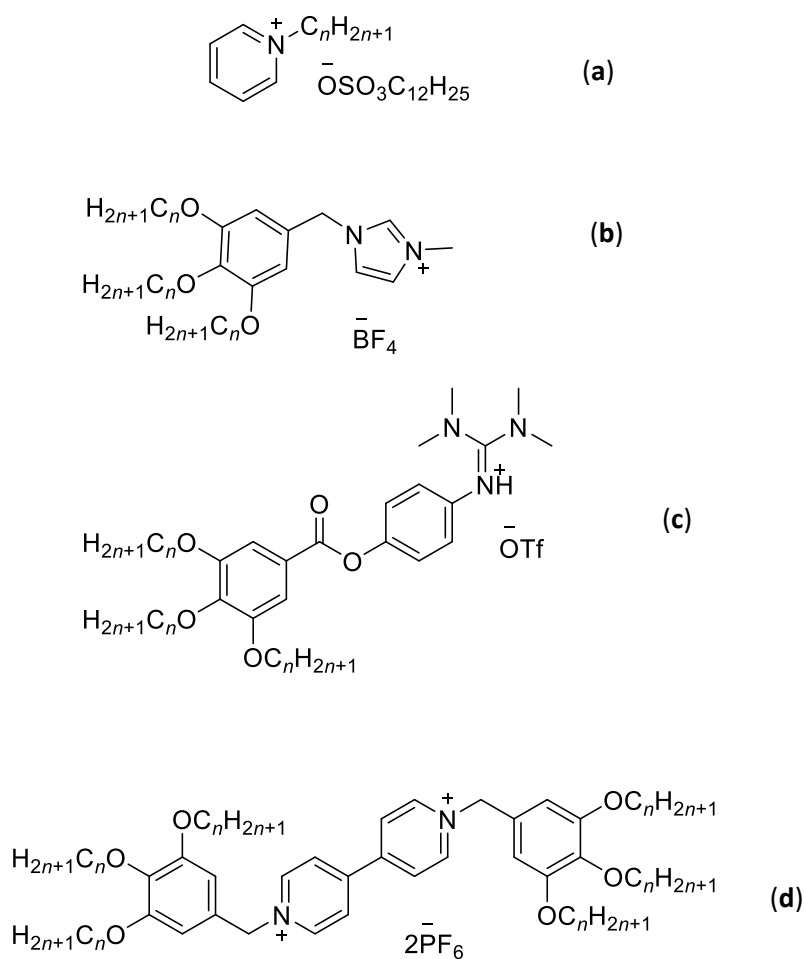
Figure 1.27. A few examples of ionic liquid crystals: (**a**) *N*-alkylpyridinium dodecylsulfates studied by Bruce *et al.*[31] (**b**) wedge-shaped imidazolium ILCs studied by Kato *et al.*[38] with anion-dependent ion conductivities, (**c**) room temperature ILCs based on the guanidinium moiety studied by Laschat *et al.*[36] and (**d**) the redox-active hexacatenar viologen salts studied by Kato *et al.*[39] for devices with anisotropic ion conduction.

Tosoni, Laschat and Baro[40] studied imidazolium ILCs with a chiral (*R*)-citronellyl chain as shown in Figure 1.28 (**a**). Interestingly, only when the length of the alkyl chain was *n*-$C_{14}H_{29}$ was mesomorphism observed, this being a monotropic SmA phase. Mesomorphism was never observed when the alkyl chain was CH_3, *n*-C_4H_9, *n*-C_6H_{13}, *n*-$C_{12}H_{25}$ and *n*-$C_{18}H_{37}$, nor even when the chain was a second (*R*)-citronellyl group. However, more stable mesomorphism was obtained when the chiral centre was moved along the chain in a series of *N*-methylated imidazolium salts[41] (Figure 1.28 (**b**)), which was achieved through modification of the (*R*)-citronellol starting material before *N*-alkylation. Interestingly, no chirality was translated into the mesophase due to the chiral substituent acting as a 'stopper' to prevent chain interdigitation and the only mesophase observed was SmA.
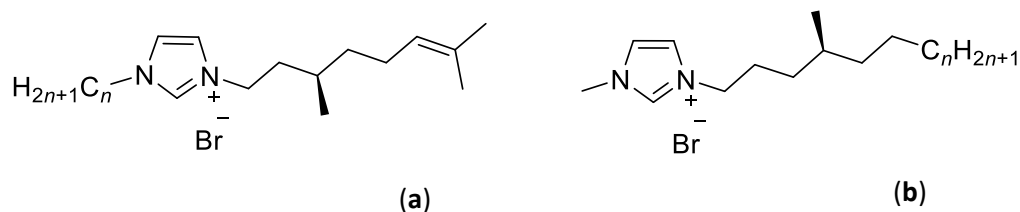
Figure 1.28. Structure of (**a**) the chiral imidazolium LCs with a (*R*)-citronellyl chain[40] and (**b**) the chiral *N*-methylated imidazolium LCs[41] where the chiral centre has moved along the chain.

Another interesting group of materials are the pyridinium ILCs studied by Circu and co-workers[42,43] presented in Figure 1.29, which exclusively form a nematic phase, a mesophase not commonly associated with ionic materials that would otherwise be expected to self-organise into smectic phases. While nematic phases have been previously reported in ionic calamitic mesogens in, for example, the rod-shaped stilbazole complexes of silver(I) studied by Bruce *et al.*,[44] they are very much an exception to the rule rather than the norm. A minimum spacer length of six carbon atoms was required to generate a mesomorphic material with bulkier anions (PF_6^- and OTf^-), but the nature of the anion and spacer length did not influence the type of mesophase observed.
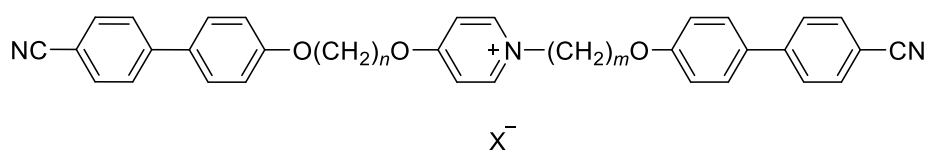
Figure 1.29. Structure of the pyridinium ILCs studied by Circu *et al.*[42] that form a nematic phase: X = Br⁻, OTf⁻, BF_4^-, PF_6^-, NO_3^- or SCN⁻.

7. Aims

The mesomorphism of neutral polycatenar liquid crystals is well understood and many variants have been synthesised to date. However, the only ionic polycatenar liquid crystals that have been studied in systematic detail are the silver(I) salts prepared by Donnio *et al.*[25] (Figure 1.26) and it was found during this work that these materials actually exist as tightly bound ion pairs, evidenced through a lack of conductivity in the liquid-crystal phases. Though formally ionic, the silver(I) salts are not completely charge separated ions pairs and to investigate how the mesomorphism of truly ionic polycatenar liquid crystals would compare an homologous series of compounds based on the *N*-phenylpyridinium moiety have been prepared (Figure 1.30). This thesis will document the synthesis and mesomorphism of such newly prepared ionic materials and a more detailed overview covering the mesomorphism of the silver(I) salts is presented in Chapter Three.
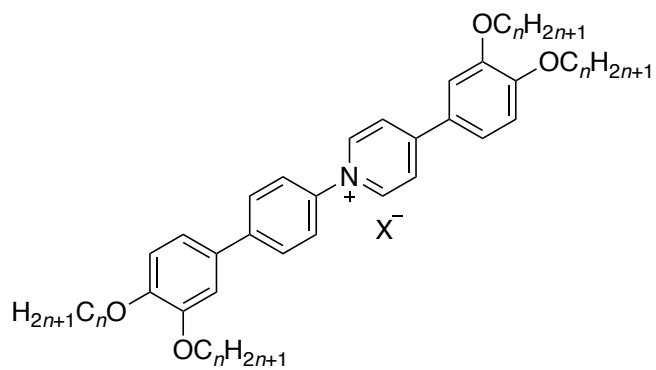
Figure 1.30. Structure of the *N*-phenylpyridinium liquid crystals that will be the major focus of this thesis: X is either triflate, a long chain alkylsulfate or triflimide.

8. References

1   F. Reinitzer, *Ann. Phys.*, 1908, **332**, 213–224.

2   S. Laschat, A. Baro, N. Steinke, F. Giesselmann, C. Hägele, G. Scalia, R. Judele, E. Kapatsina, S. Sauer, A. Schreivogel and M. Tosoni, *Angew. Chem. Int. Ed.*, 2007, **46**, 4832–4887.

3   A. Skoulios and V. Luzzati, *Nature*, 1959, **183**, 1310–1312.

4   T. K. Attwood, J. E. Lydon, C. Hall and G. J. T. Tiddy, *Liq. Cryst.*, 1990, **7**, 657–668.

5   J. Lydon, *J. Mater. Chem.*, 2010, **20**, 10071.

6   S.-W. Tam-Chang and L. Huang, *Chem. Commun.*, 2008, 1957.

7   J. N. Israelachvili, D. J. Mitchell and B. W. Ninham, *J. Chem. Soc. Faraday Trans. 2*, 1976, **72**, 1525.

8   V. Luzzati and P. A. Spegt, *Nature*, 1967, **215**, 701–704.

9   J. Charvolin and J. F. Sadoc, *J. Phys.*, 1988, **49**, 521–526.

10   X. H. Cheng, S. Diele and C. Tschierske, *Angew. Chem. Int. Ed.*, 2000, **39**, 592–595.

11   J. J. West, G. Bonsergent, G. Mackenzie, D. F. Ewing, J. W. Goodby, T. Benvegnu, D. Plusquellec, S. Bachir, P. Bault, O. Douillet, P. Godé, G. Goethals, P. Martin and P. Villa, *Mol. Cryst. Liq. Cryst.*, 2001, **362**, 23–44.

12   H. T. Nguyen, C. Destrade and J. Malthête, *Adv. Mater.*, 1997, **9**, 375–388.

13   C. Destrade, H. T. Nguyen, A. Roubineau and A. M. Levelut, *Mol. Cryst. Liq. Cryst.*, 1988, **159**, 163–171.

14   K. E. Rowe and D. W. Bruce, *J. Mater. Chem.*, 1998, **8**, 331–341.

15   A. M. Levelut, J. Malthête, C. Destrade and N. H. Tinh, *Liq. Cryst.*, 1987, **2**, 877–888.

16   J. Malthête, A. M. Levelut and H. T. Nguyen, *J. Phys. Lett.*, 1985, **46**, 875–880.

17   D. Fazio, C. Mongin, B. Donnio, Y. Galerne, D. Guillon and D. W. Bruce, *J. Mater. Chem.*, 2001, **11**, 2852–2863.

18   D. Guillon, A. Skoulios and J. Malthête, *Europhys. Lett.*, 1987, **3**, 67–72.

19   D. Guillon, B. Heinrich, A. C. Ribeiro, C. Cruz and H. T. Nguyen, *Mol. Cryst. Liq. Cryst.*, 1998, **317**, 51–64.

20   F. Hardouin, Nguyen Huu Tinh, M. F. Achard and A. M. Levelut, *J. Phys. Lett.*, 1982, **43**, 327–331.

21   A. I. Smirnova, B. Heinrich, B. Donnio and D. W. Bruce, *RSC Adv.*, 2015, **5**, 75149–75159.

22   D. W. Bruce, B. Donnio, B. Heinrich, D. Guillon, J. Kain, S. Diele and H. Allouchi, *J. Am. Chem. Soc.*, 2004, **126**, 15258–15268.

23   F. Artzner, M. Veber, M. Clerc and A.-M. Levelut, *Liq. Cryst.*, 1997, **23**, 27–33.

24   S. Diele, *Curr. Opin. Coll. Interfac. Sci.*, 2002, **7**, 333–342.

25   B. Donnio and D. W. Bruce, *New J. Chem.*, 1999, **23**, 275–286.

26   C. Mongin, B. Donnio and D. W. Bruce, *J. Am. Chem. Soc.*, 2001, **123**, 8426–8427.

27   B. Donnio and D. W. Bruce, *J. Chem. Soc. Dalt. Trans.*, 1997, 2745–2756.

28   D. W. Bruce, Y. Gao, J. N. Canongia Lopes, K. Shimizu and J. M. Slattery, *Chem. Eur. J.*, 2016, **22**, 16113–16123.

29   H. Shimura, M. Yoshio, K. Hoshino, T. Mukai, H. Ohno and T. Kato, *J. Am. Chem. Soc.*, 2008, **130**, 1759–1765.

30   T. Mukai, M. Yoshio, T. Kato, M. Yoshizawa and H. Ohno, *Chem. Commun.*, 2005, 1333–1335.

31   D. W. Bruce, S. Estdale, D. Guillon and B. Heinrich, *Liq. Cryst.*, 1995, **19**, 301–305.

32   C. Cruz, B. Heinrich, A. C. Ribeiro, D. W. Bruce and D. Guillon, *Liq. Cryst.*, 2000, **27**, 1625–1631.

33   P. K. Bhowmik, H. Han, I. K. Nedeltchev and J. J. Cebe, *Mol. Cryst. Liq. Cryst.*, 2004, **419**, 27–46.

34   Y. Haramoto, M. Yin, Y. Matukawa, S. Ujiie and M. Nanasawa, *Liq. Cryst.*, 1995, **19**, 319–320.

35   M. Yoshio, T. Kagata, K. Hoshino, T. Mukai, H. Ohno and T. Kato, *J. Am. Chem. Soc.*, 2006, **128**, 5570–5577.

36   M. Butschies, J. C. Haenle, S. Tussetschläger and S. Laschat, *Liq. Cryst.*, 2013, **40**, 52–71.

37   K. Goossens, K. Lava, C. W. Bielawski and K. Binnemans, *Chem. Rev.*, 2016, **116**, 4643–4807.

38   M. Yoshio, T. Ichikawa, H. Shimura, T. Kagata, A. Hamasaki, T. Mukai, H. Ohno and T. Kato, *Bull. Chem. Soc. Jpn.*, 2007, **80**, 1836–1841.

39   K. Tanabe, T. Yasuda, M. Yoshio and T. Kato, *Org. Lett.*, 2007, **9**, 4271–4274.

40   M. Tosoni, S. Laschat and A. Baro, *Helv. Chim. Acta*, 2004, **87**, 2742–2749.

41   G. Kohnen, M. Tosoni, S. Tussetschläger, A. Baro and S. Laschat, *Eur. J. Org. Chem.*, 2009, **2009**, 5601–5609.

42   A. Pană, I. Pasuk, M. Micutz and V. Cîrcu, *CrystEngComm*, 2016, **18**, 5066–5069.

43   A. Pană, A. L. Panait and V. Cîrcu, *Res. Chem. Intermed.*, 2018, **44**, 2025–2038.

44   D. W. Bruce, *Acc. Chem. Res.*, 2000, **33**, 831–840.

Chapter Two: Synthesis and Characterisation of a Series of Tetracatenar *N*-Phenylpyridium Ions and a Series of 3,4-Dialkoxyphenylpyridine Complexes of Silver(I) Triflate and Silver(I) Dodecylsulfate

1. Introduction

The major objective of this project was to prepare a series of truly ionic polycatenar liquid crystals that exist as charge-separated ion pairs. The only ionic polycatenar liquid crystals that have previously been prepared are the 3,4-dialkoxystilbazole complexes of silver(I) prepared by Donnio *et al.*[1] and a hexacatenar viologen salt prepared by Kato.[2] While the silver(I) salts are formally ionic, conductivity measurements show that they exist as tightly bound ion pairs and so do not provide a true representation of how charge separated materials would behave.[3] In satisfying this objective, a series of compounds were designed that were based on the *N*-phenylpyridinium unit that can readily be accessed *via* Zincke chemistry.[4] Our initial target compounds were designed to mimic closely the silver(I) salts studied by Donnio *et al.*[1] in order to remove, as far as possible, any structural differences that would otherwise influence their liquid crystal properties. These compounds would, therefore, contain vinylic groups between the terminal rings, much like the stilbazole ligands of the silver(I) salts (see a comparison between these compounds in Figure 2.1).

2. Initial Target Compounds

The initial target compounds, **1**-*n*, are presented in Figure 2.1. Multiple attempts at the preparation of **1**-*n* were made, as will now be described.
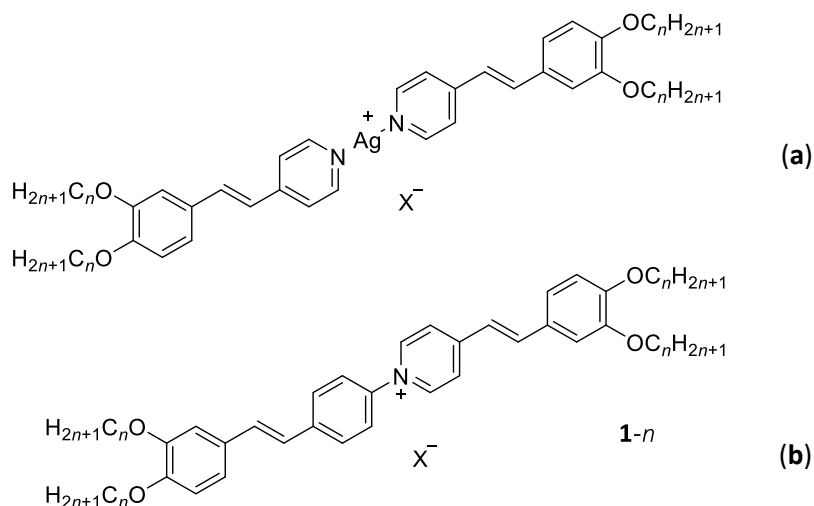
Figure 2.1. Structures of (**a**) the silver(I) stilbazole salts studied by Donnio *et al.* and (**b**) the initial *N*-phenylpyridinium targets (**1**-*n*) that would closely mimic the silver(I) salts**.**

2.1. Initial attempts at preparing the *N*-phenylpyridinium materials

Before the preparation of a tetracatenar material was attempted, it was decided to first prepare a series of analogous calamitic compounds with only two terminal chains, **2**-*n* (Figure 2.2). Two

reasons were behind this. First, the preparation of calamitic compounds ought to be more readily achieved due to the better solubility of compounds with two terminal chains that was based on previous experience of this in the group and so a base procedure could be easily established with these compounds. Second is that ionic calamitic compounds containing the *N*-phenylpyridinium core have not been studied before and so preparing such two-chained materials opens up the option to study their liquid-crystalline behaviour, too. As such, the following section documents the preparation of compounds with only two terminal chains.

The first synthetic route attempted was centred about a convergent synthesis that involved a double Siegrist reaction[5] between imine **5**-*n* and Zincke salt **7** as shown in Scheme 2.1. The use of a Siegrist reaction seemed the obvious choice at the time, as the geometry of the double bond produced would be exclusively *trans*, thus removing the need for any troublesome *cis-trans* separation techniques in the workup.
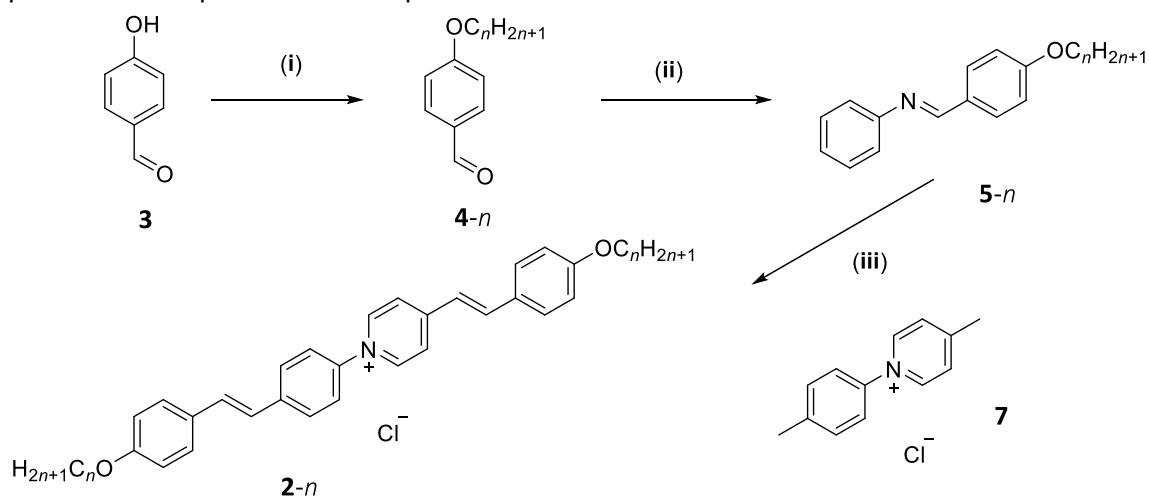
Scheme 2.1. Attempted synthesis of final compounds **2**-*n* using a double Siegrist reaction: (**i**) $C_nH_{2n+1}Br$, DMF, K_2CO_3 (**ii**) aniline, EtOH, r.t. (**iii**) DMF, KO^{t}Bu, N_2, 80 °C.

Imine **5**-*n* was readily prepared following the procedures outlined by Huck *et al.*[6] and could be isolated in yields of up to 80% depending on the length of the aliphatic chains. The preparation of **7** required the use of Zincke chemistry as shown in Scheme 2.2.[7] Following the procedures outlined by Coe and co-workers in their preparation of Ru(II) complexes with *N*-phenylpyridinium ligands,[8,9] **7** could be readily prepared from compound **6**, *via* a Zincke reaction with 4-methylaniline under reflux in *1*-butanol (Scheme 2.2). Due to the polarity of **7**, it was readily extracted into water and could be used without further purification. However, the Siegrist reaction between **7** and imine **5**-*n* (Scheme 2.1) proved troublesome and while analysis of the crude reaction mixture did show complete consumption of the starting materials, never could any product be detected.
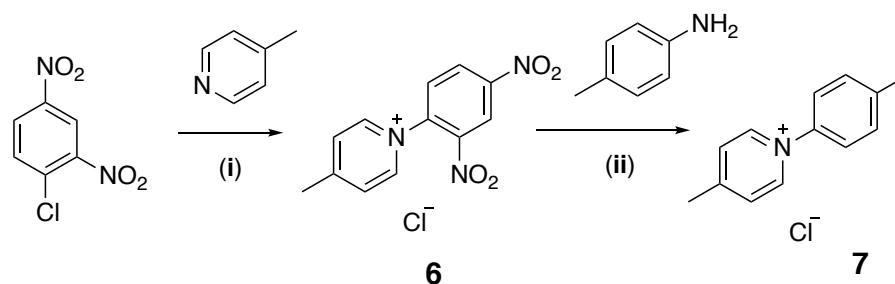
Scheme 2.2. Preparation of **7** using Zincke chemistry: (**i**) EtOH, 78 °C (**ii**) *1*-butanol, 110 °C.

In light of this, a second attempt at preparing compounds **2**-*n* was made. This approach was more divergent and involved preparation of the same 4-alkoxystilbazole intermediates that were employed as ligands in the silver(I) salts. As such, little comment will made on the synthesis of the stilbazole compounds as their preparation has been documented extensively by Donnio *et al.*[1,10] The 4-alkoxystilbazoles were reacted with 1-chloro-2,4-dinitrobenzene in a nucleophilic aromatic substitution reaction to furnish Zincke salt **9**-*n* (Scheme 2.3) as outlined by Marazano and co-workers.[11,12] This reaction proved to be extremely facile and proceeded in high yields – the product simply precipitated from the reaction mixture on cooling to room temperature and could be used without further purification.
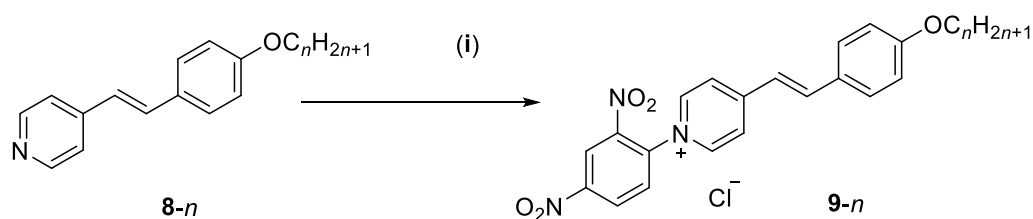
Scheme 2.3. Synthesis of Zincke salt **9**-*n*: (**i**) 1-chloro-2,4-dinitrobenzene, acetone, 60 °C.

The first Zincke reaction was attempted between compound **9**-*n* and aniline in ethanol under reflux according to Scheme 2.4. It was decided to attempt the first Zincke reaction with a simple aniline to trial the reaction conditions. This reaction was successful and compound **10**-*n* could be isolated as a pure compound after flash column chromatography on silica gel using dichloromethane:methanol (8:2) as the eluent. However, analysis of the ^{1}H NMR spectrum after several days revealed *cis-trans* isomerisation of the vinyl group in **10**-*n* as shown in Figure 2.2. This was evidenced by the appearance of two AX signals with ^3J = 12 Hz that are characteristic of a *cis* geometry of the C=C bond. Both salts **9**-*n* and **10**-*n* are bright orange in colour that suggests strong visible light absorption, and so visible light induced *cis-trans* isomerism was not so surprising. The presence of *cis* vinylic groups would destroy liquid-crystalline behaviour in the final compounds (both calamitic and tetracatenar) due to reduced anisotropy of the core. One option would be to

store these materials in the dark; however, this is not a practical option considering the use of polarising microscopy in studying the liquid-crystalline properties of these materials, which involves significant exposure to visible light. As such, modification to the structure of the final *N*-phenylpyridinium ions was required.
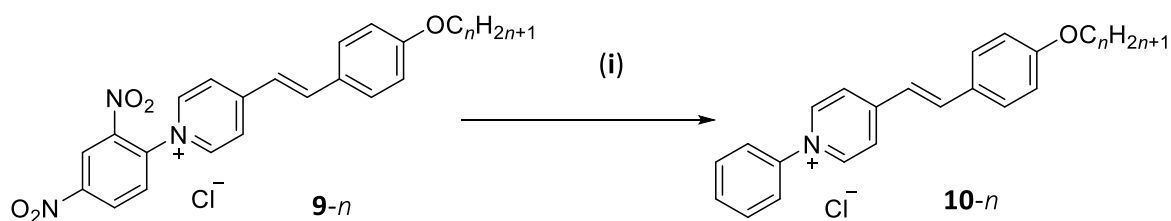
Scheme 2.4. Synthesis of compound **10**-*n*: (**i**) aniline, ethanol, 78 °C.
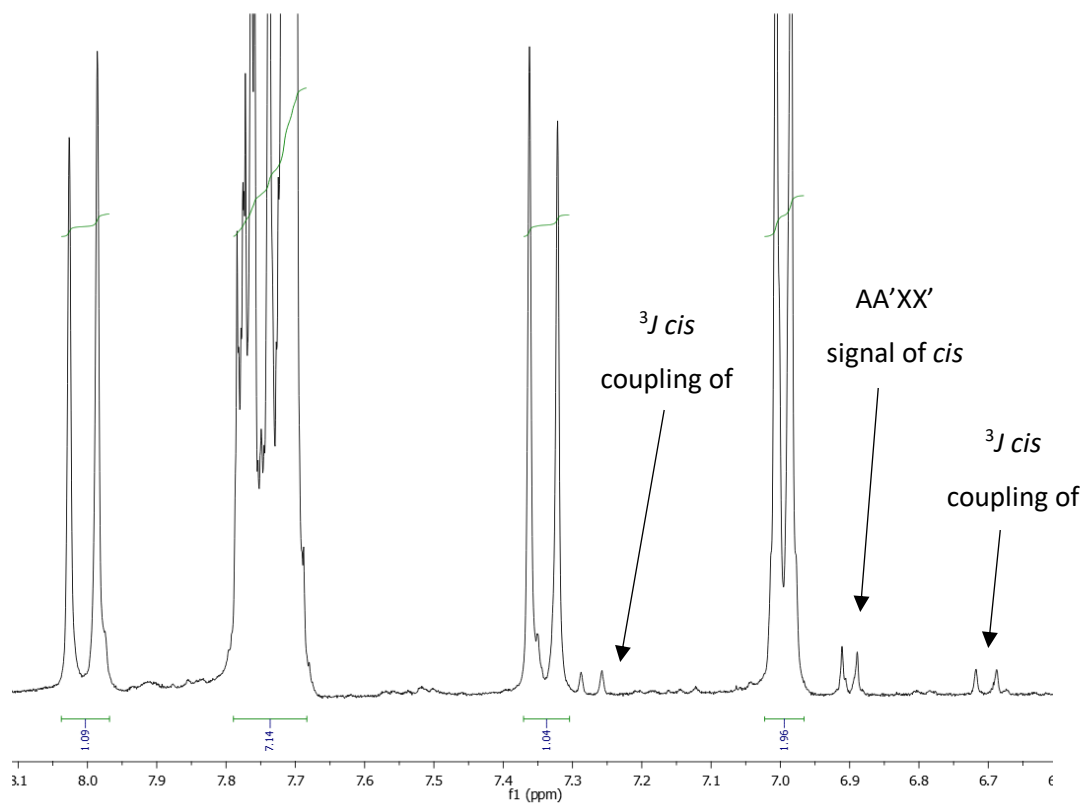
Figure 2.2. ^{1}H NMR spectrum of the aromatic region of compound **10**-*6* showing resonances that correspond to the *cis*-isomer.

2.2. Revised target compounds

In light of the fact that the *trans* vinylic groups in compounds **10**-*n* suffered from visible light induced *cis-trans* isomerism, a series of compounds containing direct aryl-aryl linking groups were designed; their structure is given in Figure 2.3.
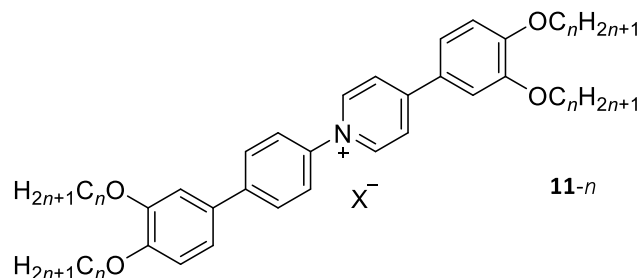
Figure 2.3. General structure of the revised tetracatenar *N*-phenylpyridinium ions with direct aryl-aryl linkages.

2.2.1. Preparation of calamitic *N*-phenylpyridinium ions

Initially, a series of calamitic compounds, **12**-*n,* were prepared for the same reasons as those outlined in Section 2.1 and the structure of these compounds is presented in Figure 2.4. The tetracatenar compounds, **11**-*n*, would then be prepared using key reactions and conditions established in the synthesis of compounds **12**-*n*.
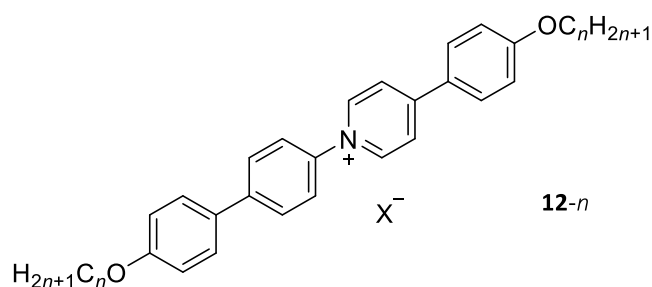
Figure 2.4. Structure of the calamitic *N*-phenylpyridinium ions prepared before the analogous tetracatenar salts.

The overall synthetic procedure for the preparation of **12**-*6* is presented in Scheme 2.5. 4-Hydroxybromobenzene was initially alkylated with 1-bromohexane in acetone under reflux using two equivalents of K_2CO_3 as a base. After washing the crude product with aqueous NaOH solution, 4-hexyloxybromobenzene (**13**-*6*) was isolated in 84% yield and could be used without further purification. Suzuki-Miyaura cross-coupling between **13**-*6* and pyridine-4-boronic acid was then achieved in a 1:1 mixture of THF/H_2O at 65 °C employing $[Pd(PPh_3)_4]$ as a catalyst at a loading of 1 mol%. Purification by flash column chromatography using dichloromethane:methanol (95:5) as the

eluent then furnished compound **14**-*6* as a pure compound in 74% yield. Zincke salt **15**-*6* was then prepared *via* a nucleophilic-aromatic substitution reaction between 4-alkoxyphenylpyridine **14**-*6* and 1-chloro-2,4-dinitrobenzene in acetone under reflux; the product precipitated from solution, and, after washing of the solid with acetone, could be used without further purification.

The difficult step in this synthesis was installation of the *para*-iodo group of **17**-*6*, which had to be achieved through the preparation of the *para*-amino intermediate **16**-*6* followed by a Sandmeyer reaction to furnish **17**-*6*. A direct Zincke reaction between chloride salt **15**-*6* and 4-iodoaniline could not be achieved and no product could ever be detected regardless of the conditions employed; quite why this was the case is unclear. The *para*-amino group was successfully installed *via* a Zincke reaction between **15**-*6* and *p*-phenylenediamine in 1-butanol under reflux; the product was purified by flash column chromatography on silica gel using dichloromethane:methanol (8:2) as the eluent. Sandmeyer chemistry was then performed on **16**-*6* using $NaNO_2$ and KI in acetonitrile at 0 °C; water was then added to the reaction mixture and the product was extracted into ethyl acetate. Crystallisation of the crude product from ethanol yielded **17**-*6* as a pure compound in 53% yield. A final Suzuki-Miyaura cross-coupling reaction between **17**-*6* and the pinacol ester of boronic acid **18**-*6* then furnished the final calamitic *N*-phenylpyridinium ions **12**-*6* that were purified by flash column chromatography on silica gel using dichloromethane:methanol (9:1) as the eluent; the yield was low for this reaction at 24%. The pinacol ester of 4-hexyloxybenzene boronic acid **18**-*6* was prepared in house *via* alkylation of 4-hydroxybenzeneboronic acid pinacol ester in acetone under reflux.

Due to time constraints, elemental analysis on the final calamitic compound **12**-*6* was not obtained and efforts were focused on preparing the analogous tetracatenar compounds **11**-*n*. Only one calamitic homologue (*n* = 6) was ever prepared.
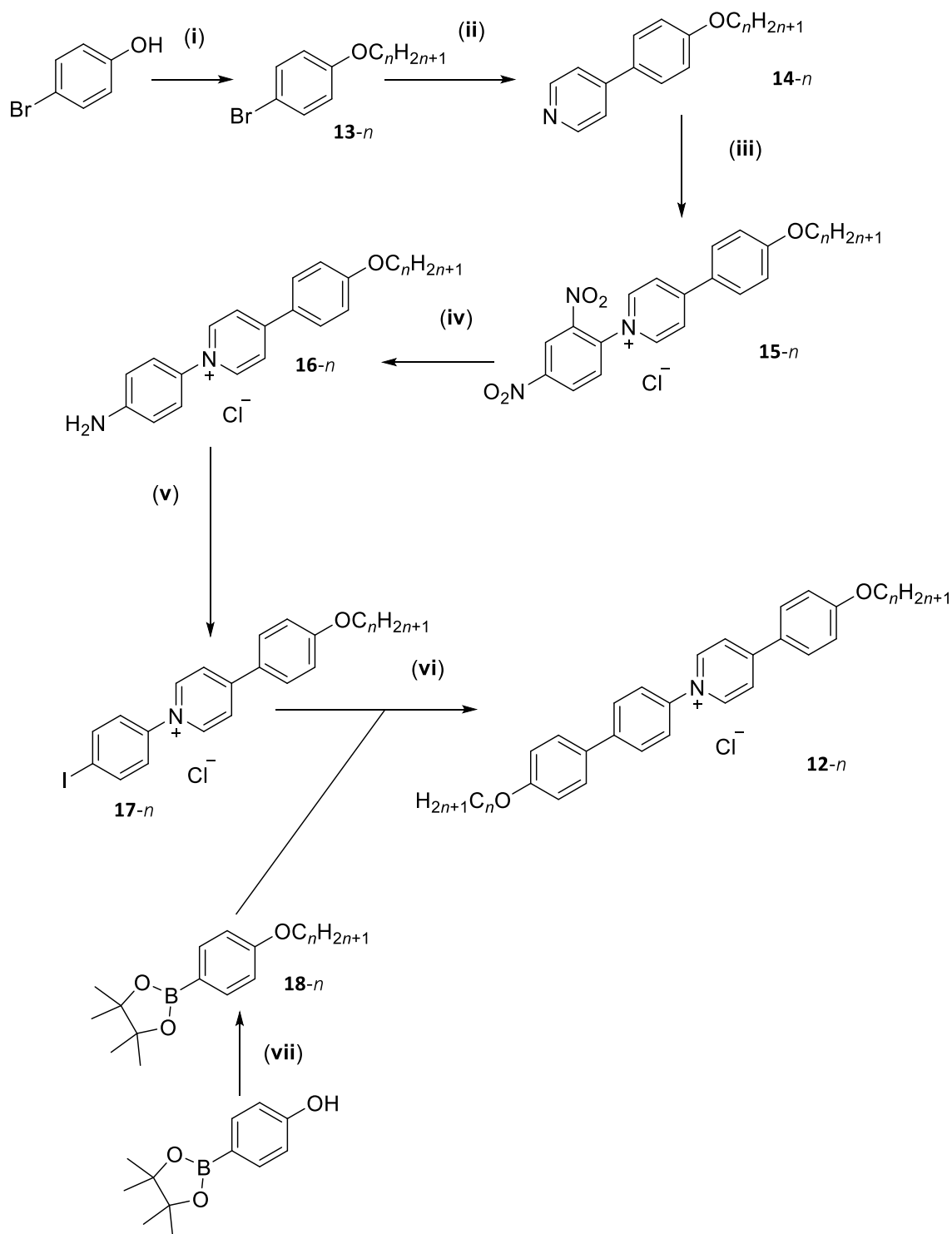
Scheme 2.5. Synthesis of the calamitic *N*-phenylpyridinium ions: conditions reported are those for the preparation of the hyexyloxy derivative (**i**) K_2CO_3, $C_6H_{13}Br$, acetone, 60 °C, (**ii**) pyridine-4-boronic acid, THF/H_2O, [Pd(PPh$_3$)$_4$], Na_2CO_3, 65 °C, N_2 (**iii**) 1-chloro-2,4-dinitrobenzene, acetone, 60 °C (**iv**) *p*-phenylenediamine, 1-butanol, 110 °C (**v**) $NaNO_2$, KI, *p*-TsOH, MeCN, 0 °C (**vi**) pinacol ester of 4-hexyloxybenzene boronic acid, THF/H_2O, [Pd(PPh$_3$)$_4$], Na_2CO_3, N_2, 65 °C (**vii**) K_2CO_3, acetone, 60 °C.

2.2.2. Preparation of the tetracatenar triflate salts, 11-*n*

Preparation of the tetracatenar *N*-phenylpyridinium ions, **11**-*n*, shown in Figure 2.3 proved extremely successful and complete reagents and conditions are presented in Scheme 2.6.[13] Some modifications were required to the procedure employed in the preparation of the calamitic compounds **12**-*n* and these are now described.

3,4-Dimethoxybromobenzene (4-bromoveratrole) was firstly de-methylated with a solution of boron tribromide in dichloromethane to furnish 4-bromocatechol **19** (whilst 4-bromocatechol is a readily available starting material, it proved more cost effective to prepare it in house from 4-bromoveratrole). The terminal alkoxy chains were then installed *via* Williamson ether reactions between 4-bromocatechol and two molar equivalents of the desired 1-bromoalkane employing Cs_2CO_3 as the base. Cs_2CO_3 was used as the base as it proved effective in reducing reaction times compared to K_2CO_3, presumably due to its better solubility in the acetone solvent. Homologues with aliphatic chain lengths $n > 8$ could be readily crystallised from hot acetone in yields typically between 60-70%; derivatives with $n < 8$ were purified by flash column chromatography on silica gel using dichloromethane:petroleum ether (40-60 °C) (1:1) as the eluent. The 3,4-dialkoxybromobenzene, **20**-*n*, then underwent a Suzuki-Miyaura cross-coupling reaction with the pinacol ester of pyridine-4-boronic acid following the procedure outlined by Woodring and co-workers[14] to furnish the 3,4-dialkoxyphenylpyridine, **21**-*n*, in good yield. These conditions differ to those outlined in Scheme 2.5 in that toluene/ethanol/water was used as the solvent system as compared to THF/water due to the higher temperature that this solvent system provided access to. The presence of the *meta* chain had a dramatic effect of deactivating the aryl-bromide and yields of only 10% could be isolated following the procedure in THF/water outlined in Scheme 2.5. Furthermore, it was more cost effective to use the pinacol ester of pyridine-4-boronic rather than pyridine-4-boronic acid itself and so this modification was made between Schemes 2.5 and 2.6.

Salt **22**-*n* was then accessed *via* a nucleophilic-aromatic substitution reaction with 1-chloro-2,4-dinitrobenzene in acetone under reflux; once again, the product precipitated from the reaction mixture on cooling and, after washing with acetone, was used without further purification. Reaction of **22**-*n* with 4-iodoaniline in a Zincke reaction[15,16] provided access to the *para*-iodo species **23**-*n*; yields of this reaction were typically poor, being between 25-50% depending on the aliphatic chain length. Unlike the preparation of **17**-*n* in Scheme 2.5, direct access to the *para*-iodo species **23**-*n* could be achieved from reaction the Zincke salt **22**-*n* with 4-iodoaniline without the need of going through a *para*-amino intermediate. A procedure outlined by Kassel *et al.*[16] was found that

documented a Zincke reaction with 4-iodoaniline in 1-butanol under reflux and these procedures were effective in the synthesis of **23**-*n*. Metathesis of the chloride anion in **23**-*n* for triflate was next performed on account of better solubility of the triflate salt for the final Suzuki-Miyaura cross-coupling reaction.

The boronic acid pinacol ester, **25**-*n*, was prepared from **20**-*n* in a Suzuki-Miyaura borylation reaction[17] in anhydrous DMSO using 3 mol% of [PdCl$_2$(dppf)] (dppf = bis(diphenylphosphino)ferrocene). The final tetracatenar triflate salts were then purified by flash column chromatography on silica gel using dichloromethane:methanol (95:5) as the eluent. The compounds were finally dried in a vacuum oven at 70 °C. Analytical data and yields for the final compounds are collected in Table 2.1 and an assigned ^{1}H NMR spectrum for the dodecyloxy derivative, **11**-*12*, is presented in Figure 2.5.
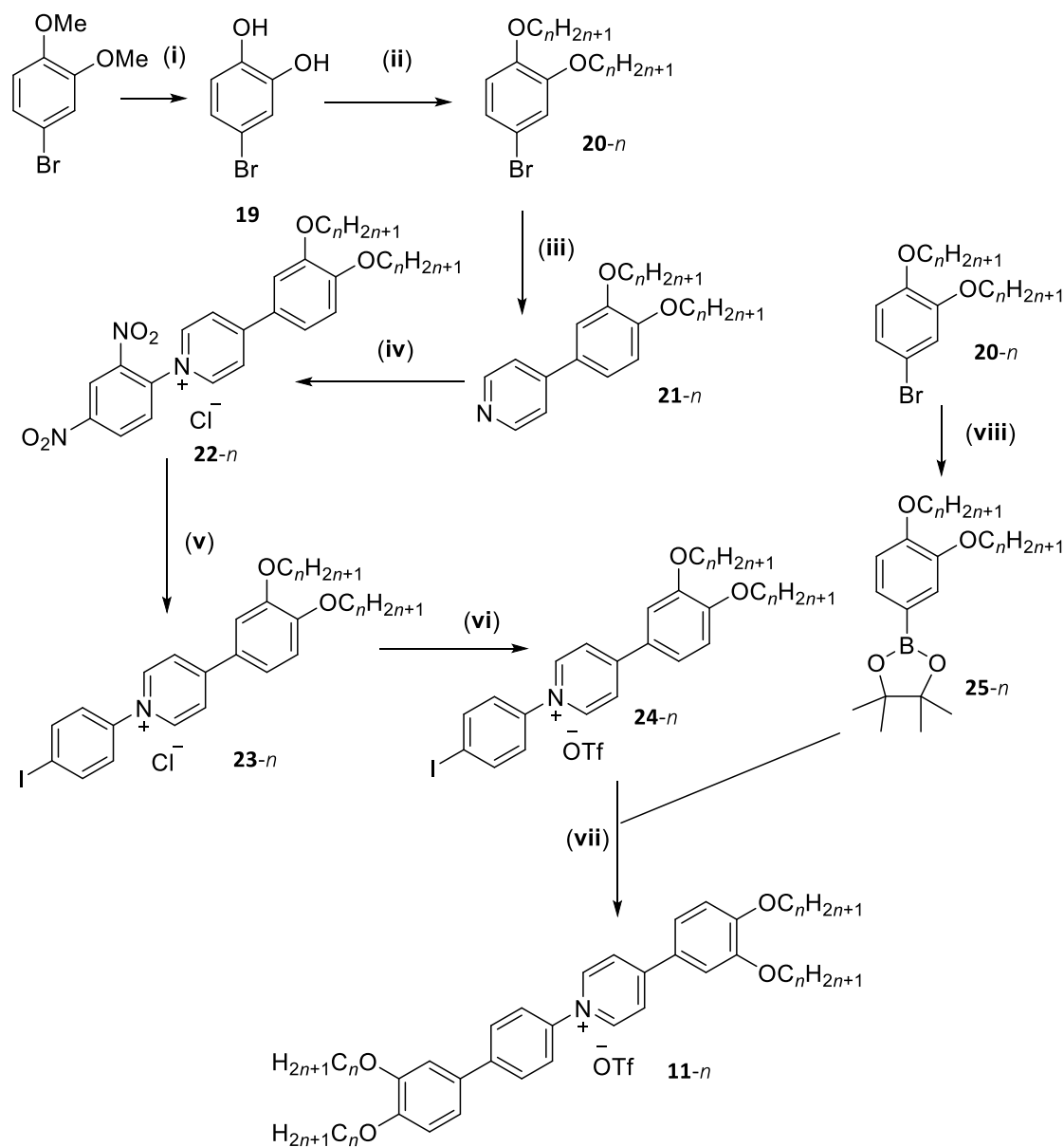
Scheme 2.6. Synthesis of the tetracatenar *N*-phenylpyridinium salts containing direct aryl-aryl linking groups: (**i**) BBr$_3$, 0 °C, N$_2$ (**ii**) C$_n$H$_{2n+1}$Br, acetone, Cs$_2$CO$_3$, 58 °C (**iii**) pyridine-4-boronic acid pinacol ester, Toluene/EtOH/H$_2$O (3:1:1), Na$_2$CO$_3$, [Pd(OAc)$_2$], SPhos (**iv**) 1-chloro-2,4-dinitrobenzene, acetone, 60 °C (**v**) 4-iodoaniline, 1-butanol, 110 °C (**vi**) AgOTf, DMF, 70 °C (**vii**) 3,4-dialkoxybenzene boronic acid pinacol ester, THF/H$_2$O (1:1), Na$_2$CO$_3$, N$_2$, [Pd(OAc)$_2$], SPhos, 65 °C (**viii**) bis-pinacolato diborane, NaOAc, [Pd(dppf)Cl$_2$], DMSO, 80 °C, N$_2$.

.

Figure 2.5 shows the ^{1}H NMR spectrum of compound **11**-*12* along with the assignment of each resonance. Aromatic protons **a**, **b**, **c**, and **d** are AA'XX' signals due to the 1,4-disubstitution pattern of the central aromatic rings; these protons resonate more downfield than those typical of an aromatic system due to the positively charged nitrogen atom of the pyridinium moiety. Hydrogens **a** and **b** resonate downfield at 9.0 and 8.4 ppm, respectively, both with 2H integrations. The resonance at 8.4 ppm can be specifically assigned to H$^{\mathbf{b}}$ from correlation spectroscopy shown in Figure 2.6, which clearly shows that hydrogen atoms **a** and **b** are coupled to one another. The 400 MHz spectrometer is unable to distinguish hydrogen atoms **c** and **d** due to their similarities in chemical shift. Hydrogen atom **e** exists as a doublet of doublets due to ^3J coupling to **I** and ^4J coupling to **f** with respective coupling constants of 9.0 and 2.0 Hz. Hydrogen atom **f** then resonates at 7.4 ppm as a doublet of 2.0 Hz due to ^4J coupling to H$^{\mathbf{e}}$. These hydrogen atoms can be distinguished from hydrogens **g**, **j** and **h** from the ^{1}H NMR spectrum of the precursor compound **24**-*12*. The ^{1}H NMR spectrum of compound **24**-*12* is presented in Figure 2.7, and specifically, the AMX spin system of hydrogens **e**, **f** and **I** can be seen at δ 7.50, 7.37 and 6.95 ppm, respectively. These chemical shifts are extremely similar to those assigned as **e**, **f** and **I** in the ^{1}H NMR spectrum of **11**-*12* in Figure 2.5, and provides good evidence for the assignments made in the final compound.

Hydrogen atoms **g** and **h** then overlap at 7.13 ppm, but ^4J coupling between H$^{\mathbf{g}}$ and H$^{\mathbf{h}}$ can be identified as 2.0 Hz. Hydrogen atoms **I** and **j** then resonate extremely close together, both showing respective ^3J coupling to hydrogens **e** and **g** of 9.0 Hz. Methylene protons **k** are observed at 4.1 ppm, and whilst only one signal can be clearly detected as a triplet with ^3J = 6.5 Hz, the remaining three CH_2 signals overlap as a multiplet. Hydrogen atoms **l** then appear at 1.87 ppm as a multiplet of 8H integration. Terminal CH_3 hydrogen atoms **n** can then be identified at 0.9 ppm with integration of 12H.

The triflate anion can be detected as a singlet *via* ^{19}F NMR spectroscopy at δ = -78.08 ppm as shown in Figure 2.8.

j g d c a b f

k l m n
OCH₂CH₂(CH₂)₉CH₃

$H_3C(H_2C)_9H_2CH_2CO$

h

$H_3C(H_2C)_9H_2CH_2CO$

OTf

e i

OCH₂CH₂(CH₂)₉CH₃

CHCl₃

c,d

g,h

m

a

b

e

f

i,j

n

k

l
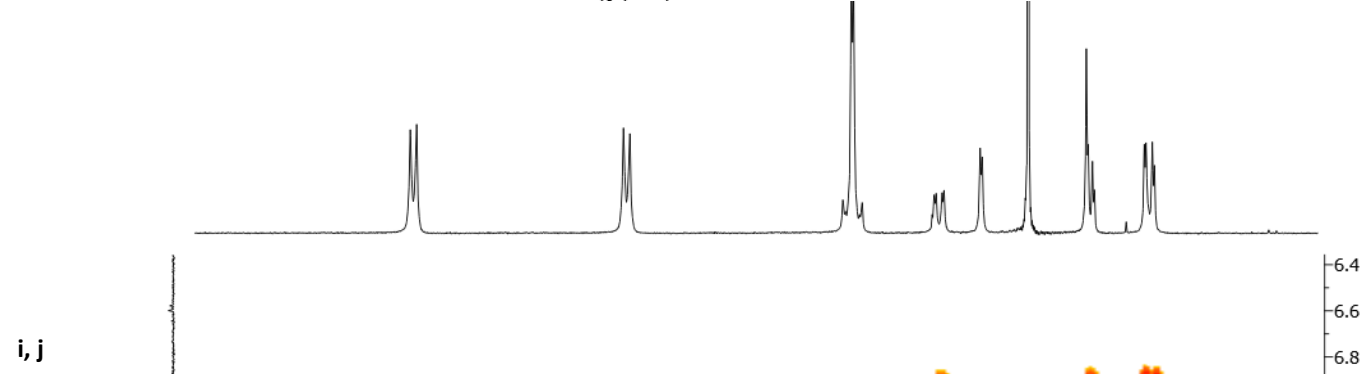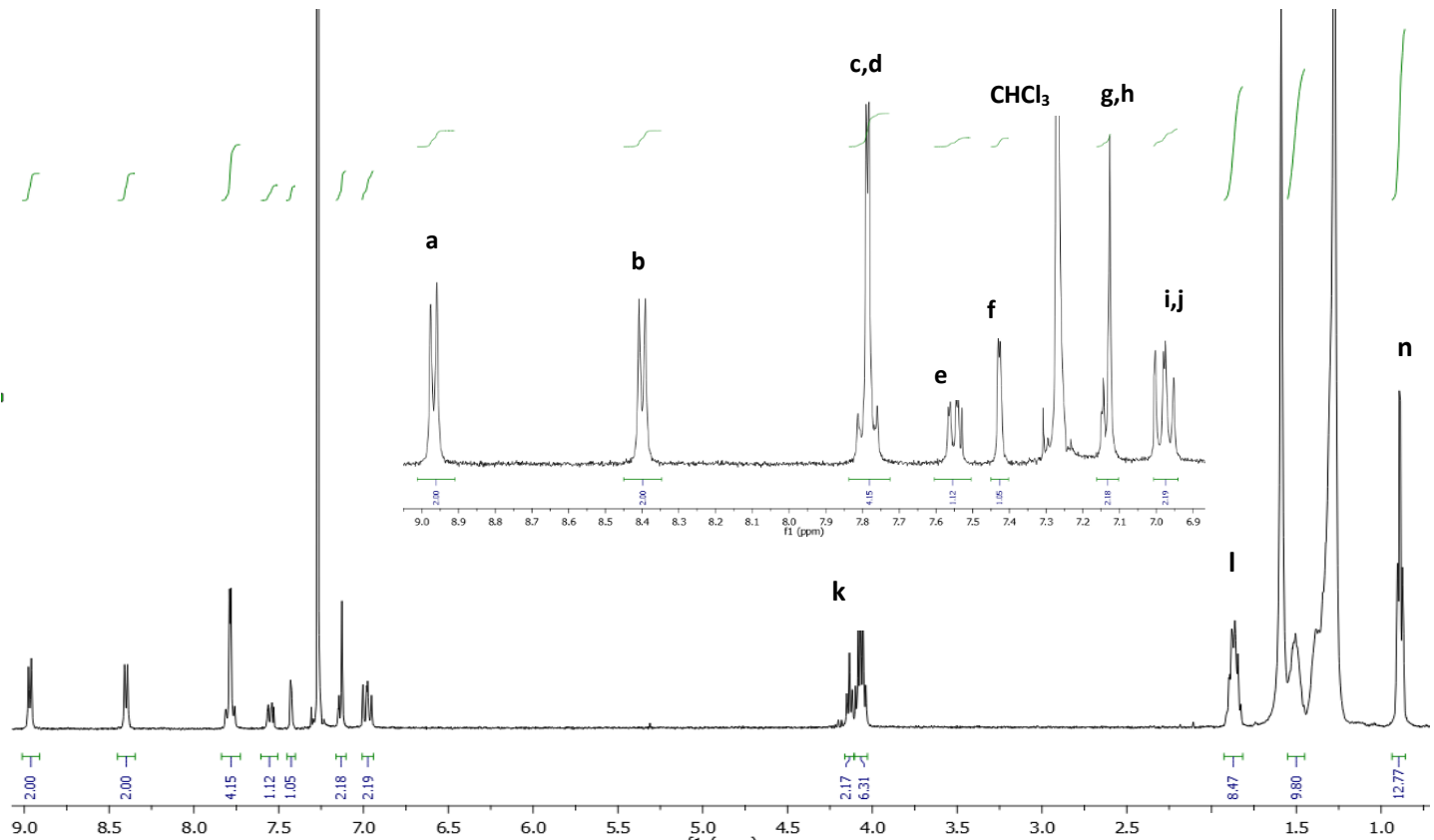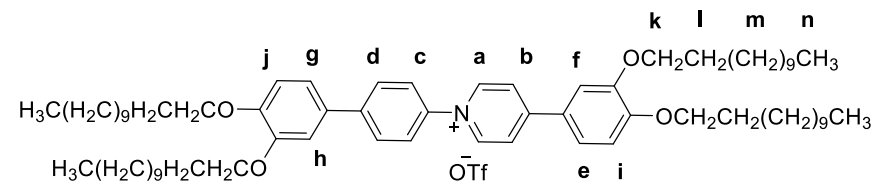
Figure 2.6. ^{1}H-^{1}H COSY NMR spectrum of the aromatic region of compound **11**-*12.*
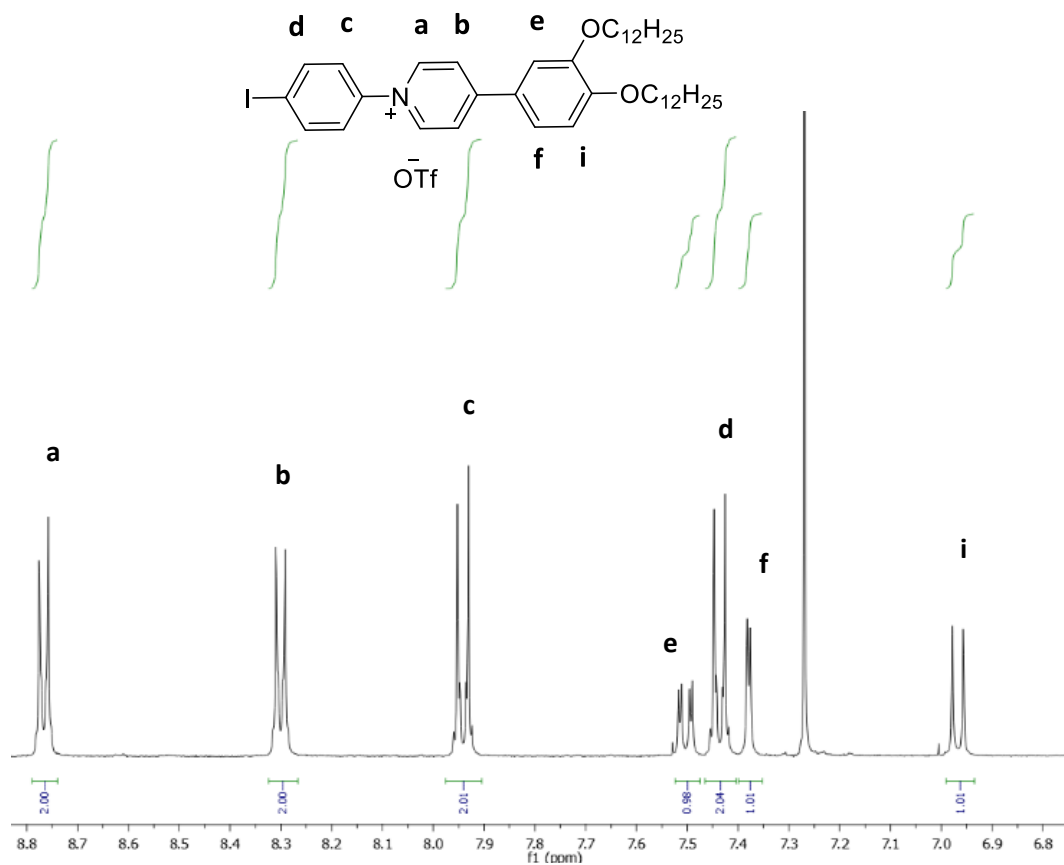
Figure 2.7. ¹H NMR spectrum of the aromatic region of **24**-*12* to aid assignment of the two AMX spin systems of **11**-*12*: the same lettering system has been used for consistency.
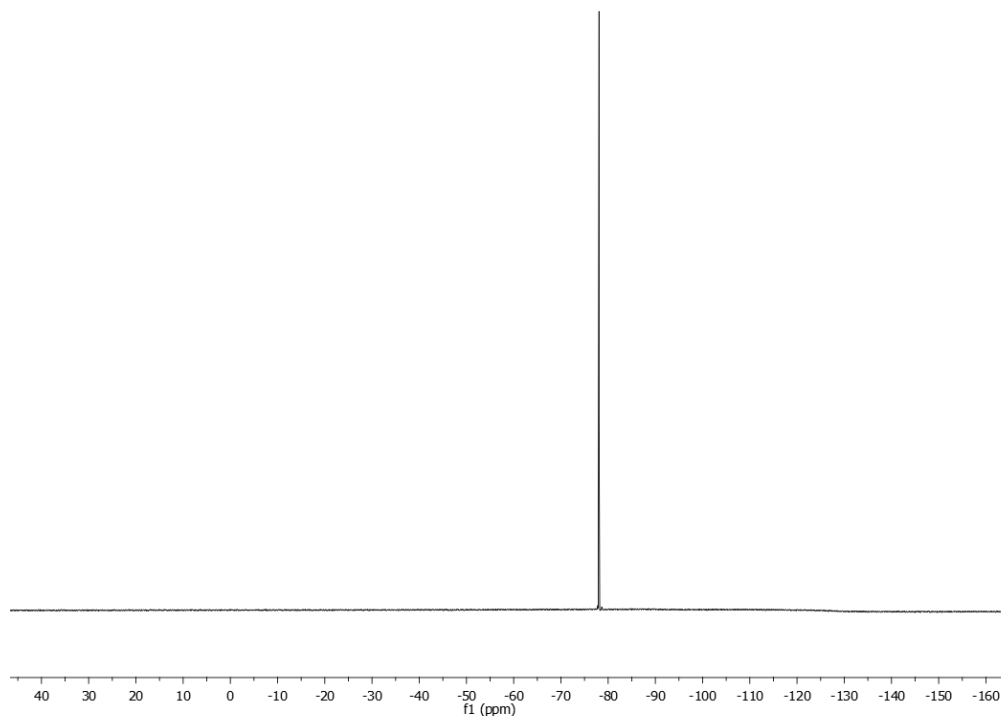
Figure 2.8. ¹⁹F NMR spectrum of the tetracatenar triflate salt **11**-*12*.

2.2.3. X-Ray single crystal structure of compound 11-*8*
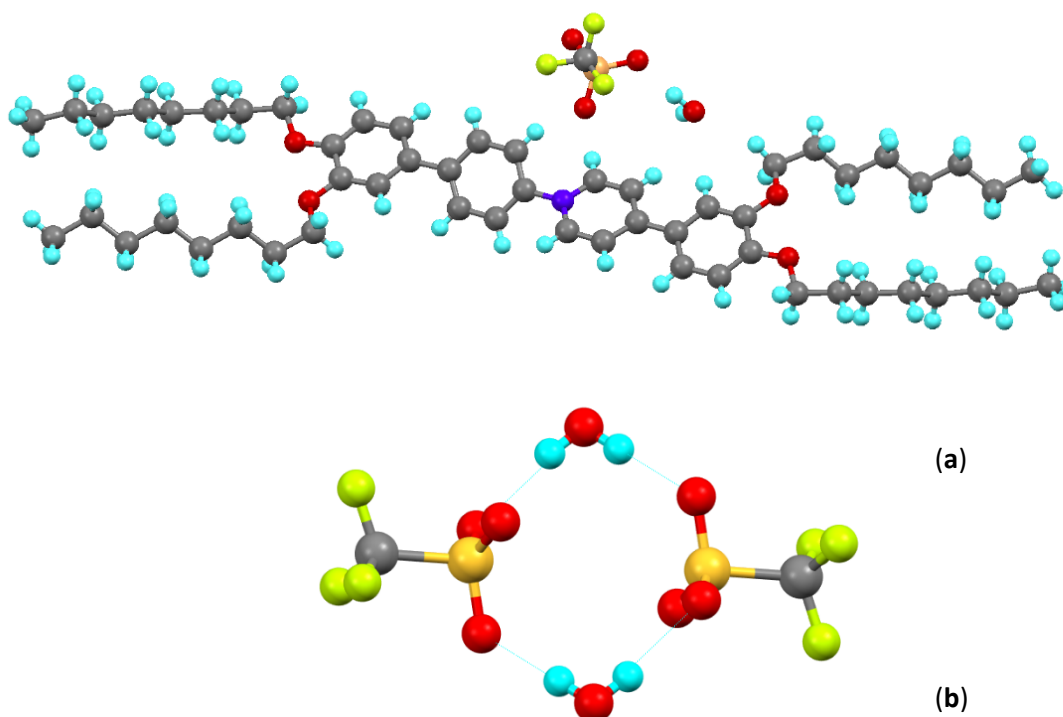
Figure 2.9. Single crystal X-ray structure of **11**-*8* (**a**) with disorder removed for clarity and (**b**) the 2+2 hydrogen bonded adduct of the triflate anion with water.

Single crystals of the octyloxy derivative were successfully grown *via* vapour-diffusion from dichloromethane/pentane solutions and the structure is presented in Figure 2.9.

One of the octyloxy side chains was disordered and modelled in two positions with refined occupancies of 0.714:0.286(4). The C-C bond lengths in the disordered part of the chain were restrained to be 1.54 Å except for the terminal C-C bond lengths that were restrained to be 1.52 Å. The triflate anion/water showed minor disorder with the triflate being modelled in two positions with refined occupancies of 0.9598:0.0402(15). For the minor form, the C-F bond lengths were restrained to be 1.33 Å, the S-O bond lengths restrained to be 1.44 Å and the C-S bond length restrained to be the same as that of the major form.

The structure in Figure 2.9 shows location of the triflate anion in close proximity to the pyridine moiety, as expected. Two water molecules bridge adjacent triflate moieties forming a 2+2 hydrogen bonded adduct as shown in Figure 2.10 (**b**). The packing of **11**-*8* in the solid state shows an anti-parallel alignment of neighbouring cations (Figure 2.10 (**a**)). The *N*-phenylpyridinium core unit

displays a torsion angle of 31.3°. There are no interactions between the triflate oxygen atoms and the pyridinium hydrogen atoms as shown in Figure 2.10 (**b**).

(**a**)

(**b**)
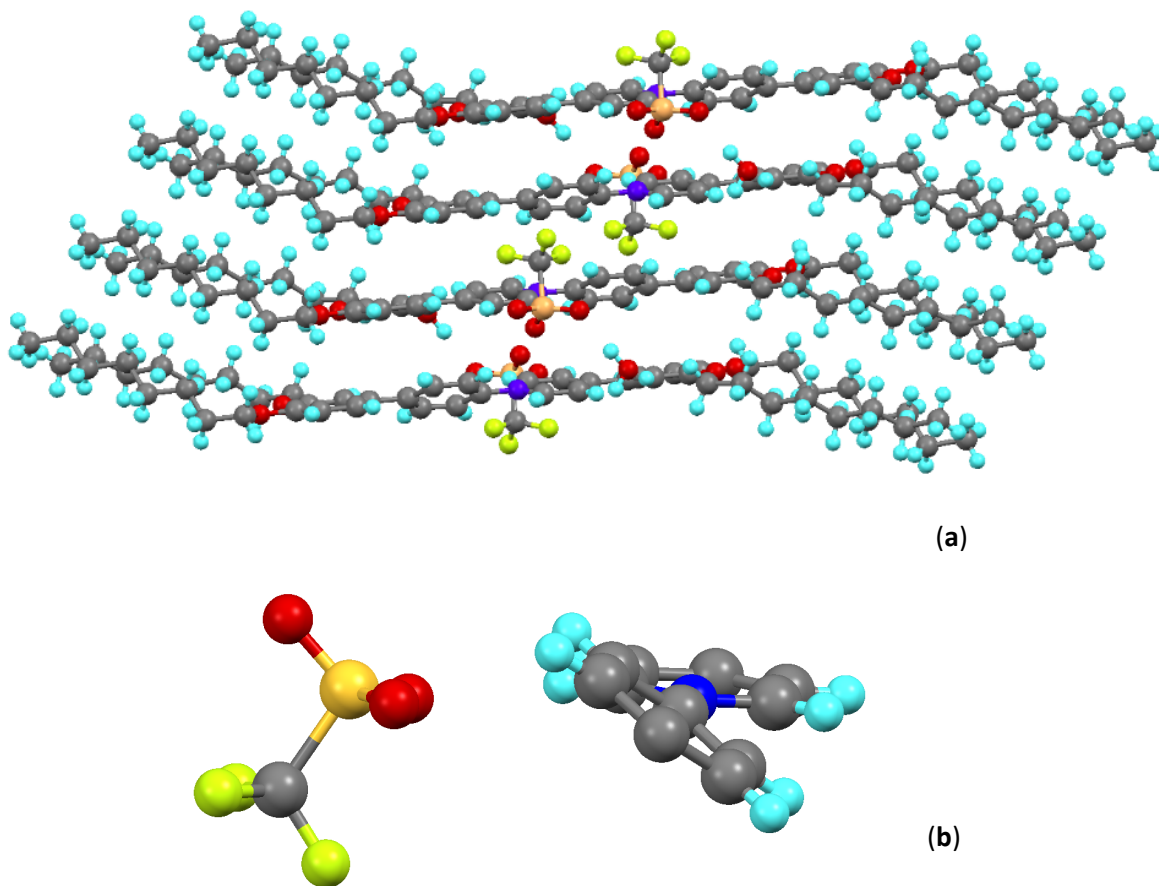
Figure 2.10. Packing of **11**-*8* in the solid state with disordered chains removed for clarity (**a**) and the torsion angle of the *N*-phenylpyridinium core with terminal rings and chains removed for clarity (**b**).

2.3. Metathesis of the counter-ion

A major objective to this work was to investigate the influence of different counter-ions on the mesomorphism of the ionic polycatenar liquid crystals based on the *N*-phenylpyridinium core. In so doing, a series of *N*-phenylpyridinium materials were also prepared that contained octylsulfate and dodecylsulfate anions, much like the work involving the stilbazole complexes of various silver(I) alkylsulfates. Bis(trifluoromethanesulfonyl)imide (NTf$_2^-$) was also employed successfully as a counter-ion *via* direct metathesis from the triflate salts, as will also be described.

Initial attempts at preparing a series of tetracatenar alkylsulfate salts involved stirring the required triflate compound, **11**-*n*, with three molar equivalents of the desired sodium alkylsulfate in hot methanol according to Scheme 2.7. Water was then added dropwise to the reaction mixture to precipitate the compound as its alkylsulfate salt. Whilst ^{1}H NMR spectroscopy could detect the correct stoichiometry of the alkylsulfate anion, small amounts of triflate could also be detected *via* ^{19}F NMR spectroscopy and so complete exchange from triflate to alkylsulfate had not been achieved. Even repeating the exchange up to three times proved ineffective in removing these trace amounts of triflate.
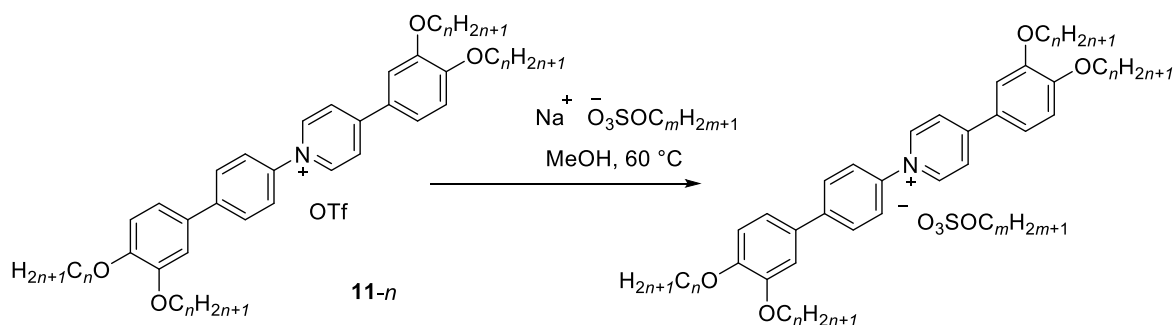
Scheme 2.7. Attempted metathesis from triflate **11**-*n* to alkylsulfate.

In order to prepare analytically pure alkylsulfate materials, first, the final tetracatenar *N*-phenylpyridinium ions had to be prepared as their chloride salts from which complete metathesis could be achieved. The following section, therefore, documents the preparation of the tetracatenar chloride salts, **26**-*n*.

2.3.1. Preparation of the *N*-phenylpyridinium chloride salts, **26**-*n*

As discussed in Section 2.2.2 the *para*-iodo intermediate **23**-*n* displayed poor solubility in a range of solvents and had to be metathesised to its triflate salt, **24**-*n*, in order to be successfully cross-coupled with the corresponding 3,4-dialkoxybenzene boronic acid pinacol ester **25**-*n*. Considering the success of Binnermans *et al.*[18] in exchanging halide anions for dodecylsulfate anions, efforts were re-focussed on preparing the final compounds as their chloride salts from which metathesis

to an alkylsulfate might be more successful. Rather than employing the *para*-iodo salt, **23**-*n*, in the Suzuki-Miyaura cross-coupling reaction, the analogous *para*-bromo species, **27**-*n*, was prepared in a Zincke reaction between 4-bromoaniline and the 2,4-dinitro salt **22**-*n* (see Scheme 2.8). The resulting *para*-bromo salt, **27**-*n*, was purified in an identical fashion to that employed in the purification of **23**-*n* (isolation of the precipitate followed by trituration with dichloromethane and acetone). Compound **27**-*n* was a little more soluble than the iodo analogue, **23**-*n*, so allowing Suzuki-Miyaura cross-coupling with **25**-*n* in THF/H_2O with 20% ethanol as a co-solvent; this was performed under reflux. The chloride products, **26**-*n*, were purified *via* flash column chromatography on silica gel using dichloromethane:methanol (95:5) as the eluent.

However, further purification of final compounds, **26**-*n*, was required that involved trituration with dichloromethane (see the ^{1}H NMR spectrum of **26**-*12* in Figure 2.11). Despite this, compounds **26**-*n* still could not be isolated in analytical purity and these materials were consistently low in carbon content from combustion analyses. Tiny traces of organic impurities could still be identified in the ^{1}H NMR spectra of the chloride salts between 3.5 – 2.0 ppm, but these could not be removed in any further purification attempts; however, it seems unlikely that such small impurities fully account for the poor elemental analysis data obtained. The small signals in the aromatic region that do not correspond to the compound are not impurities but are in fact ^{13}C satellites from the chloroform solvent with $^1J_{HC}$ = 210 Hz; these are visible due to the poor solubility of **26**-*12* in the chloroform solvent and ^{1}H NMR spectra had to be recorded on dilute solutions. Table 2.3 presents CHN data for compounds **26**-6 to **26**-*12*. Yields of the chloride products **26**-*n* were poorer than those for the triflate analogues, being typically in the region of 60%.
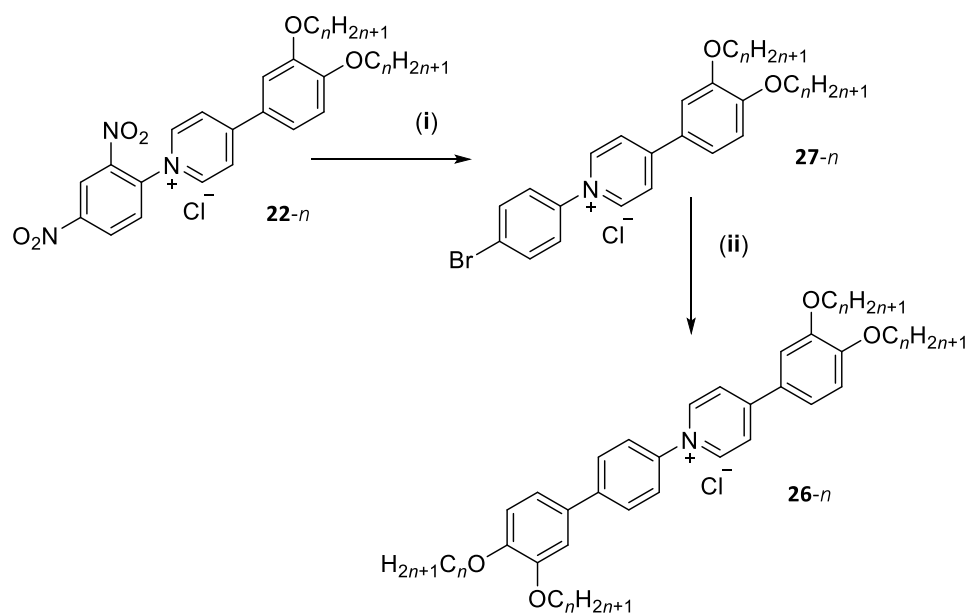
Scheme 2.8. Preparation of the tetracatenar chloride salts **26**-*n*: (**i**) 4-bromoaniline, 1-butanol, 110 °C (**ii**) 3,4-dialkoxybenzene boronic acid pinacol ester, THF/H₂O/EtOH (3:3:1), Na₂CO₃, [Pd₃(OAc)₆], SPhos, N₂, 65 °C.
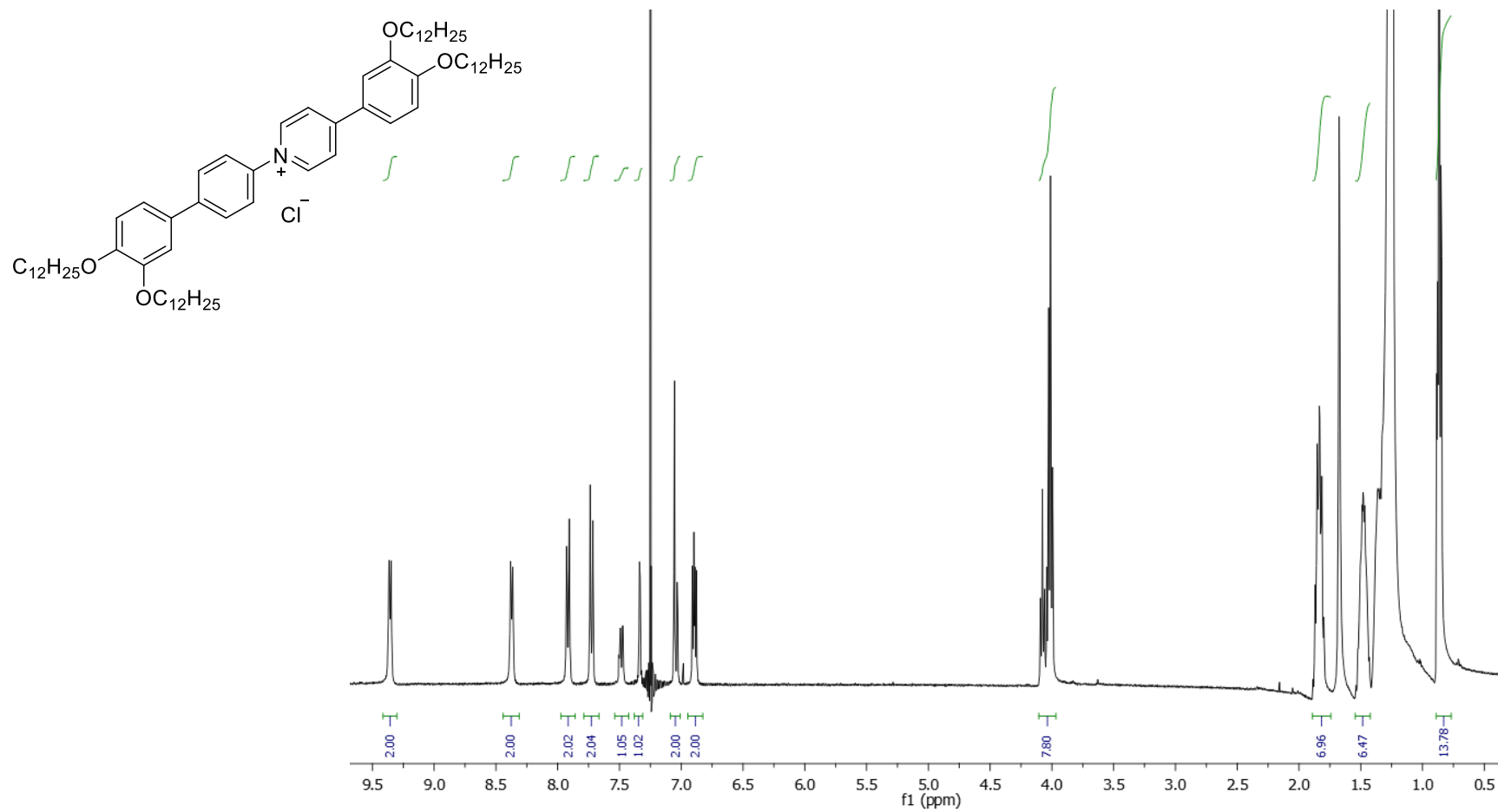
Figure 2.11. ¹H NMR spectrum of chloride salt **26**-*12*.

2.3.2. Preparation of the octylsulfate and dodecylsulfate salts **28**-*n* and **29**-*n*

Metathesis of the chloride counter-ion for the desired long-chain alkylsulfate was achieved by dissolving in hot methanol saturated with the desired sodium alkylsulfate according to Scheme 2.9. Hot ethanol was employed as the solvent for the longer-chained derivatives ($n \geq 12$) due to insolubility of the chloride precursor in hot methanol. After stirring for 3 hours, the product was then precipitated from solution by the dropwise addition of water and could be isolated readily *via* filtration. Crystallisation from hot ethanol and subsequent filtration of the solid in dichloromethane through a 0.2 μm PTFE filter yielded the desired alkylsulfate salts in analytical purity.
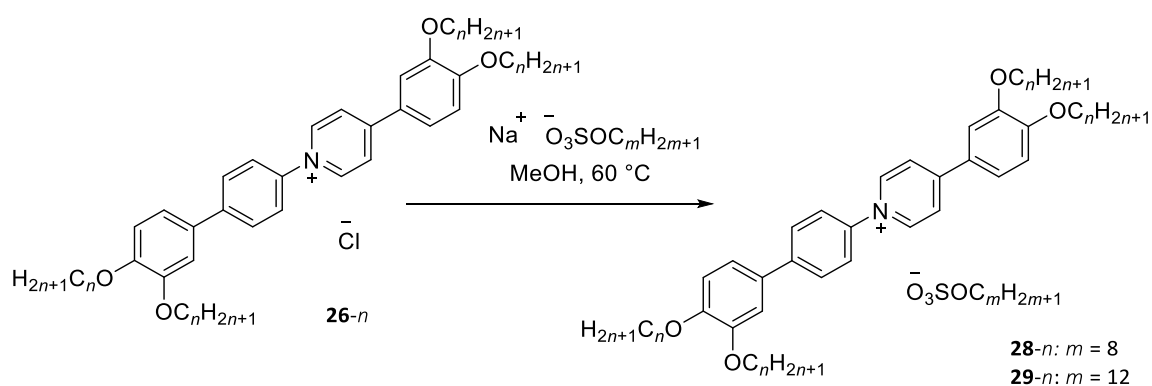
Scheme 2.9. Preparation of the tetracatenar alkylsulfate salts.

The alkylsulfate anion can be clearly seen *via* ^{1}H NMR spectroscopy as evidenced from Figure 2.13. The hydrogen atoms adjacent to the sulfate moiety resonate as a triplet with 2H integration at δ = 3.94 ppm. The analytical purity of the alkylsulfate salts was proved by combustion analysis (Tables 2.4 and 2.5); however, CHN values for the hexyloxy compounds, **28**-*6* and **29**-*6*, fall slightly outside the acceptable limits and possible explanation for these findings is the presence of residual chloride in the samples. To qualitatively test this hypothesis, stirring the salts in a solution of silver nitrate could be performed that would indicate the presence of chloride upon the formation of a white precipitate of silver chloride. This test was not performed owing to the poor solubility of the pyridinium salts in aqueous acid solutions.

However, calculations were performed on one compound, **28**-*6*, in order to indicate the maximum amount of chloride that can be tolerated within these systems while still falling within the acceptable limits of CHN analysis (±0.5% on each element). For compound **28**-*6*, theoretical carbon content for the pure compound is 71.9%, whereas that for the pure chloride salt, **26**-*6*, is 75.8%. Performing linear regression between these values (Figure 2.12, assuming compound **26**-*6* contains 1,000,000 ppm chloride and the pure alkylsulfate salt contains 0 ppm chloride) indicates a

maximum concentration of 125,000 ppm of chloride ions that can be tolerated within the sample, giving a carbon content of 72.4%. The observed carbon content in compound **28**-*6* was actually 71.3% (lower than the theoretical value of a sample contaiminated with chloride) and so impurities other than or in addition to residual chloride ions are responsible for these findings.

$$y = 4 \times 10^{-6}x + 71.9$$
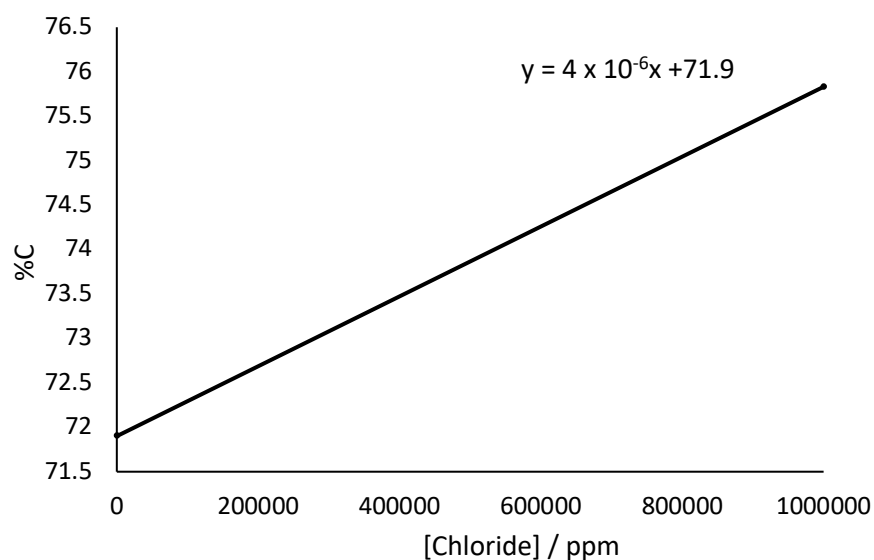
Figure 2.12. Linear regression to calculate maximum chloride concentration tolerated within CHN limits for compound **28**-*6*.
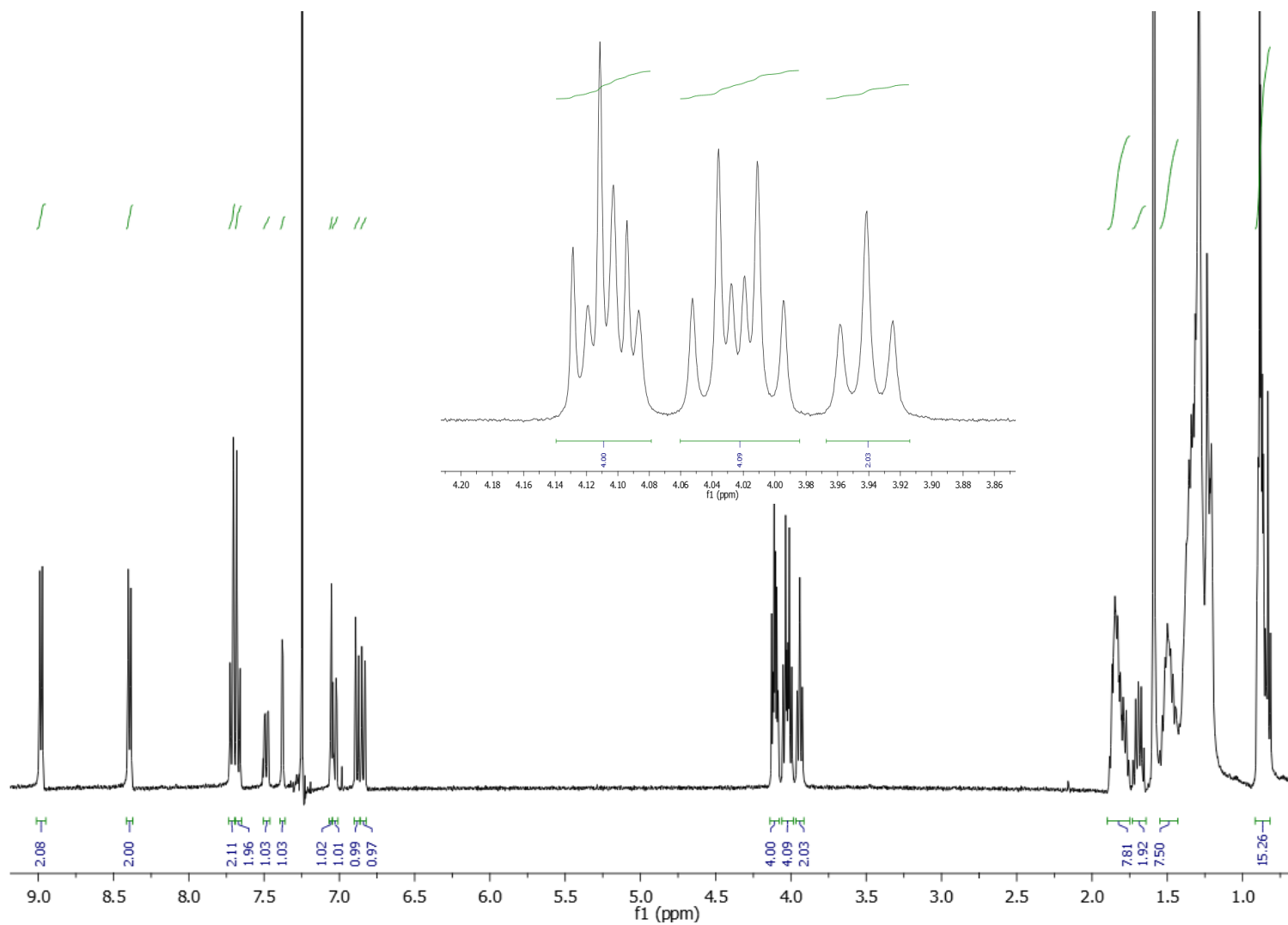
Figure 2.13. ^{1}H NMR spectrum of **28**-*8*: inset shows zoomed in region to show the CH_2 signal at δ = 3.94 ppm arising from the octylsulfate anion.

2.3.3. Preparation of the tetracatenar bis(trifluoromethanesulfonyl)imide (NTf$_2^-$) salts

Preparation of the NTf$_2^-$ salts, **30**-*n*, were readily achieved following a procedure outlined by Riccobono,[19] which involved heating the triflate compound, **11**-*n*, in methanol:ethanol (1:1) under reflux with three molar equivalents of LiNTf$_2$ for two hours (Scheme 2.10). The dropwise addition of water precipitated the product as its NTf$_2^-$ salt, which was then isolated *via* filtration and washed multiple times with water to remove any excess LiNTf$_2$ and LiOTf side-product. The analytical purity of these salts was evidenced by combustion analyses and these data are presented in Table 2.2. ^{19}F NMR spectroscopy detected a new resonance at δ = -78.5 ppm corresponding to the NTf$_2^-$ anion (Figure 2.14); this new resonance appeared at a different chemical shift to that of the triflate compounds and is consistent with metathesis from OTf$^-$ to NTf$_2^-$.
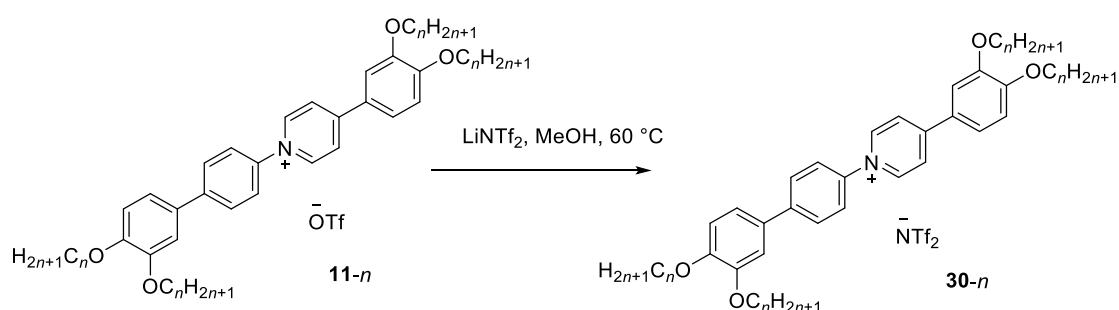
Scheme 2.10. Preparation of the NTf$_2^-$ salts, **30**-*n*.
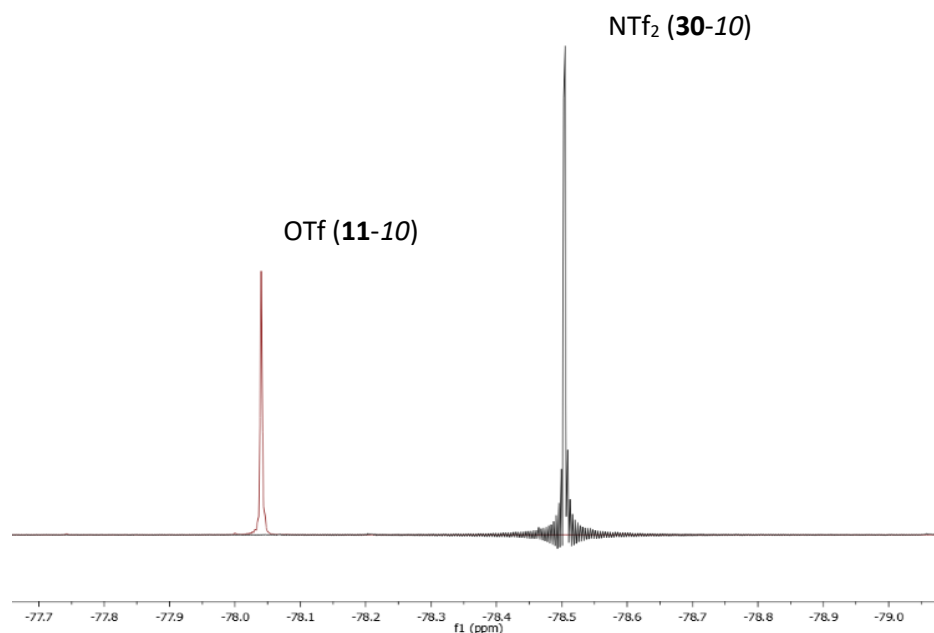
Figure 2.14. Overlaid ^{19}F NMR spectra of the tetracatenar OTf$^-$ compound **11**-*10* (red) and NTf$_2^-$ compound **30**-*10* (black) to show the different ^{19}F resonances.

3. Preparation of tetracatenar 3,4-dialkoxyphenylpyridine complexes of silver(I)

Having to hand the 3,4-dialkoxyphenylpyridines, **21**-*n*, as intermediates in the synthesis of the target tetracatenar *N*-phenylpyridinium materials, it was decided to take advantage of these compounds and prepare the analogous silver(I) complexes bearing phenylprididine ligands. Their preparation thus allowing a better comparison between the silver(I) materials and the *N*-phenylpyridinium ions. Procedures outlined by Donnio *et al.*[1] were followed.

Synthesis of the 3,4-dialkoxyphenylpyridine complexes of silver(I) triflate was achieved *via* reaction of the 3,4-dialkoxyphenylpyridine and silver(I) triflate in acetone in a vessel protected from light as outlined in Scheme 2.11. After 4 hours of stirring at room temperature, the reaction mixture was cooled to -18 °C and the resulting precipitate isolated *via* filtration, washed with multiple portions of cold acetone and dried. 3,4-Dialkoxyphenylpyridine ligands with aliphatic chains *n* > 12 were not soluble in acetone at room temperature, and so these ligands were stirred in acetone at 50 °C. Yields and micro-analytical data for the silver(I) triflate salts are collected in Table 2.6.
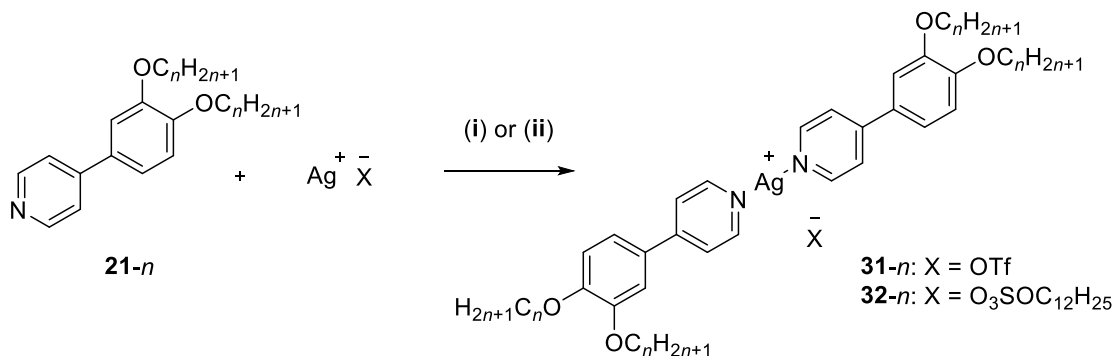
Scheme 2.11. Preparation of the 3,4-dialkoxyphenylpyridine complexes of silver(I) triflate and silver(I) dodecylsulfate: (**i**) AgOTf, acetone, (Δ) (**ii**) $AgO_3SOC_{12}H_{25}$, dichloromethane, r.t.

Preparation of the 3,4-dialkoxyphenylpyridine complexes of silver(I) dodecylsulfate were prepared by stirring the ligand with an excess of silver dodecylsulfate overnight in dichloromethane at room temperature in a vessel protected from light (Scheme 2.11). The reaction mixture was then filtered through celite and the filtrate evaporated to dryness; the residue was then crystallised from hot acetone and washed with diethyl ether to afford the silver(I) complexes. Yields and microanalytical data of these silver(I) salts are presented in Table 2.7. The silver(I) dodecylsulfate was also prepared in house following literature procedures,[20] which involved stirring of sodium dodecylsulfate and silver nitrate in water for three hours at room temperature in the dark followed by isolation of the precipitate; the solid was dried in a desiccator and used without further purification.

Complexation of the phenylpyridine ligands was confirmed by ^{1}H NMR spectroscopy, mass spectrometry and elemental analysis. A downfield shift in the resonances of hydrogen atoms *ortho* to the nitrogen of 0.15 ppm was observed in the ^{1}H NMR spectra of all the complexes – Figure 2.15 shows overlaid spectra of the silver(I) dodecylsulfate salt **32**-*8* and free ligand. Furthermore, the alkylsulfate anion is clearly visible *via* ^{1}H NMR spectroscopy in the case of the dodecylsulfate salts: specifically, the CH_2 signal adjacent to the sulfate moiety can be clearly resolved as a triplet of 2H integration at δ 4.10 ppm. In the case of the triflate salts, **31**-*n*, the presence of fluorine is confirmed by ^{19}F NMR spectroscopy; there is also a downfield shift of protons *ortho* to the nitrogen atom in ^{1}H NMR spectra to distinguish the triflate salts from the free ligand, too. Mass spectrometry also confirmed the molecular mass of each cation and anion, while elemental analysis confirms the purity of each compound (Tables 2.6 and 2.7).
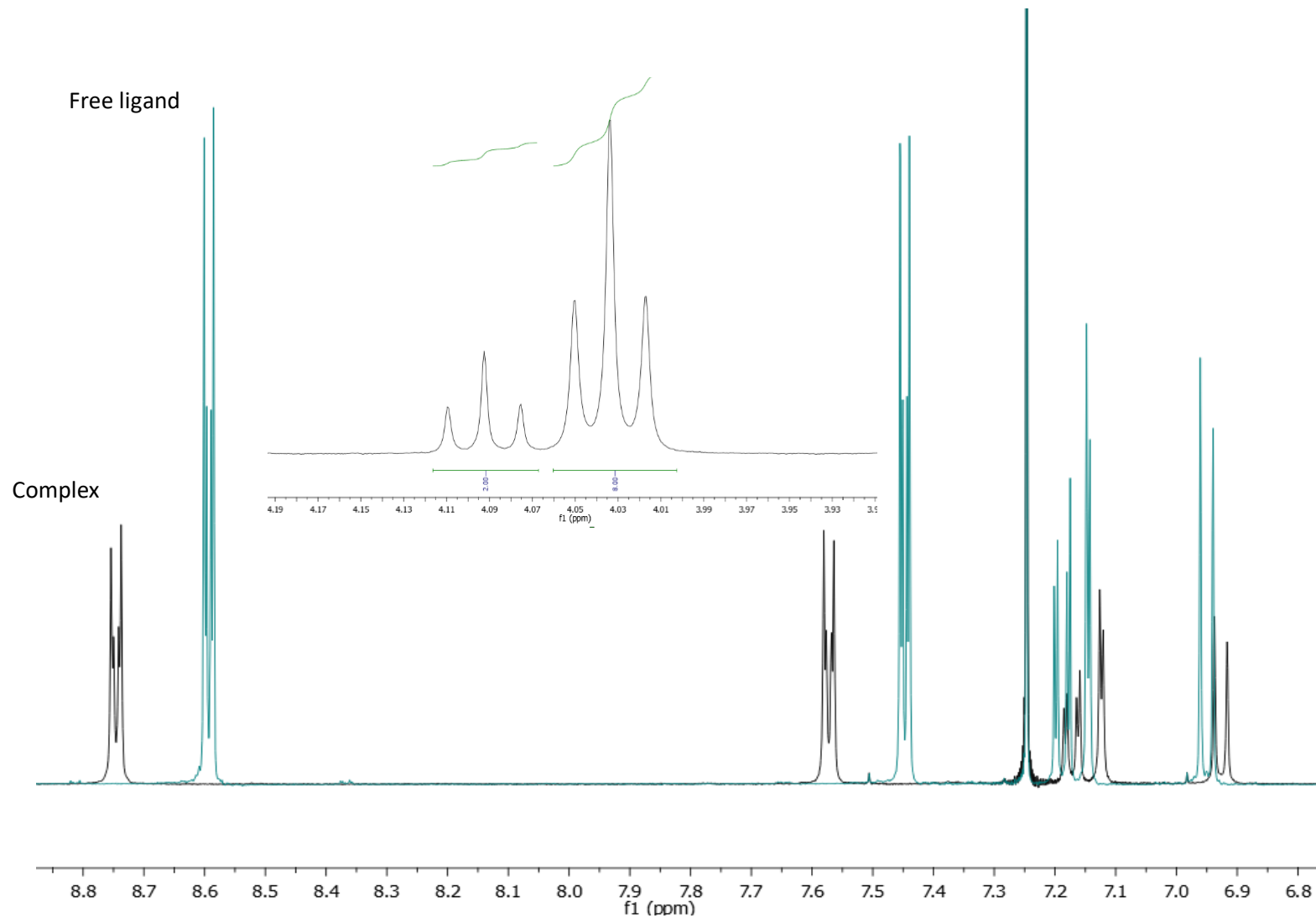
Figure 2.15. Overlaid ¹H NMR spectra of the free ligand, **21**-*8*, and the tetracatenar silver(I) dodecylsulfate salt, **32**-*8*, to show a shift in the resonances on complexation: inset shows the zoomed in region of the ¹H NMR spectrum of compound **32**-*8* at δ 4 ppm to show the CH_2 resonance of the dodecylsulfate anion.

4. Experimental

^{1}H, ^{19}F and ^{13}C{^{1}H} NMR spectra were recorded on a Jeol ECS400 spectrometer equipped with a sample changer operating at 400 MHz (^{1}H), 376 MHz (^{19}F) and 101 MHz (^{13}C), each at a temperature of 298 K. The solvent used to record each NMR spectrum is indicated in the respective experimental procedure. All NMR spectra were processed using MestReNova software. Chemical shifts are reported to two decimal places in ^{1}H, ^{13}C{^{1}H} and ^{19}F NMR spectra and coupling constants in ^{1}H NMR spectra are quoted to the nearest 0.5 Hz for the sake of consistency.

Mass spectra were recorded using a Bruker Daltronics micrOTOF MS Agilent series 1200LC with electrospray ionization (ESI and APCI) or on a Thermo LCQ using electrospray ionization. Mass spectral data are quoted as the m/z (mass/charge) ratio; m/z ratios are reported in units of Daltons.

Elemental analyses were performed by Dr Graeme McAllister at the University of York using an Exeter Analytical Inc CE 440 Elemental Analyzer and a Sartorius SE2 analytical balance.

4.1. Preparation of the calamitic *N*-phenylpyridinium ion, **12**-*6*

4.1.1. Preparation of **13**-*6*
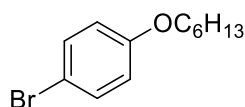
4-Hydroxybromobenzene (10 g, 58.2 mmol) was taken into acetone and to this solution was added K$_2$CO$_3$ (16 g, 116 mmol) and 1-bromohexane (7.3 ml, 52.9 mmol). The reaction mixture was heated under reflux for 24 h after which time the K$_2$CO$_3$ was filtered off through a plug of celite and the filtrate evaporated. The crude residue was then taken into diethyl ether (200 ml) and washed with aqueous NaOH solution (200 ml, 10 wt%), deionised water (200 ml) and aqueous NaCl solution (200 ml, saturated). The organic extract was dried over anhydrous MgSO$_4$ and the solvent removed under reduced pressure to yield a colourless oil (84%): ^{1}H NMR (400 MHz, CDCl$_3$) δ 7.35 (2H, AA'XX', J = 9.0 Hz), 6.76 (2H, AA'XX', J = 9.0 Hz), 3.90 (2H, t, J = 6.5 Hz), 1.75 (2H, m), 1.43 (2H, m), 1.32 (4H, m), 0.89 (3H, t, J = 7.0 Hz).

4.1.2. Preparation of **14**-6
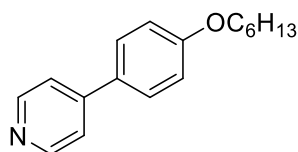
A three-necked round-bottomed flask was charged with 4-hexyloxybromobenzene (5.7 g, 22.2 mmol). THF (200 ml), aqueous Na_2CO_3 (200 ml, 2 mol dm^{-3}) and pyridine-4-boronic acid (3.0 g, 24.4 mmol) were then added and the resulting reaction mixture was degassed with argon whilst undergoing agitation in an ultrasonic bath. The bi-phasic reaction mixture was heated to 65 °C under a steady flow of nitrogen and [Pd(PPh$_3$)$_4$] (0.25 g, 1 mol%) was added. After complete consumption of the limiting reagent (after 16 h) the reaction mixture was cooled to r.t. and the biphasic mixture separated. The aqueous layer was extracted with dichloromethane (2 x 75 ml) and the combined organic extracts were washed with aqueous NaCl solution (100 ml, saturated) and dried over anhydrous $MgSO_4$. The solvent was removed under reduced pressure and the product was purified by flash column chromatography on silica gel using dichloromethane:methanol (95:5) as the eluent and then crystallised from hot *n*-hexane (74%): ^{1}H NMR (400 MHz, CDCl$_3$) δ 8.59 (2H, AA'XX', *J* = 6.5 Hz), 7.57 (2H, AA'XX', *J* = 8.5 Hz), 7.45 (2H, AA'XX', *J* = 6.5 Hz), 6.98 (2H, AA'XX', *J* = 8.5 Hz), 4.00 (2H, t, *J* = 7.0 Hz), 1.79 (2H, m), 1.47 (2H, m), 1.34 (4H, m), 0.90 (3H, t, *J* = 7.0 Hz).

4.1.3. Preparation of **15**-6
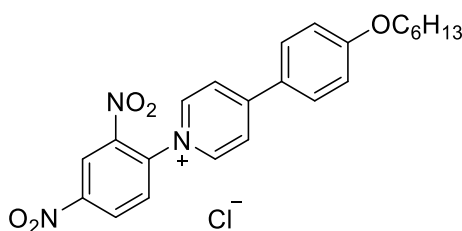
4-Hexyloxyphenylpyridine **13**-6 (3.0 g, 11.8 mmol) was taken into acetone and 1-chloro-2,4-dinitrobenzene (2.2 g, 10.7 mmol) added. The resulting solution was heated under reflux for 48 h. The reaction mixture was then cooled to r.t. and the resulting orange precipitate isolated *via* filtration, washed with acetone and used without further purification (62%): ^{1}H NMR (400 MHz, MeOD) δ 9.24 (1H, d, *J* = 2.5 Hz), 9.05 (2H, AA'XX', *J* = 7.0 Hz), 8.89 (1H, dd, *J* = 8.5, 2.5 Hz), 8.57 (2H,

AA'XX', J = 7.0 Hz), 8.29 (1H, d, J = 9.0 Hz), 8.18 (2H, AA'XX', J = 9.0 Hz), 7.20 (2H, AA'XX', J = 9.0 Hz), 4.13 (2H, t, J = 6.5 Hz), 1.82 (2H, m), 1.50 (2H, m), 1.37 (4H, m), 0.92 (3H, t J = 7.0 Hz).

4.1.4. Preparation of 16-6
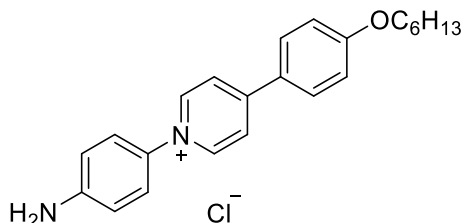
Compound 14-*6* (0.51 g, 1.12 mmol) was taken into 1-butanol (50 ml) and to this solution was added *p*-phenylenediamine (0.97 g, 9.0 mmol). The resulting solution was heated under reflux for 16 h, after which time the reaction mixture was cooled to r.t. and the solvent removed under reduced pressure. The product was then purified by flash column chromatography on silica gel using dichloromethane:methanol (8:2) and the resulting orange solid was triturated with acetone (75%): ^{1}H NMR (400 MHz, MeOD) δ 8.91 (2H, AA'XX', J = 8.0 Hz), 8.34 (2H, AA'XX', J = 8.0 Hz), 8.04 (2H, AA'XX', J = 9.0 Hz), 7.45 (2H, AA'XX', J = 8.0 Hz), 7.15 (2H, AA'XX', J = 9.0 Hz), 6.85 (2H, AA'XX', J = 8.0 Hz), 4.09 (2H, t, J = 6.5 Hz), 1.83 (2H, m), 1.49 (2H, m), 1.36 (4H, m), 0.91 (3H, t, J = 7.0 Hz).

4.1.5. Preparation of 17-6
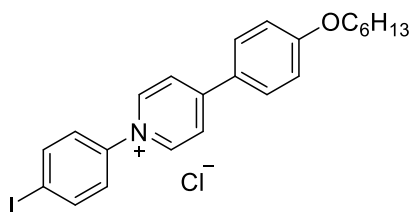
p-TsOH (0.31 g, 1.62 mmol) was dissolved in acetonitrile (15 ml) and 15-*6* (0.2 g, 0.54 mmol) added. The resulting suspension was cooled to 0 °C and to this was added $NaNO_2$ (0.075 g, 1.08 mmol) and KI (0.22 g, 1.35 mmol) in water (5 ml). The resulting orange suspension was stirred at 0 °C for 10 min before being allowed to warm to r.t. and stirred for a further hour. Water (10 ml) and aqueous $NaHCO_3$ (saturated) was added until a pH of 9 was reached. The product was then extracted into ethyl acetate (3 x 100 ml) and the combined organic extracts were washed with aqueous NaCl solution (100 ml, saturated) and dried over anhydrous $MgSO_4$. The solvent was then removed under reduced pressure. The product was crystallised from hot ethanol to afford a dark orange

microcrystalline solid (53%): ^{1}H NMR ((CD$_3$)$_2$SO, 400 MHz) δ 9.21 (2H, AA'XX', J = 7.5 Hz), 8.59 (2H, AA'XX', J = 7.5 Hz), 8.23 (2H, AA'XX', J = 9.0 Hz), 8.12 (2H, AA'XX', J = 9.0 Hz), 4.12 (2H, t, J = 6.5 Hz), 1.76 (2H, q, J = 6.5 Hz), 1.44 (2H, m), 1.33 (4H, m), 0.89 (3H, t, J = 7.0 Hz).

4.1.6.   Preparation of **12**-6
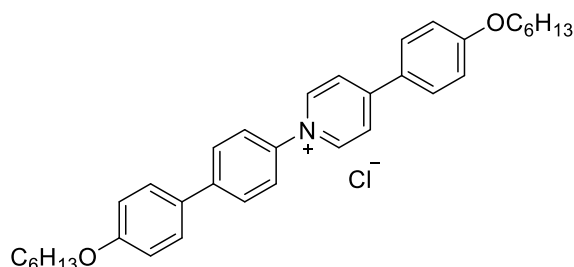
Compound **16**-*6* (0.3 g, 0.61 mmol) was added to a three-necked round bottomed flask previously purged with nitrogen and dissolved in anhydrous THF (60 ml). 4-Hexyloxybenzene boronic acid pinacol ester (0.2 g, 0.67 mmol) was then added along with aqueous sodium carbonate (60 ml, 2 mol dm^{-3}); the resulting biphasic mixture was sparged with an argon balloon whilst being agitated in an ultrasonic bath. The reaction mixture was heated under reflux under a flow of nitrogen and [Pd(PPh$_3$)$_4$] (1 mol%) added. After 20 h the biphasic reaction mixture was cooled to r.t. and separated. The aqueous layer was extracted with dichloromethane (2 x 100 ml) and the combined organic layers washed with aqueous NaCl (100 ml, saturated) and dried over MgSO$_4$ before removal of the solvent *in vacuo.* The product was purified by flash column chromatography on silica gel using dichloromethane:methanol (90:10) as the eluent to afford a yellow solid (24%): ^{1}H NMR (CDCl$_3$, 400 MHz) δ 9.24 (2H, AA'XX', J = 7.0 Hz), 8.44 (2H, AA'XX', J = 7.0 Hz), 7.91 (2H, AA'XX', J = 8.5 Hz), 7.86 (2H, AA'XX', J = 8.5 Hz), 7.76 (2H, AA'XX', J = 8.5 Hz), 7.50 (2H, AA'XX', J = 8.5 Hz), 7.03 (2H, AA'XX', J = 8.5 Hz), 6.98 (2H, m, AA'XX', J = 8.5 Hz), 4.02 (2H, t, J = 6.5 Hz), 4.01 (2H, t J =6.5 Hz), 1.82 (4H, m), 1.48 (4H, m), 1.36 (8H, m), 0.94 (3H, t, J = 7.0 Hz), 0.93 (3H, t, J =7.0 Hz).

4.2. Preparation of tetracatenar salts, **11**-*8*

4.2.1.   *Preparation of 3,4-dihydroxybromobenzene (4-bromocatechol) 19*
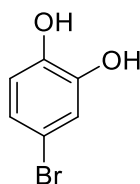
To a three-necked round bottom flask purged with nitrogen was added 4-bromoveratrole (6.61 ml, 46 mmol) and anhydrous dichloromethane (200 ml). The solution was cooled to 0 °C under a flow of nitrogen and BBr_3 solution (101 ml, 1 mol dm^{-3} in dichloromethane) added drop wise. The reaction mixture was then stirred at 0 °C for a further 10 min before being allowed to warm to r.t. and stirred for a further hour, after which time the reaction was quenched with water (200 ml) and the biphasic mixture separated. The aqueous layer was extracted with dichloromethane (3 x 150 ml) and the combined organic layers dried over $MgSO_4$ and the solvent removed to leave a grey oil that slowly crystallised with time (90%): ^{1}H NMR (400 MHz, CDCl$_3$) 7.02 (1H, d, *J* = 2.5 Hz), 6.92 (1H, dd, *J* = 8.5, 2.5 Hz), 6.74 (1H, d, *J* = 8.5 Hz), 5.63 (1H, s), 5.44 (1H, s).

4.2.2.   *Preparation of 3,4-dioctyloxybromobenzene 20-8*
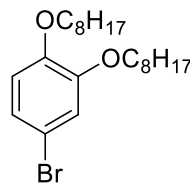
3,4-Dihydroxybromobenzene (7.8 g, 41.3 mmol) was dissolved in acetone (200 ml) and to this solution was added Cs_2CO_3 (26.9 g, 82.6 mmol) and 1-bromooctane (14.5 g, 13.0 ml, 75.1 mmol); the resulting suspension was heated under reflux for 2 days. The reaction mixture was then cooled to room temperature, diluted with dichloromethane (150 ml) to prevent the product from crystallising and the residual potassium carbonate removed *via* filtration. The filtrate was then evaporated to dryness and the residue taken into diethyl ether (200 ml), washed with aqueous NaOH (200 ml, 10 wt%), water (200 ml) and aqueous NaCl (200 ml, saturated). The organic layer was then dried over $MgSO_4$ and the solvent removed. The product was crystallised from hot acetone to leave a white microcrystalline solid (51%): ^{1}H NMR (400 MHz, CDCl$_3$) δ 6.98 (2H, m), 6.73

(1H, d, J = 9.0 Hz), 3.96 (2H, t, J = 6.5 Hz), 3.95 (2H, t, J = 6.5 Hz), 1.79 (4H, m), 1.45 (4H, m), 1.30 (16H, m), 0.88 (6H, t, J = 7.0 Hz).

The preparation of all other homologues was performed in an identical fashion.

4.2.3. *Preparation of 3,4-dioctyloxy-4'-phenylpyridine* **21**-8
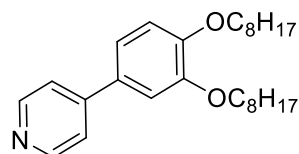
To a three-necked round bottomed flask purged with nitrogen was added 3,4-dioctyloxybromobenzene (4.27 g, 10.3 mmol), toluene (120 ml), ethanol (40 ml) and water (40 ml). Pyridine-4-boronic acid pinacol ester was then added (4.24 g, 20.7 mmol) along with Na_2CO_3 (3.3 g, 31 mmol). The biphasic reaction mixture was the degassed with argon for 30 min whilst undergoing ultrasonic agitation. The catalyst ([$Pd_3(OAc)_6$] and Sphos, 1 mol%, pre-mixed in THF) was then added to the reaction mixture, which was then heated to 105 °C under a flow of nitrogen for 16 h. The biphasic mixture was then separated and the aqueous layer extracted with dichloromethane (3 x 75 ml); the combined organic extracts were then dried over $MgSO_4$ and the solvent removed. The product was purified by flash column chromatography on silica gel using dichloromethane:methanol (98:2) as the eluent. The resulting product was finally crystallised from hot *n*-hexane to yield a white microcrystalline solid (62%): ^{1}H NMR (400 MHz, CDCl₃) δ 8.60 (1H, AA'XX', J = 6.5 Hz), 7.45 (2H, AA'XX', J = 6.5 Hz), 7.19 (1H, dd, J = 8.5, 2.5 Hz), 7.15 (1H, d, J = 2.5 Hz), 6.95 (1H, d, J = 8.5 Hz), 4.05 (2H, t, J = 6.5 Hz), 4.03 (2H, t, J = 6.5 Hz), 1.84 (4H, m), 1.47 (4H, m), 1.31 (16H, m), 0.87 (6H, m).

The preparation of all other homologues was performed in an identical fashion.

4.2.4. Preparation of Zincke salt **22**-8
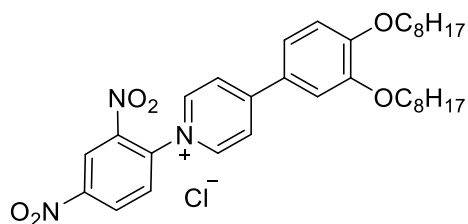
3,4-dioctyloxy-4'-phenylpyridine (3.25 g, 7.91 mmol) was taken into acetone (75 ml) and 1-chloro-2,4-dinitrobenzene (1.76 g, 8.7 mmol) was added; the resulting suspension was heated under reflux for 4 days. The reaction mixture was then cooled to r.t. and the orange precipitate isolated *via* filtration and washed repeatedly with acetone: ^{1}H NMR (400 MHz, CD$_3$OD) δ 9.25 (1H, d, J = 2.5 Hz), 9.02 (2H, AA'XX', J = 9.0 Hz), 8.88 (1H, dd, J = 8.5, 2.5 Hz), 8.58 (2H, AA'XX', J = 7.0 Hz), 8.26 (1H, d, J = 8.5 Hz), 7.82 (1H, dd, J = 8.5, 2.5 Hz), 7.69 (1H, d, J = 2.5 Hz), 7.20 (1H, d, J = 9.0 Hz), 4.16 (2H, t, J = 6.5 Hz) 4.15 (2H, t, J = 6.5 Hz), 1.84 (4H, m), 1.54 (4H, m), 1.33 (16 H), 0.87 (6H, t, J = 7.0 Hz).

The preparation of all other homologues was performed in an identical fashion.

4.2.5. Preparation of 4-iodo species **23**-8
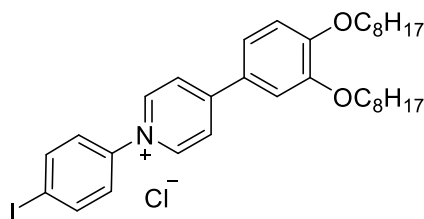
A three-necked round bottomed flask purged with nitrogen was charged with Zincke salt **22**-8 (0.25 g, 0.41 mmol) and dissolved in *n*-butanol (6 ml). 4-Iodoaniline (0.36 g, 1.64 mmol) was added and the resulting suspension heated under reflux for 16 h after which time the reaction mixture had become a deep yellow solution. The solution was cooled to room temperature and the resulting precipitate was isolated *via* filtration, triturated with cold dichloromethane and acetone and dried (53%): ^{1}H NMR (400 MHz, DMSO-*d*) δ 9.19 (2H, AA'XX', J = 7.0 Hz), 8.64 (2H, AA'XX', J = 7.0 Hz), 8.13 (2H, AA'XX', J = 8.5 Hz), 7.86 (1H, dd, J = 8.5, 2.0 Hz), 7.74 (1H, d, J = 2.0 Hz), 7.68 (2H, AA'XX', J = 8.5 Hz), 7.21 (1H, d, J= 8.5 Hz), 4.14, (2H, t, J = 6.5 Hz) 4.12 (2H, t, J = 6.5 Hz), 1.75 (4H, m), 1.45 (4H, m), 1.30 (16H, m), 0.85 (3H, t, J = 7.0 Hz).

The preparation of all other homologues was performed in an identical fashion.

4.2.6. Preparation of triflate salt 24-8
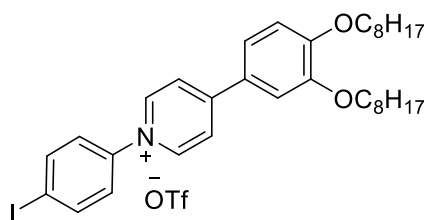
Chloride salt **23**-8 (0.42 g, 0.65 mmol) was taken into DMF (80 ml) and the resulting solution heated to 65 °C. Silver triflate (0.42 g, 1.62 mmol) was then added after which time a yellow suspension immediately formed; the reaction mixture was stirred at 65 °C for 16 h before being cooled to r.t. and the precipitate removed. The filtrate was then evaporated to dryness and the residue taken into dichloromethane (50 ml), washed repeatedly with water (4 x 75 ml) and dried over MgSO$_4$. The solvent was removed under reduced pressure and the compound subsequently crystallised from hot ethanol to yield a yellow solid (58%): ^{1}H NMR (400 MHz, DMSO-*d*) δ 9.19 (2H, AA'XX', *J* = 7.0 Hz), 8.64 (2H, AA'XX', *J* = 7.0 Hz), 8.13 (2H, AA'XX', *J* = 8.5 Hz), 7.86 (1H, dd, *J* = 8.5, 2.0 Hz), 7.74 (1H, d, *J* = 2.0 Hz), 7.68 (2H, AA'XX', *J* = 8.5 Hz), 7.21 (1H, d, *J*= 8.5 Hz), 4.14 (2H, t, *J* = 6.5 Hz) 4.11 (2H, t, *J* = 6.5 Hz), 1.75 (4H, m), 1.45 (4H, m), 1.30 (16 H, m), 0.85 (3H, t, *J* = 7.0 Hz).

The preparation of all other homologues was performed in an identical fashion.

4.2.7. Preparation of tetracatenar triflate salt 11-8
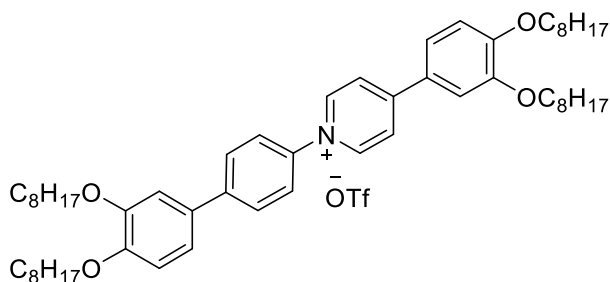
A three-necked round bottomed flask purged with nitrogen was charged with triflate salt **24**-8 (0.25 g, 0.33 mmol) and anhydrous THF (15 ml). To this yellow solution was added borate ester **25**-8 (0.18 g, 0.39 mmol) and aqueous sodium carbonate (15 ml, 2 mol dm^{-3}). Argon was then bubbled through the biphasic mixture whilst undergoing agitation in an ultrasonic bath to rigorously remove oxygen

from the reaction mixture. [Pd$_3$(OAc)$_6$] (7.4 x 10^{-4} g, 3.3 x 10^{-3} mmol) and Sphos (1.35 x 10^{-3} g, 3.3 x 10^{-3} mmol) were dissolved in anhydrous THF (1 ml) and stirred under nitrogen until the mixture became red. This pre-prepared catalyst was then added to the reaction mixture, which was then heated to 65 °C under a steady flow of nitrogen. On complete consumption of the limiting reagent (after 16 h), the reaction mixture was cooled to r.t., the biphasic mixture separated and the aqueous layer extracted with dichloromethane (2 x 25 ml). The combined organic layers were dried over MgSO$_4$ and the solvent removed under reduced pressure. The product was purified by flash column chromatography on silica gel using dichloromethane:methanol (95:5) as the eluent. The product was finally crystallised from hot ethanol to afford a yellow microcrystalline solid (68%): ^{1}H NMR (400 MHz, CDCl$_3$) δ 8.80 (2H, AA'XX', J = 7.0 Hz), 8.25 (2H, AA'XX', J = 7.0 Hz), 7.41 (1H, dd, J = 8.0, 2.0 Hz), 7.31 (1H, d, J = 2.0 Hz), 7.03 (1H, d, J = 2.0 Hz), 7.00 (1H, dd, J = 8.0, 2.0 Hz), 6.84 (1H, d, J = 8.0 Hz), 6.81 (1H, d, J = 8.0 Hz), 4.06 (2H, t, J = 7.0 Hz), 4.01 (2H, t, J = 7.0 Hz), 3.97 (2H, t, J = 7.0 Hz), 3.90 (2H, t, J = 7.0 Hz), 1.82 (8H, m), 1.47 (8H, m), 1.29 (32H, m), 0.85 (12H, m). ^{19}F NMR (376 MHz, CDCl$_3$) δ -78.09, (s). ^{13}C NMR (101 MHz, CDCl$_3$) δ 14.22, 22.80, 22.06, 26.15, 26.18, 26.21, 29.10, 29.40, 29.43, 29.52, 29.57, 31.96, 69.17, 69.25, 69.58, 69.63, 112.01, 112.55, 113.10, 113.72, 119.90, 120.93 (J_{CF} = 320 Hz), 122.60, 123.58, 124.06, 124.59, 125.71, 128.58, 130.84, 139.79, 142.50, 144.00, 149.61, 150.03, 153.99, 155.99. APCI: found 820.6243 [M$^+$], 148.9523 [M$^-$].

The preparation of all other homologues was performed in an identical fashion.

Table 2.1. Micro-analytical data for the tetracatenar triflate salts **11**-*8:* theoretical values in parentheses.

n	Yield / %	%C	%H	%N
8	68	69.4 (69.3)	8.7 (8.5)	1.5 (1.4)
10	72	70.9 (71.0)	9.2 (9.1)	1.2 (1.2)
12	69	72.3 (72.4)	9.6 (9.6)	1.2 (1.2)
13	81	72.5 (73.0)	10.2 (9.8)	1.0 (1.1)
14	75	73.6 (73.5)	10.3 (10.0)	1.0 (1.1)
16	70	74.7 (74.5)	10.4 (10.4)	1.3 (1.0)
18	61	75.0 (75.3)	10.7 (10.7)	1.3 (0.9)

4.2.8. Preparation of **25**-*n*
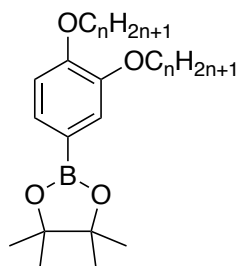
A three-necked round bottom flask purged with N_2 was charged with 3,4-didodecyloxybromobenzene (2.47 g, 5.3 mmol) and dissolved in anhydrous DMSO (40 ml). *Bis*-pinacolato diboron (1.50 g, 5.8 mmol) and NaOAc (1.5 g, 18.5 mmol) were added and the reaction mixture heated to 80 °C under a flow of N_2. [PdCl$_2$(dppf)] (0.15g, 0.19 mmol, 3 mol%) was then added and the resulting solution stirred at 80 °C for 16 h. The reaction mixture was cooled to RT, diluted with water (100 ml) and the product extracted into diethyl ether (4 x 100 ml). The combined organic layers were then washed repeatedly with water (5 x 150 ml) to remove any residual DMSO, dried over MgSO$_4$ and the solvent removed under reduced pressure. The product was purified via column chromatography using 40-60 °C petroleum spirit:EtOAc (9:1) to afford a white solid (54%): ^{1}H NMR (400 MHz, CDCl$_3$) 7.38 (1H, dd, *J* = 8.0, 1.5 Hz), 7.29 (1H, d, *J* = 1.5 Hz), 6.87 (1H, d, *J* = 8.0 Hz), 4.02 (4H, m), 1.81 (4H, m), 1.46 (4H, m), 1.33 (12H, s), 1.26 (32 H, m), 0.88 (6H, m).

4.3. Preparation of the tetracatenar chloride salts, **25**-*n*

4.3.1. *Preparation of chloride salt* **26**-*n*
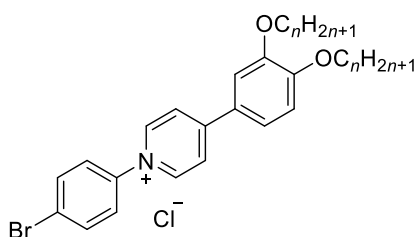
2,4-Dinitro salt **21**-*8* (2.79 g, 4.55 mmol) was taken into *n*-butanol and heated to 110 °C under a flow of nitrogen. 4-Bromoaniline (3.12 g, 18.2 mmol) was then added and the reaction mixture stirred for 16 h before being cooled to r.t. and the precipitate isolated *via* filtration. The resulting orange solid was washed multiple times with acetone and then triturated with dichloromethane to afford a bright yellow solid (45%): ^{1}H NMR (400 MHz, CDCl$_3$) δ 8.94 (2H, AA'XX', *J* = 7.5 Hz), 8.32 (2H,

AA'XX', J = 7.5 Hz), 7.76 (2H, AA'XX', J = 8.5 Hz), 7.67 (2H, AA'XX', J = 8.5 Hz), 7.57 (1H, dd, J = 8.5, 2.5 Hz), 7.40 (1H, d, J = 2.5 Hz), 6.98 (1H, d, J = 8.5 Hz), 4.06 (2H, t, J = 6.5 Hz), 4.04 (2H, t, J = 6.5 Hz), 1.80 (4H, m), 1.43 (4H, m), 1.26 (16H, m), 0.82 (3H, t, J = 7.0 Hz), 0.81 (3H, t, J = 7.0 Hz).

4.3.2. Preparation of tetracatenar chloride salt, 26-n
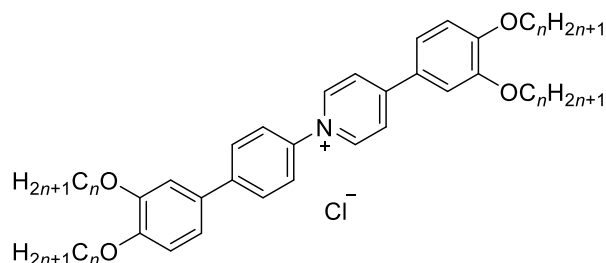
4-Bromo chloride salt **27**-*8* (0.05 g, 0.076 mmol) and 3,4-dialkoxybenzeneboronic acid pinacol ester **25**-*8* (0.047 g, 0.09 mmol) were added to a three-necked round-bottomed flask already purged with nitrogen and taken into THF (50 ml) and ethanol (25 ml). Aqueous sodium carbonate (50 ml, 2 mol dm^{-3}) was then added and the biphasic solution degassed with arogon whilst undergoing agitation in an ultrasonic bath. [$Pd_3(OAc)_6$] (3.5 x 10^{-3} g, 1.52 x 10^{-3} mmol) and Sphos (7.0 x 10^{-3} g, 3.0 x 10^{-3} mmol) were dissolved in anhydrous THF (1 ml) and stirred under nitrogen until the mixture became red. This pre-prepared catalyst was then added to the reaction mixture, which was then heated to 75 °C under a steady flow of nitrogen. After complete consumption of the limiting reagent (after 6 h), the reaction mixture was cooled to r.t. and the biphasic mixture separated. The aqueous layer was extracted with dichloromethane (3 x 50 ml) and the combined organic extracts were washed with aqueous NaCl (100 ml, saturated) and dried over anhydrous $MgSO_4$ before evaporation of the solvent under reduced pressure. The product was purified by flash column chromatography on silica gel using dichloromethane:methanol (95:5) as the eluent. On evaporation of the solvent, the solid was finally triturated with dichloromethane (50 ml) to afford a bright orange solid (86%): ^{1}H NMR (400 MHz, CDCl$_3$) δ 9.37 (2H, AA'XX', J = 7.0 Hz), 8.40 (2H, AA'XX', J = 7.0 Hz), 7.92 (2H, AA'XX', J = 9.0 Hz), 7.76 (2H, AA'XX', J = 9.0 Hz), 7.53 (1H, dd, J = 8.5, 2.5 Hz), 7.36 (1H, d, J = 2.5 Hz), 7.09 (2H, m), 6.94 (1H, d, J = 8.5 Hz), 6.92 (1H, d, J = 8.5 Hz), 4.09 (2H, t, J = 6.5 Hz), 4.04 (6H, m), 1.84 (8H, m), 1.49 (8H, m), 1.31 (32H, m), 0.87 (12H, m).

Table 2.2. Micro-analytical data for the tetracatenar chloride salts, **26**-*n*: theoretical values in parentheses.

n	Yield / %	%C	%H	%N
6	81	72.8 (75.8)	8.8 (8.9)	2.0 (1.9)
8	62	75.4 (77.1)	9.3 (9.7)	1.5 (1.6)
10	67	75.1 (78.1)	9.7 (10.2)	1.5 (1.5)
12	64	77.7 (78.9)	10.6 (10.6)	1.3 (1.3)

As mentioned in Section 2.3.1. the chloride salts could not be isolated in analytical purity owing to traces of organic impurities that could not be removed. However, this was not a major issue as the chloride salts were used only as intermediates in the preparation of the final alkylsulfate salts, which were subsequenrtly isolated in acceptable purity to be studied.

4.4. Preparation of the tetracatenar octylsulfate salts, **28**-*n*
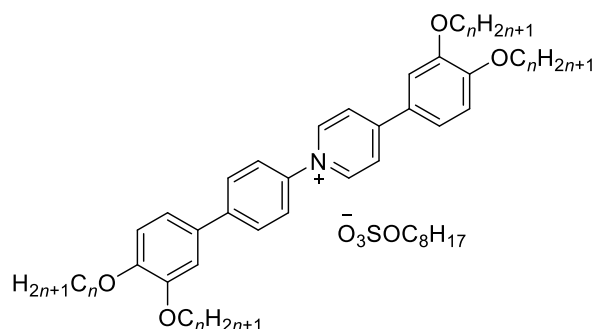
The following procedure documents the preparation of the octyloxy octyllsulfate salt: All other derivatives were prepared in an analogous fashion, except that ethanol was used as the reaction solvent for the *n* = 12 homologue due to the insolubility of this compound in hot methanol. The tetradecyloxy derivative was, however, prepared successfully in an identical fashion from the triflate salt using ethanol as the reaction solvent.

Chloride salt **26**-*8* (0.03 g, 0.035 mmol) was taken into methanol (75 ml) and the solution heated to 60 °C. The solution was then saturated with sodium octylsulfate and stirred at this temperature for 2 h. Water was then added dropwise to precipitate the product as its octylsulfate salt, which was subsequently isolated *via* filtration and washed with multiple portions of water. The compound was then crystallised from hot ethanol and the solid taken into dichloromethane and filtered through a

0.2 µm PTFE filter to remove any insoluble impurities. The solvent was then removed and the compound dried under vacuum (66%): ^{1}H NMR (400 MHz, CDCl$_3$) δ 8.98 (2H, AA'XX', J = 7.0 Hz), 8.41 (2H, AA'XX', J = 7.0 Hz), 7.72 (2H, AA'XX', J = 8.5 Hz), 7.67 (2H, AA'XX', J = 8.5 Hz), 7.49 (1H, dd, J = 8.5, 2.5 Hz), 7.38 (1H, d, J = 2.5 Hz), 7.05 (1H, d, J = 2.5 Hz), 7.03 (1H, dd, J = 8.5, 2.5 Hz), 6.88 (1H, d, J = 8.5 Hz), 6.84 (1H, d, J = 8.5 Hz), 4.11 (4H, m), 4.04 (2H, t, J = 6.5 Hz), 4.01 (2H, t, J = 6.5 Hz), 3.94 (2H, t, J = 7.0 Hz), 1.84 (8H, m), 1.69 (2H, m), 1.29 (42 H, m), 0.87 (12 H, m), 0.83 (3H, t, J = 7.0 Hz).

Table 2.3. Micro-analytical data for the tetracatenar octylsulfate salts, **28**-*n*: theoretical values in parentheses.

n	Yield / %	%C	%H	%N
6	82	71.3 (71.9)	9.3 (9.1)	1.5 (1.5)
8	66	73.5 (73.4)	10.1 (9.7)	1.6 (1.4)
10	71	74.3 (74.6)	10.2 (10.1)	1.1 (1.2)
12	74	75.6 (75.2)	10.4 (10.5)	1.0 (1.1)
14	68	76.1 (76.4)	11.3 (10.8)	1.0 (1.0)

4.5. Preparation of the tetracatenar dodecylsulfate salts, **29**-*n*
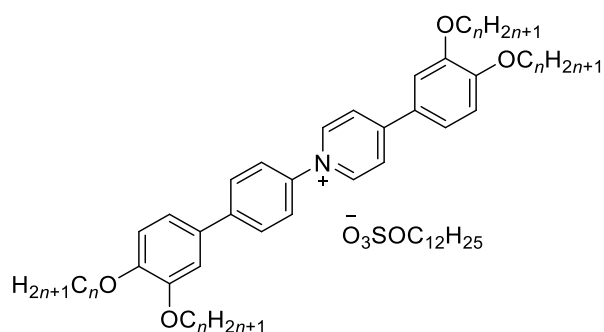
The following procedure documents the preparation of the octyloxy dodecylsulfate salt, all other derivatives were prepared in an analogous fashion except that ethanol was used as the reaction solvent for the *n* = 12 derivative due to the insolubility of this compound in hot methanol.

Chloride salt **26**-*8* (0.03 g, 0.035 mmol) was taken into methanol (75 ml) and heated to 60 °C. This solution was then saturated with sodium dodecylsulfate and the reaction mixture stirred at this temperature for 2 h. Water was then added dropwise to precipitate the product as its dodecylsulfate salt, which was subsequently isolated *via* filtration and the solid washed multiple

times with water. The product was then crystallised from hot ethanol and the resulting solid taken into dichloromethane and filtered through a 0.2 μm PTFE filter to remove any insoluble impurities. The solvent was then removed and the product dried under vacuum (65%): ^{1}H NMR (400 MHz, CDCl$_3$) δ 8.99 (2H, AA'XX', J = 6.5 Hz), 8.39 (2H, AA'XX', J = 6.5 Hz), 7.73 (2H, AA'XX', J = 8.5 Hz), 7.68 (2H, AA'XX', J = 8.5 Hz), 7.49 (1H, dd, J = 8.5, 2.5 Hz), 7.39 (1H, d, J = 2.5 Hz), 7.05 (2H, m), 6.89 (1H, d, J = 8.5 Hz), 6.86 (1H, d, J = 8.5 Hz), 4.11 (4H, t, J = 7.0 Hz), 4.04 (2H, t, J = 7.0 Hz), 4.01 (2H, t, J = 7.0 Hz), 3.96 (2H, t, J = 7.0 Hz), 1.84 (8H, m), 1.69 (2H, m), 1.49 (8H, m), 1.30 (50H, m), 0.87 (15H, m).

Table 2.4. Micro-analytical data for the tetracatenar dodecylsulfate salts, **29**-n: theoretical values in parentheses.

n	Yield / %	%C	%H	%N
6	78	72.1 (72.7)	8.9 (9.4)	0.9 (1.4)
8	65	73.8 (74.1)	10.0 (9.90)	0.7 (1.3)
10	69	75.1 (74.7)	10.3 (10.4)	1.2 (1.3)
12	73	75.4 (76.0)	10.6 (10.7)	1.4 (1.1)

4.6. Preparation of the tetracatenar NTf$_2$ salts, **30**-n
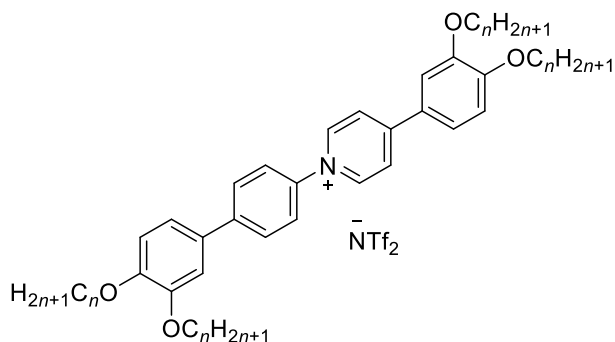
Triflate salt **11**-8 (0.05 g, 0.052 mmol) was taken into ethanol:methanol (1:1, 50 ml) and heated to 70 °C. LiNTf$_2$ (0.037 g, 0.13 mmol) was then added in methanol (5 ml) and the reaction mixture stirred for 2 h. Water was then added dropwise to precipitate the product as its NTf$_2$ salt, which was subsequently isolated *via* filtration and washed multiple times with water. The product was then purified by flash column chromatography on silica gel using dichloromethane:methanol as the eluent (95:5) to afford a bright orange solid on evaporation of the solvent (76%): ^{1}H NMR (400 MHz,

CDCl$_3$) δ 8.76 (2H, AA'XX', J = 7.0 Hz), 8.30 (2H, AA'XX', J = 7.0 Hz), 7.80 (2H, AA'XX', J = 8.5 Hz), 7.68 (2H, AA'XX', J = 8.5 Hz), 7.52 (1H, dd, J = 8.5, 2.5 Hz), 7.42 (1H, d, J = 2.5 Hz), 7.14 (2H, m), 7.01 (1H, d, J = 8.5 Hz), 6.97 (1H, d, J = 8.5 Hz), 4.11 (2H, t, J = 6.5 Hz), 4.08 (2H, t, J = 6.5 Hz), 4.07 (2H, t, J = 6.5 Hz), 4.04 (2H, t, J = 6.5 Hz), 1.85 (8H, m), 1.49 (8H, m), 1.32 (32 H, m), 0.88 (12H, m). ^{19}F NMR (376 MHz, CDCl$_3$) δ -78.54 (s).

The preparation of all other homologues was performed in an identical fashion.

Table 2.5. Micro-analytical data for the tetracatenar NTf$_2$ salts, **30**-n: theoretical values in parentheses.

n	Yield / %	%C	%H	%N
4	64	56.2 (56.2)	5.7 (5.8)	2.9 (3.2)
8	76	62.2 (62.2)	7.5 (7.5)	2.4 (2.5)
10	81	64.6 (64.3)	8.3 (8.1)	2.2 (2.3)
12	69	66.2 (66.1)	8.7 (8.7)	2.1 (2.1)
14	83	67.6 (67.7)	9.3 (9.1)	1.8 (2.0)

4.7. Preparation of the tetracatenar 3,4-dialkoxyphenylpyridine silver(I) triflates, **31**-n
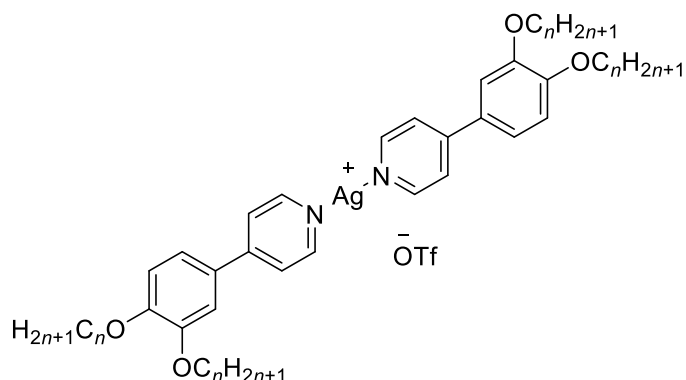
3,4-Didodecyloxyphenylpyridine **20**-*12* (0.30 g, 0.57 mmol) was taken into acetone (20 ml) and the vessel protected from light. Silver triflate (0.08 g, 0.32 mmol) was then added and the reaction mixture stirred at 50 °C for 4 hours, after which time it was placed in the freezer and the solid isolated *via* filtration. The product was then re-crystallised from hot acetone and washed three times with diethyl ether. The resulting solid was then taken into dichloromethane and filtered through a plug of celite to remove any insoluble by-products; the solvent was then evaporated under reduced pressure to furnish a white powder (51%): ^{1}H NMR (400 MHz, CDCl$_3$) δ 8.71 (4H,

AA'XX', J = 6.5 Hz), 7.56 (4H, AA'XX', J = 6.5 Hz), 7.13 (2H, dd, J = 8.5, 2.0 Hz), 7.10 (2H, d, J = 2.0 Hz), 6.90 (2H, d, J = 8.5 Hz), 4.04 (4H, t, J = 7.0 Hz), 4.03 (4H, t, J = 7.0 Hz), 1.86 (8H, m), 1.50 (8H, m), 1.31 (64 H, m), 0.89 (6H, t, J = 6.5 Hz), 0.89 (6H, t, J = 6.5 Hz). ^{19}F NMR (376 MHz, CDCl$_3$) δ_F -77.68, (s). ESI: found 1156.7916 [M+1[+]], 148.9525 [M[-]].

Table 2.6. Micro-analytical data for the phenylpyridine complexes of silver(I) triflate, **31**-*n*.

n	Yield / %	%C	%H	%N
4	48	54.7 (54.7)	6.0 (5.9)	3.1 (3.3)
6	63	58.0 (58.3)	6.8 (6.9)	2.6 (2.9)
8	47	61.1 (61.2)	7.5 (7.7)	2.3 (2.6)
10	57	63.3 (63.5)	8.6 (8.3)	2.2 (2.4)
12	81	65.2 (65.4)	8.9 (8.8)	2.1 (2.2)
14	71	66.9 (67.0)	9.4 (9.3)	2.0 (2.0)
18	62	69.6 (69.5)	10.0 (10.0)	1.7 (1.7)

4.8. Synthesis of 3,4-dialkoxyphenylpyridine complexes of silver(I) dodecylsulfate, **32**-*n*
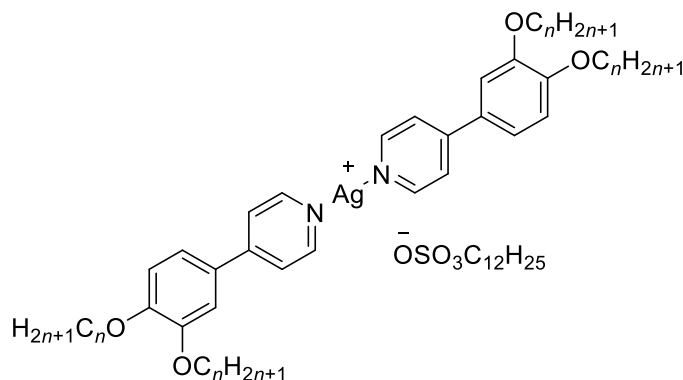
3,4-Didodecyloxyphenylpyridine **20**-*12* (0.30 g, 0.57 mmol) was taken into dichloromethane (7 ml) and added dropwise to a stirred suspension of silver(I) dodecylsulfate (0.12 g, 0.32 mmol) in dichloromethane (7 ml) in a vessel protected from light. The reaction mixture was stirred at room temperature overnight before filtration through a plug of celite followed by evaporation of the filtrate. The brown residue was then crystallised from hot acetone and the solid washed repeatedly with diethyl ether. The resulting solid was then taken into dichloromethane and filtered once more through a plug of celite to remove any insoluble by-products; the filtrate was the evaporated under reduced pressure to leave a white solid (43%): ^{1}H NMR (400 MHz, CDCl$_3$) δ 8.74 (4H, AA'XX', J = 6.5

Hz), 7.52 (4H, AA'XX', J = 6.5 Hz), 7.14 (2H, dd, J = 8.5, 2.0 Hz), 7.10 (2H, d, J = 2.0 Hz), 6.90 (2H, d, J = 8.5 Hz), 4.11 (2H, t, J = 7.0 Hz), 4.02 (4H, t, J = 7.0 Hz), 4.02 (4H, t, J = 7.0 Hz), 1.84 (8H, m), 1.59 (2H, m), 1.47 (8H, m), 1.26 (82H, m), 0.85 (15 H, m). ESI: found 1156.7916 [M+1$^+$], 265.1485 [M$^-$].

Table 2.7. Micro-analytical data for the phenylpyridine complexes of silver(I) dodecylsulfate, **32**-*n*.

n	Yield / %	%C	%H	%N
4	47	61.5 (61.8)	8.1 (7.8)	2.8 (2.9)
6	59	64.2 (64.3)	8.6 (8.5)	2.2 (2.6)
8	54	65.9 (66.3)	9.1 (9.0)	2.2 (2.3)
10	57	67.4 (67.9)	10.1 (9.5)	2.1 (2.1)
12	43	65.2 (65.4)	8.9 (8.8)	2.1 (2.2)
14	65	66.9 (67.0)	9.4 (9.3)	2.0 (2.0)

4.9. Single Crystal X-Ray Diffraction

Diffraction data were collected at 110 K on an Oxford Diffraction SuperNova diffractometer with Cu-K$_\alpha$ radiation (λ = 1.54184 Å) using an EOS CCD camera. The crystal was cooled with an Oxford Instruments Cryojet. Diffractometer control, data collection, initial unit cell determination, frame integration and unit-cell refinement was carried out with Crysalis. Face-indexed absorption corrections were applied using spherical harmonics, implemented in SCALE3 ABSPACK scaling algorithm. OLEX2 was used for overall structure solution, refinement and preparation of computer graphics and publication data. Within OLEX2, the algorithms used for structure solution were ShelXT dual-space using the ShelXL refinement by full-matrix least-squares used the SHELXL-97 algorithm within OLEX2. All non-hydrogen atoms were refined anisotropically. Hydrogen atoms were placed using a "riding model" and included in the refinement at calculated positions. One of the octyl side chains was disordered and modelled in two positions with refined occupancies of 0.714:0.286(4). The C-C bond lengths in the disordered part of the chain were restrained to be 1.54 angstroms except for the terminal C-C bond lengths which were restrained to be 1.52 angstroms. Two pairs of ADPs in the disordered chains were constrained to be equal, namely: C26 & C26a and C28 & C28a. The triflate anion/water showed minor disorder with the triflate being modelled in two positions with refined occupancies of 0.9598:0.0402(15). For the minor form, the C-F bond lengths were restrained to be 1.4 angstroms, the S-O bond lengths restrained to be 1.5 angstroms and the

C-S bond length restrained to be the same as that of the major form. ADP of O5A was constrained to be equal to that of O5 and the ADP of C56a, F1a, F2a, F3a, O6a, O7a were restrained to be approximately isotropic.

5. References

1   B. Donnio and D. W. Bruce, *New J. Chem.*, 1999, **23**, 275–286.

2   K. Tanabe, T. Yasuda, M. Yoshio and T. Kato, *Org. Lett.*, 2007, **9**, 4271–4274.

3   D. W. Bruce, D. A. Dunmur, S. A. Hudson, E. Lalinde, P. M. Maitlis, P. Malcolm, McDonald, R. Orr, P. Styring, A. S. Cherodian, R. M. Richardson, J. L. Feijoo and G. Ungar, *Mol. Cryst. Liq. Cryst.*, 1991, **206**, 79–92.

4   T. Zincke, G. Heuser and W. Möller, *Liebigs. Ann. Chem.*, 1904, **333**, 296–345.

5   H. Meier, *Angew. Chemie Int. Ed.*, 1992, **31**, 1399–1420.

6   D. M. Huck, H. L. Nguyen, P. N. Horton, M. B. Hursthouse, D. Guillon, B. Donnio and D. W. Bruce, *Polyhedron*, 2006, **25**, 307–324.

7   W.-C. Cheng and M. J. Kurth, *Org. Prep. Proced. Int.*, 2002, **34**, 585–608.

8   L. Boubekeur-Lecaque, B. J. Coe, J. A. Harris, M. Helliwell, I. Asselberghs, K. Clays, S. Foerier and T. Verbiest, *Inorg. Chem.*, 2011, **50**, 12886–12899.

9   B. J. Coe, J. A. Harris, L. J. Harrington, J. C. Jeffery, L. H. Rees, S. Houbrechts and A. Persoons, *Inorg. Chem.*, 1998, **37**, 3391–3399.

10   B. Donnio, B. Heinrich, T. Gulik-Krzywicki, H. Delacroix, D. Guillon and D. W. Bruce, *Chem. Mater.*, 1997, **9**, 2951–2965.

11   D. Barbier, C. Marazano, B. C. Das and P. Potier, *J. Org. Chem.*, 1996, **61**, 9596–9598.

12   A. Kaiser, X. Billot, A. Gateau-Olesker, C. Marazano and B. C. Das, *J. Am. Chem. Soc.*, 1998, **120**, 8026–8034.

13   J. D. Herod, M. A. Bates, A. C. Whitwood and D. W. Bruce, *Soft Matter*, 2019, **15**, 4432–4436.

14   J. L. Woodring, N. D. Bland, S. O. Ochiana, R. K. Campbell and M. P. Pollastri, *Bioorg. Med. Chem. Lett.*, 2013, **23**, 5971–5974.

15   D. Gnecco, J. Juárez, A. Galindo, C. Marazano and R. G. Enríquez, *Synth. Commun.*, 1999, **29**, 281–287.

16   C. J. Kassl, D. C. Swenson and F. C. Pigge, *Cryst. Growth Des.*, 2015, **15**, 4571–4580.

17   T. Ishiyama, M. Murata and N. Miyaura, *J. Org. Chem.*, 1995, **60**, 7508–7510.

18   K. Lava, Y. Evrard, K. Van Hecke, L. Van Meervelt and K. Binnemans, *RSC Adv.*, 2012, **2**, 8061.

19   A. Riccobono, *PhD Thesis,* University of York, 2018.

20   D. W. Bruce, B. Donnio, D. Guillon, B. Heinrich and M. Ibn-Elhaj, *Liq. Cryst.*, 1995, **19**, 537–539.

Chapter Three: Mesomorphism of an Homologous Series of Ionic Tetracatenar Liquid Crystals Based on the *N*-Phenylpyridinium Moiety: Influence of Terminal Chain Length and Counter-Ion

1. Introduction

Ionic liquid crystals are a unique class of materials as they combine the properties inherent to ionic liquids with the long-range anisotropic order of liquid crystals.[1] Kato *et al.* have demonstrated that ionic liquid crystals forming columnar mesophases can show temperature dependent ion conductivity.[2,3] Furthermore, liquid-crystalline viologens have been a topic of interest due to their diverse redox properties that can be combined with liquid-crystalline self-assembly to produce materials with anisotropic electrochromic, thermochromic and photochromic properties.[4,5]

However, the mesomorphic properties of ionic polycatenar liquid crystals remains a relatively unexplored field. Whilst formally ionic polycatenar liquid crystals have been studied in the form of the 3,4-dialkoxystilbazole complexes of various silver(I) salts,[6] these materials actually exist as tightly bound ion pairs and so they do not provide a true representation of how truly ionic, charge-separated materials would behave. This chapter will, therefore, present the liquid-crystalline properties of a series of truly ionic polycatenar liquid crystals that are built upon the *N*-phenylpyridinium moiety whose synthesis has been extensively documented in Chapter Two. An introduction to the silver(I) salts is first presented to set the new results into context.

1.1. Calamitic 4-alkoxystilbazole complexes of silver(I)

The first liquid-crystalline silver(I) salts were built from 4-alkoxystilbazole ligands and the structure of these calamitic complexes is presented in Figure 3.1. These materials displayed a rich mesomorphism that was dependent on the length of the alkoxy chains and the identity of the anion.
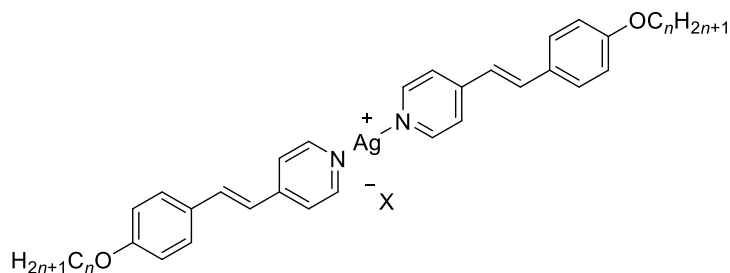
Figure 3.1. Structure of the 4-alkoxystilbazole complexes of various silver(I) salts: X^- = BF_4, NO_3, OTf or $O_3SOC_mH_{2m+1}$ where m is 8 or 12.

The first materials studied were the BF_4^- salts and these compounds displayed SmA and SmC mesophases.[7] The transition temperatures of the BF_4^- salts were high and often these materials suffered from thermal decomposition in the upper reaches of the mesophase; furthermore, these compounds displayed poor stability to light.

A series of related compounds containing nitrate and triflate anions[8] were then made and these materials displayed similar behaviour to the tetrafluoroborate salts in that SmC and SmA mesophases were observed. The phase diagrams of the OTf⁻ and NO_3^- salts are presented in Figure 3.2. However, one significant difference in the thermal behaviour of the triflate salts was apparent at short terminal chain lengths and this was the formation of a nematic phase. This was surprising as the formation of a nematic phase is often attributed to weak anisotropic dispersion forces rather than strong isotropic Coulombic interactions; this feature is discussed in more detail in the forthcoming section. The triflate and nitrate salts both also suffered thermal decomposition in the upper reaches of the SmA phase due to the high mesophase-isotropic transition temperatures.
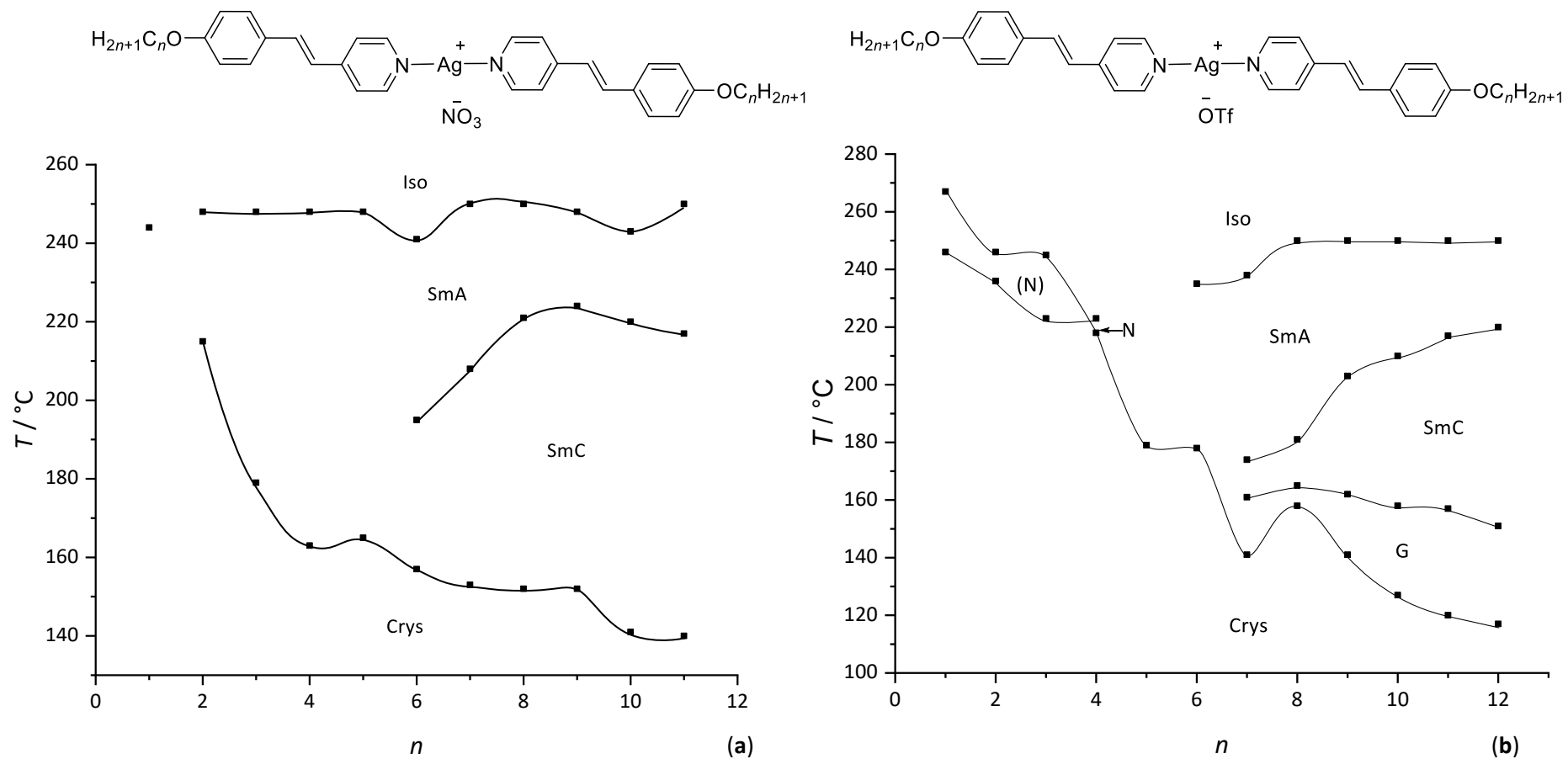
Figure 3.2. Phase diagram of (**a**) the 4-alkoxystilbazole complexes of silver(I) nitrate and (**b**) the 4-alkoxystilbazole complexes of silver(I) triflate.

In an attempt to reduce the transition temperatures of these 4-alkoxystilbazole salts, an analogous series of compounds were prepared that contained a dodecylsulfate anion.[8] Bruce *et al.* postulated that the flexible alkyl chain of the alkylsulfate anion should destabilise the crystal and liquid crystal phases. The flexible anion did indeed depress the melting and clearing temperatures, but it also changed the mesomorphism quite significantly – a cubic phase was now observed between the SmC and SmA phases (Figure 3.3). This was extremely surprising at the time, as the only other compounds known to display a thermotropic cubic phase were the biphenylcarboxylic acids studied by Gray[9] and a series of hydrazines studied by Demus.[10] The preparation of a number of alkoxystilbazole complexes of silver(I) dodecylsulfate had effectively doubled the number of compounds known to form a thermotropic cubic phase at that time.

Next, a series of compounds with a shorter octylsulfate anion were prepared.[11] The phase diagrams of the octylsulfate and dodecylsulfate salts were largely superimposable except that the cubic phase had been totally supressed by the shorter anion (Figure 3.3). Crystals suitable for single crystal X-ray analysis were grown for one octylsulfate compound and the results were interesting on a number of levels. First, was the dimeric structure with two silver cations being bridged by sulfate groups with silver-oxygen distances of 2.7-2.9 Å (typical of ionic interactions). Second, the silver-silver distance was also found to be 3.2 Å, which is consistent with some silver-silver interaction. Third, and believed to be crucial, is that the octylsulfate chain does not extend past the rigid core of the cation so that it cannot contribute to the terminal chain volume. The single crystal structure of this complex is presented in Figure 3.4.
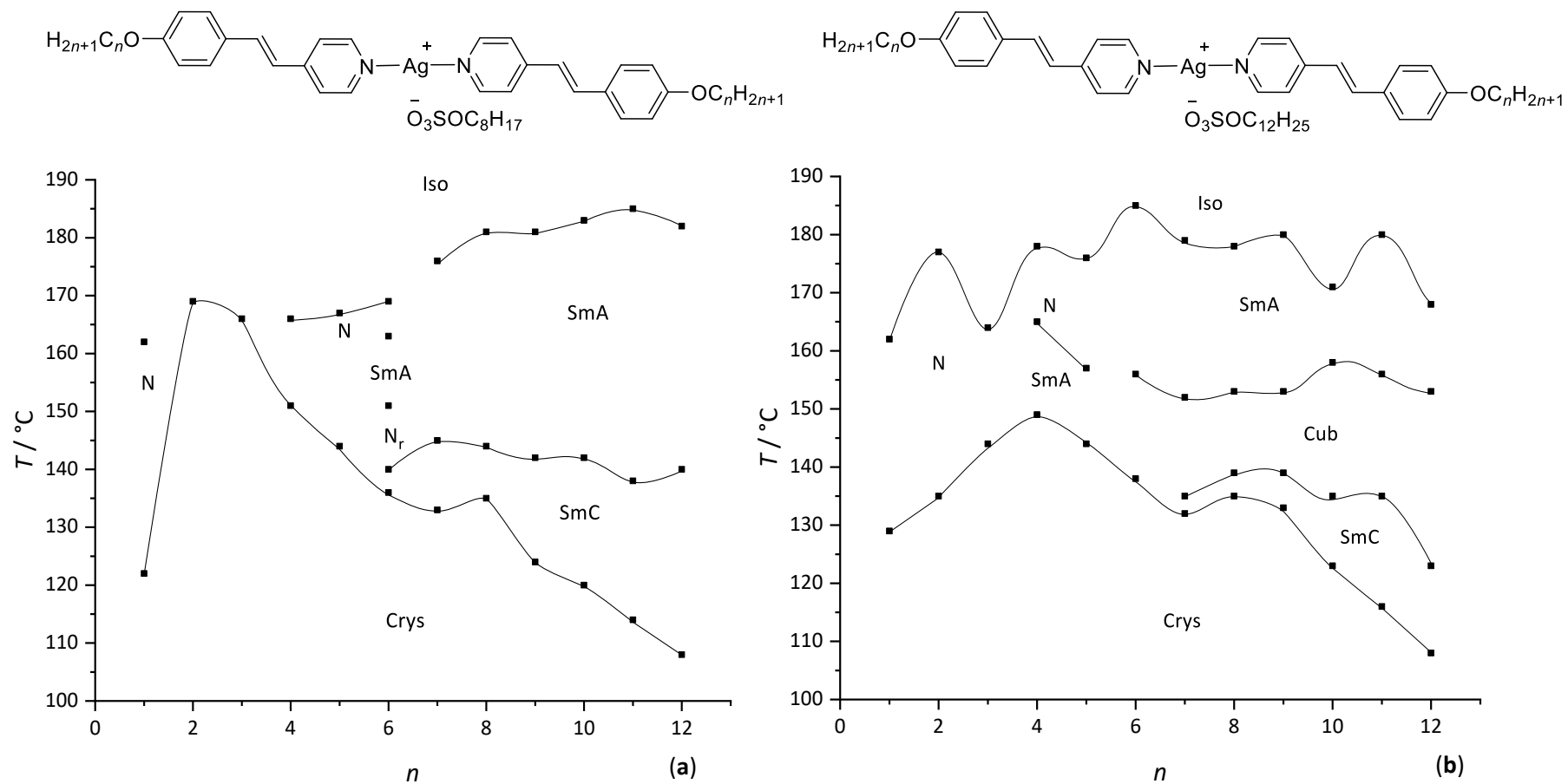
Figure 3.3. Phase diagram of (**a**) the 4-alkoxystilbazole complexes of silver(I) octylsulfate and (**b**) silver(I) dodecylsulfate.
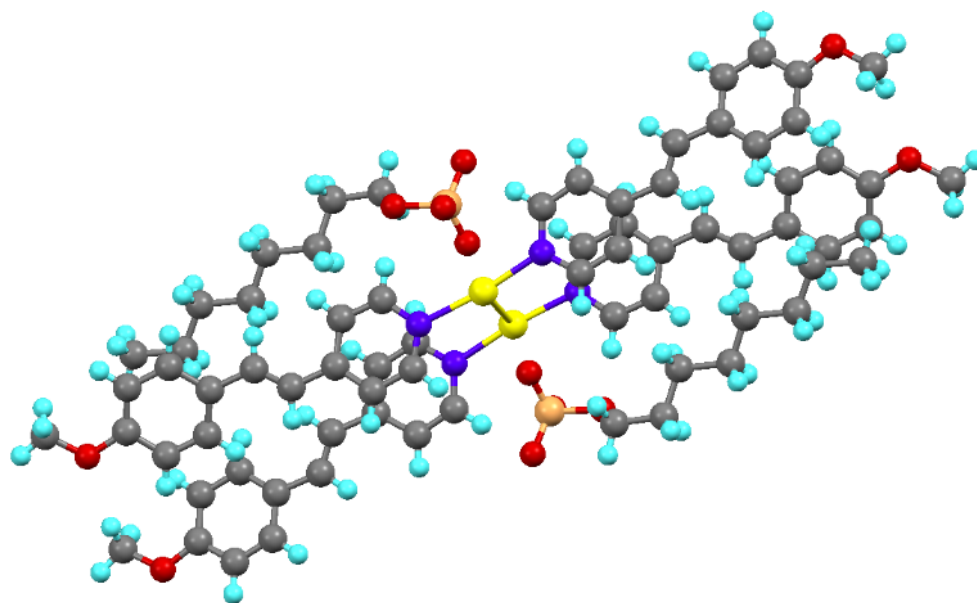
Figure 3.4. X-Ray single crystal structure of the 4-methoxystilbazole silver(I) octylsulfate salt.[11]

The diverse mesomorphism of the silver(I) salts requires interpretation. Starting with the nematic phase formed by the triflate and alkylsulfate salts, how does a phase commonly associated with weak anisotropic dispersion interactions form in the presence of strong, isotropic Coulombic forces? While the compounds are formally ionic, conductivity in the mesophases formed by the silver(I) dodecylsulfate salts was found to be non-existent, which is consistent with tight pairing between the anion and cation.[12] So the relative dispositions of the anion and cation found in the crystal structure must remain broadly true in the liquid-crystal phase. However, within the same homologous series of compounds, SmC and SmA phases form, the latter of which is typical of an ionic liquid crystal. How can this be explained? Generally speaking, laterally substituting a calamitic mesogen suppresses smectic phases and promotes nematic organisation by disrupting side-to-side self-organisation of the molecules. The silver(I) salts effectively contain a lateral chain in the form of the anion.

From the general shape of the phase diagrams, a nematic phase forms at very short chain lengths due to the steric effects of the anion and also because nematic phases tend to be formed by compounds with the shortest terminal chain length in an homologous series. On moving across the phase diagram from left to right, smectic phases then appear. This is common in neutral calamitic compounds and has largely been associated with nanophase segregation between the aromatic and aliphatic parts of the molecule to promote layering. However, this effect is suppressed in

compounds bearing a lateral chain. So clearly an additional factor is responsible for smectic phase formation in the silver(I) salts. This factor is almost certainly the presence of intermolecular electrostatic interactions between neighbouring anions and cations. As a nematic phase forms in the same homologous series, however, ionic interactions are not too strong as otherwise smectic mesomorphism would be observed across the whole phase diagram. It is the combination of intermolecular ionic interactions coupled with lengthening of the terminal chains that stabilises the smectic phases formed by the silver(I) salts.[13]

To understand the formation of the cubic phase by the silver(I) dodecylsulfate compounds those formed by surfactants must be reconsidered and the factors that control the lyotropic liquid crystal phases formed by surfactants have been well documented in the Introduction chapter. The interconnecting rod model (Figure 3.5 (**a**) and (**b**)) for the bicontinuous cubic phases assumes that the rods contain the hydrophilic head groups and the chains extend out filling space in between. Extending this idea to the cubic phases formed by thermotropic compounds, the rods consist of the rigid cores with the chains filling space between. The infinite minimal periodic surface model relates to the interconnecting rods as the surface divides space into two parts. The Schwartz P surface shown in Figure 3.5 (**c**) contains the symmetry elements of the $Im\overline{3}m$ space group of the interconnecting rod model and shows how the two are related, giving rise to two non-interconnected rod networks. It becomes clear from these models how important interfacial curvature is in the formation of bicontinuous cubic phases.

(**a**)   (**b**)   (**c**)
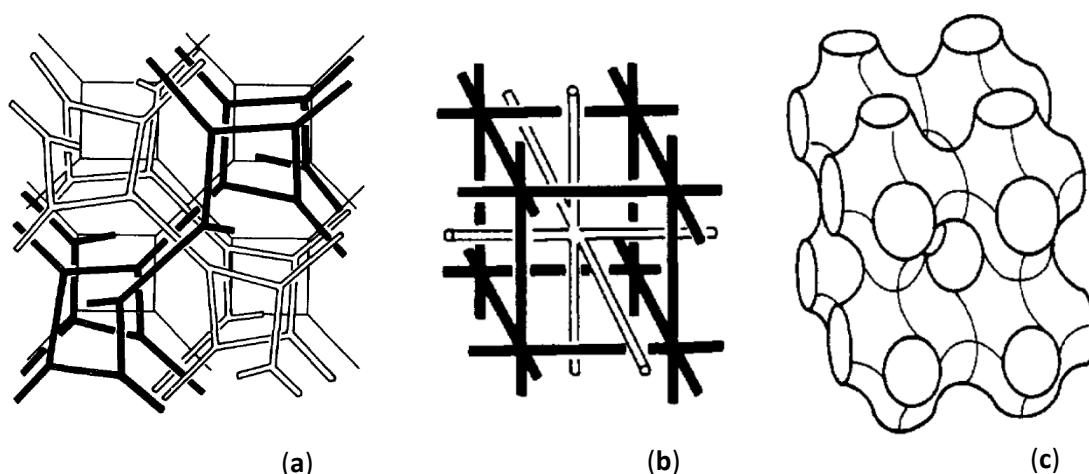
Figure 3.5. Interconnecting rod model for the $Ia\overline{3}d$ space group (**a**) the $Im\overline{3}m$ space group (**b**) and the infinite periodic minimal surface representation for the $Im\overline{3}m$ space group (**c**). Figures taken from ref.[13]

The curvature invoked by these models aid our understanding of cubic phase formation in the calamitic silver(I) alkylsulfates. Octylsulfate and decylsulfate chains do not extend past the core of the cation, and, as a consequence, these materials do not form a cubic phase. In the compounds containing longer dodecylsulfate and tetradecylsulfate anions (where the anion chain extends past the core) the cubic phase now appears. This provides qualitative evidence for the need of the alkylsulfate chain to extend past the rigid core to contribute to the volume occupied by the terminal chains. As the volume of the core remains the same in each case, there is now the possibility for a mismatch in volume between the charged core and the aliphatic periphery in the case of longer anions. The curvature generated at the core-chain interface as a result of longer anion chains would allow a cubic phase to form.

Whereas the imbalance of core and chain volumes with longer anion chains does account for the interfacial curvature required to stabilise a cubic phase, it does not explain its appearance between two lamellar phases. Levelut *et al.*[14] rationalised this as spatial frustration of the layers in the SmA-SmC transition that resulted in the formation of an intermediate cubic phase. The whole mesomorphic sequence can actually be explained by variation of the core and chain volumes on changing temperature. At high temperature, the core and chain volumes are equal and so a SmA phase forms. On decreasing temperature, the core volume decreases more rapidly than the chain volume due to the strong intermolecular electrostatic interactions between neighbouring cores that results in the formation of a curved interface; thus, a cubic phase forms. Further cooling induces a rapid decrease in chain area (due to reduced chain mobility) and the ratio of core-chain volumes tends to unity once again, therefore giving way to another lamellar phase.

1.2. Polycatenar alkoxystilbazole complexes of silver(I)

In order to investigate the relative effects of core and chain volumes, a series of polyalkoxystilbazole complexes of silver(I) were prepared.

1.2.1. 3,4-Dialkoxystilbazole complexes of silver(I) alkylsulfates

The first polycatenar salts prepared were the 3,4-dialkoxystilbazole complexes of silver(I) dodecylsulfate and the phase diagram of an homologous series of the silver(I) dodecylsulfate salts is presented in Figure 3.6.[6] Clearly these compounds display some characteristics common to neutral polycatenar liquid crystals in that a columnar hexagonal (Col$_h$) mesophase is formed by homologues with the longest terminal chain lengths. However, rather than forming a SmC phase at

short chain lengths, these complexes form a cubic phase that persists down to n = 4. Whereas cubic phases are not uncommon in the phase sequence of a polycatenar compound, they are usually found at intermediate chain lengths between the SmC and Col_h phases. Also interesting was that the additional *meta* chains had destabilised the crystal phase and all tetracatenar compounds melted at lower temperatures than their calamitic analogues. The clearing temperatures of derivatives upwards of n = 6 (forming Col_h phases) were comparable to those of the SmA phase formed by the 4-alkoxystilbazole complexes. The butyloxy derivative, on the other hand, formed only a cubic mesophase that was not as stable as the Col_h phase and cleared to the isotropic liquid at 100 °C.
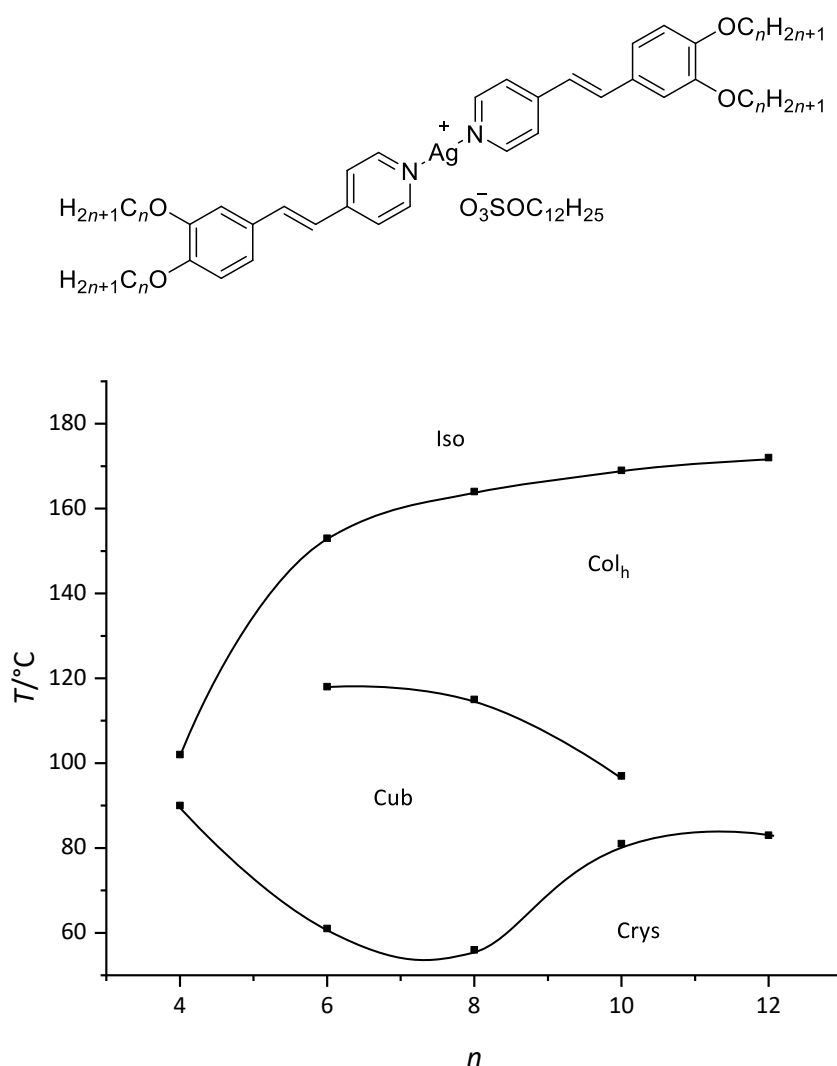
Figure 3.6. Structure and phase diagram of the tetracatenar 3,4-dialkoxystilbazole complexes of silver(I) dodecylsulfate.

Much like the 4-alkoxystilbazole complexes, the length of the alkylsulfate anion also affected the mesomorphism of the polycatenar stilbazole complexes as shown in Figure 3.7.[15] Using the $n = 12$ homologue as an example, the use of octylsulfate and decylsulfate anions ($m = 8$ and 10) induced a cubic phase below the Col$_h$ phase. However, analogous compounds with dodecylsulfate and tetradecylsulfate anions ($m = 12$ and 14) formed only Col$_h$ mesophases; Figure 3.7 shows these data as a bar chart for clarity. It has already been demonstrated from crystal structures of the 4-alkoxystilbazole complexes that the shorter octylsulfate and decylsulfate anions do not extend past the rigid core of the cation, and so cannot contribute to the terminal chain volume. This argument again explains the reduced interfacial curvature of the polycatenar octylsulfate and decylsulfate salts such that they form a cubic mesophase below the Col$_h$ phase. The longer dodecylsulfate and tetradecylsulfate anions then suppress the cubic phase by generating additional curvature at the aromatic-aliphatic interface.
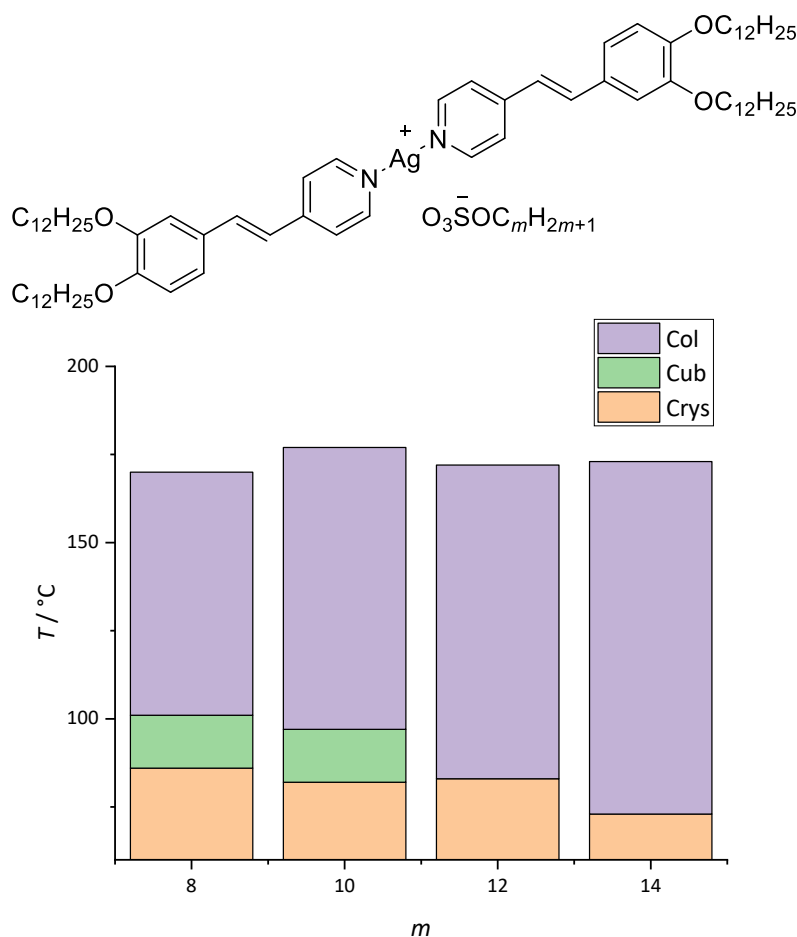
Figure 3.7. Influence of the alkylsulfate chain length of the anion, m, on the mesomorphism of the teracatenar silver(I) stilbazole salts with dodecyloxy chains.

1.2.2.   3,4-Dialkoxystilbazole complexes of silver(I) triflate

After the study of various alkylsulfate anions, an analogous series of silver(I) triflate salts were prepared and their mesomorphism is presented in Figure 3.8.[6] On inspection of the phase diagram, a number of differences are observed between the triflate and dodecylsulfate salts. First, are the lower melting temperatures of the dodecylsulfate materials due to the flexible alkyl chain of the sulfate moiety destabilising the crystal phase. The clearing temperatures, on the other hand, remain relatively constant in both series, which suggests that the mesophase-to-isotropic transition is not driven by a breakdown of the ionic interactions and instead is driven by the terminal chains. The second difference is the observation that the Col_h phase is found at much longer terminal chain lengths in the triflate series.
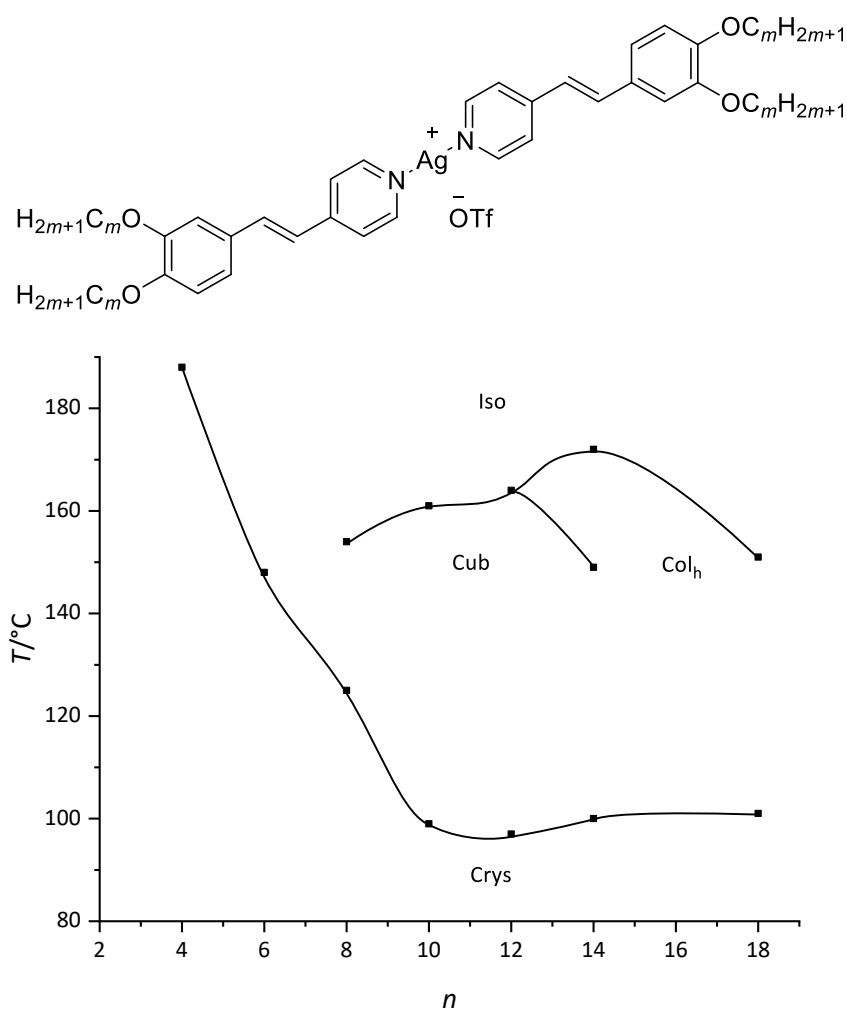
Figure 3.8. Structure and phase diagram of the tetracatenar 3,4-dialkoxystilbazole complexes of silver(I) triflate.

104

The mesomorphism of the ionic polycatenar stilbazole complexes of silver(I) can be explained using the same arguments as those that underpin the behaviour of typically neutral polycatenar materials, that is space filling and the extent of interfacial curvature established at the core-chain interface. However, additional factors must also be considered that include the spatial requirements of the anion and intermolecular ionic interactions, much like those influencing the mesomorphism of the 4-alkoxystilbazole complexes of silver(I).

Recall that neutral polycatenar liquid crystals usually form a SmC phase at short chain lengths, but in the case of the polycatenar silver(I) dodecylsulfate and silver(I) triflate series this mesophase is absent. First of all, it is rather bold to classify the stilbazole complexes as typical polycatenar materials as they contain the extra chemical moiety of an anion that, in the case of the alkylsulfate salts, is essentially an extra flexible chain. The anion behaves as a lateral substituent much like it does in the 4-alkoxystilbazole complexes. Whereas the calamitic compounds do form a lamellar phase, the added *meta* chains of the polycatenar materials in combination with the steric effects of the anion are now sufficient to suppress the SmC phase altogether. Thus, the cubic phase persists down to very short chain lengths.

Considering the shape of the phase diagrams of the triflate and dodecylsulfate materials, it is clear that the cubic phase persists in homologues with longer chain lengths in the former series. This is again consistent with the chain of the alkylsulfate anion being able to contribute to the terminal chain volume in order to modify the curvature established at the core-chain interface. Thus, shorter terminal chains are required to establish the curvature necessary to stabilise the Col_h phase in the dodecylsulfate salts. This is entirely consistent with the behaviour observed in Figure 3.7 where short alkylsulfate anions generate less curvature, thereby allowing formation of a cubic phase below the Col_h phase.

1.3. Related Ionic Compounds

Whist there is no evidence for the study of charge-separated, ionic polycatenar liquid crystals, Kato *et al.*[4] have prepared a series of viologen compounds that closely mimic classic hexacatenar materials from a structural standpoint; the structure of the viologen salts is presented in Figure 3.9. These materials were of interest due to a combination of their liquid-crystalline self-organisation and redox activity such that devices with anisotropic electrochemical functions could be investigated. Their mesomorphism was dominated by the formation of columnar rectangular and columnar hexagonal mesophases due to the plurality of terminal chains, much like the behaviour of true hexacatenar liquid crystals. Kato and co-workers postulated that despite the bent structure imparted by the terminal benzyl groups, liquid crystal self-assembly is achieved through nanophase segregation of the ionic and aliphatic parts of the molecule.
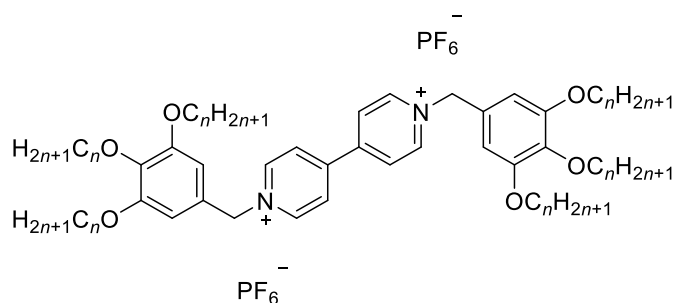
Figure 3.9. Structure of the liquid-crystalline viologen salts studied by Kato *et al.* that formed Col$_h$ and Col$_r$ phases.

Wang *et al.*[16] have also studied a series of *N,N'*-diphenylviologen salts with various counter-ions of the general structure shown in Figure 3.10 (these materials were also synthesised using Zincke chemistry). Due to the presence of only two terminal alkoxy chains, the mesomorphism of the diphenylviologens was dominated by the formation of SmA phases, typical of calamitic ionic compounds. However, a systematic study was conducted on the influence of the counter-ion on the stability and structure of the SmA phases. Clearing temperatures were highest for OTf$^-$ and BF$_4^-$ anions due to their moderate size and spherical shape that did not disrupt self-organisation into layers. Substituting the anion for a long-chain alkylsulfate resulted in a reduced clearing point owing to the flexible chain attached to the sulfate moiety that was postulated to disrupt packing in the liquid-crystalline state. The authors also postulated that the SmA phase was destabilised in the case of the alkylsulfate salts due an imbalance in the relative volumes of the ionic and aliphatic parts of the material, akin to the relative volumes of core and chains that controls the mesomorphism of

polycatenar liquid crystals. This latter argument is almost certainly a factor that dictates mesophase stability as will be evidenced throughout this chapter. The use of NTf_2^- resulted in a clearing point intermediate between OTf^- and $ROSO_3^-$ due to its larger size (compared to OTf^-). The d-spacing in the SmA phase also decreased with increasing ionic radius of the anion, such that SCN^- compounds had the largest d-spacing and NTf_2^- the smallest. This effect was observed due to greater side-to-side separations of neighbouring cations in the case of NTf_2^-, thus a greater extent of chain interdigitation occurred in order to fill space efficiently. Data showing the influence of anion size on the SmA d-spacing is plotted in Figure 3.10.
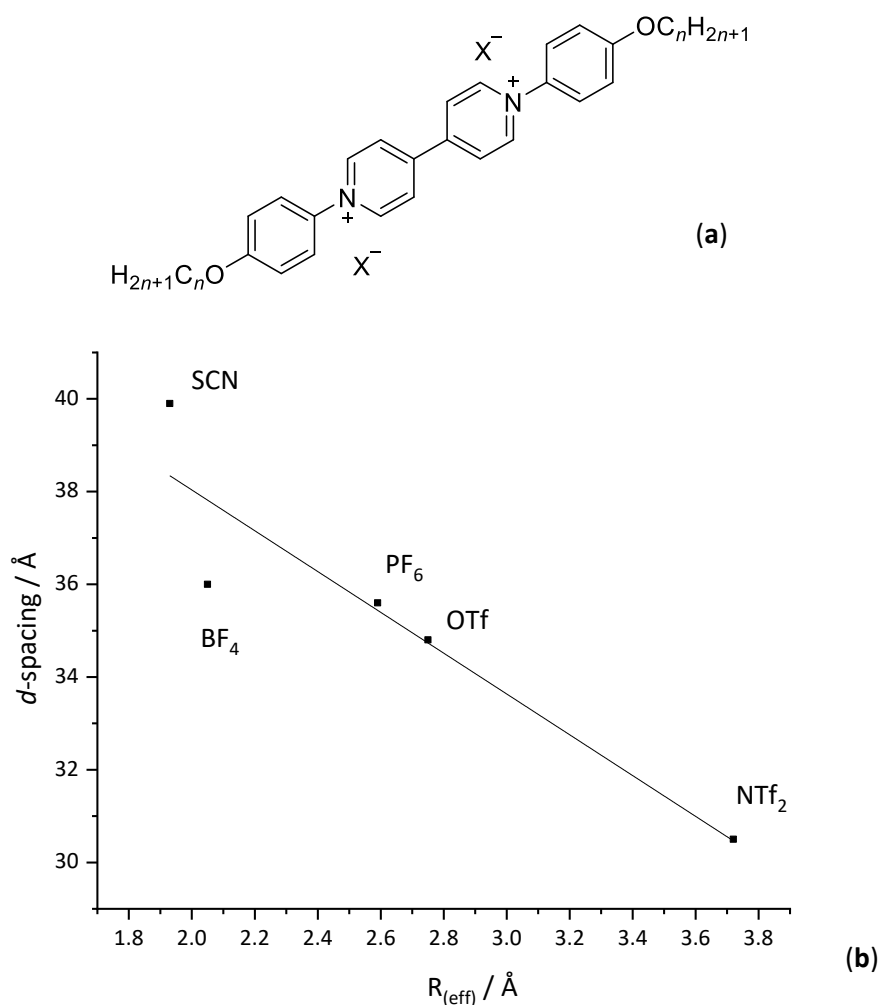
Figure 3.10. General structure of the diphenylviologen salts studied by Wang *et al.* (**a**): X^- is either SCN^-, BF_4^-, OTf^-, PF_6^-, NTf_2^- or $ROSO_3^-$ and variation of d-spacing in the SmA phase with different anions (**b**): $R_{(eff)}$ is the effective anion volume.

2. Results

2.1. Thermal behaviour of the tetracatenar triflate salts, **11**-*n*

The structure of the tetracatenar *N*-phenylpyridinium triflate salts, **11**-*n*, is shown in Figure 3.11; their preparation has been documented extensively in Chapter 2.
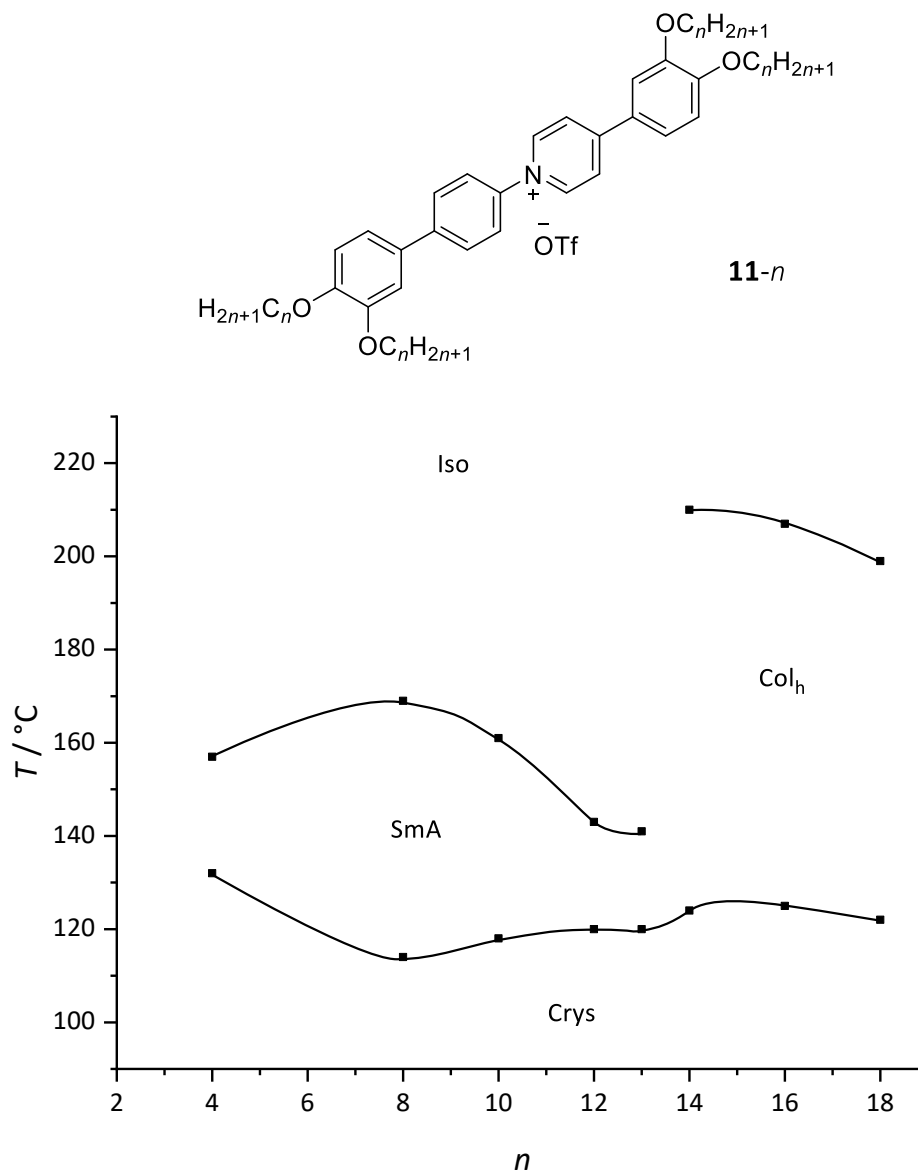
Figure 3.11. Structure and phase diagram of the tetracatenar triflate salts, **11**-*n*: transition temperatures are from microscopy on heating.

All of the tetracatenar materials studied from *n* = 4 – 18 were liquid-crystalline, transitioning from SmA-to-Col$_h$ mesomorphism on increasing chain length; the phase diagram of the tetracatenar

triflate salts is presented in Figure 3.11 and thermal data is collected in Table 3.1. The melting point remains relatively constant across the series, an observation that is in contrast to the stilbazole complexes of silver(I) triflate where initially a sharp drop in the melting point was observed on increasing chain length. While there is a slight drop in the melting point on moving from **11**-*4* to **11**-*8*, this effect is rather subtle. This provides strong evidence that the melting temperature of the pyridinium materials is predominantly driven by a breakdown of the ionic lattice rather than that of the chains, which presumably remains relatively constant as *n* increases. This contrasts the ideas invoked by Geoffrey in which he postulated that the melting of a series of carbohydrate liquid crystals was driven by increasing mobility of the chains.[17] With the exception of compound **11**-*4*, the melting point of all compounds forming a SmA phase was clearly detected *via* DSC. The absence of a melting endotherm for compound **11**-*4* was surprising, and despite several repeat experiments, the transition was never observed. The clearing points of compounds **11**-*14* to **11**-*18*, each forming a Col_h phase, were not detected by DSC presumably due to decomposition in the upper reaches of the mesophase. All derivatives crystallise on cooling to room temperature in both microscopy and DSC experiments, akin to the thermal behaviour of the stilbazole complexes of silver(I) triflate.

The first significant observation, however, is that the mesophase formed at short terminal chain lengths is SmA rather than the more conventional SmC phase as typically observed in neutral tetracatenar materials (or cubic in the case of the tetracatenar silver(I) salts). The SmA phase was identified from its characteristic focal-conic fan texture and dark regions of homeotropic alignment as shown in Figure 3.12 (**a**). The X-ray scattering pattern of this phase shown in Figure 3.13 (**b**) also shows a single sharp reflection (d_{001}) in the small angle regime and further supports this assignment. A steady increase in the layer spacing was observed on increasing *n* that was consistently about 70% of the calculated all *trans* molecular length as evidenced by Figure 3.14; this most likely arises from chain interdigitation or chain folding in order to fill space efficiently. Recording multiple diffraction patterns as a function of temperature showed no variation in d_{001}, and so the layer spacing appeared to be temperature independent.

The SmA phase is destabilised as the chain length increases from *n* = 8-13, which almost certainly arises from frustration of the lamellae on increasing steric bulk of the terminal chains. Then, at compound **11**-*14*, the SmA phase is replaced by the Col_h phase as the volume of the terminal chains becomes so great that the lamellae are disrupted. It is interesting to note that this change in mesomorphism is not accompanied by the formation of a cubic phase. The columnar hexagonal

phase was identified from its distinctive spine defects and pseudo focal-conic defects when viewed down the polarising microscope as shown in Figure 3.12 (**b**), supported by X-ray diffraction patterns where both d_{10} and d_{11} reflections were observed for compounds **11**-*16* and **11**-*18*. Diffraction data are collected in Table 3.2 and a diffraction pattern of compound **11**-*16* is presented in Figure 3.13 (**a**). However, the d_{11} reflection cannot be seen in the diffraction pattern of **11**-*14*, but this phase was identified as columnar hexagonal owing to its miscibility with the columnar hexagonal phase of **11**-*16* as shown in Figure 3.12 (**c**). Furthermore, contact preparations between the n = 12 (SmA) and n = 14 (Col$_h$) homologues showed a lack of miscibility shown in Figure 3.12 (**d**).

(**a**) (**b**)

(**c**) (**d**)
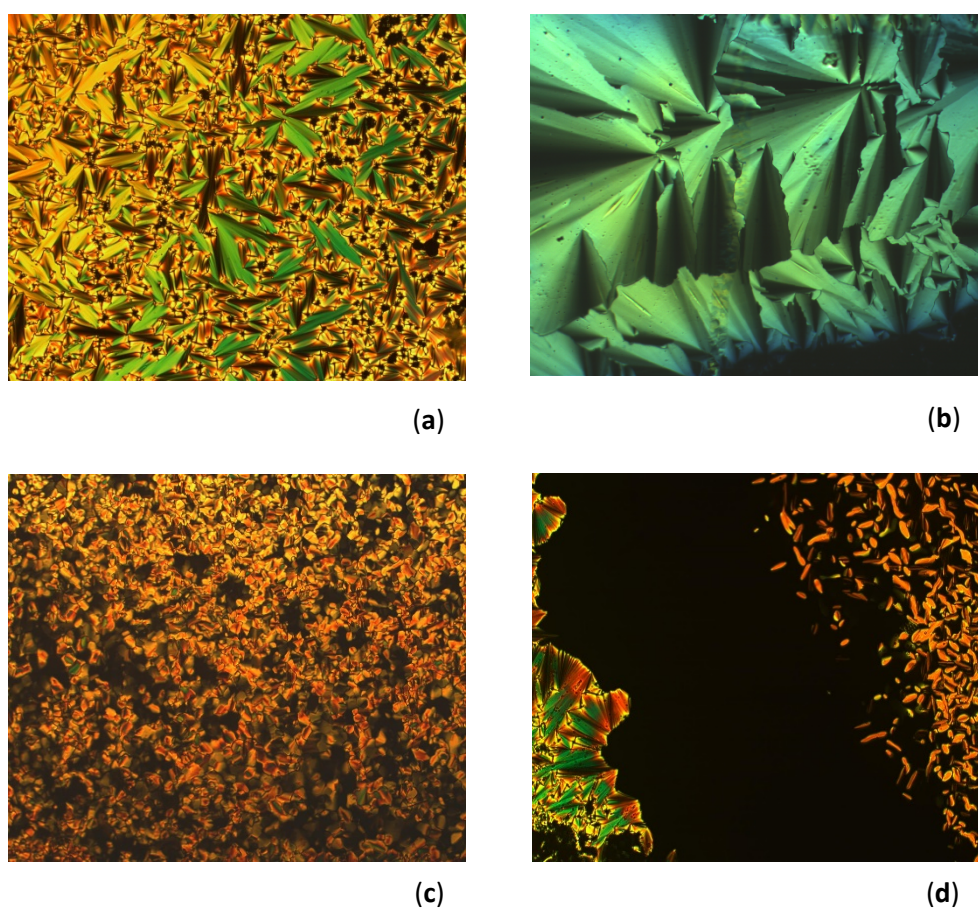
Figure 3.12. Optical texture of (**a**) the SmA phase of compound **11**-*8* at 162 °C, (**b**) optical texture of the hexagonal columnar phase of compound **11**-*18* at 128 °C, (**c**) co-miscibility of **11**-*14* and **11**-*16* Col$_h$ phases and (**d**) miscibility gap in the contact preparation performed between compound **11**-*12* (SmA) and **11**-*14* (Col$_h$). All textures are at x10 magnification.

The second significant observation apparent from the phase diagram in Figure 3.11 is the huge stabilisation of the Col$_h$ phase compared to that of the preceding SmA phase; the clearing temperature of compound **11**-*14* is 69 °C higher than that of **11**-*13*. It should also be stressed here

that the derivatives from *n* = 14 – 18 suffer from decomposition in the upper reaches of their columnar phases, and so the clearing temperatures reported are only approximate, representing a conservative estimate of the phase stability. A similar, albeit less pronounced, stabilisation of the columnar hexagonal phase also occurred in the phase diagram of the tetracatenar stilbazole complexes of silver(I) triflate and silver(I) dodecylsulfate; this point will be discussed in more detail later.

Table 3.1. Transition temperatures and thermal data for the triflate series: * marks transitions that cannot be detected by DSC.

n	Transition	*T* / °C	ΔH / kJ mol^{-1}
4	Crys-SmA	132	*
	SmA-Iso	157	*
8	Crys – SmA	114	19
	SmA -Iso	169	0.9
10	Crys – SmA	118	18
	SmA -Iso	161	0.7
12	Crys – SmA	120	54
	SmA -Iso	143	0.6
13	Crys – SmA	120	69
	SmA -Iso	141	1.0
14	Crys – Col$_h$	124	37
	Col$_h$ – Iso	210	*
16	Crys – Col$_h$	125	38
	Col$_h$ – Iso	207	*
18	Crys – Col$_h$	122	51
	Col$_h$ – Iso	199	*
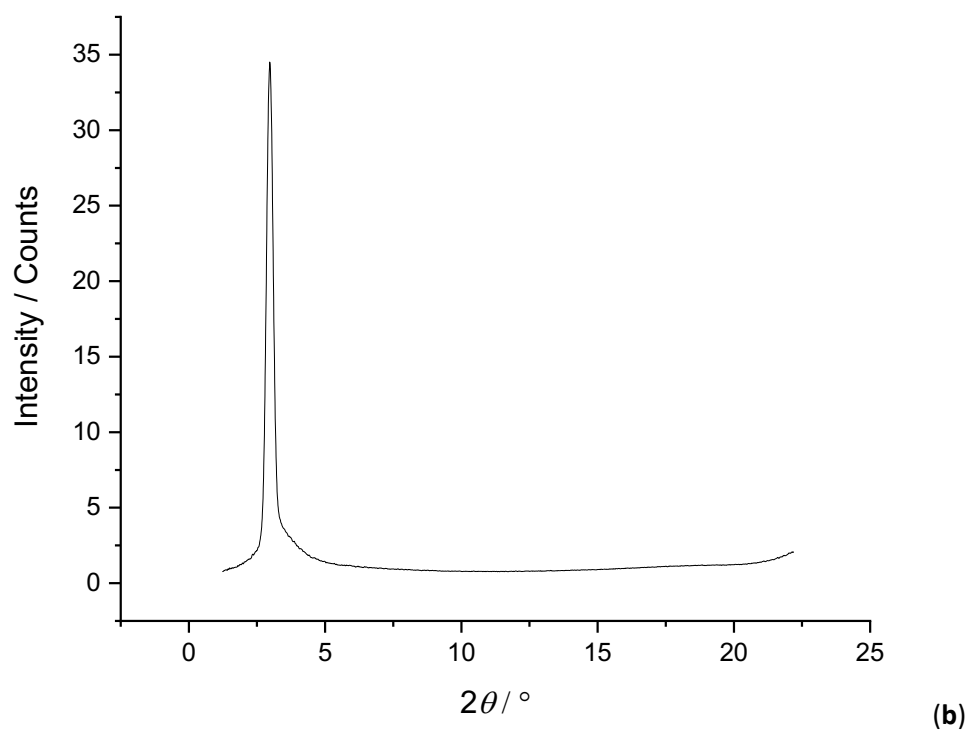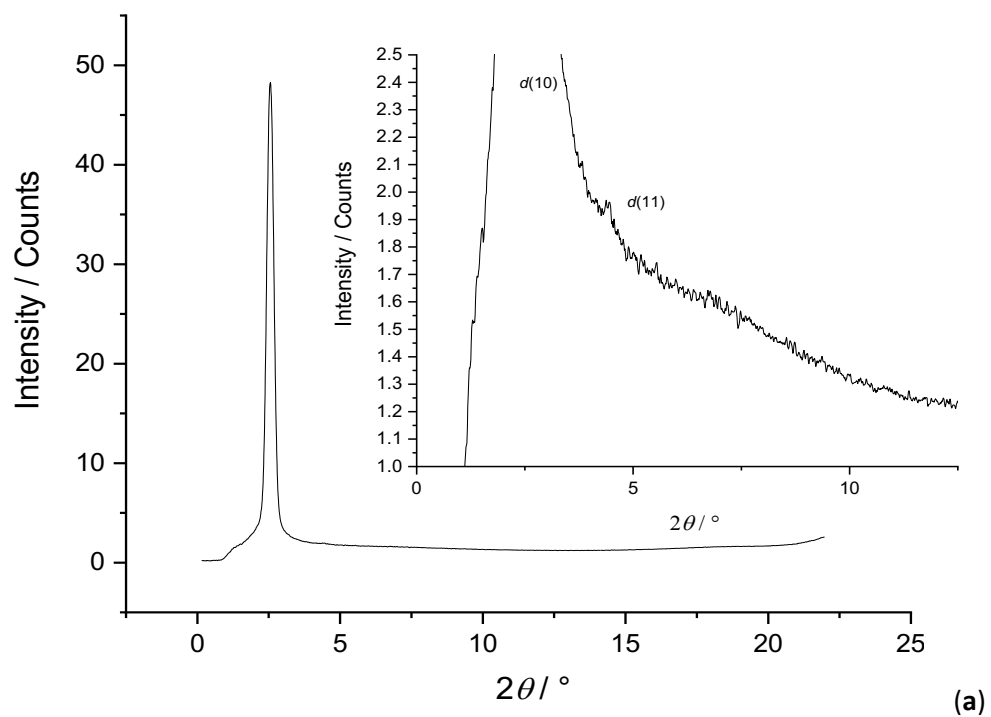
Figure 3.13. X-Ray scattering patterns of (**a**) the hexagonal columnar phase of compound **11**-*16* at 127 °C and (**b**) the SmA phase of compound **11**-*8* at 139 °C.

Table 3.2. X-Ray diffraction data for the OTf series, **11**-*n*.

n	*d* / A	*hk(l)*	*Molecular length* / Å	*Parameter* / Å
8	29.7	*001*	38.9	
	4.7	halo		
10	30.6	*001*	44.9	
	4.7	halo		
12	32.1	*001*	50.0	
	4.7	halo		
13	32.9	*001*	52.5	
	4.7	halo		
14	32.8	*10*	55.1	*a* = 37.9
	-	*11*		
	4.7	halo		
16	34.5	*10*	60.1	*a* = 39.8
	19.9	*11*		
	4.7	halo		
18	35.2	*10*	65.1	*a* = 40.6
	20.3	*11*		
	4.7	halo		
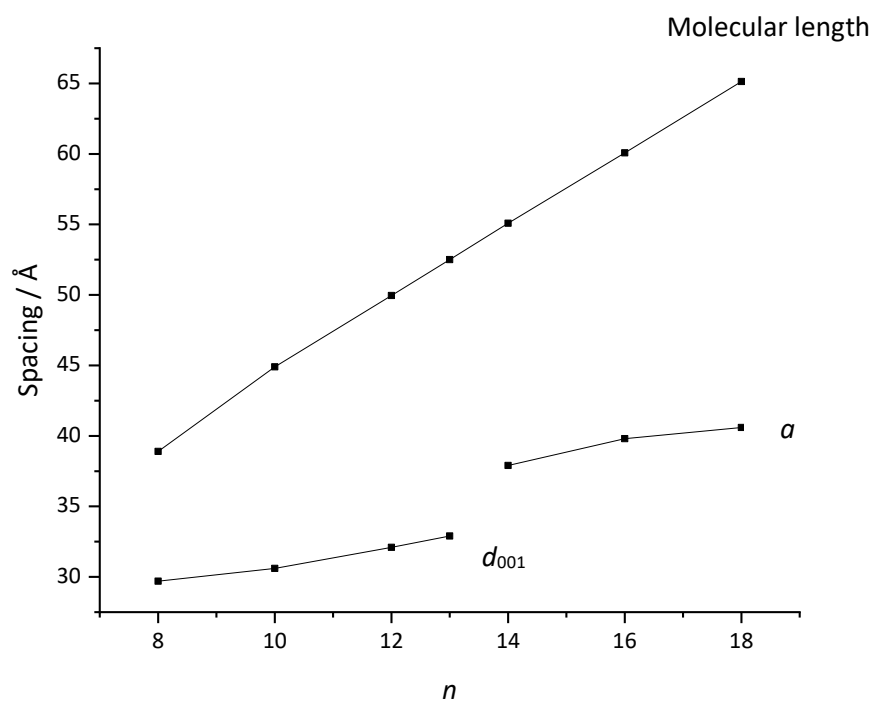
Figure 3.14. Calculated molecular length *vs* d_{001} and *a* parameter in series **11**-*n*.

2.2. Thermal behaviour of the tetracatenar alkylsulfate salts

2.2.1. Octylsulfate salts, 27-n

A phase diagram of the octylsulfate series, **27**-*n*, is presented in Figure 3.15 and the thermal data in Table 3.4.
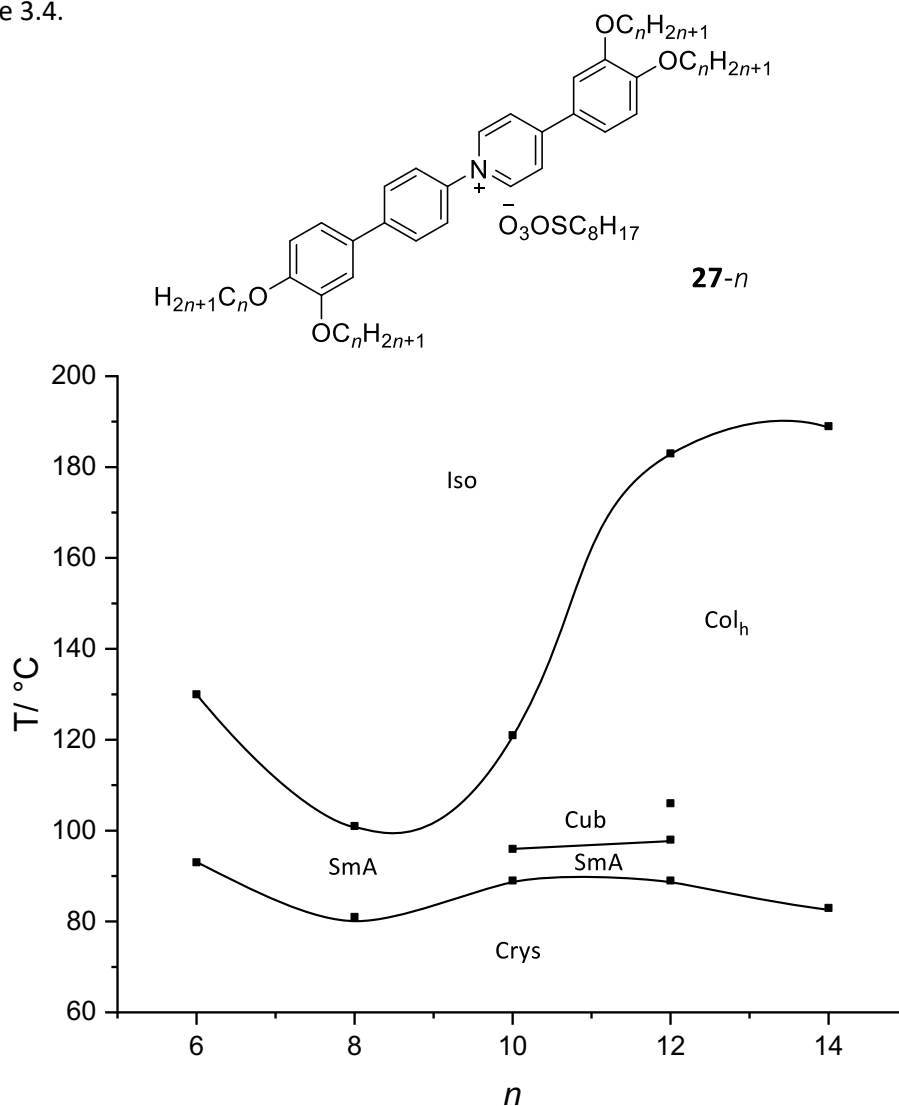
Figure 3.15. Phase diagram of the tetracatenar octylsulfate salts: transition temperatures are from microscopy on heating.

On moving across the series from left to right a change in mesomorphism from SmA-to-Col$_h$ is observed *via* an intermediate cubic phase. The octylsulfate salts demonstrate well the transition from lamellar through cubic and to columnar self-organisation on increasing chain length, much like the behaviour of the 2,2'-bipyridines studied by Rowe and Bruce.[18] The melting point remains

relatively constant across the series and is clearly independent of chain length, much like the melting behaviour of the triflate series. However, the melting temperatures of the ocylsulfate salts are consistently lower than those of the triflate series, and this most probably arises due to the flexible chain of the alkylsulfate anion that disrupts packing in the crystalline state.

Compounds **27**-*6* and **27**-*8* form only a SmA phase, which clear into the isotropic liquid at 130 and 101 °C, respectively. Compounds **27**-*10* and **27**-*12*, on the other hand, show an additional cubic phase above the SmA phase that was exemplified by the loss of birefringence and an increase in viscosity on the polarising microscope (Figure 3.16 (**b**)). Compound **27**-*12* also forms a Col_h phase that clears to the isotropic liquid at 183 °C, 62 °C higher than the cubic-to-isotropic transition displayed by **27**-*10*. Compound **27**-*14* forms only a Col_h phase that clears to the isotropic liquid at 189 °C.

Pseudo focal-conic textures with spine-like defects were observed for the Col_h phases formed by compounds **27**-*14* and **27**-*12* when cooled from their isotropic liquids (Figure 3.16 (**c**) and (**d**)). The cubic phase formed by compound **27**-*12* grows in from the Col_h phase as sharp edges. The SmA phase formed by **27**-*6* and **27**-*8* showed focal-conic fan defects and were indistinguishable from the SmA textures formed by the triflate series (Figure 3.16 (**a**)). Also interesting was that no homologue of series **27**-*n* crystallised on cooling to room temperature, a feature observed both by microscopy and DSC experiments. DSC was able to detect glass transitions for all homologues on the second heating cycle, demonstrating glass formation rather than crystallisation. The DSC trace of compound **27**-*10* is presented in Figure 3.17. The stilbazole complexes of the silver(I) alkylsulfates also formed glasses on cooling to room temperature and is most probably a feature inherent to the flexible anion.
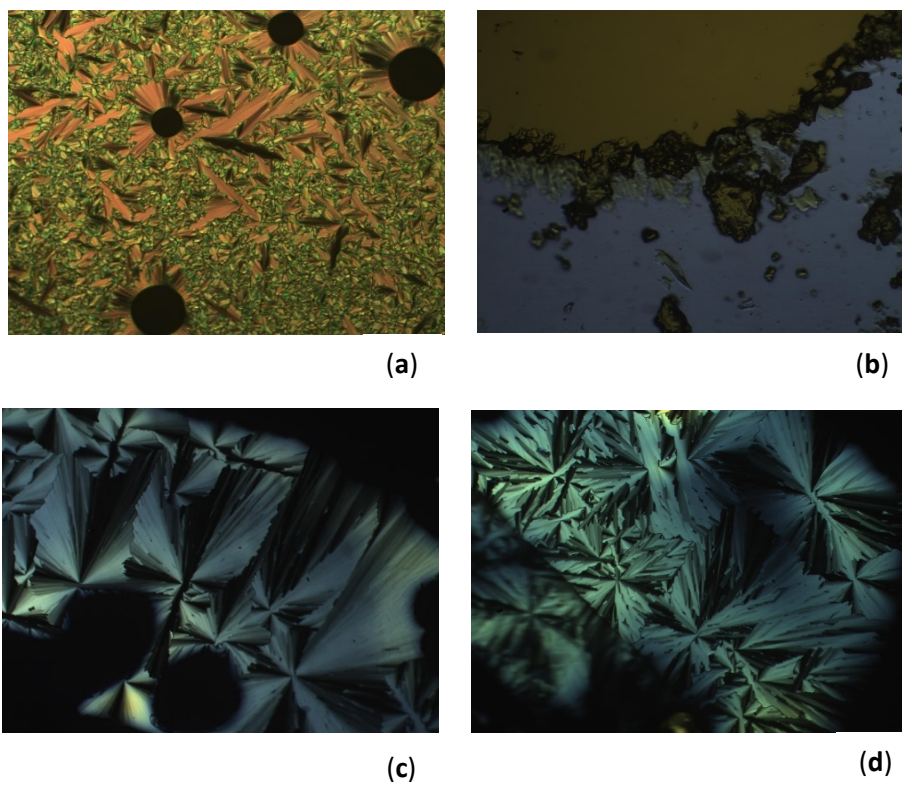
Figure 3.16. Optical textures of (**a**) the SmA phase formed by compound **27**-*6* at 116 °C, (**b**) the cubic phase formed by **27**-*10* with polarisers slightly uncrossed at 105 °C, (**c**) the Col$_h$ phase formed by compound **27**-*12* at 154 °C and (**d**) the Col$_h$ phase of **27**-*14* at 162 °C. Textures are at x10 magnification.
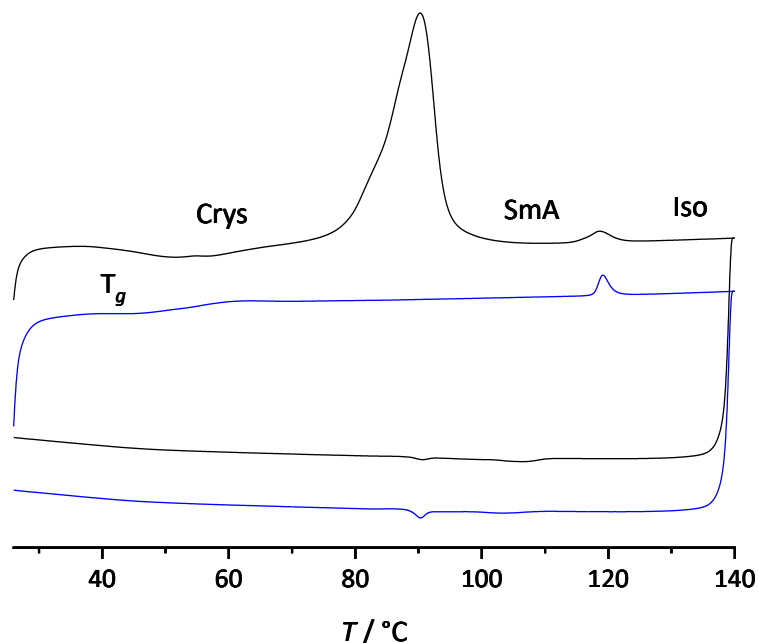
Figure 3.17. DSC of compound **27**-*10* with first heat/cool cycle in black and second cycle in blue. A glass transition (T_g) is clearly seen on the second heating cycle: note, the cubic phase was not detected *via* DSC.

Whilst X-ray diffraction could detect the two-dimensional order of the hexagonal columnar phase formed by **27**-*14* (Figure 3.18), the d_{11} reflection of the Col$_h$ phase formed by compound **27**-*12* was not detected. Whereas the optical texture of this phase was characteristically hexagonal, contact preparations between the two columnar phases confirm their co-miscibility and, therefore, proved the symmetry of compound **27**-*12* as hexagonal. Unfortunately, the space group of the cubic phase formed by **27**-*10*, and any other compound for that matter, could not be determined *via* X-ray scattering experiments due to a lack of higher order reflections – only two small angle reflections were detected as shown in Figure 3.19. It should be stressed that the relative *d*-spacings of the two small-angle reflections in Figure 3.19 do not correspond to a ratio of 1 : 1/√3, and thus the diffraction pattern is not simply that of a Col$_h$ phase. Furthermore, X-ray scattering experiments could not detect the SmA phases formed by compounds **27**-*10* and **27**-*12*, presumably due to the narrow temperature range over which this mesophase exists in these compounds. Compounds **27**-*6* and **27**-*8* showed only a single reflection in their diffraction patterns that was consistent with the formation of a lamellar phase; diffraction data for all homologues is collected in Table 3.3.

118

Table 3.3. Diffraction data for series **27**-*n*.

n	d_obs / Å	hk(l)	Mesophase
6	26.4	*001*	SmA
	13.2	*002*	
	4.7	halo	
8	28.7	*001*	SmA
	4.7	halo	
10	30.5	-	Cub
	26.6	-	
	4.7	halo	
12	30.1	*10*	Col_h
	-	*11*	
	4.7	halo	
14	33.1	*10*	Col_h
	19.1	*11*	
	4.7	halo	
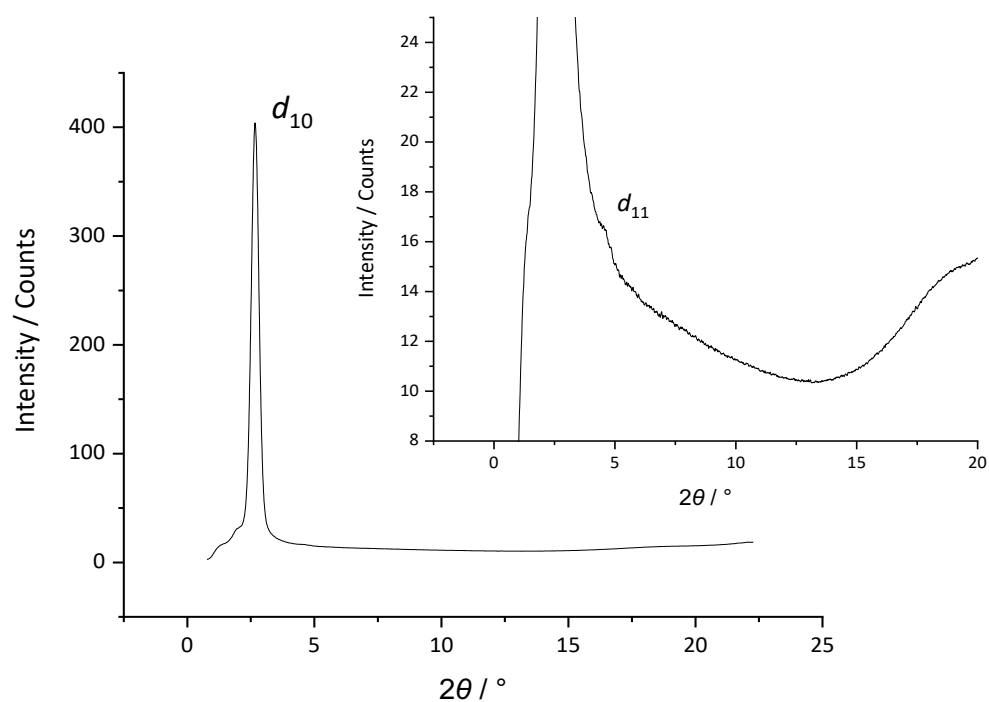
Figure 3.18. SAXS pattern of the hexagonal columnar phase formed by compound **27**-*14* at 116 °C: inset shows the d_{11} reflection.

119
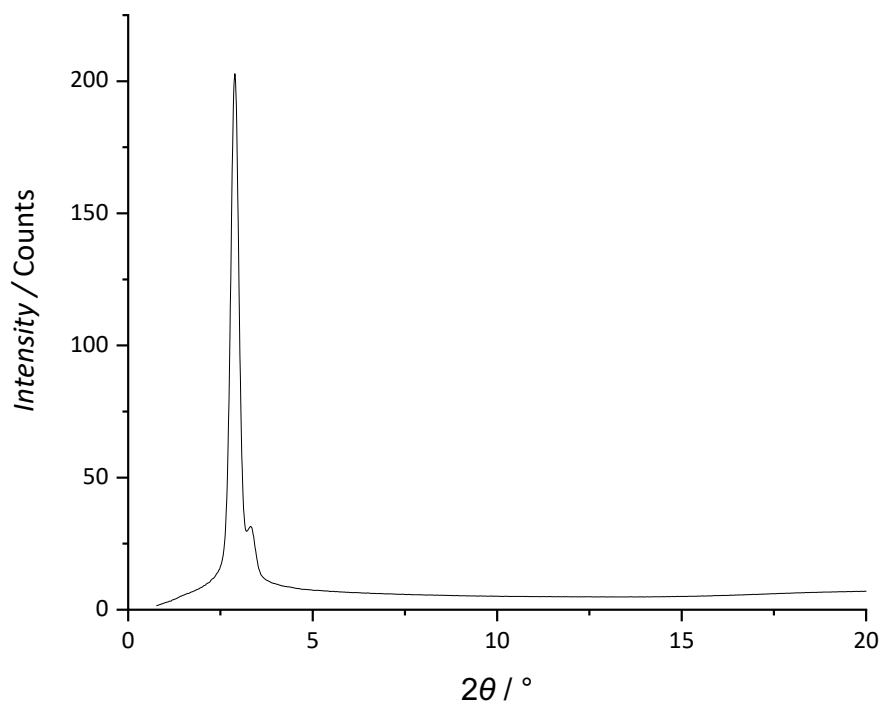
Figure 3.19. X-Ray diffraction pattern of the cubic phase formed by compound **27**-*10* at 105 °C.

DSC was unable to detect the Col_h-to-isotropic transitions of compounds **27**-*12* and **27**-*14*, most probably due to decomposition at these elevated temperatures. Furthermore, the SmA-to-cubic transitions are not detected for **27**-*10* and **27**-*12* regardless of the heating rate, probably due to the slow kinetics of cubic phase formation. The clearing points, on the other hand, are clearly visible for the SmA-to-isotropic transition displayed by compounds **27**-*6* and **27**-*8*, as is the clearing point of compound **27**-*10* that is presumably a SmA-to-isotropic transition given that the SmA-to-cubic transition was not observed *via* DSC.

Table 3.4. Transition temperatures and thermal data for the octylsulfate salts: * marks transitions that cannot be detected by DSC.

n	Transition	T / °C	ΔH / kJ mol^{-1}
6	Crys-Crys'	54	0.9
	Crys'-SmA	93	42.9
	SmA-Iso	130	0.8
8	Crys-Crys'	53	11.6
	Crys'-SmA	81	40.5
	SmA-Iso	101	1.8
10	Crys-SmA	89	65
	SmA-Cub	96	*
	Cub-Iso	121	1.5
12	Crys-SmA	89	35.2
	SmA-Cub	94	*
	Cub-Col$_h$	106	*
	Col$_h$-Iso	183	*
14	Crys-Col$_h$	83	33.5
	Col$_h$-Iso	189	*

2.2.2. Dodecylsulfate salts, 28-n
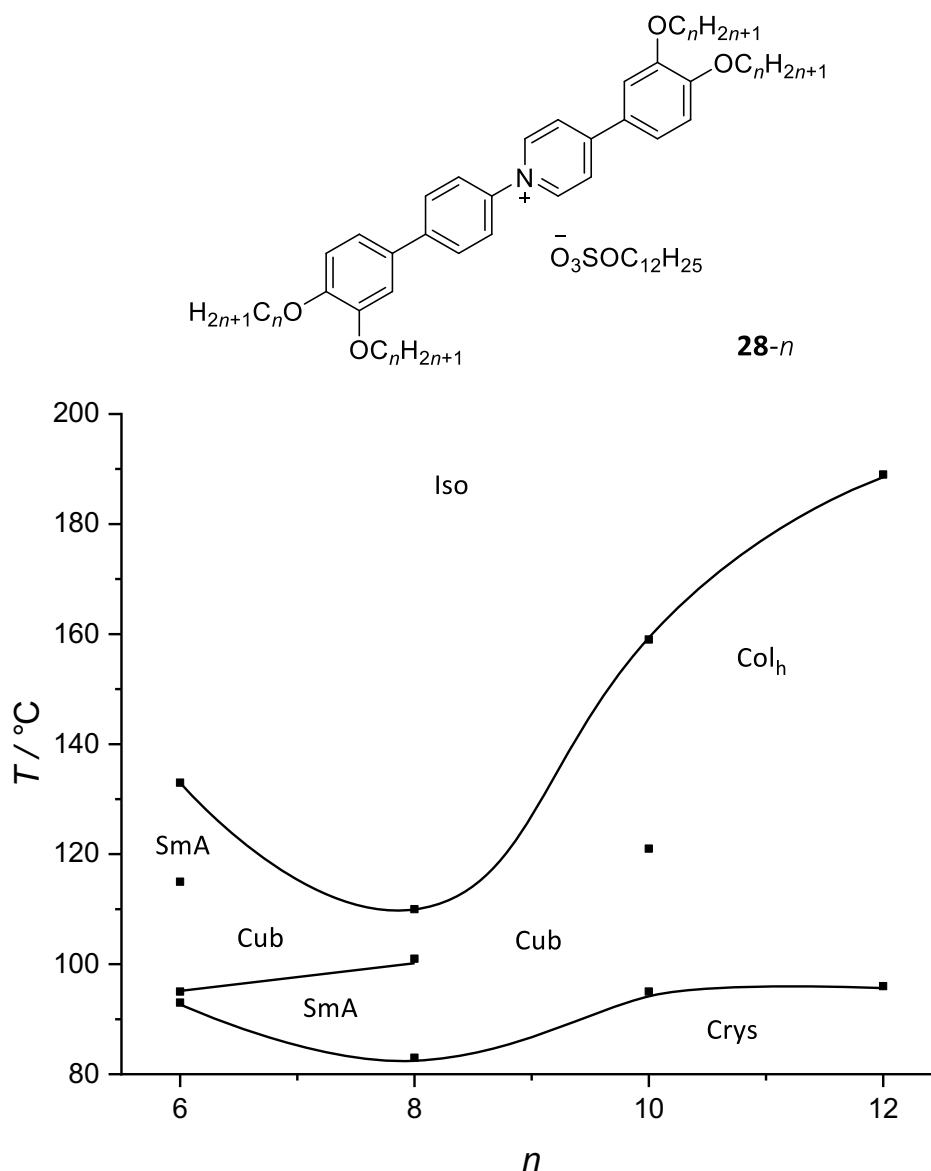
Figure 3.20. Phase diagram of the tetracatenar dodecylsulfate salts **28**-*n*: transition temperatures are from microscopy on heating.

The phase diagram of the tetracatenar dodecylsulfate salts, **28**-*n*, is presented in Figure 3.20. On moving across the series from **28**-*8* to **28**-*12*, a change in mesomorphism from SmA-to-Col$_h$ is observed *via* an intermediate cubic phase. Compound **28**-*8* melts into a SmA phase at 83 °C before a transition to a cubic phase was observed at 101 °C, which then gave way to the isotropic liquid at 110 °C. On cooling compound **28**-*8*, however, only a cubic phase was observed and this phase persisted all the way down to room temperature. On the second heating cycle, crystallisation

occurred at 60 °C and the sample then melted into a SmA phase, much like the thermal behaviour on the first heating cycle. Compound **28**-*10* melted into a cubic phase at 95 °C that was identified by the total loss of birefringence and the formation of a mesophase with high viscosity. The cubic phase then gave way to a Col$_h$ phase at 121 °C that was exemplified by the reappearance of birefringence and a reduction in viscosity. The Col$_h$ phase then cleared to the isotropic liquid at 159 °C, demonstrating an increase in the clearing point on moving from **28**-*8* to **28**-*10*. Compound **28**-*12* melted into a Col$_h$ phase at 96 °C and then cleared directly into the isotropic liquid at 189 °C. Pseudo focal-conic textures with spine defects were observed on cooling compounds **28**-*12* and **28**-*10* from the isotropic liquid (Figure 3.21), being characteristic of a columnar hexagonal mesophase. The cubic phase formed by compound **28**-*10* grows in from the Col$_h$ phase as square edges as shown in Figure 3.21 (**a**).

(**a**)　　　　　　　　　　　　　　　　　　　(**b**)
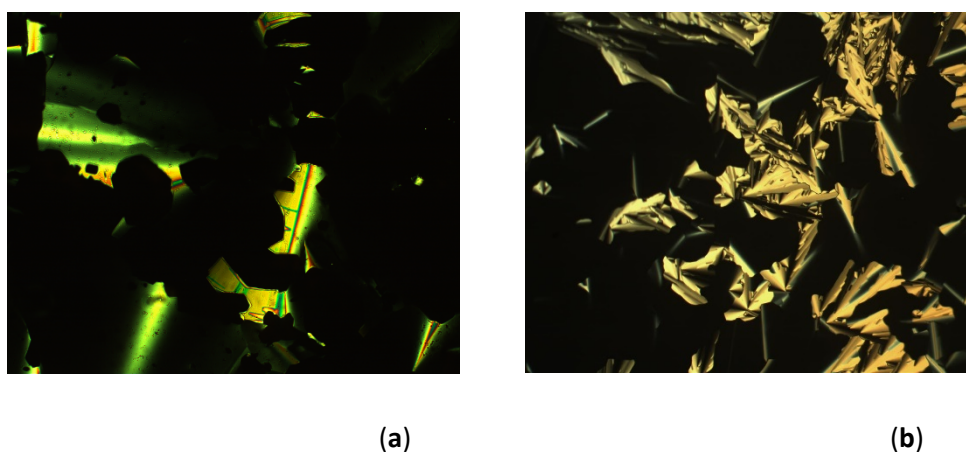
Figure 3.21. (**a**) Cubic phase growing in from Col$_h$ phase of compound **28**-*10* at 108 °C and (**b**) Col$_h$ phase formed by compound **28**-*12* at 172 °C. Textures are at x10 magnification.

However, compound **28**-*6* behaved a little different and melted into a SmA phase at 93 °C, which then almost instantly gave way to an optically isotropic cubic phase at 95 °C that persisted up to 115 °C when a SmA phase formed once again. The higher-temperature SmA phase then cleared to the isotropic liquid at 133 °C. This mesomorphism was extremely repeatable regardless of the heating rate. Furthermore, the cubic mesophase was never observed on cooling compound **28**-*6* from the isotropic liquid, and instead only a SmA phase was observed all the way down to room temperature (at which point glass formation occurred). While this behaviour seems odd at first glance, it is not unheard of considering the slow kinetics often associated with the formation of cubic mesophases.

On comparing the phase diagrams of the octylsulfate and dodecylsulfate materials (series **27**-*n* and **28**-*n*, respectively), it becomes apparent that the change to Col$_h$ mesomorphism takes place at a shorter alkoxy chain length for the dodecylsulfate materials. The melting points remain broadly similar across both series so that the additional methylene groups of the dodecylsulfate anion are not sufficient to destabilise the crystal phase further. In addition, compounds **27**-*n* and **28**-*n* display a similar trend in their clearing points in that SmA phases formed at short terminal chain lengths are steadily destabilised on increasing *n*, then, at the transition to Col$_h$ mesomorphism, the clearing point increases dramatically.

X-Ray diffraction data for series **28**-*n* is collected in Table 3.5. A single reflection was observed in the diffraction patterns of compounds **28**-*6* and **28**-*8* that is consistent with the formation of a SmA phase. The space group of the cubic phases formed by compounds **28**-*8* and **28**-*10* could not be identified due to a lack of higher order reflections. However, X-ray diffraction was able to detect a mesophase above the SmA phase in compound **28**-*8* that was consistent with the formation of a cubic phase, and a second reflection in the small-angle regime was observed that corresponded to something other than a d_{002} reflection. The d_{11} reflection of the Col$_h$ phase formed by compound **28**-*10* was also detected as shown in Figure 3.22; however, whilst a diffraction pattern that was consistent with the formation of a cubic phase was detected on the first heating cycle, only the hexagonal packing of the columnar phase was detected on cooling all the way down to room temperature.

Table 3.5. Diffraction data for series **28**-*n*.

n	d_{obs} / Å	hk(l)	Mesophase
6	26.8	001	SmA
	4.7	halo	
8	28.8	001	SmA
	4.7	halo	
8	34.0	-	Cub
	25.8	-	
	4.7	halo	
10	30.2	-	Cub
	26.4	-	
	4.7	halo	
10	31.1	10	Col$_h$
	17.9	11	
	15.5	20	
	4.7	halo	
12	32.1	10	Col$_h$
	-	11	
	16.0	20	
	4.7	halo	

Some phase transitions could not be detected *via* DSC as evidenced from Table 3.6, being mainly the transitions into and out of a cubic phase. Even running DSC experiments as slow as 2 °C min^{-1} were unable to detect such transitions. However, the Col$_h$-to-isotropic transition could be detected by DSC for compounds **28**-*10* and **28**-*12,* previously not possible in the triflate and octylsulfate series owing to decomposition at these elevated temperatures.

Table 3.6. Transition temperatures and thermal data for the dodecylsulfate salts: * represents a transition that could not be detected via DSC.

n	Transition	T / °C	ΔH / kJ mol^{-1}
6	Crys-SmA	93	42.6
	SmA-Cub	95	*
	Cub-SmA	115	0.8
	SmA-Iso	133	0.7
8	Crys-SmA	83	32.5
	SmA-Cub	101	*
	Cub-Iso	110	1.1
10	Crys-Cub	95	58
	Cub-Col$_h$	121	0.8
	Col$_h$-Iso	159	0.5
12	Crys-Col$_h$	96	87.9
	Col$_h$-Iso	189	1.7
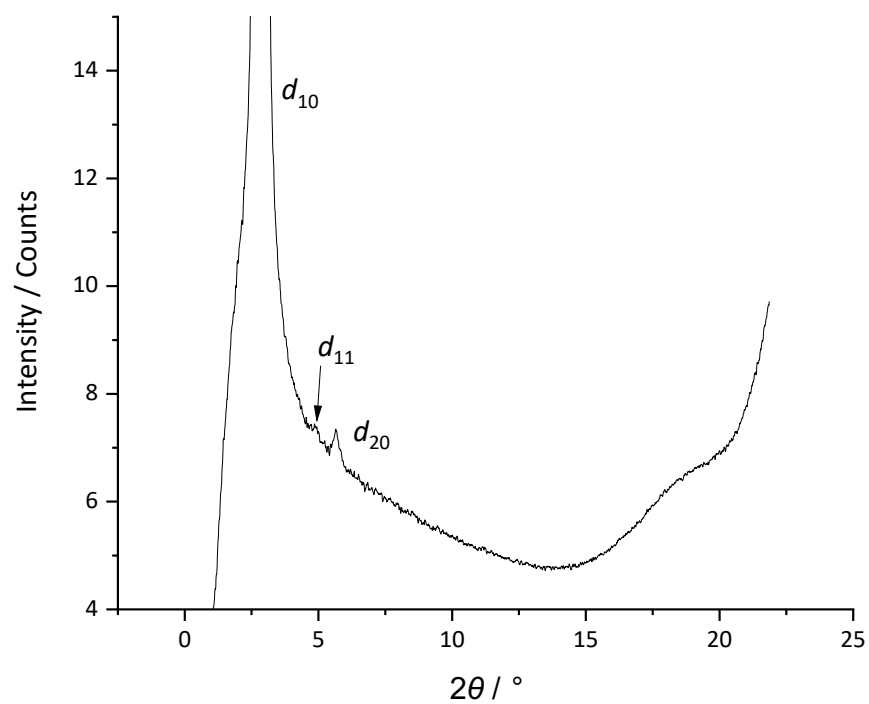
Figure 3.22. Diffraction pattern of the Col_h phase formed by compound **28**-*10* at 105 °C on cooling: note, the cubic phase cannot be detected on cooling and instead the hexagonal lattice of the columnar phase is detected all the way to room temperature.

2.3. Bis(trifluoromethanesulfonyl)imide salts

Bis(trifluoromethanesulfonyl)imide (bistriflimide or NTf_2^-) is a commonly used anion in ionic liquids due to its high thermal stability and ability to provide accessible melting temperatures.[19] However, it is much less common to incorporate the NTf_2^- anion into ionic liquid crystals, and the few ionic liquid-crystalline NTf_2^- salts reported are typically viologens that have been investigated due to their extensive redox properties.[20,21] NTf_2^- was also successful in the viologen compounds in reducing the transition temperatures compared to the parent halide salts due to its larger size and more diffuse charge. Thus, it was postulated how the larger size of the NTf_2^- anion (compared to OTf^-) might influence the liquid crystal properties of ionic polycatenar materials.
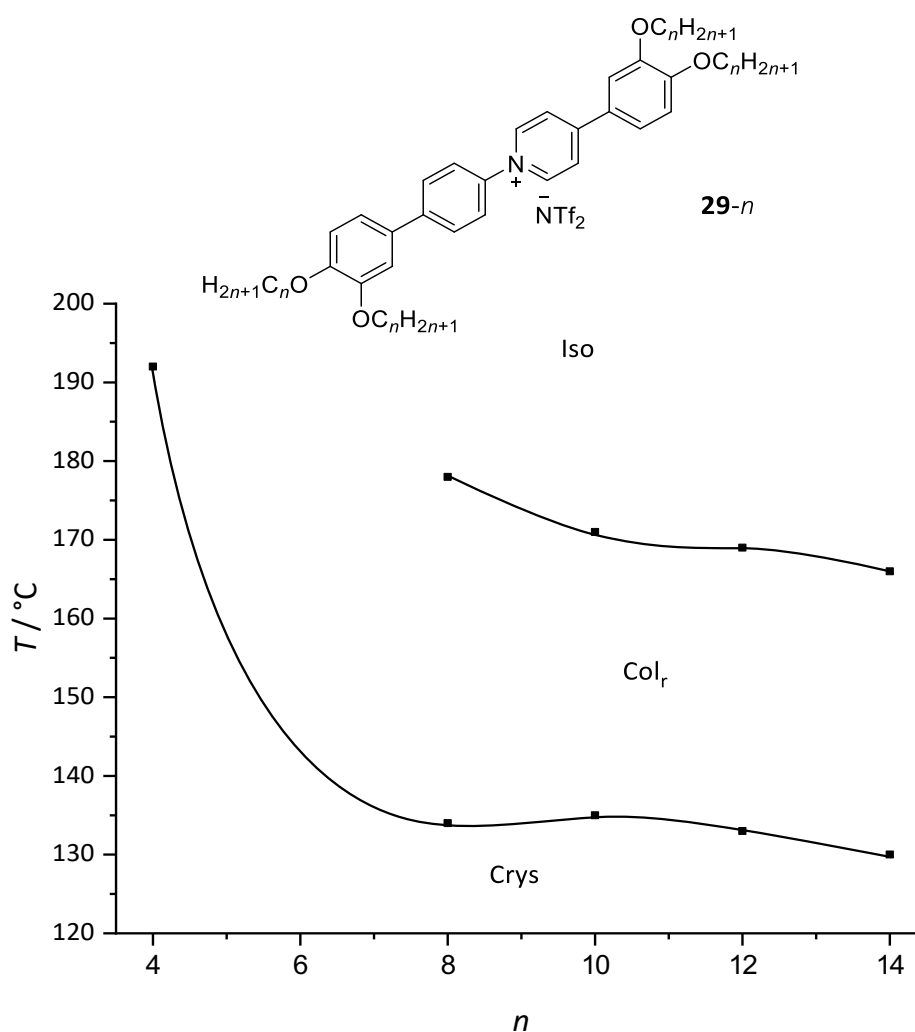
Figure 3.23. Phase diagram of the tetracatenar NTf_2^- salts, **29**-n: transition temperatures are from microscopy.

The phase diagram of the NTf_2^- salts is presented in Figure 3.23 and even-numbered homologues **29**-*8* to **29**-*14* were prepared and found to be mesomorphic; compound **29**-*4* was also prepared and was not liquid-crystalline. Compounds **29**-*8* to **29**-*14* melted into a mesophase with an odd spherulitic texture that corresponded neither to a SmA nor a Col_h phase. In fact, only on cooling extremely slowly from the isotropic liquid (at 0.1 °C min^{-1}) could any clear textures be obtained, which showed large pseudo focal-conic defects that would normally be associated with some kind of columnar mesophase. However, X-ray scattering experiments did not show the higher-order reflections typical of hexagonal symmetry, and instead only a single reflection was observed that provided little useful information. Contact preparations between the NTf_2^- materials and the SmA and Col_h phases of the OTf^- series showed a miscibility gap, so failing to provide any evidence as to the identity of this mesophase (see Figure 3.24 (**c**) and (**d**) for photomicrographs of these miscibility studies).

The melting temperatures of compounds **29**-*8* to **29**-*14* were comparable to those of the triflate salts and remained fairly constant across the series (thermal data are collected in Table 3.7). The melting enthalpies detected *via* DSC were consistently higher than the melting enthalpies displayed by the triflate and alkylsulfate compounds. A steady decrease in the clearing point was seen on moving across the series, indicating that the mesophase was steadily destabilised on increasing chain length, much like that of the SmA phase formed by the triflate materials. Much like the OTf^- compounds, all derivatives in the NTf_2^- series crystallised on cooling (with very little supercooling effects) in both DSC and microscopy experiments. Melting of the non-mesomorphic homologue **29**-*4* was accompanied by the formation of biphasic crystal plus isotropic regions, presumably due to decomposition at these elevated temperatures. This results in the formation of more than one species that melt into the isotropic liquid at different temperatures (elemental analysis proved that this compound was analytically pure). DSC also detected two melting endotherms of compound **29**-*4*, which is consistent with the behaviour observed *via* microscopy

Table 3.7. Transition temperatures and thermal data of the NTf_2^- salts.

n	Transition	T / °C	ΔH / kJ mol^{-1}
4	Crys-Iso	188	6.4
	Crys'-Iso	193	5.3
8	Crys – Col$_r$	134	10.9
	Col$_r$ – Iso	178	5.7
10	Crys – Crys'	70	16.1
	Crys'- Col$_r$	135	15.3
	Col$_r$ – Iso	171	7.8
12	Crys – Crys'	79	49.7
	Crys'- Col$_r$	133	34.2
	Col$_r$ – Iso	169	21.6
14	Crys-Crys'	88	78.5
	Crys'- Col$_r$	130	52.1
	Col$_r$ – Iso	166	29.8
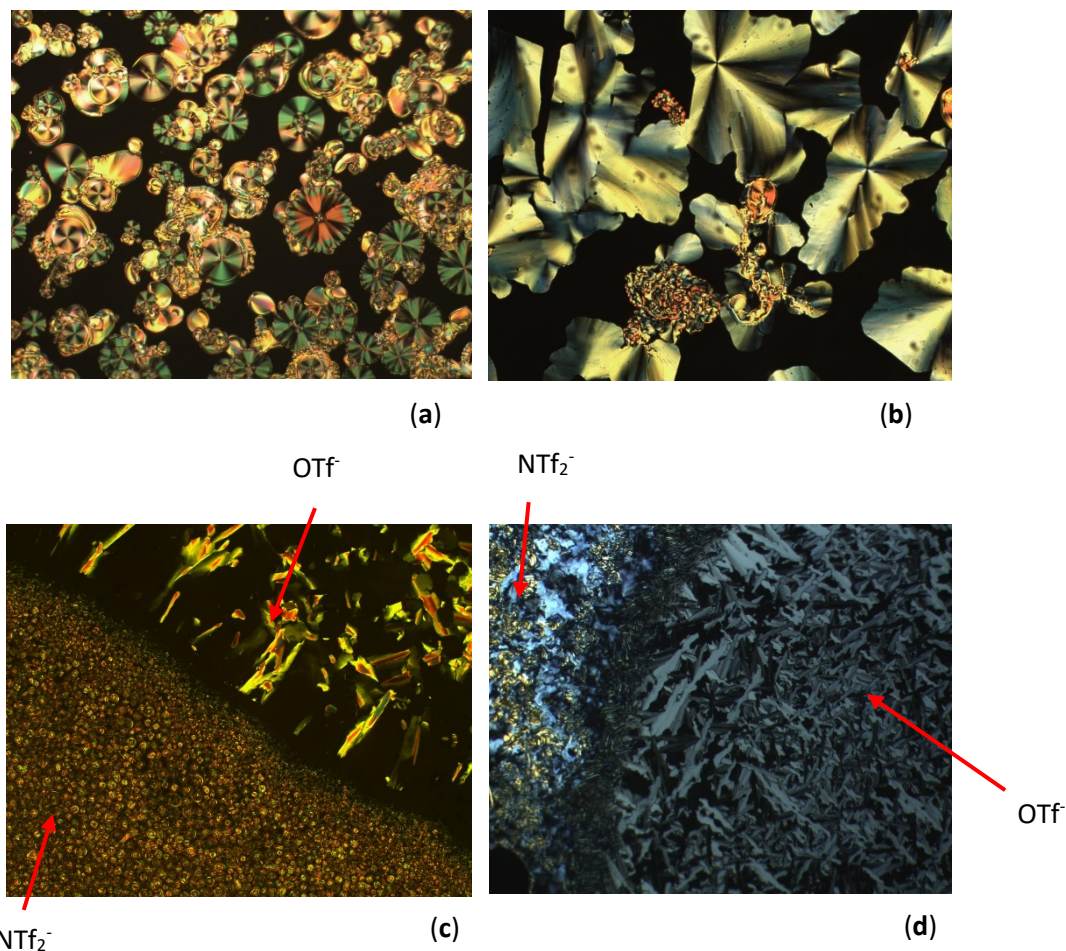
Figure 3.24. Photomicrographs of the Col$_r$ phase formed by compound **29**-*8*: (**a**) cooling from the isotropic liquid at 10 °C min^{-1} at 158 °C, (**b**) slow cooling of the same compound at 0.1 °C min^{-1} at 159 °C, (**c**) miscibility gap between this phase and the Col$_h$ phase of the OTf compound **10**-*18* and (**d**) miscibility gap between this phase and the SmA phase of the OTf compound **10**-*12*. Textures are at x10 magnification.

Reinvestigating the diffraction patterns of compounds **29**-*n* then showed an additional reflection that can be identified in the medium-angle regime only on prolonged exposure in the beam (diffraction data are collected in Table 3.8 and the diffraction pattern of **29**-*10* is presented in Figure 3.25). One explanation consistent with these data is the formation of a mesophase with rectangular symmetry where one of the lattice parameters is rather small and correlations along this dimension are quite weak owing to the low intensity of the medium-angle reflection. These reflections can be indexed according to Table 3.8, giving lattice parameters of a = 47.6 Å and b = 10.9 Å for compound **29**-*8*.

Table 3.8. Diffraction data for series **29**-*n*.

n	*d*$_{obs}$ / Å	*hk*	*Parameter* / Å
8	23.8	*20*	*a* = 47.6
	11.8	*40*	
	10.6	*11*	*b* = 10.9
	8.8	*60*	
	5.3	halo	
10	27.0	*20*	*a* = 54.0
	13.5	*40*	
	10.7	*11*	*b* = 10.9
	9.0	*60*	
	5.3	halo	
12	29.9	*20*	*a* = 59.8
	15.0	*40*	
	10.5	*11*	*b* = 10.7
	10.0	*60*	
	5.3	halo	
14	32.8	*20*	*a* = 65.6
	16.4	*40*	
	10.6	*11*	*b* = 10.7
	5.3	halo	
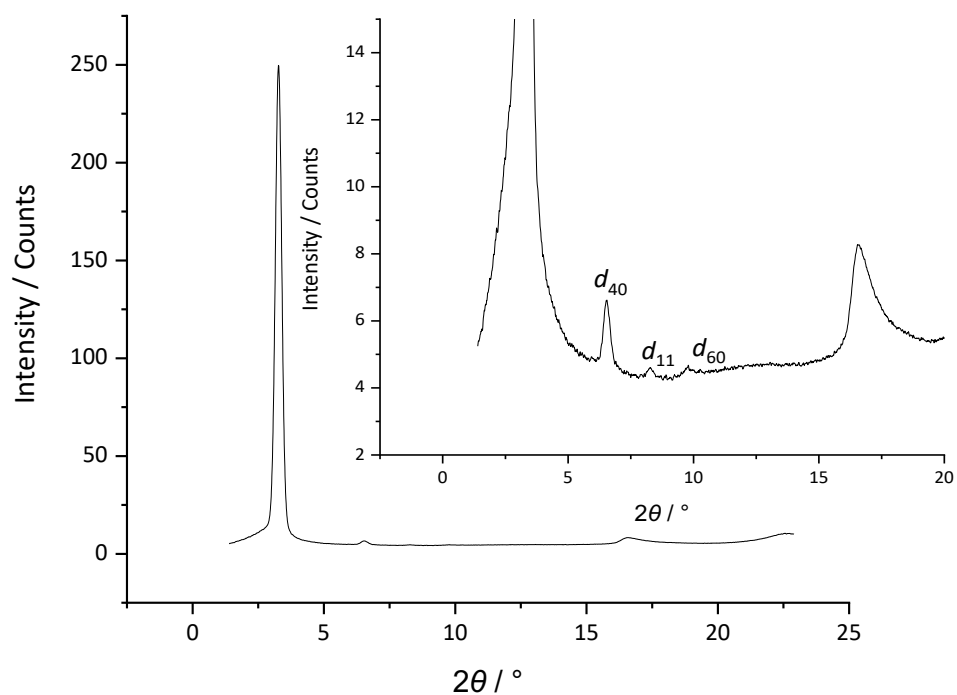
Figure 3.25. Diffraction pattern of compound **29**-*10* at 139 °C: insert represents the zoomed in region for clarity of the low intensity reflections.

A number of rectangular plane groups are of course possible and specific assignment can only be achieved by the presence of multiple higher-order reflections. The two most common plane groups that columnar rectangular phases belong to are typically *c2mm* or *p2gg*; models for these are presented in Figure 3.26.[22,23] The condition that *h0 = 2n* and *k0 = 2n* must be satisfied for *p2gg* symmetry. Whereas for *c2mm* symmetry, all *hk* reflections must additionally satisfy *h+k = 2n* such that the presence of *h+k = 2n+1* reflections excludes *c2mm* symmetry. However, in the case of the NTf$_2^-$ materials, an absence of higher order reflections does not allow equivocal assignment of the plane group, and so the tentative assignment is *c2mm* as it is common to assume the highest symmetry when discrimination cannot be achieved.

p2gg   C2mm
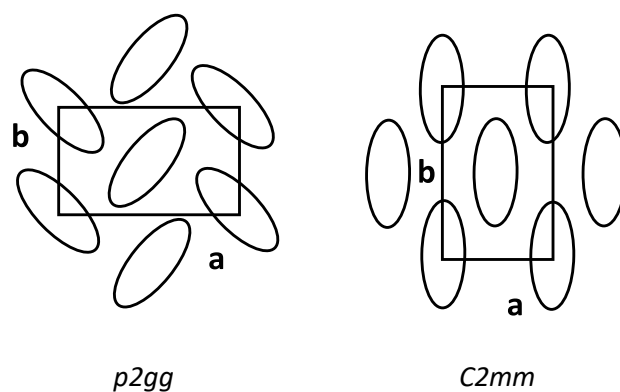
Figure 3.26. Rectangular space groups possible for columnar rectangular phases: **a** and **b** represent the two lattice parameters.

Note also the difference in d-spacings of the NTf$_2^-$ and OTf$^-$ materials in the wide-angle regions of their X-ray diffraction data (Table 3.8 and Table 3.2), where the diffuse diffraction signals corresponding to the average side-to-side distances of the NTf$_2^-$ series are consistently larger at 5.3 Å as compared to 4.7 Å for the triflate salts. This observation is consistent with that observed by Wang *et al.*[16,20] and is attributed to the more voluminous NTf$_2^-$ anion leading to greater side-to-side separations between neighbouring cations. Krossing *et al.*[38] calculated the molecular volumes of various anions to investigate the lattice and solvation effects of ionic liquids. The authors found that the volume of triflate was 0.131 nm^3, whereas the volume of triflimide was almost double that of triflate at 0.232 nm^3.

3. Discussion

3.1. Formation of the SmA phase

The preparation of the ionic polycatenar *N*-phenylpyridinium liquid crystals has uncovered some interesting features that were not apparent in the phase behaviour of the silver(I) salts previously prepared by the group. The first significant observation is the formation of the SmA phase by the triflate and alkylsulfate materials when the length of the terminal aliphatic chains are short. This mesophase actually forms across a significant region of the phase diagram in the triflate series up to and including the tridecyloxy derivative, **11**-*13*. How can the formation of a SmA phase be explained?

The most common mesophase formed by ionic liquid crystals is the SmA phase due to intermolecular ionic interactions between anions and cations that stabilise self-organisation into layers. But, recall that typical tetracatenar materials have a tendency to form a SmC phase at short terminal chain lengths due to a mismatch between core and chain volumes;[24] the schematic presented in Figure 3.27 demonstrates the origin of this tilt. To accommodate the volume of four terminal chains, the molecules tilt so that the cross-sectional area of the core and that of the chains projected onto the core-chain interface are equal; the molecules can then arrange in layers to fill space efficiently. However, the formation of a SmC phase, which is also lamellar, would also be consistent with strong ionic intermolecular interactions, yet, it is not observed. However, in ionic materials, the spatial requirements of the anion must also be taken into account in addition to the strong electrostatic interactions.
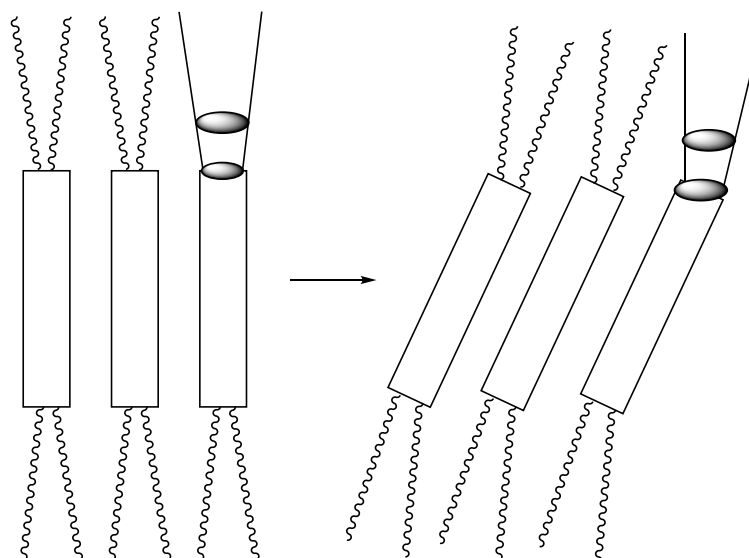
Figure 3.27. Schematic to show the origin of the tilt in the SmC phase formed by neutral tetracatenar materials: the cones show the relative volumes of the core and the terminal chains projected onto the core-chain interface.

To better understand how electrostatics and space filling tension against one another in these systems, DFT calculations of the electrostatic potential of the cation-anion system (for the OTf⁻ series) were performed by Dr Martin Bates. DFT calculations of the electrostatic potential were performed using Gaussian 16[e] using the B3LYP functional and 6-311G(d,p) basis set. They revealed that the positive charge is localised predominantly on the pyridinium ring as shown in Figure 3.28 (**b**). Calculations were then run on the anion-cation system and the triflate anion was found always next to the pyridinium ring, off to the side and never above the plane of the ring, in a disposition that placed the three oxygen atoms of the triflate closest to the positive charge (Figure 3.28 (**a**)). This behaviour is consistent with the single crystal structure presented in Figure 2.9 (Chapter Two) whereby the triflate moiety is located preferentially next to the pyridinium ring. Assuming similar dispositions of the anion and cation in the mesophase, then the effective core volume has been increased due to the associated anion. As such, the increased volume of the two terminal alkoxy chains is readily accommodated, therefore removing the need for the molecules to tilt in order to self-organise into layers and so a SmA phase is formed.
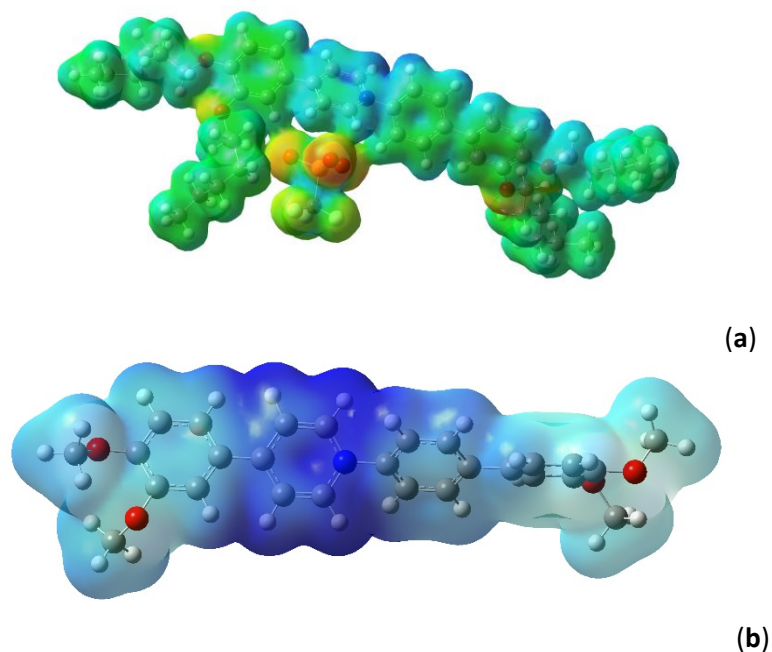
Figure 3.28. Location of (**a**) ion-pairs with respect to one another and (**b**) electrostatic potential map where *n* = 1. Surface computed for isoval = 0.001, with electrostatuic potential shading between –0.15 (red) and +0.15 (blue).

Further support for these assertions come from two related studies. The first is that conducted by Pelzl *et al.*[25] who demonstrated that a SmA phase can be induced when a *bis*-swallow-tailed mesogen is doped with an appropriately sized calamitic compound. *Bis*-swallow-tailed compounds are structurally similar to tetracatenar mesogens and contain a total of four flexible chains grafted to an elongated core. The structure of the materials investigated are shown in Figure 3.29. It is assumed that the dopant located itself next to the core of the swallow-tailed host as this provided the most efficient space-filling, which, in turn, induced a SmA phase by removing the imbalance between core and chain volumes. The second piece of supporting evidence comes from a study performed by Bruce and Smirnova[26,27] who found that lamellar phases can be induced in contact preparations between tetracatenar stilbazole complexes of silver(I) and polar aprotic solvents such as DMSO. These compounds displayed cubic or Col_h mesophases as dry materials, and so the addition of external solvent induced a lamellar phase by interacting preferentially with the charged core to increase the effective core volume. These ideas are discussed in more detail in Chapter Four, but the key point to consider for the present discussion is that the volume of certain parts of the molecule can be effectively increased by the addition of external agents. In the case of the *N*-

phenylpyridinium materials, the triflate anion behaves in an identical fashion to the external agents and increases the effective core volume, thereby allowing self-organisation into a SmA phase.
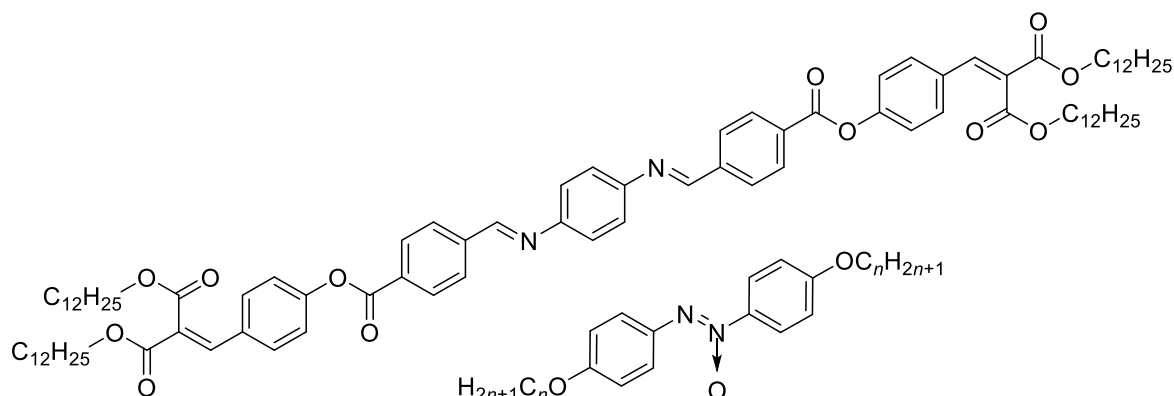
Figure 3.29. Structure of the *bis*-swallow-tailed compound and calamitic dopant used to form an induced SmA phase:[25] n = 1, 6 or 12.

In one sense, the alkylsulfate anions are similar to triflate inasmuch as they increase the effective cross-sectional area of the cation core, removing the need for them to tilt. However, while in the triflate salts the Col_h phase (indicative of surface curvature) appeared at n = 14, for octylsulfate a cubic phase was observed at n = 10 and for dodecylsulfate a cubic phase appeared at n = 6. Comparison of the length of the octylsulfate anion (11.3 Å) with half of the length of the phenylpyridinium core (8.4 Å) shows that the alkylsulfate anion extends past the cation core and so contributes to the terminal chain volume. Thus, promoting formation of the cubic phase in a manner analogous to that in the stilbazole complexes of silver(I) discussed earlier. The longer dodecylsulfate anion contributes even more to the terminal chain volume and so the cubic phase is seen at a shorter terminal chain length still. Figure 3.30 shows a schematic of this where the alkylsulfate anions have been drawn to scale.
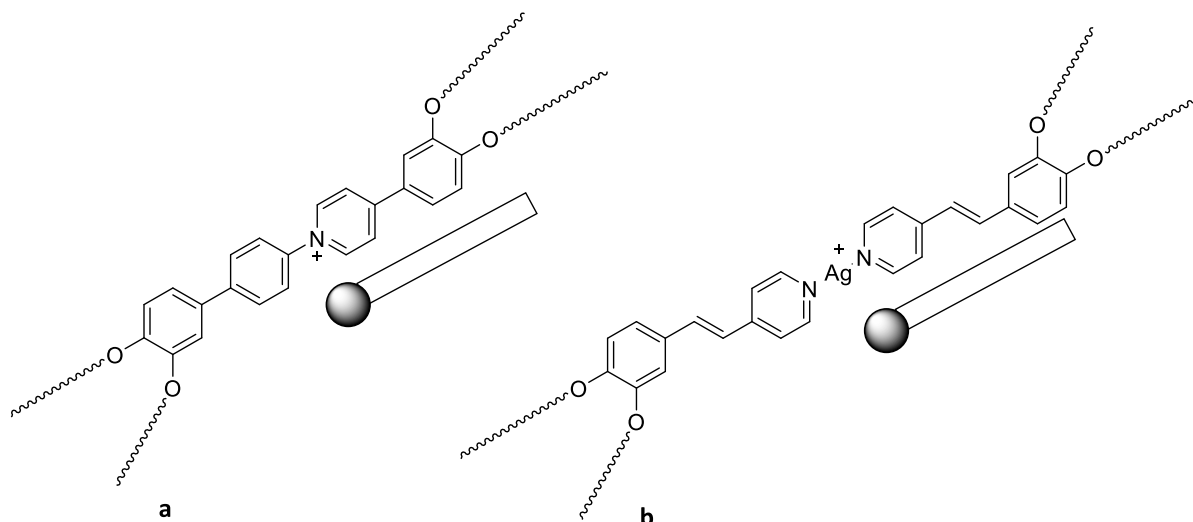
Figure 3.30. Schematic showing (**a**) how the octylsulfate anion extends past the cation in the *N*-phenylpyridinium materials and (**b**) how it does not extend past the core of the silver(I) stilbazole cation, both drawn to scale.

1.1. Stabilisation of the columnar hexagonal phase

The second striking feature of the phase diagrams formed by these *N*-phenylpyridinium salts is the consistent and significant stabilisation of the Col$_h$ phase when compared to the preceding SmA or cubic mesophases. Also apparent is the gradual suppression in the clearing point of the SmA phase (and cubic phase for the alkylsulfates) on moving across the phase diagrams to increasing cation chain length. For example, the clearing point in the triflate series decreases from 169 °C at **11**-*8* to 141 °C at **11**-*13*, then, as the mesomorphism switches to Col$_h$ the clearing point increases significantly to 210 °C at compound **11**-*14*. This is a significant mesophase stabilisation on the addition of only one methylene group per chain (a total of four methylene groups in chain volume).

This behaviour may be contrasted with that typical of neutral tetracatenar liquid crystals, where a steady decrease in the clearing point is observed for the SmC phase that tends to level off when the mode of packing transitions to columnar (examples are presented in Figure 3.31 and Figure 3.32).[28,29] Even when neutral tetracatenar materials contain a lateral substituent[30,31] the shape of the phase diagram remains much the same as any other neutral compound and a plateau of the clearing point is again observed on entering the columnar phase. Compare this to the form of the phase diagrams displayed by the silver(I) triflates and silver(I) dodecylsulfates,[6] and the behaviour is quite different. In the case of the silver(I) dodecylsulfates, the clearing point increases by 35 °C

on moving from the $n = 6$ to $n = 8$ derivative where the mesomorphism switches from cubic to Col_h. This is similar to the stabilisation of the Col_h phases formed by the N-phenylpyridinium ions. As such, this behaviour seems to be common to ionic polycatenar liquid crystals in general, and not simply a result of a lateral substituent that the anion could otherwise mimic.
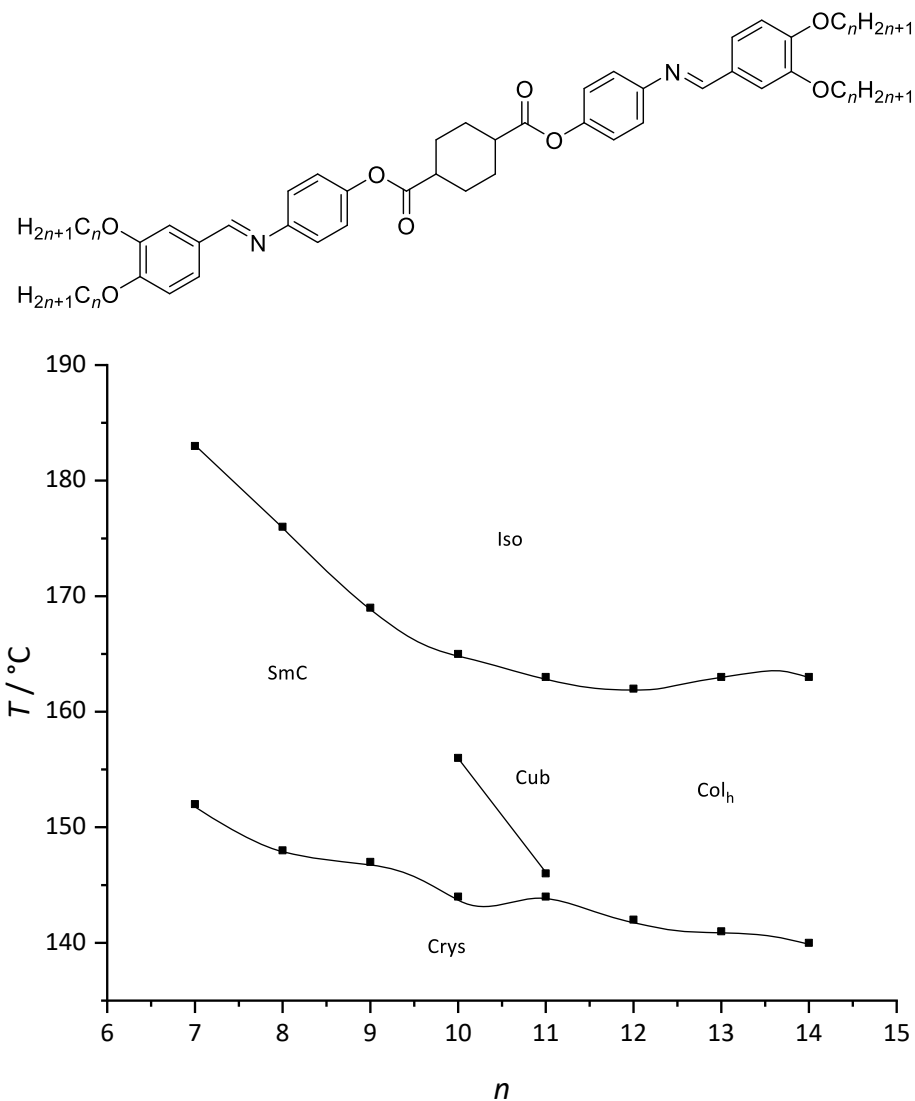
Figure 3.31. Phase diagram of the neutral tetracatenar liquid crystals from ref.[28]
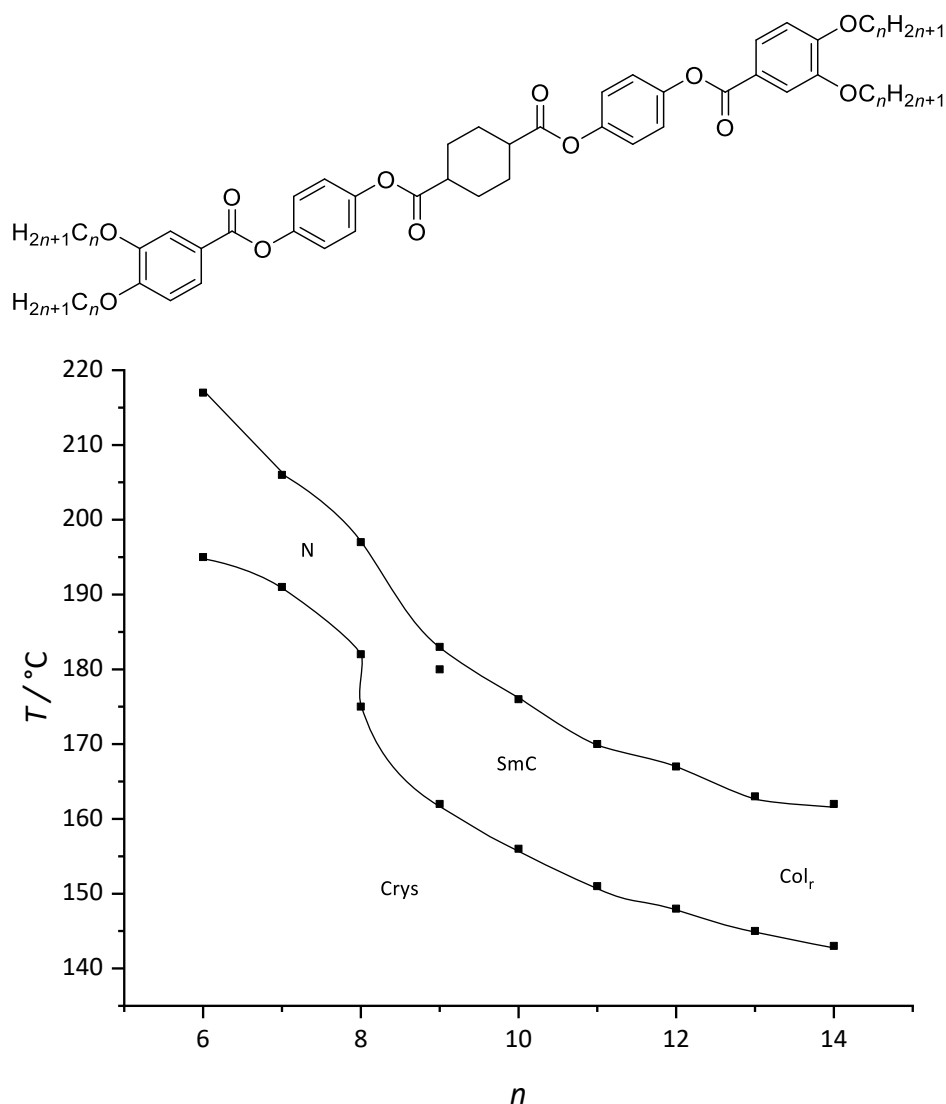
Figure 3.32. Phase diagram of the neutral tetracatenar liquid crystals from ref.[29]

Why exactly is stabilisation of the columnar hexagonal phase observed in ionic polycatenar liquid crystals? Is it that the preceding lamellar and cubic phases are destabilised or that the hexagonal columnar phase is more stabilised?

In considering the general shape of the phase diagrams formed by the *N*-phenylpyridinium materials, the lamellar phases are gradually destabilised on increasing chain length as already discussed. However, at no point (even at very short *n*) are the clearing points of the SmA or cubic phases ever as high as those of the Col$_h$ phase. It is postulated, therefore, that the spatial requirements of the anion act to destabilise lamellar and cubic modes of organisation in general, and only when the aliphatic chains become long enough that the mode of packing switches to Col$_h$

can the spatial requirements of the anion be better accommodated. It seems that lamellar phases are destabilised to a greater extent than cubic phases; this is discussed in more detail in Chapter Five.

3.2. Formation of a rectangular phase

While the triflate and alkylsulfate salts all show SmA and Col_h phases with cubic also seen for the alkylsulfate salts, the triflimide salts, **29**-*n*, are quite different in showing what appears to be a rectangular phase. Indeed, contact preparations performed between the mesophase formed by the triflimide salts and the SmA and Col_h phases formed by the triflate salts showed a lack of miscibility. Contact preparations were also performed between compounds **29**-*n* and a series of smectogenic triflimide salts prepared by Riccobono,[32] and still a miscibility gap was observed. While nothing can be learned from a miscibility gap between two phases, this observation coupled with the odd optical textures and a diffraction pattern showing short-range two-dimensional order is consistent with a mesophase that is neither lamellar nor Col_h.

The two-dimensional order of this mesophase could suggest the formation of a columnar rectangular phase (Col_r), or, more simply, the formation of a lamellar phase with short-range order perpendicular to the layers (in other words a biaxial SmA phase). However, considering that the optical texture of this phase is nothing like that of a SmA phase and that the texture does not change when viewed in alignment cells, results are more consistent with the formation of a ribbon-like phase. Two-dimensional ribbon phases are analogous to the SmÃ phase formed by calamitic mesogens and the B_1 phase formed by bent-core mesogens[33,34] – all possess rectangular symmetry and the general structure is presented in Figure 3.33.[35]
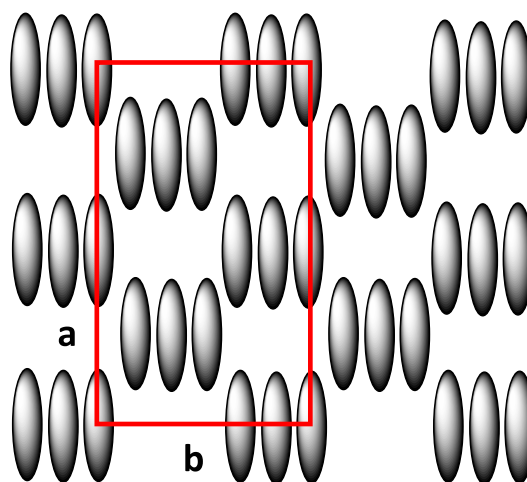
Figure 3.33. Generalised organisation of mesoogens in the SmÃ phase: **a** and **b** represent the lattice parameters of the rectangular arrangement.

A plot of the calculated molecular length of compounds **29**-*n* and the *a* parameter *vs* terminal chain length is presented in Figure 3.34, and whilst the *a* parameter is slightly larger than the molecular length for each homologue, both show a monotonic increase with chain length. The *b* parameter, on the other hand, remains constant across the series at roughly 11 Å. These parameters could suggest a structure of a rectangular phase given in Figure 3.34, where the *a* parameter would in fact increase monotonically with chain length and the *b* parameter would remain constant across the series. What is not clear, however, is why the *a* parameter would be consistently larger than the all-*trans* length of the cation.
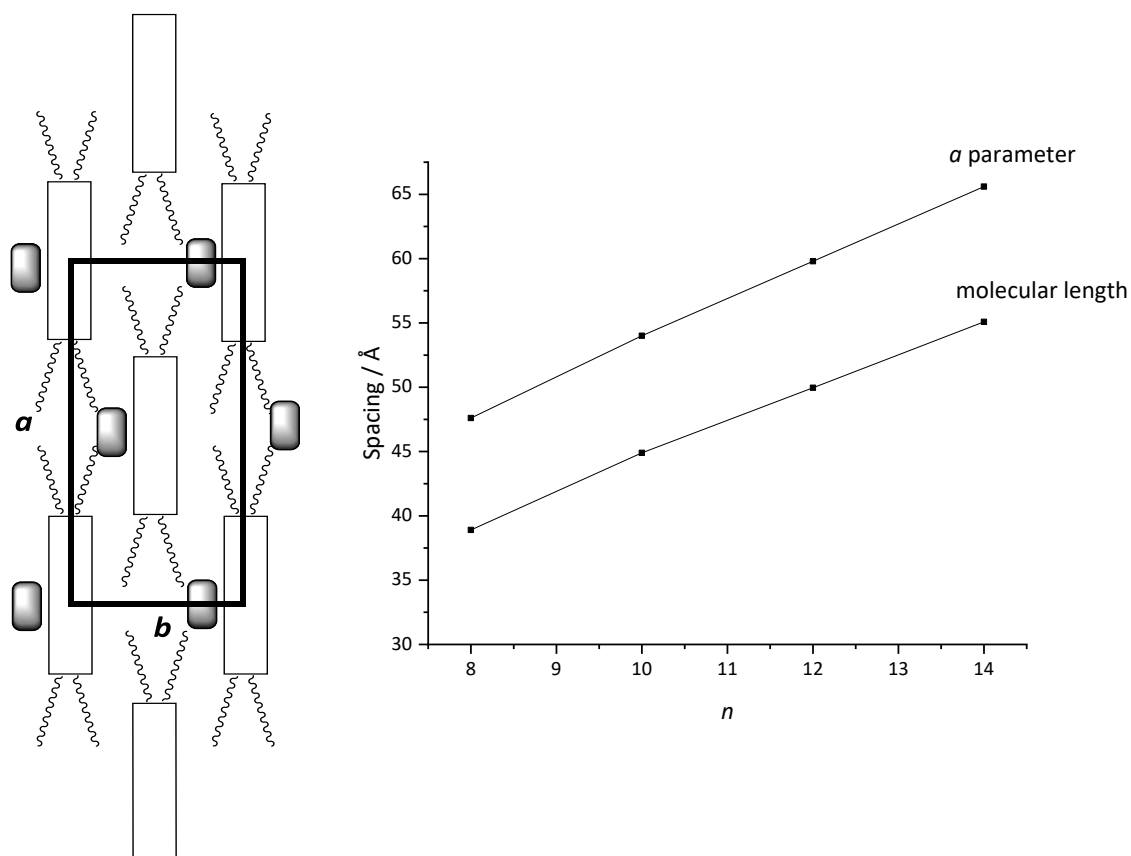
Figure 3.34. Proposed model of the rectangular phase formed by the teracatenar NTf$_2$ salts, **29**-*n*, showing *a* and *b* parameters (left) and molecular length and a parameter *vs* chain length (right).

Tschierske *et al.*[36] also studied a series of amphiphilic and bolaamphiphilic calamitic compounds, and, in mixtures of the two, ribbon phases possessing rectangular symmetry could be induced. These phases displayed optical textures that contained spherulitic defects akin to those observed in the textures of the triflimide salts, **29**-*n*, as shown in Figure 3.35. Tschierske postulated that the different molecular lengths of the two calamitic components caused interruption of the layers to induce a modulated or ribbon-like structure. The proposed model shown in Figure 3.35 (**b**) contains the bolaamphiphilic molecules at the boundaries between adjacent ribbons and an analogy between this ribbon phase and the SmÃ phases[37] was drawn.
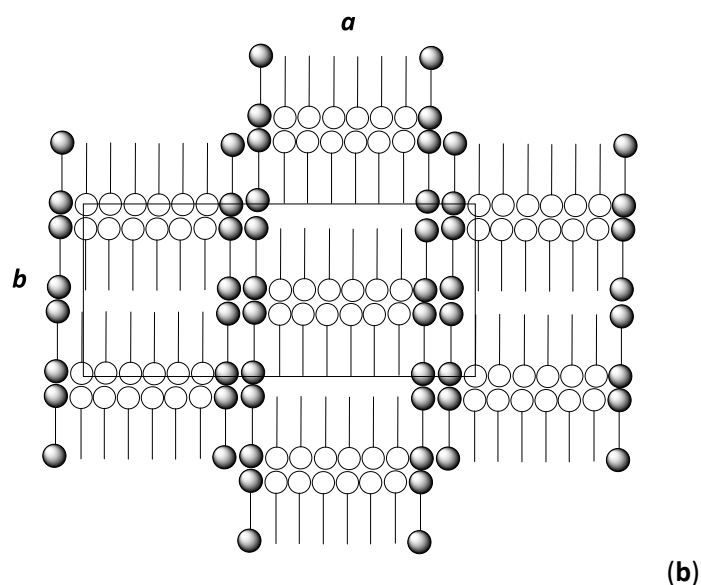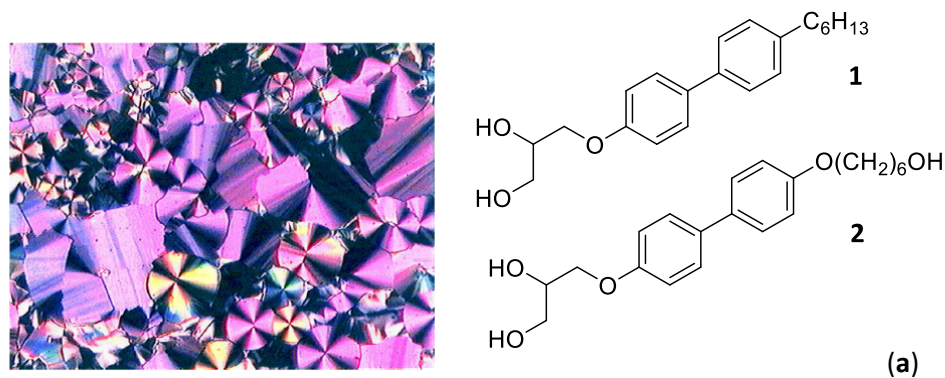
Figure 3.35. (**a**) Optical texture of the SmÃ phase formed by a 1:9 mixture of compounds **1:2** and (**b**) arrangement of the molecules in the SmÃ phase: white spheres represent amphiphiles and dark spheres represent bolaamphiphiles.

What is not quite clear is why a larger, more charge diffuse, anion would promote this type of self-organisation. Whereas the OTf⁻ salts form a SmA phase at short chain lengths due to the spatial requirements of the anion increasing the effective core volume, one would predict that an even larger triflimide anion would give rise to similar behaviour. It could be that the weaker electrostatics imparted by the more charge disperse triflimide anion are sufficient to destabilise the SmA phase causing a break-up of the layers and promoting the formation of ribbons. This could demonstrate the need for strong intermolecular electrostatic interactions in addition to the space-filling arguments of the anion to stabilise the SmA phase formed by the *N*-phenylpyridinium materials. Although the exact nature of the mesophase cannot be conclusively identified from the data

presented, the tendency is to assign this phase as Col_r due to similar optical textures to those formed by the SmÃ phases and diffraction data that suggests local two-dimensional ordering.

4. Conclusion

The polycatenar *N*-phenylpyridinium ions show different mesomorphism to the stilbazole complexes of silver(I) in that a SmA phase is formed at short terminal chain lengths when the anion is triflate, octylsulfate or dodecylsulfate. Intermolecular electrostatic interactions help drive mesomorphism into the SmA phase for the same reason as the SmA phase is the most common mesophase formed by calamitic ionic liquid crystals. Arguably more important than electrostatics, however, is the size and shape of the anion. In the case of OTf^-, the anion increases the effective core volume to remove the imbalance between core and chain volumes that typically drives the formation of a SmC phase in tetracatenar mesogens. However, as the chain volume increases, the mode of packing changes to Col_h rather than first being compensated for by the formation of a SmC or cubic phase, whereas the transition from SmA to Col_h self-organisation in the alkysulfate compounds does in fact take place *via* the formation of an intermediate cubic phase. Thus, the SmC phase is not well-stabilised in these materials and the cubic phase is clearly absent in the triflate series, its formation being dependent on the identity of the anion.

The thermotropic cubic phases formed by polycatenar liquid crystals are not well-understood in general, and so it is not clear why a cubic phase is formed only when the anion is a long-chain alkylsulfate. All that can be concluded is that its position in the phase diagram (of the alkylsulfate salts) is consistent with curvature intermediate between lamellar and columnar modes of assembly. In the case of all the materials studied here, a very significant stabilisation of the Col_h phase is observed compared to the preceding SmA or cubic phases. The general shape of the phase diagram displayed by these materials therefore show three general features. First, is the gradual depression in the clearing point of the SmA phase on increasing terminal chain length. Second, is the steady increase in the clearing point on entering the cubic phase (for the alkylsulfates). Third, and most significant, is the significant stabilisation of the Col_h phase at the longest terminal chain lengths in all materials. So, it would appear that the curvature of the mesophase has a strong influence on its stability such that SmA phases are destabilised to a greater extent than cubic phases; the Col_h phase is then by far the most stable mode of self-organisation. This behaviour almost certainly arises due

to the steric requirements of the anion, which can be more readily incorporated into the structure of the Col_h phase. In no neutral compound is stabilisation of the columnar phase ever observed.

The triflimide salts are quite different again and only a single mesophase was formed by all homologues in this series. The nature of this mesophase is still unclear, but diffraction patterns show two-dimensional order that is consistent with the formation of a ribbon phase with rectangular symmetry. However, correlations along the second dimension are evidently weak as X-ray diffraction patterns show only one low-intensity reflection that does not correspond to a lamellar periodicity. The most likely explanation for this is a collapse of the lamellar structure due to the more charge disperse triflimide anion that results in the formation of ribbons. From the parameters extracted from diffraction studies, these ribbons likely comprise of a single cation-anion pair.

5. Experimental

5.1. Polarised Optical Microscopy (POM)

Liquid crystal textures were observed using an Olympus BX50 Optical Microscope equipped with a Linkam Scientific LTS350 heating stage, Linkam LNP2 cooling pump and a Linkam TMS92 controller. Samples were prepared by placing a small amount of material (0.1 mg) onto a microscope slide which was then covered with a coverslip. The sample was then heated between crossed polarisers allowing phase transitions to be observed. Contact preparations between two different materials were conducted in much the same fashion, except that the samples were placed directly next to each other on the microscope slide and allowed to mix when melted.

5.2. Differential Scanning Calorimetry (DSC)

Calorimetry scans were run on a Mettler Toledo DSC822e, (running on a Stare software) equipped with a TSO801R0 sample robot and calibrated using pure indium. Samples were run at heating/cooling rates of 5 °C min^{-1}. DSC data mentioned in this chapter are onset temperatures from the first heating cycle.

5.3. Small-Angle X-ray Scattering (SAXS)

Small angle X-ray scattering was performed using a Bruker D8 Discover equipped with a temperature controlled, bored graphite rod furnace, custom built at the University of York. The radiation used was copper Kα (λ = 0.154056 nm) from a 1 µS microfocus source. Diffraction patterns were recorded on a 2048x2048 pixel Bruker VANTEC 500 area detector set at a distance of 127 mm from the sample. Samples were filled into 0.9 mm capillary tubes. Two-dimensional diffraction patterns were collected every 10 °C on heating to the isotropic liquid and subsequent cooling to room temperature at a rate of 10 °C min^{-1}. The data were then processed using Origin.

6. References

1   K. Goossens, K. Lava, C. W. Bielawski and K. Binnemans, *Chem. Rev.*, 2016, **116**, 4643–4807.

2   H. Shimura, M. Yoshio, K. Hoshino, T. Mukai, H. Ohno and T. Kato, *J. Am. Chem. Soc.*, 2008, **130**, 1759–1765.

3   M. Yoshio, T. Mukai, H. Ohno and T. Kato, *J. Am. Chem. Soc.*, 2004, **126**, 994–995.

4   K. Tanabe, T. Yasuda, M. Yoshio and T. Kato, *Org. Lett.*, 2007, **9**, 4271–4274.

5   P. K. Bhowmik, H. Han, J. J. Cebe, R. A. Burchett, B. Acharya and S. Kumar, *Liq. Cryst.*, 2003, **30**, 1433–1440.

6   B. Donnio and D. W. Bruce, *New J. Chem.*, 1999, **23**, 275–286.

7   D. W. Bruce, D. A. Dunmur, E. Lalinde, P. M. Maitlis and P. Styring, *Nature*, 1986, **323**, 791–792.

8   D. W. Bruce, S. C. Davis, D. A. Dunmur, S. A. Hudson, P. M. Maitlis and P. Styring, *Mol. Cryst. Liq. Cryst.*, 1992, **215**, 1–11.

9   G. W. Gray, B. Jones and F. Marson, *J. Chem. Soc.*, 1957, 393–401.

10   D. Demus, A. Gloza, H. Hartung, A. Hauser, I. Rapthel and A. Wiegeleben, *Krist. und Tech.*, 1981, **16**, 1445–1451.

11   H. Adams, N. A. Bailey, D. W. Bruce, S. C. Davis, D. A. Dunmur, P. D. Hempstead, S. A. Hudson and S. Thorpe, *J. Mater. Chem.*, 1992, **2**, 395.

12   D. W. Bruce, D. A. Dunmur, S. A. Hudson, E. Lalinde, P. M. Maitlis, P. Malcolm, McDonald, R. Orr, P. Styring, A. S. Cherodian, R. M. Richardson, J. L. Feijoo and G. Ungar, *Mol. Cryst. Liq. Cryst.*, 1991, **206**, 79–92.

13   D. W. Bruce, *Acc. Chem. Res.*, 2000, **33**, 831–840.

14   D. W. Bruce, B. Donnio, S. A. Hudson, A.-M. Levelut, S. Megtert, D. Petermann and M. Veber, *J. Phys. II*, 1995, **5**, 289–302.

15 B. Donnio and D. W. Bruce, *J. Mater. Chem.*, 1998, **8**, 1993–1997.

16 R.-T. Wang, G.-H. Lee and C. K. Lai, *CrystEngComm*, 2018, **20**, 2593–2607.

17 G. A. Jeffrey and L. M. Wingert, *Liq. Cryst.*, 1992, **12**, 179–202.

18 K. E. Rowe and D. W. Bruce, *J. Mater. Chem.*, 1998, **8**, 331–341.

19 P. Bonhôte, A.-P. Dias, N. Papageorgiou, K. Kalyanasundaram and M. Grätzel, *Inorg. Chem.*, 1996, **35**, 1168–1178.

20 R.-T. Wang, G.-H. Lee and C. K. Lai, *J. Mater. Chem. C*, 2018, **6**, 9430–9444.

21 P. K. Bhowmik, H. Han, I. K. Nedeltchev and J. J. Cebe, *Mol. Cryst. Liq. Cryst.*, 2004, **419**, 27–46.

22 D. W. Bruce, B. Donnio, B. Heinrich, D. Guillon, J. Kain, S. Diele and H. Allouchi, *J. Am. Chem. Soc.*, 2004, **126**, 15258–15268.

23 S. Laschat, A. Baro, N. Steinke, F. Giesselmann, C. Hägele, G. Scalia, R. Judele, E. Kapatsina, S. Sauer, A. Schreivogel and M. Tosoni, *Angew. Chem. Int. Ed.*, 2007, **46**, 4832–4887.

24 D. Fazio, C. Mongin, B. Donnio, Y. Galerne, D. Guillon and D. W. Bruce, *J. Mater. Chem.*, 2001, **11**, 2852–2863.

25 G. Pelzl, S. Diele, K. Ziebarth, W. Weissflog and D. Demus, *Liq. Cryst.*, 1990, **8**, 765–773.

26 A. I. Smirnova and D. W. Bruce, *J. Mater. Chem.*, 2006, **16**, 4299–4306.

27 A. I. Smirnova and D. W. Bruce, *Chem. Commun.*, 2002, **2**, 176–177.

28 C. Alstermark, M. Eriksson, M. Nilsson, C. Destrade and H. T. Nguyen, *Liq. Cryst.*, 1990, **8**, 75–80.

29 H. T. Nguyen, C. Destrade and J. Malthête, *Liq. Cryst.*, 1990, **8**, 797–811.

30 A. I. Smirnova, B. Heinrich, B. Donnio and D. W. Bruce, *RSC Adv.*, 2015, **5**, 75149–75159.

31   A. I. Smirnova, N. V. Zharnikova, B. Donnio and D. W. Bruce, *Russ. J. Gen. Chem.*, 2010, **80**, 1331–1340.

32   A. Riccobono, *PhD Thesis,* University of York, 2018.

33   M. Šepelj, A. Lesac, U. Baumeister, S. Diele, D. W. Bruce and Z. Hameršak, *Chem. Mater.*, 2006, **18**, 2050–2058.

34   M. Šepelj, A. Lesac, U. Baumeister, S. Diele, H. L. Nguyen and D. W. Bruce, *J. Mater. Chem.*, 2007, **17**, 1154–1165.

35   R. A. Reddy and C. Tschierske, *J. Mater. Chem.*, 2006, **16**, 907–961.

36   C. Sauer, S. Diele and C. Tschierske, *Liq. Cryst.*, 1997, **23**, 911–917.

37   G. Sigaud, F. Hardouin, M. F. Achard and A. M. Levelut, *J. Phys.*, 1981, **42**, 107–111.

38   I. Krossing, J. M. Slattery, C. Daguenet, P. J. Dyson, A. Oleinikova and H. Weingartner, *J. Am. Chem. Soc.,* 2006, **128**, 13427-13434.

Chapter Four: Solvent-Induced Liquid Crystal Properties of the Polycatenar *N*-Phenylpyridinium Ions

1. Introduction

Chapter Three discussed the thermotropic mesomorphism of a series of *N*-phenylpyridinium ions and their behaviour has been compared to the formally ionic polycatenar stilbazole complexes of silver(I). Some years ago, Smirnova and Bruce reported the solvent-induced liquid crystal properties of these silver(I) salts in a variety of solvents:[1,2] these included apolar alkanes, aliphatic alcohols and small polar aprotic solvents (MeCN, DMSO, DMF). This study was the first to document the solvent-induced liquid crystal properties of a polycatenar material and a number of induced mesophases were observed that demonstrated well the amphiphilic nature of the silver(I) salts. This chapter will document the solvent-induced properties of the newly prepared *N*-phenylpyridinium ions.

1.1. Lyotropic liquid-crystal phases

Lyotropic mesomorphism is brought about by changing the concentration of the mesogenic species in a solvent (usually water or another polar solvent) and three general types of lyotropic behaviour are normally identified: surfactant,[3] polymeric[4] and chromonic.[5,6] Surfactant lyotropic behaviour has been extensively covered in the Introduction chapter.

1.1.1. Polymeric lyotropic behaviour

This type of lyotropic behaviour is in fact not confined to polymers, but also describes that of rigid anisometric rods in solution. Thus, rod-shaped polymers form nematic phases in solution (aqueous or non-aqueous) due to a favoured gain in entropy. The theory that hard rods could self-organise in solution to give rise to a nematic phase was first proposed by Onsager in 1949.[7] The theory assumes that rods can arrange in an isotropic fashion at low concentrations, yet, as their concentration increases, maintaining an isotropic distribution of the rods becomes increasingly difficult due to mutual repulsions. Thus, a phase transition occurs to a more ordered state that is purely dependent on concentration; the rods are oriented in roughly the same direction and the lyotropic nematic phase forms. This transition is driven by a change in entropy (assuming there are no intermolecular interactions, which is of course almost impossible to achieve in reality). It seems counterintuitive that forming a more ordered state actually results in an increase in entropy, but it is the minimisation of the excluded volume on forming the nematic phase that increases the translational entropy of the system. This theory holds true extremely well in practice. DNA,[8]

cellulose[9] and viruses such as the tobacco mosaic virus[10,11] are all examples of this type of mesomorphism. DNA in fact forms a multiple mesophases in solution with the identity of the phase being dependent on concentration. At dilute DNA concentrations in water the chiral nematic phase forms, but highly concentrated samples in the region of 250 mg ml^{-1} form a two-dimensional mesophase initially thought to be smectic[12] and now known to be hexagonal as demonstrated by Livolant *et al*.[13]

1.1.2. Chromonic behaviour

Chromonic behaviour is a field of lyotropic liquid-crystalline behaviour that has only really been explored over the past five decades.[4,5] The chemical components of chromonic liquid-crystalline phases tend to be flat or board-like, often aromatic molecules that contain ionic or polar functionalities on the periphery to aid solubility in water. In fact, ionic dyes[5] and drug molecules[5] were among the first compounds discovered to display chromonic behaviour and two examples are presented in Figure 4.1. These species self-organise to form columns in aqueous solution due to π-π interactions and van der Waals forces between neighbouring molecules. As such, the formation of chromonic aggregates is an enthalpically driven process unlike the aggregation of surfactants into micelles, a process that has an entropic driving force.[14] These columns can then form nematic (N) or hexagonal columnar (M) arrangements in water, and so the mesogenic moiety is not the aromatic molecule but the columnar aggregate of a number of molecules stacked on top of one another (see the structure of these phases formed in Figure 4.2). In many ways, chromonic behaviour closely resembles the thermotropic mesomorphism of disc-like molecules where the flexible aliphatic chains of the discotic mesogen are analogous to the solvent.
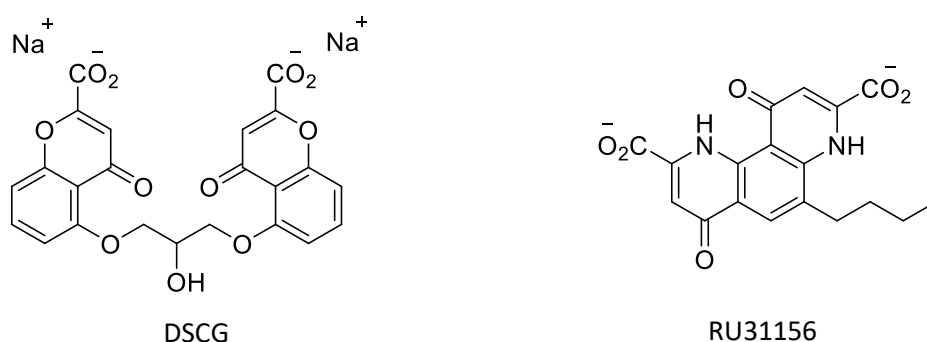
Figure 4.1. Structure of the anti-asthmatic drug disodium cromoglycate (DSCG) and the anti-allergy drug RU31156, both of which demonstrate chromonic behaviour.

153
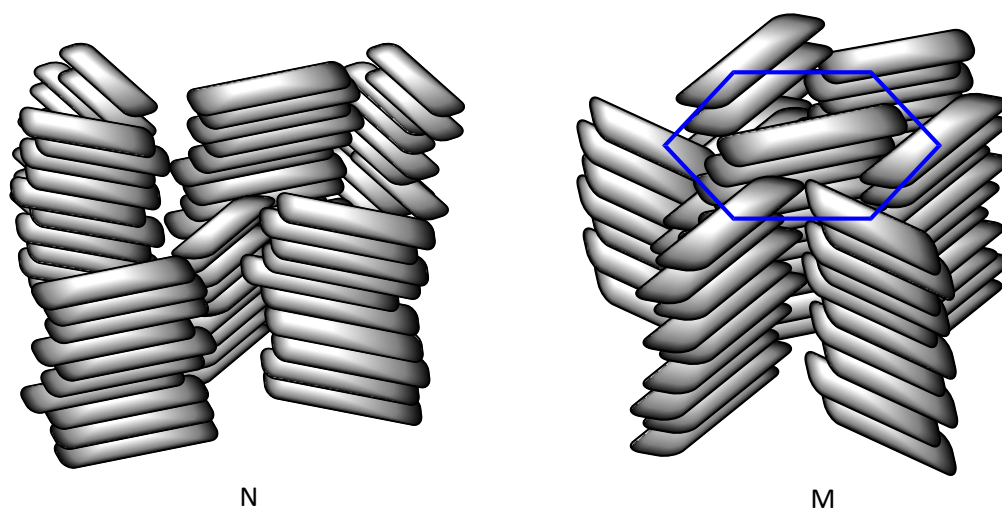
Figure 4.2. Structure of the chromonic nematic (N) phase and columnar hexagonal (M) phase.

Unlike the lyotropic behaviour of surfactants, there is no analogous critical micelle concentration for chromonics and good evidence now exists for the formation of chromonic aggregates in dilute solution (before the manifestation of liquid crystal properties). Interestingly, because the mesomorphism of chromonic systems does not depend on flexible aliphatic chains, the mobility of the liquid crystal phase is often supressed only on the freezing of water.

1.2. Lyotropic behaviour in non-polar solvents

It is much less common for lyotropic liquid crystal phases to form in apolar solvents such as long-chain alkanes and cyclic hydrocarbons. Usol'tseva *et al.* have, however, probed the effects of added alkanes on some discotic mesogens (organometallic[15–17] and organic[18]) and found that a number of mesophases can be induced. The first compounds studied were a series of tetrapalladium organyls[15] with a board-like molecular shape (see structure in Figure 4.3). Thermotropically, these materials displayed a columnar oblique phase and one other mesophase that was highly birefringent but could not be assigned. However, on the addition of long-chain alkanes from heptane to icosane, solvent-induced mesomorphism was observed. A phase diagram was constructed for the compound with *n* = 12 and X = chloro with pentadecane (Figure 4.3), and at very low solvent concentration, the columnar oblique phase persisted. On increasing the concentration of pentadecane this mesophase then transformed to a columnar nematic mesophase and eventually to an isotropic phase (always separated by biphasic regions). Therefore, the addition of non-polar solvent molecules to the already mesomorphic *tetra*-palladium organyls either allowed the

mesophase displayed by the dry material to persist, or induced a new mesophase altogether. Similar results were obtained with the platinum congeners and the bridging groups were either chloro, bromo, iodo or isocyanato.[19,20] This behaviour is, therefore, not limited to a select combination of the metal and bridging group, but instead seems to be a characteristic common to disc-shaped metallomesogens in general. In fact, metallomesogens are not the only disc-like molecules to display lyomesomorphism in apolar solvents as is now described.
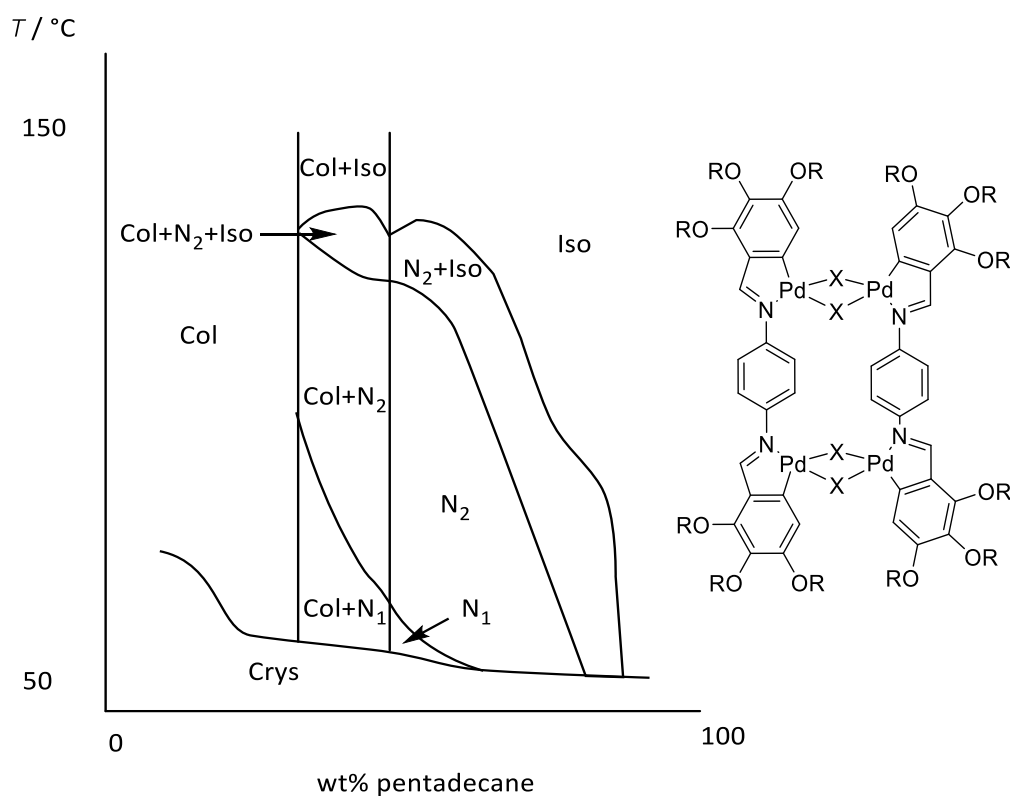
Figure 4.3. Phase diagram and general structure of the tetrapalladium organyls with a board-like shape.

Usol'tseva and Praefcke[18] also studied the behaviour of a series of hexaesters of hexahydroxybenzene and cyclohexane in a range of non-polar solvents and the results from this study were particularly interesting. The general structures of the two series of hexaesters are presented in Figure 4.4 – compound **1**-*n* possesses a phenylene core and **2**-*n* a cyclohexyl core. The thermotropic mesomorphism of both series is dominated by the formation of Col_h mesophases, as would be expected for conventional, disc-shaped mesogens. The columnar phases formed by the hexahydroxybenzene esters are disordered, whereas those formed by the cyclohexyl esters are ordered. However, their different behaviour in response to added solvent is extremely interesting,

and the lyomesomorphism of series **2**-*n* (with cyclohexyl cores) is much richer than that of series **1**-*n* (with phenylene cores). For example, **2**-*5* to **2**-*11* showed the induction of nematic and hexagonal columnar mesophases (of the chromonic type) with linear alkanes from heptane to hexadecane; whereas there was no induction for series **1**-*n* with any linear alkane. This behaviour was observed due to the weaker intra-columnar interactions in the case of the hexahydroxybenzene esters due to the thinner, planar aromatic core that results in poorer space filling effects between neighbouring molecules within the columns. This was explained as weaker core-core interactions and consequently a reduction in intramolecular contact within the columnar aggregates, which is also the reason why series **1**-*n* form disordered Col$_h$ phases in the thermotropic sense. Thus, the addition of solvent molecules to the weakly segregated columns of **1**-*n* completely disrupts liquid-crystalline self-organisation; the solvent molecules intercalate with the peripheral chains grafted to core of series **2**-*n* and allows the hexagonal columnar phase to persist. Due to the stronger core-core interactions in this series, the addition of more solvent does eventually overcome the inter-columnar interactions (the interactions between columnar aggregates) but the intra-columnar interactions (between stacked molecules) remain intact and a chromonic nematic phase then forms.
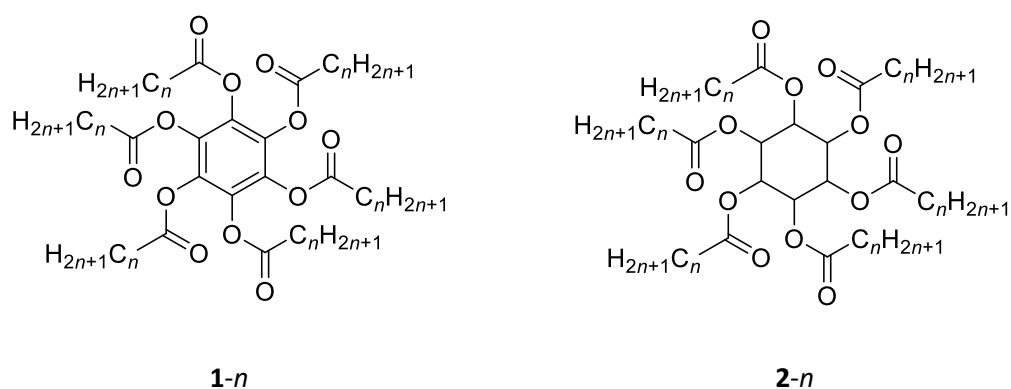
Figure 4.4. Structures of the hexahydroxybenzene hexaesters **1**-*n* and the scyllitol hexaesters **2**-*n* where *n* represents the number of carbon atoms in the aliphatic chains.

However, series **1**-*n* do show induced mesomorphism on the addition of some cyclic hydrocarbon and aromatic solvents and it had already been demonstrated before this study that **1**-*5* forms a lyotropic columnar hexagonal phase on the addition of benzene.[21] In fact, all of the hexahydroxy esters from **1**-*5* to **1**-*11* also displayed an induced hexagonal columnar phase with benzene and with other cyclic solvents that included cyclohexane and cyclohexene. This demonstrated that

aromaticity of the solvent was not required in order for series **1**-*n* for form induced mesophases in hydrocarbon solvents. What was interesting, however, was that a hexagonal columnar phase was only induced with larger cyclic solvents (cyclooctane and cyclodecane) for longer chained homologues upwards of **1**-*6*. This revealed that a certain amount of space was required between the aliphatic chains for the solvent molecules to intercalate; thus, induced phases were only formed with larger cyclic solvents where sufficient space was available between the chains (clearly, lengthening of the aliphatic chains attached to the mesogen provided this necessary space). Once more, the scyllitol hexaesters showed even richer lyomesomorphism with cyclic solvents, and an additional nematic phase (as well as hexagonal chromonic phase) was observed for all homologues upwards of **2**-*5* with cyclopentane, cyclohexane and cyclodecane. This is very much the same as that observed with linear alkanes.

It was from this work that the concept of *'internal'* and *'external'* solvent was proposed.[18] The *internal* solvent is thought of as the flexible aliphatic chains grafted to the mesogenic core and the *external* solvent is clearly the added solvent used to bring about lyotropic mesomorphism. The lyomesomorphism of the disc-shaped materials presented here is controlled by a delicate balance between the *internal* and *external* solvents.

1.3. Solvent induced mesomorphism of the stilbazole complexes of silver(I)

The solvent-induced liquid crystal properties of the disc-shaped mesogens encouraged Smirnova and Bruce to probe the effects of added solvent (external solvent) on the mesomorphism of the polycatenar silver(I) salts. These materials displayed rich mesomorphism in a range of external solvents, both polar and non-polar, due to their amphiphilic character. The results from these studies were readily interpreted by the same concepts as those that underpin the thermotropic behaviour of polycatenar liquid crystals *i.e.* interfacial curvature and space-filling.

The tetracatenar salts shown in Figure 4.5 were studied in a range of solvents including DMF, DMSO, MeOH and a range of linear alkanes and aliphatic alcohols. Tables 4.1 and 4.2 document the induced mesomorphism for a range of compounds differing in terminal chain length and anion; Figure 4.5 shows the general structure of the silver(I) salts referred to in the text.

Table 4.1. Induced mesomorphism of **3a** and **3b** in a range of solvents: phases in brackets are observed monotropically.

Solvent	3a ($n = 4$)	3b ($n = 12$)
MeCN	-	L, Cub
DMF	(L)	L, Cub
DMSO	L	L, Cub
MeOH	N, (T)	L, Cub
EtOH	(N), (L), (T)	Cub
PrOH	(Cub)	Cub
BuOH	(Cub)	Cub
Pentanol	(Cub)	Cub
Decanol	(Cub)	-
Undecanol	(Cub)	-
Thermotropic mesomorphism	None	Col_h

Table 4.2. Induced mesomorphism of **4a** and **4b** in a range of solvents: phases in brackets are observed monotropically.

Solvent	4a ($n = 4$)	4b ($n = 6$)
MeCN	L	L
DMF	L	L
DMSO	L	L
MeOH	N, L, (T)	N, L, (T)
EtOH	(N), (T)	(N), (T)
PrOH	(N), (T)	-
BuOH	(Col_h)	-
Pentanol	Col_h	-
Decanol	Col_h	Cub
Undecanol	Col_h	Cub
Thermotropic mesomorphism	Cub	Cub, Col_h
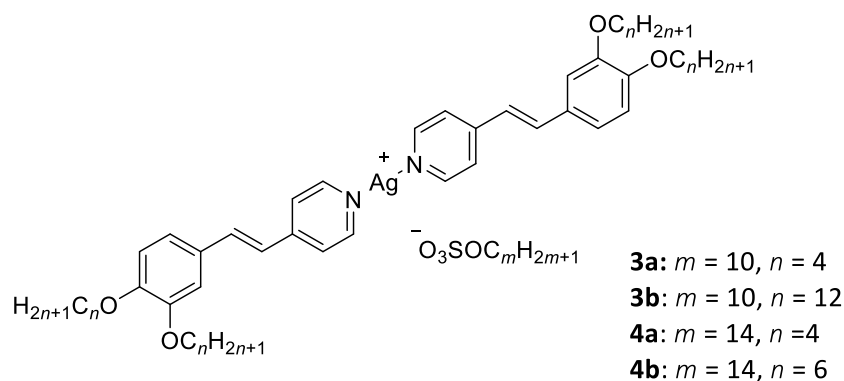
Figure 4.5. General structure of **3a**, **3b**, **4a** and **4b** studied with added solvents presented in Tables 4.1 and 4.2.

A significant observation from Table 4.1 is that added solvent was able to induce lyomesomorphism in a compound that was non-mesomorphic as a dry material. It is also clear that small polar aprotic solvents such as DMSO reduce the interfacial curvature present in **3b** to induce lamellar and cubic mesophases (recall that this compound exhibits a Col_h phase as a dry material). This is consistent with the idea of the solvent molecules locating with the charged core of the compound to increase the effective core volume, and thus accounting for a transition to a mesophase with reduced curvature at the core-chain interface. The opposite effect was observed in contact preparations with linear and cyclic hydrocarbons and the induced phases formed suggest that the solvent locates preferentially with the terminal chains. Compound **3a** is non-mesomorphic as a dry material, but the first thermotropic mesophase observed on increasing terminal chain length was cubic. The fact that all non-polar solvents presented in Table 4.3 induced a cubic mesophase supports solvent location with the aliphatic chains to increase curvature at the core-chain interface, much the same as lengthening the terminal chains in the thermotropic sense.

Table 4.3. Induced mesomorphism of **3a** in a range of non-polar solvents: monotropic mesophases are shown in brackets.

Solvent	3a (n = 4)
Heptane	(Cub)
Decane	(Cub)
Pentadecane	(Cub)
Cyclohexane	(Cub)
Cyclohexene	(Cub)
Benzene	(Cub)
Tetraline	(Cub)
Thermotropic mesomorphism	None

The behaviour in the presence of added alcohols is a little more complex and depends on the chain length of the alcohol solvent and the nature of the polycatenar mesogen in general. Higher alcohols from butanol to undecanol show behaviour that implies they can equally locate with either the chains or the core depending on the specific compound being investigated. For example, compounds **3a** and **4a** show induced cubic and hexagonal columnar phases, respectively, which indicates association of the solvent molecules with the terminal chains. Compound **3a** is non-mesomorphic as a dry material, but on lengthening of the stilbazole chains, mesomorphism is first observed in the form of a cubic phase, and so the formation of an induced cubic phase on the addition of higher alcohols suggests solvent location with the terminal chains. Compound **4a** shows a cubic phase as a dry compound; thus, the formation of a Col_h phase in contact preparations with alcohols is again consistent with solvent association with the peripheral chains.

Compounds **3b** and **4b**, on the other hand, both show induced cubic mesophases with long-chain alcohols, which would suggest solvent location with the core (these compounds both form Col_h phases as dry materials). Smirnova and co-workers rationalised this observation by the space available to the solvent molecules. Both compounds **3b** and **4b** form Col_h phases and so already possess significant interfacial curvature as dry materials. There would then be more space available by the polar core for solvent location here and so a reduction in core-chain curvature is observed. Identical behaviour was observed for the related OTf⁻ salt, **5**, in contact preparations with the alcohols presented in Table 4.4 and a reduction in the core-chain curvature was observed.[1] This is because of the small size of the triflate moiety, which leaves sufficient space besides the core for the solvent to associate here *via* the hydroxyl functionality.

Table 4.4. Structure and induced mesomorphism of compound **5**: monotropic mesophases are shown in brackets.
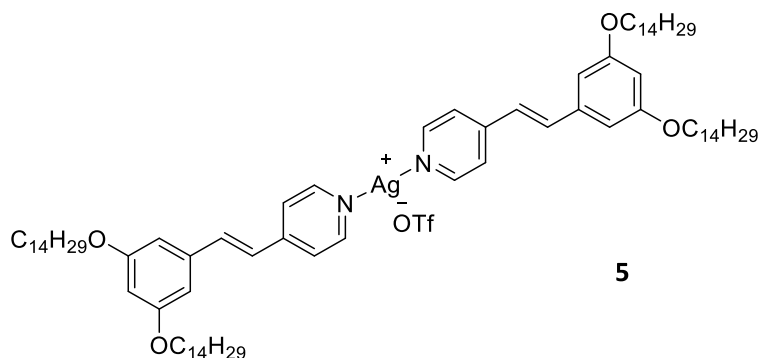
Solvent	5
Methanol	(Cub)
Ethanol	(Cub)
Propanol	(Cub)
Butanol	(Cub)
Pentanol	(Cub)
Decanol	(Cub)
Undecanol	(Cub)
Thermotropic mesomorphism	Col_h

Arguably, it is the behaviour of the silver(I) complexes in short-chain alcohols and DMSO that is most intriguing and really poises the question as to the nature of the species giving rise to the mesomorphism. The results gathered from the addition of DMSO question whether this behaviour is conventionally lyotropic or not; hence the loosely used term of solvent-induced throughout this chapter that provides less specific information as to the nature of the mesogenic moiety.

In the case of an amphiphile in water, micelles form and it is the ordering of these micelles at different concentrations that results in the formation of lyotropic liquid crystal phases.[22,23] The situation is very simple for polymeric species and it is the ordering of these rod-shaped objects in solution into a more ordered phase; thus, it is the polymer itself that acts as the mesogenic species. Chromonics are then quite similar to polymeric systems and aggregates of flat, disc-shaped molecules stacked on top of one another behave as the mesogen. It is also quite clear with the silver(I) salts that the induced mesophases formed on the addition of alkanes and (some) higher alcohols essentially swell the terminal chains and so the structure of these lyomesophases are probably similar to those formed by the dry materials.

161

In the majority of cases, MeOH and EtOH result in the formation of nematic and tetragaonal phases (in addition to, in some cases, a lamellar phase). To better understand the structure of these induced mesophases a binary phase diagram was constructed between methanol and compound **4b**, which is presented in Figure 4.6. The phase diagram displays characteristics typical of chromonic systems with transitions from L to (L+N) to N on decreasing concentration of **4b**. Also interesting was the dramatic destabilisation of the Col_h phase on the addition of only 5 wt% methanol; this corresponds to two solvent molecules per mesogen. The structure of the mesophase formed is clearly very dependent on the concentration of solvent, or, in other words, the nature of the mesogenic species is dynamic and changes with concentration. Bruce and co-workers actually classified this behaviour as conventionally lyotropic due to the similarities with typical chromonic systems and postulated that long aggregates formed with solvent molecules located between the cores of stacked molecules to form a hydrogen-bonded chain or column. At very low concentrations in methanol the complexes simply dissolve, then, as their concentration increases, aggregates do form that expel solvent molecules leading to an increase in entropy.
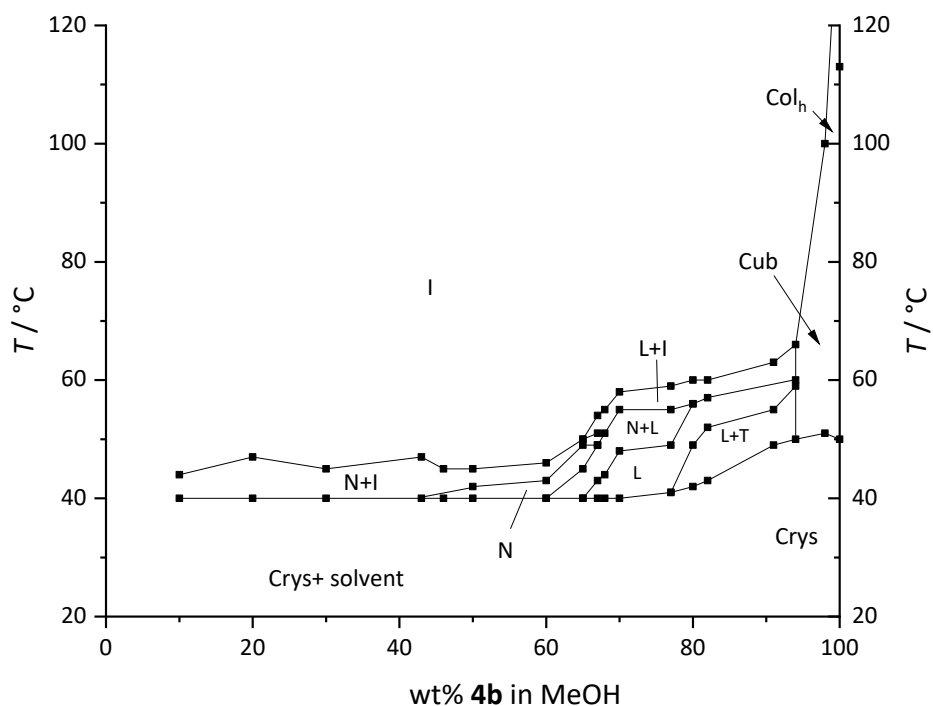
Figure 4.6. Phase diagram of **4b** in methanol.

162

This behaviour does, however, contrast the shape of the phase diagram seen in DMSO as presented in Figure 4.7. In this case, the addition of DMSO does initially destabilise the Col_h phase observed in the dry material in that cubic and lamellar phases are formed on increasing temperature. However, increasing the concentration of DMSO further does not change the form of the phase diagram after about 10 %wt (all the way to 90 %wt). The addition of 10 %wt DMSO represents two solvent molecules per complex, much the same as 5 wt% MeOH also represents two solvent molecules per complex and this is the point at which maximum destabilisation of the Col_h phase occurs in both cases. However, as the shape of the phase diagram in DMSO is invariant with composition thereafter, the tendency was to assign this behaviour to the thermotropic mesomorphism of a solvated species; this is not conventionally lyotropic. This is consistent with the idea that DMSO molecules essentially swell the charged core of the complex to remove the imbalance between core and chain volumes.
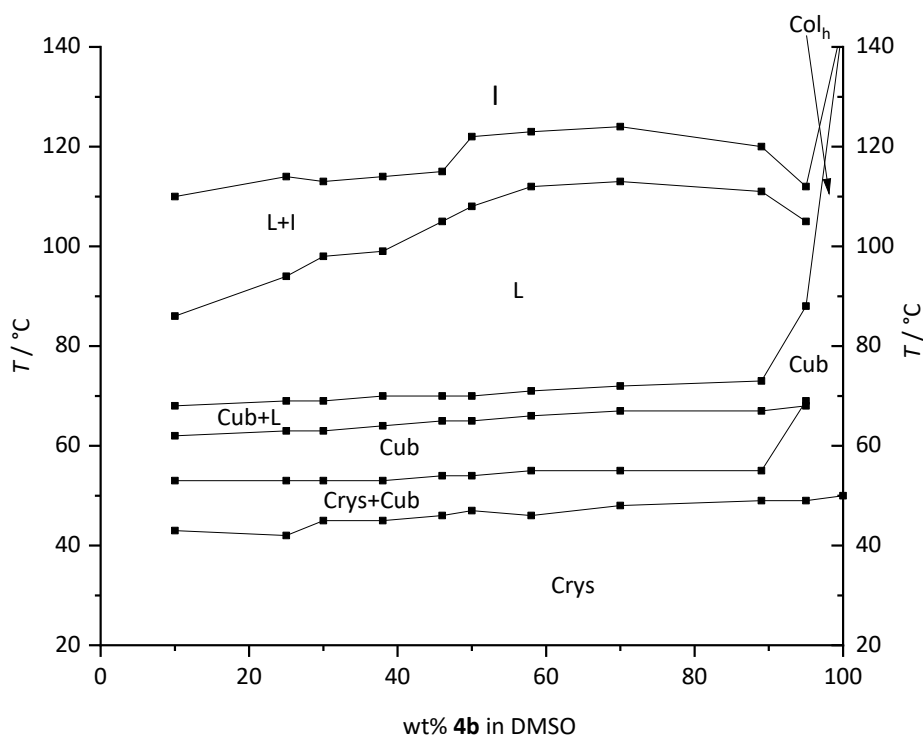
Figure 4.7. Phase diagram of **4b** in DMSO.

2. Results

To better understand the driving forces behind liquid crystal self-assembly on the addition of external solvent, contact preparations between the polycatenar *N*-phenylpyridinium ions and a range of solvents (much the same as those probed with the silver(I) salts) were performed. In two cases, binary phase diagrams were also plotted and these results are reported herein. Mesophase identification was achieved through polarising optical microscopy, and, in some cases, small-angle X-ray scattering (SAXS).

2.1. Triflate compounds

The triflate series were the first studied and the results from contact preparations performed between compounds **11**-*12* and **11-***16* are presented in Table 4.5. The same numbering system for the *N*-phenylpyridinium ions has been carried over from previous chapters for the sake of consistency.

Table 4.5. Induced mesomorphism of compounds **11**-*12* and **11**-*16* in a range of solvents: () indicates that the mesophase is observed monotropically.
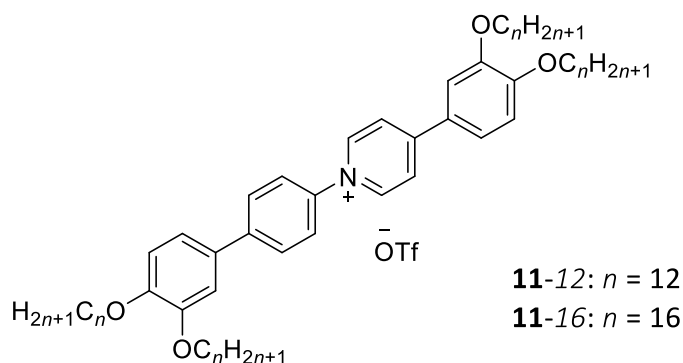
11-*12*: $n = 12$
11-*16*: $n = 16$

Solvent	**11**-*12* ($n = 12$)	**11**-*16* ($n = 16$)
Decane	-	-
Dodecane	-	-
Methanol	-	-
Ethanol	-	-
Propanol	-	-
Butanol	-	-
Hexanol	-	-
Octanol	-	-
Nonanol	-	-
Decanol	(Col$_h$)	-
Dodecanol	(Col$_h$)	-
Tetradecanol	(Col$_h$)	-
Pentadecanol	(Col$_h$)	-
DMSO	-	SmA
DMF	-	-
Thermotropic mesomorphism	SmA	Col$_h$

Compound **11**-*12* displays a SmA phase as a dry material, but in higher alcohols upwards of decanol, an induced Col$_h$ phase is formed. However, the Col$_h$ phase formed in contact preparations between **11**-*12* and higher alcohols appears only monotropically.

A binary phase diagram was plotted for mixtures of compound **11**-*12* and dodecanol and is presented in Figure 4.8. Significant destabilisation of the SmA phase was observed on the addition of 5 wt% dodecanol after which point the mesophase observed is Col$_h$. The Col$_h$ phase existed over a narrow concentration range of 80-95 wt% dodecanol and transitions from isotropic to Col$_h$ and

Col$_h$ to crystal were always accompanied by biphasic regimes, which is acceptable from the condensed phase rule for a two-component system. Below a concentration of 80 wt% dodecanol the Col$_h$ phase is supressed and only crystal and isotropic liquid phases were observed. The transition temperatures remained fairly constant across all compositions forming the Col$_h$ phase.

DSC was able to detect the formation of the Col$_h$ phase on cooling in mixtures containing 87 and 91 wt% **11**-*12*; an example DSC trace is presented in Figure 4.9. However, X-ray diffraction could not detect the hexagonal lattice of the columnar phase and only a single reflection was ever detected. The optical texture of this phase was characteristically Col$_h$ as shown in Figure 4.11 (**a**) and so this is the assignment given.
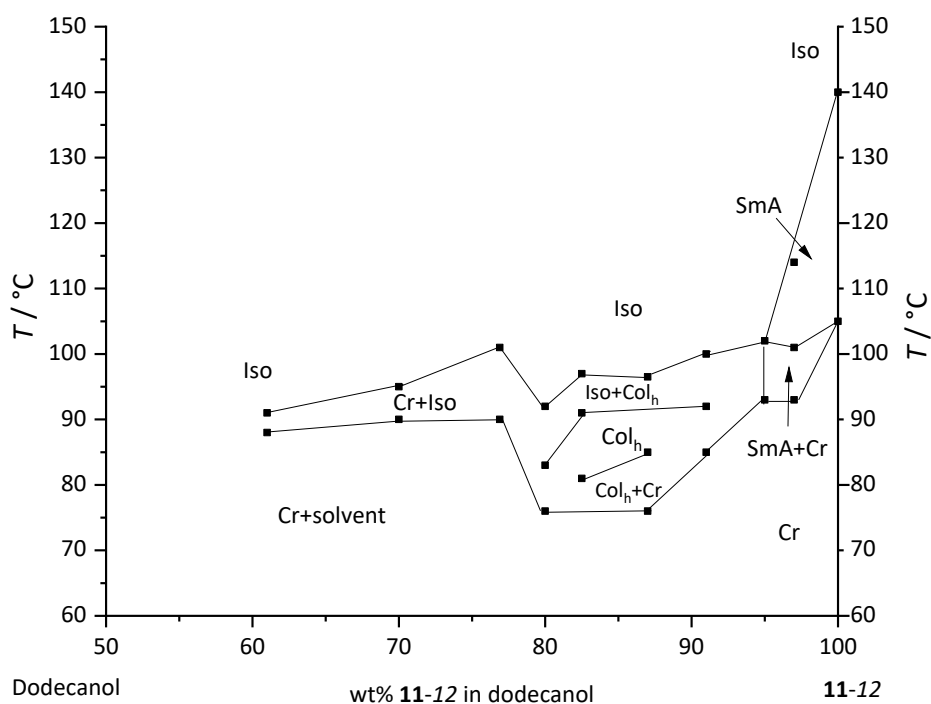
Figure 4.8. Phase diagram between compound **11**-*12* and dodecanol on cooling (mesomorphism is only observed monotropically).
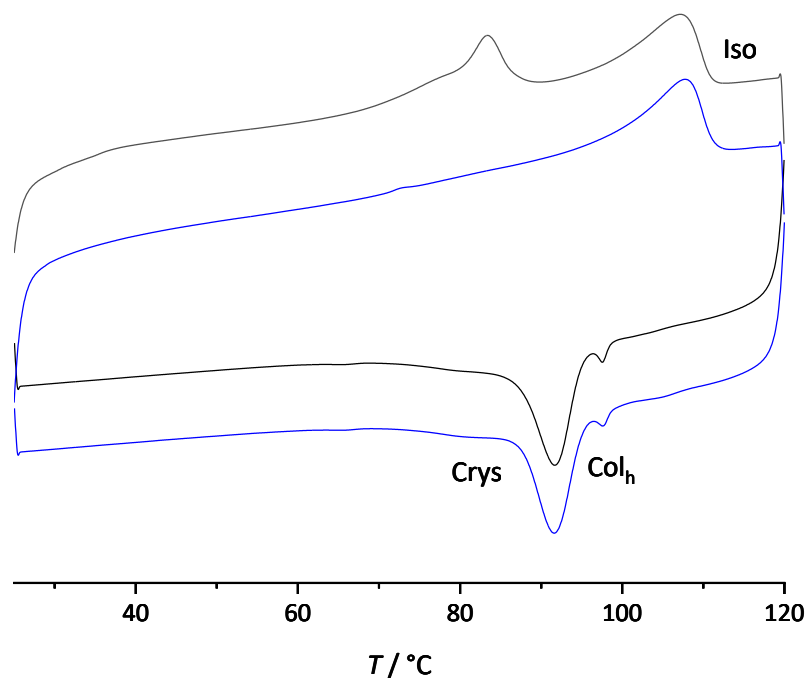
Figure 4.9. DSC trace showing induced Col_h phase on cooling in a mixture of 91 wt% **11**-*12* and dodecanol: first heat/cool cycle shown in black and second heat/cool cycle in blue.

The addition of DMSO had the opposite effect and behaviour consistent with an increase in core volume was observed; contact preparations between compound **11**-*16* and DMSO induced an enantiotropic SmA phase (this compound is Col_h as a dry material). No induction was observed with acetonitrile due to its volatility and the solvent evaporated too rapidly above 70 °C. Much the same was true for methanol, ethanol and propanol.

A binary phase diagram was constructed between compound **11**-*16* and DMSO and is presented in Figure 4.10. The Col_h phase exists down to 70 wt% **11**-*16* after which a SmA phase appeared that persisted down to 25 %wt. The SmA phase may in fact be formed by mixtures below 25 %wt **11**-*16*, but mixtures at such a low concentration of the mesogen were difficult to prepare accurately due to the small amount of compound required. The melting and clearing points were significantly reduced below 80 %wt, after which point the form of the phase diagram remained broadly the same, with perhaps a small decrease in the clearing point on moving from 50 to 35 %wt **11**-*16*. Transitions from crystal to SmA and SmA to isotropic were always accompanied by the formation

of biphasic regimes. The shape of the phase diagram presented in Figure 4.10 is broadly similar to that of the silver(I) salt, **5b**, in DMSO as shown in Figure 4.7.
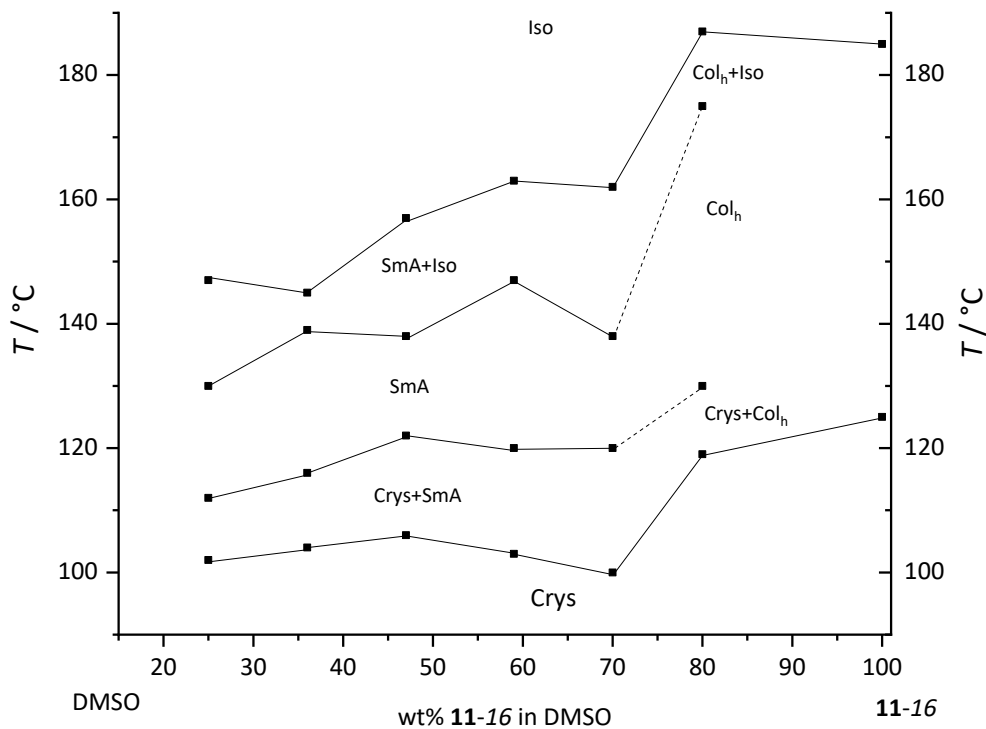
Figure 4.10. Binary phase diagram between compound **11**-*16* and DMSO*.

An interesting observation from Table 4.5 is that no linear alkanes induced lyomesomorphism in compounds **11**-*12* or **11**-*16* – in fact, no compound with a triflate anion showed any induction on the addition of linear alkanes. This could well be an effect of the OTf⁻ anion as no induction was achieved in contact preparations between the silver(I) triflates and alkanes – only the silver(I) alkylsulfates formed induced mesophases in contact preparations with linear alkanes. This point will be addressed in the discussion.
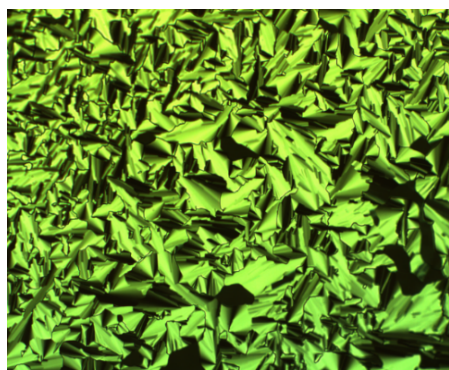
(a)
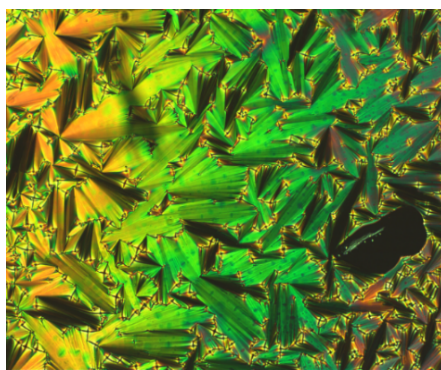
(b)
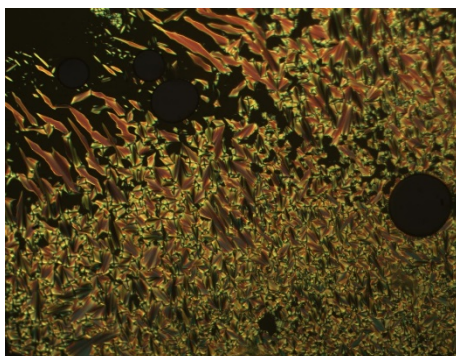
(c)
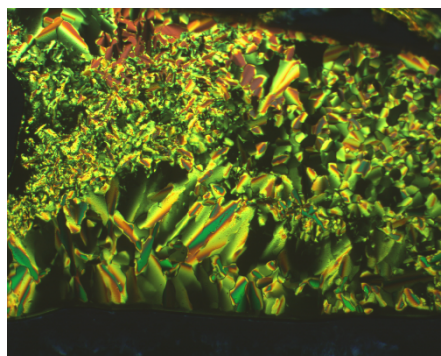
(d)

Figure 4.11. Photomicrographs of (**a**) the induced Col$_h$ phase in contact preparations between **11**-*12* and dodecanol at 90 °C on cooling, (**b**) induced SmA phase in contact preparations between *11*-16 and DMSO at 105 °C on cooling, (**c**) thermotropic SmA phase formed by **11**-*12* and (**d**) thermotropic Col$_h$ phase formed by **11**-*16*. Textures are at x10 magnification.

2.2. Alkylsulfate salts

Contact preparations performed between the alkylsulfate salts and a range of solvents suggested much the same behaviour as the triflate series and these results are presented in Table 4.6. Small polar solvents such as DMSO and DMF (and in one case MeCN) induced lamellar mesomorphism in materials that were cubic or Col_h in the thermotropic sense. The opposite effect was observed in higher alcohols and these solvents induced a Col_h phase with greater interfacial curvature than that displayed by the dry compound, consistent with location of the solvent molecules with the aliphatic chains of the mesogen.

Table 4.6. Induced mesomorphism for compounds **27**-*8*, **28**-*8*, **27**-*10* and **28**-*10* in a range of solvents: () represents a mesophase observed monotropically.

27-*8*: $n = 8$, $m = 8$
28-*8*: $n = 8$, $m = 12$
27-*10*: $n = 10$, $m = 8$
28-*10*: $n = 10$, $m = 12$
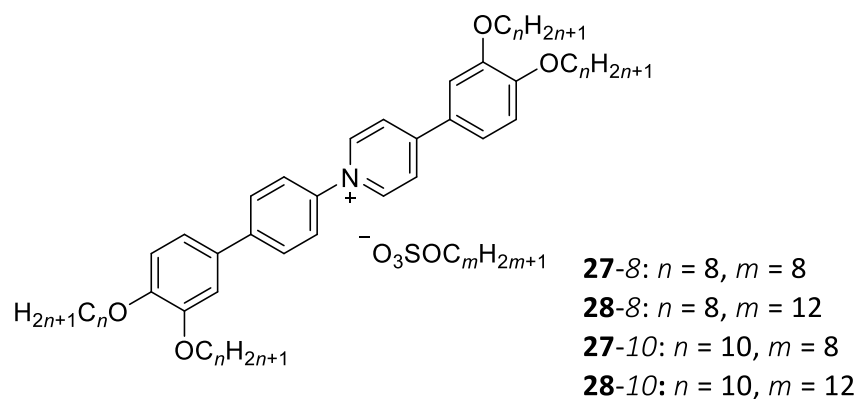
Solvent	**27**-*8* ($n = 8$, $m = 8$)	**28**-*8* ($n = 8$, $m = 12$)	**27**-*10* ($n = 10$, $m = 8$)	**28**-*10* ($n = 10$, $m = 12$)
Decane	-	-	Col_h	Col_h
Dodecane	-	-	Col_h	Col_h
Pentadecane	-	-	Col_h	Col_h
Propanol	(Col_h)	Col_h	Col_h	Col_h
Butanol	Col_h	Col_h	Col_h	Col_h
Decanol	Col_h	Col_h	Col_h	Col_h
MeCN	-	-	(SmA)	-
DMF	-	(SmA)	(SmA)	(SmA)
DMSO	-	SmA	SmA	SmA
Thermotropic mesomorphism	SmA, (Cub)	SmA, Cub	SmA, Cub	Cub, Col_h

X-Ray scattering experiments were able to detect the hexagonal symmetry of the columnar phases induced by some alcohols as evidenced by Figure 4.12 (**a**), which shows a diffraction pattern typical of a Col_h phase induced in **28**-*10* with 30 wt% decanol. Even though compound **28**-*10* displays a Col_h phase as a dry material, a thermotropic cubic phase exists below the Col_h phase that was totally suppressed on the addition of higher alcohols. Figure 4.12 (**a**) was recorded at 55 °C on the first heating cycle, at which point the dry compound would be crystalline and so the Col_h phase displayed at this temperature has been induced by the solvent. This actually represents a rather interesting situation as the structural parameters of the thermotropic Col_h phase can be compared against those of the solvent-induced Col_h phase displayed by the same mesogen. Surprisingly, the columnar lattice parameter of the induced mesophase is 4.3 Å smaller than that of the dry compound as shown in Table 4.7. There also appears to be no appreciable difference between the full width half maxima (fwhm) of the d_{10} reflections between the dry and solvent induced Col_h phases (Figure 4.12 (**b**) and (**c**)).

Table 4.7. Diffraction data for compound **28**-*10*, showing how the *a* parameter varies with decanol.

Decanol concentration / wt%	d_{10} / Å	d_{11} / Å	*a* Parameter / Å	*Mesophase*
0	31.1	17.9	35.9	Col_h
30	27.4	15.8	31.6	Col_h

However, in contrast to the behaviour of the triflate salts, linear alkanes do now induce lyomesomorphism (in some compounds), which is consistent with increasing the effective chain volume; compounds that are SmA or cubic as dry materials form Col_h phases on the addition of alkanes. Thus, the lack of induction by linear alkanes in the triflate series is clearly a function of the anion. Compound **27**-*10* forms an induced Col_h phase in contact preparations with decane up to pentadecane. Compound **28**-*10* also forms an induced Col_h phase in contact preparations with alkanes from decane to pentadecane. As mentioned above, **28**-*10* displays cubic and Col_h phases as a dry compound, but much like the behaviour of this compound in higher alcohols, the cubic phase was totally suppressed on the addition of alkanes and so a change in mesomorphism has been induced.

It is interesting, however, that no induction was observed for compound **27**-*8* with any linear alkane, and bi-phasic regions of SmA + isotropic are observed on heating along with cubic + isotropic on cooling; these are the same mesophases formed by the dry material. Recall here that compound

27-*8* forms only a cubic mesophase on cooling from the isotropic liquid, and the SmA phase is only ever observed on a heating cycle. As such, no induction was observed in contact preparations with linear alkanes. Similarly, no induction with linear alkanes was observed for compound **28**-*8* (also with octyloxy chains).
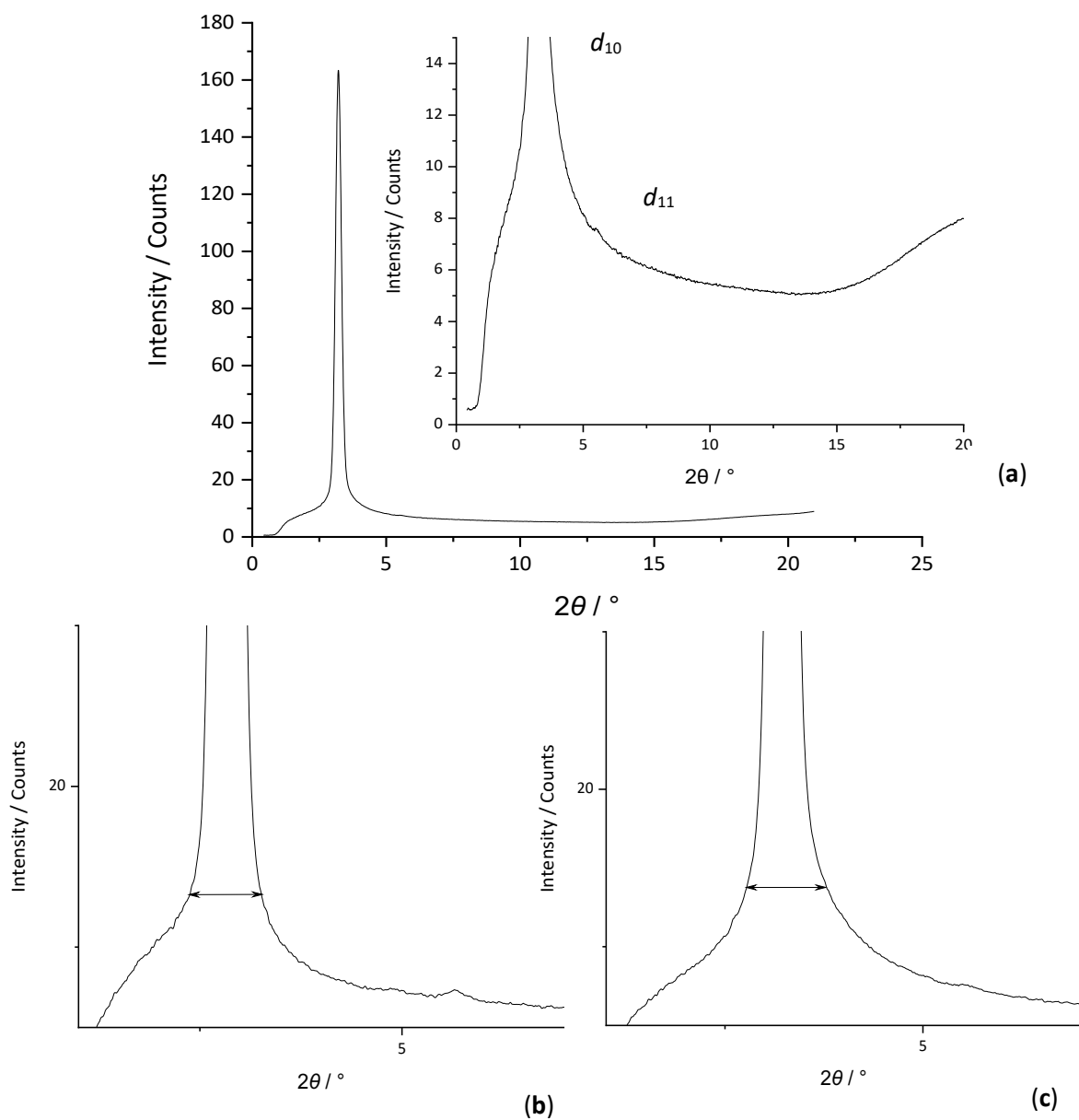
Figure 4.12. Diffraction pattern of (**a**) the induced Col$_h$ phase between compound **28**-*10* and 30 wt% decanol at 55 °C on the first heating cycle, (**b**) the fwhm of the d_{10} reflection in the dry compound and (**c**) the fwhm of the d_{10} reflection in the solvent induced phase at 30 wt% DMSO.
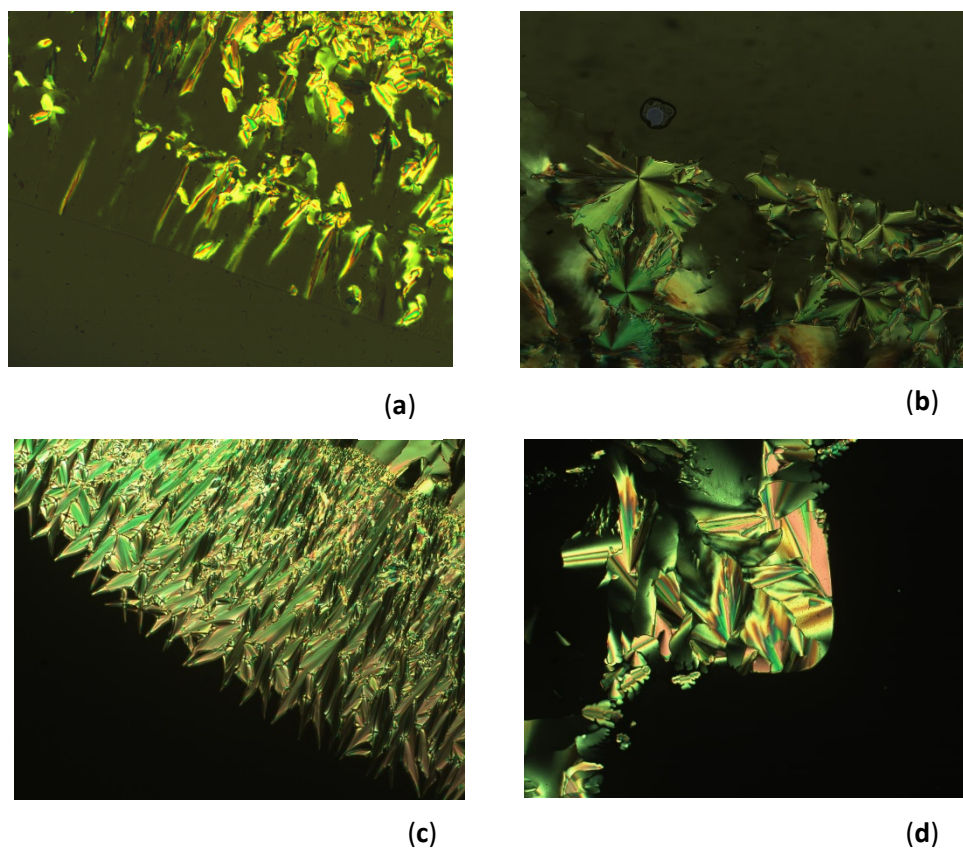
Figure 4.13. Photomicrograph of (**a**) the Col_h phase induced in contact preparations between **27**-*10* and decane, (**b**) the induced Col_h phase between **28**-*10* and decane, (**c**) the induced SmA phase between **28**-*10* and DMF and (**d**) the induced Col_h phase between **27**-*8* and decanol. Textures are at x10 magnification.

It seems odd that compounds with octyloxy chains do not form induced mesophases with alkanes whereas those with decyloxy chains do. To investigate this effect further, contact preparations were performed between compound **27**-*6* (with hexyloxy chains). Compound **27**-*6* displays a SmA phase as a dry material, whereas the addition of alkanes from octane to pentadecane induced a cubic mesophase, albeit monotropically. A photomicrograph of this cubic phase induced in contact preparations with decane is presented in Figure 4.14. It is extremely difficulty to capture the viscosity of the cubic phase on the polarising microscope, but on close inspection of Figure 4.14 a boundary can be seen where the viscous cubic phase meets the isotropic liquid on decreasing concentration of **27**-*6*; the photo in Figure 4.14 has been enlarged for clarity. The SmA phase can even be seen (top left of Figure 4.14) where the concentration of decane is lowest.

Table 4.8. Structure and induced mesophases formed in contact preparations with compound *27-6*: () represents a mesophase that is observed only monotropically.
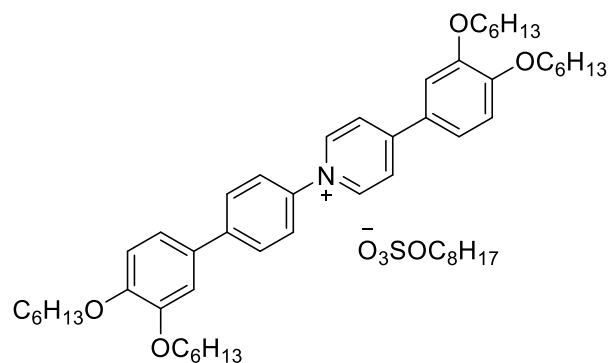
Solvent	27-6
Octane	(Cub)
Decane	(Cub)
Dodecane	(Cub)
Pentadecane	(Cub)
Decanol	Col$_h$
Thermotropic mesomorphism	SmA

Boundary between Iso and Cub
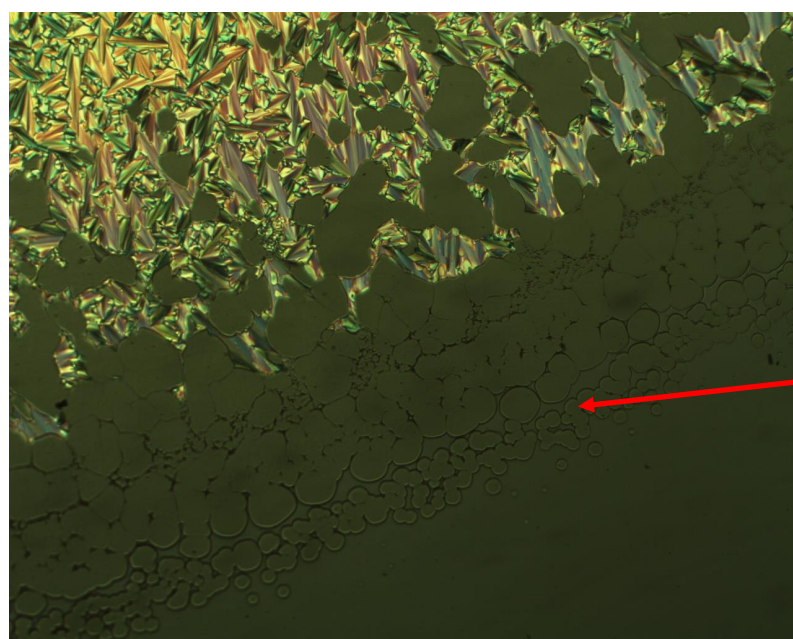
Figure 4.14. Photomicrograph (with polarised uncrossed slightly) of the induced cubic phase in contact preparations between *27-6* and doecane: *T* = 35 °C on cooling.

Once more, higher alcohols such as decanol induced an enantiotropic Col$_h$ phase in compound **27**-*6*. The hexagonal symmetry of the induced columnar phase between a mixture of **27**-*6* and decanol at 13 %wt solvent could be detected by X-ray scattering as evidenced by Figure 4.15. Unlike the induction of a Col$_h$ phase by decanol in the case of **28**-*10*, this represents the induction of a new mesophase that does not exist in the phase sequence of the dry material.

(a)   **(b)**
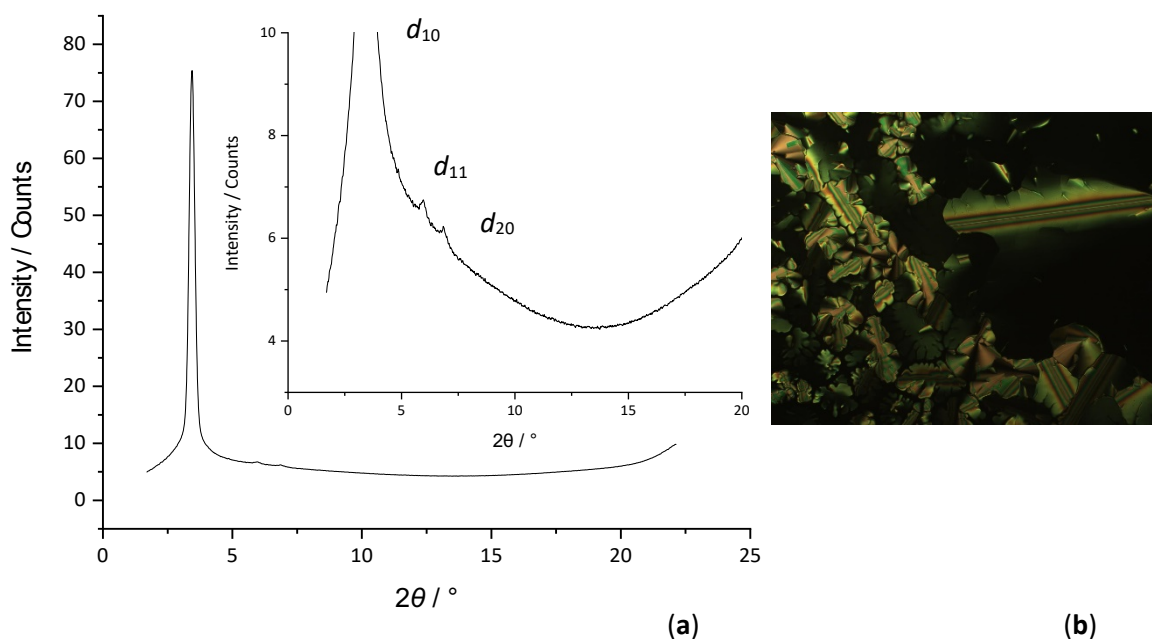
Figure 4.15. Diffraction pattern of (**a**) the induced Col$_h$ phase of compound **27**-*6* with 13 %wt decanol at 66 °C and (**b**) photomicrograph of the same phase.

2.3. NTf$_2^-$ salts

A SmA phase can be induced with all NTf$_2^-$ salts on the addition of polar aprotic solvents such as DMSO, consistent with solvent location at the polar core (Table 4.9). No induction was observed with linear alkanes or linear alcohols, and the same spherulitic texture as the dry material was observed in each case. Figure 4.16 shows a photomicrograph of the induced SmA phase on the addition of DMSO and compares the texture of this phase to that of the thermotropic Col$_r$ phase.

Table 4.9. Structure and induced mesomorphism for compound **29**-*10*.
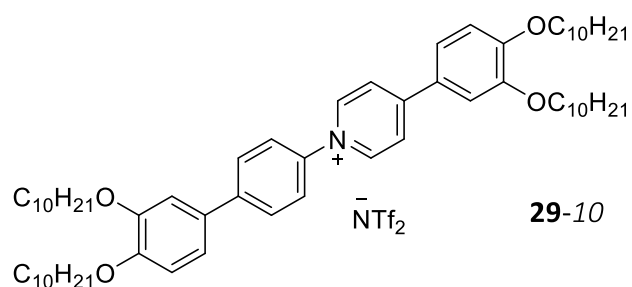
Solvent	**29**-*10*
Undecanol	-
Pentadecane	-
DMSO	SmA
Thermotropic mesomorphism	Col

X-Ray scattering experiments could be performed on mixtures of compound **29**-*10* with 30 %wt DMSO and a diffraction pattern consistent with a lamellar mode of organisation was obtained as shown in Figure 4.17; only a single reflection was observed in the small-angle regime.

(a)

(b)
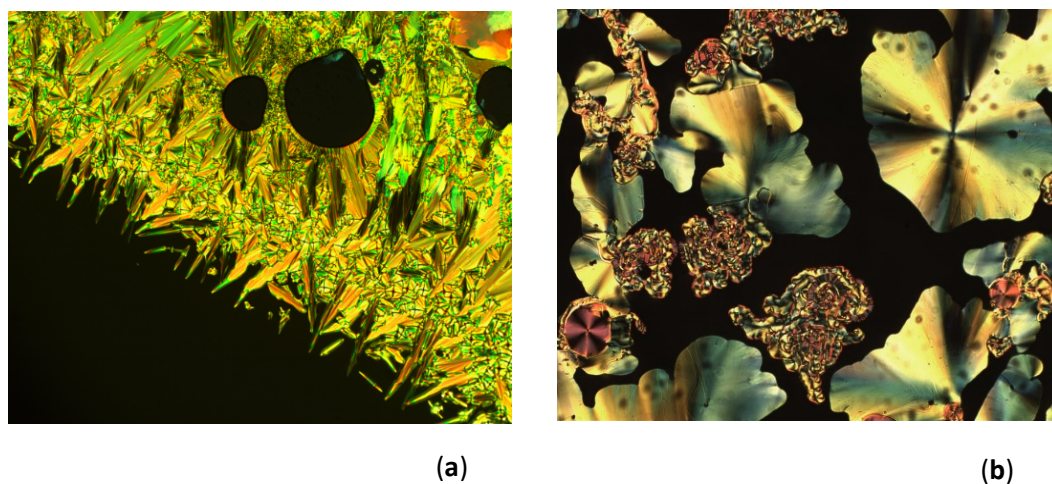
Figure 4.16. Photomicrograph of (**a**) the induced SmA phase on the addition of DMSO to compound **29**-*10*: isotropic regions (bottom left) and induced SmA phase (top right) and (**b**) thermotropic texture of the same compound. Textures are at x10 magnification.
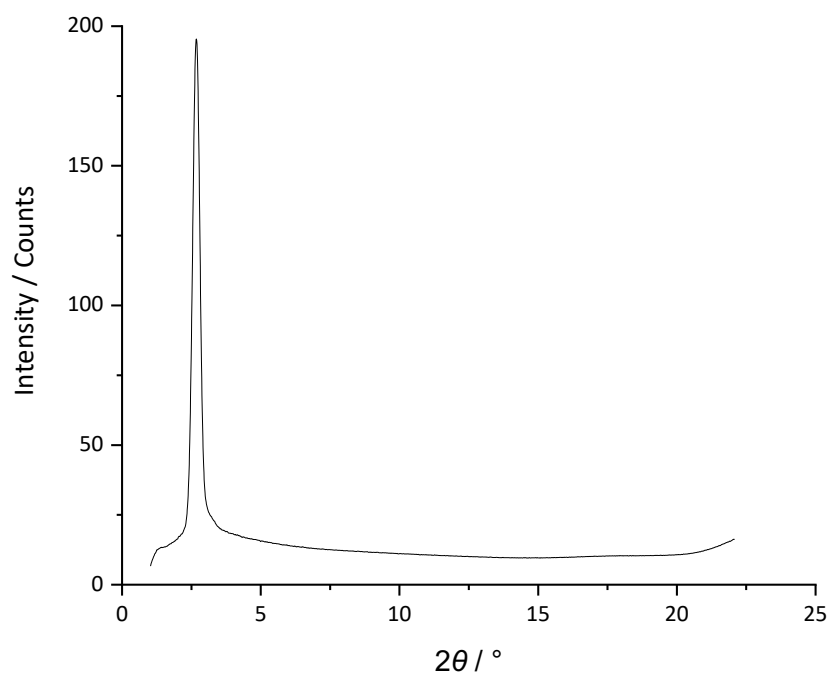
Figure 4.17. Diffraction pattern of compound **29**-*10* with 30%wt DMSO.

3. Discussion

3.1. General remarks

The formation of the induced mesophases can be explained by the principles of amphiphilicity, space-filling, interfacial curvature and incompatibility of the solvent with a certain part of the mesogen. These are very much the same driving forces as those used to explain the formation of induced mesophases between the silver(I) salts and added solvent.[1] That is, polar aprotic solvents such as DMSO and DMF locate preferentially with the charged core of the mesogen to increase the effective core volume, influencing interfacial curvature thereby to induce the formation of a lamellar phase in compounds that are cubic, Col_h or Col_r as dry materials. In contrast, higher alcohols and, in some cases, linear alkanes, locate preferentially with the aliphatic chains to increase the effective chain volume, which in turn lends a transition to a mesophase with greater curvature at the core-chain interface. The higher alcohols always induced a Col_h phase in compounds that were cubic or SmA as dry materials.

However, the effect of linear alkanes is a little different and not all mesogens that were SmA or cubic as dry compounds formed induced mesophases on their addition. Compounds **27**-*10* and **28**-*10*, for example, formed induced Col_h phases with linear alkanes from decane to pentadecane where these compounds were SmA or cubic in the thermotropic sense. Similarly, compound **27**-*6* formed an induced cubic phase on the addition of octane up to pentadecane, whereas this compound was SmA as a dry material. Compounds **27**-*8* and **28**-*8*, on the other hand, showed no induction with any linear alkane, and the same mesomorphism as the dry material was always observed (SmA and cubic phases). Much the same behaviour was true for the triflate salts and no induction with linear alkanes was ever observed. The influence of linear alkanes on the induced mesomorphism will be discussed in more detail in the forthcoming sections, but for now, where induction is observed, their behaviour is consistent with preferential location with the aliphatic chains to form a mesophase with greater curvature at the core-chain interface.

3.2. Phase diagrams

Some crucial differences exist between the induced mesomorphism displayed by the silver(I) salts and the *N*-phenylpyridinium ions and these will now be discussed. Starting with a comparison between the binary phase diagrams of compounds **4b** and **11**-*16* in DMSO shown in Figure 4.18, it is clear that the general form of the two phase diagrams is similar. Thus, the thermotropic

mesophase (Col$_h$ in both cases) is strongly destabilised on the addition of small concentrations of solvent, and at a certain point the mesomorphism transitions to a new mesophase with reduced curvature at the core-chain interface that persists down to very high solvent concentrations (low mesogen concentrations). Whereas compound **4b** forms induced cubic and lamellar phases, only a lamellar mesophase is induced in **11**-*16*; this behaviour is still consistent with location of the solvent with the charged core. However, the important point is that the shape of each phase diagram is largely invariant with solvent concentration after the transition to the induced mesophase.

Destabilisation of the Col$_h$ phase formed by **4b** occurs at roughly 10 %wt DMSO, corresponding to two solvent molecules per mesogen, whereas destabilisation of the Col$_h$ phase formed by **11**-*16* occurs at 30 %wt DMSO, corresponding to eight solvent molecules per mesogen. Thus, the *N*-phenylpyridinium ions require more solvent than the silver(I) salts before the mesomorphism changes from Col$_h$ to lamellar. Quite why this is the case is unclear, but the longer aliphatic chains of **11**-*16* are consistent with the higher concentration of solvent required to remove the imbalance between core and chain volumes that would allow the formation of a lamellar phase. Then, on further increasing the solvent concentration, the system becomes saturated and free solvent is observed alongside the SmA phase. This is clearly observed by microscopy as shown in Figure 4.19 – compound **11**-*16* is bright orange and additional regions of colourless liquid can be seen that must correspond to free solvent. This behaviour is much the same as that observed between the silver(I) salt **4b** and DMSO, and at concentrations also below 70 %wt mesogen free solvent was also seen alongside the mesophase.

Destabilisation of the induced lamellar phase relative to the Col$_h$ phase is consistent with the behaviour displayed by the dry materials, where the clearing temperature from the SmA phase is consistently lower than that from a columnar mesophase formed at the longest terminal chain lengths. However, the increase in the clearing point on changing from SmA to Col$_h$ mesomorphism in the dry materials is 69 °C, which is significantly greater than that displayed on the addition of solvent to compound **11**-*16*, being 25 °C on moving from 70 to 80 %wt DMSO (Figure 4.18). Thus, for some reason, the lamellar phase formed on the addition of solvent appears to be more stable than the lamellar phase formed by the dry materials.
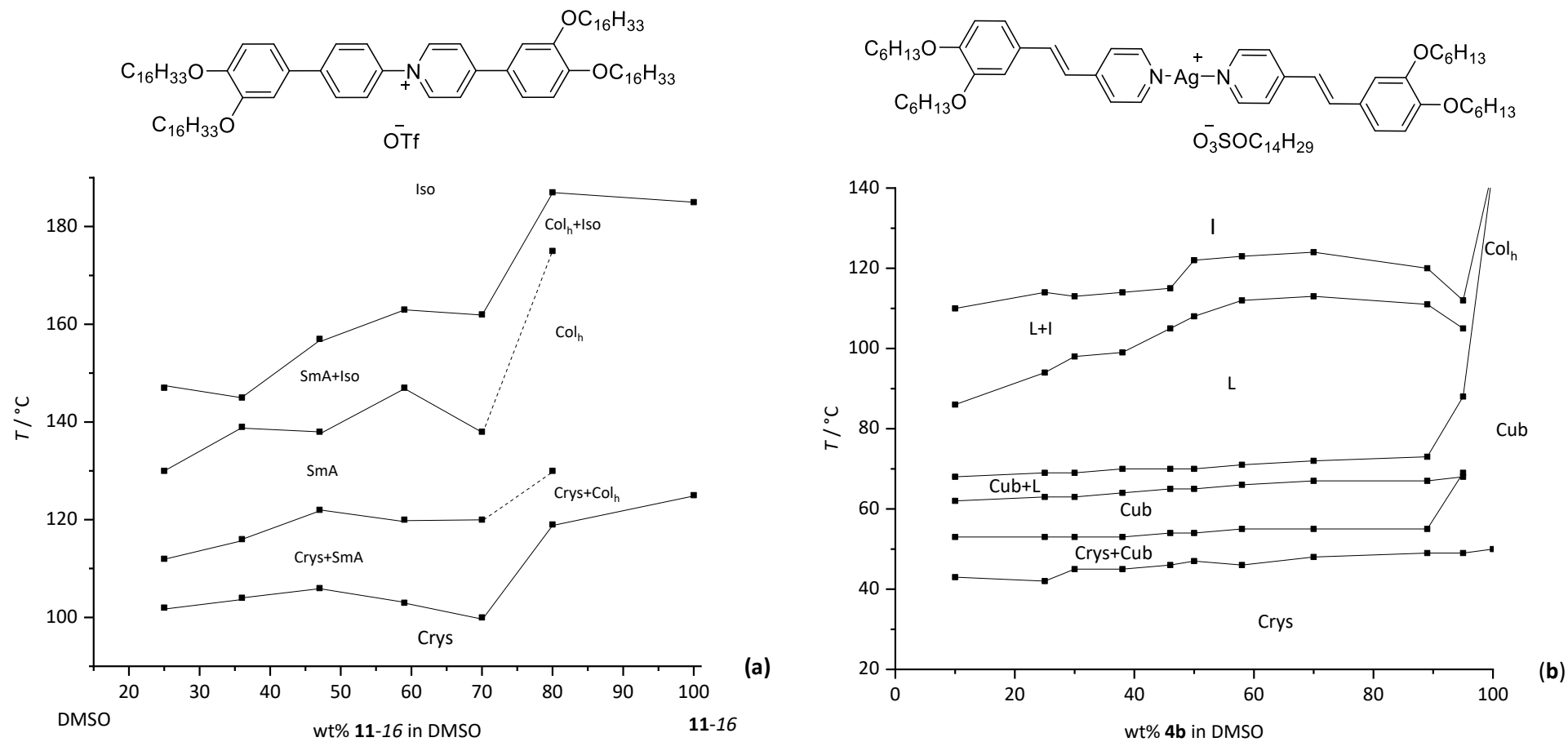
Figure 4.18. Comparison of phase diagrams formed by compound **11**-*16* (**a**) and silver(I) salt **4b** (**b**) in DMSO.

Concentrating on the fact that free solvent is observed below 70 %wt **11**-*16* in addition to the biphasic regimes requires some discussion as this clearly contradicts the condensed phase rule for a two-component system. Bruce and Smirnova[1] rationalised one possibility for the observation of free solvent in the phase diagram of **4b** with DMSO as a result of the slow kinetics of transitions into and out of cubic phases, and so the biphasic regions observed were not true biphasic regimes, but in fact a manifestation of the slow kinetics of the phase transition. In the case of compound **11**-16 in DMSO, at no point was a cubic phase observed and so there is probably an additional factor responsible for the biphasic regimes observed.
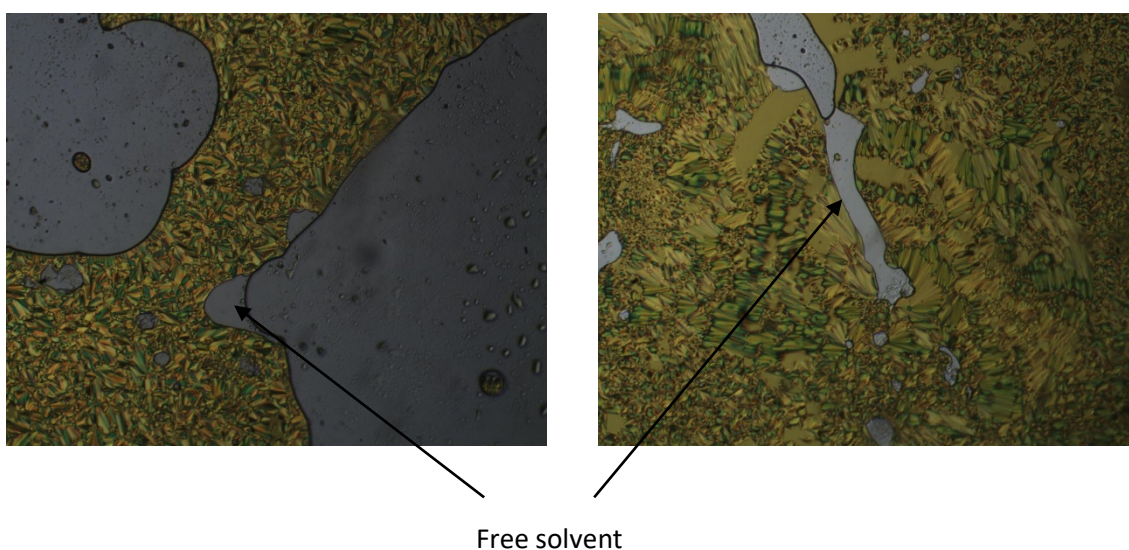
Free solvent

Figure 4.19. Photomicrographs of the induced SmA phase of 51 %wt **11**-*16* in DMSO showing regions of free solvent: T = 145 °C. Textures are at x10 magnification.

Another explanation proposed by Bruce and Smirnova[1] was that the solvent behaves like an impurity to the mesogen, which was responsible for the appreciable drop in the clearing point on the addition of a small amount of solvent. Then, at the concentration where the mesomorphism transitioned from Col_h to lamellar it was proposed that the mesomorphism observed was the thermotropic mesomorphism of a formally solvated mesogen (or solvent-mesogen complex) that did not change composition on the further addition of solvent. A very similar trend is observed when varying the concentration of **11**-16 in DMSO, and after destabilisation of the Col_h phase at 70 wt% **11**-16, the shape of the phase diagram becomes invariant. At the point of maximum destabilisation of the Col_h phase there exists eight molecules of DMSO per mesogen, and so the proposed mesogen-solvent complex giving rise to the induced SmA phase is [**11**-16.8DMSO]. Then

further reducing the concentration of **11**-16 results in the solvation of this species where some additional solvent is observed as free solvent alongside the induced mesophase.

Not only is this behaviour consistent with the mesomorphism of the silver(I) salts in DMSO but also with the solvent-induced behaviour of a series of calamitic diols studied by Kölbel *et al.*[24] They found that the calamitic diols presented in Figure 4.20 could take up a defined maximum amount of solvent, and described this as a guest-host relationship where the mesomorphism was the thermotropic behaviour of a solvated compound rather than being lyotropic behaviour in the traditional sense. The dry compound shown in Figure 4.20 formed an intercalated SmA phase due to segregation of the polar 1,2-diol unit and the biphenyl core and the addition of glycerol stabilised the SmA phases and also induced a columnar mesophase above the SmA phase. Formation of the columnar mesophase can be explained either by a reduction in the coordinated solvent molecules to the diol unit, and/or by an increase in the effective volume of the aromatic moieties due to increased mobility at higher temperature. This caused a collapse of the layers into ribbons as shown in Figure 4.20 (**b**), thus forming a columnar mesophase.
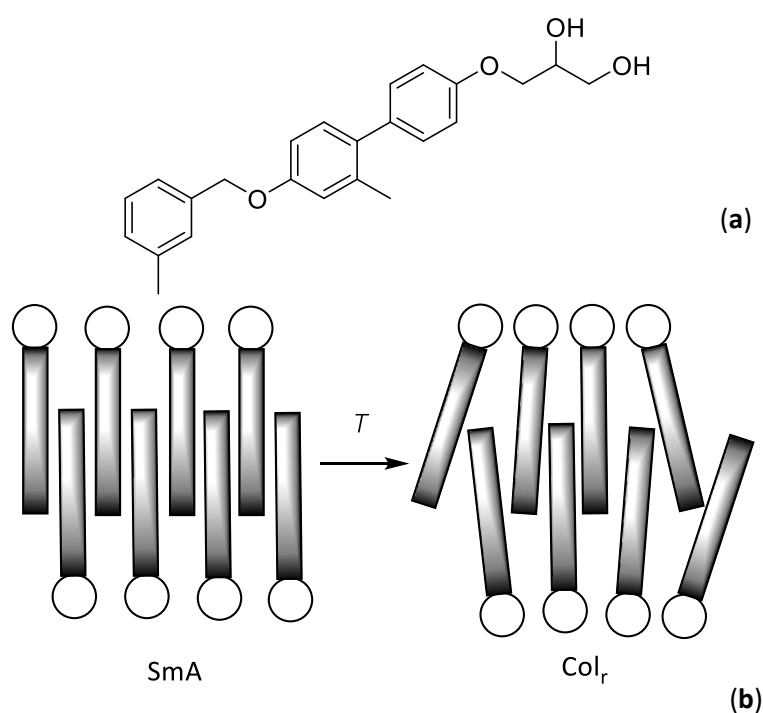
Figure 4.20. 1,2-Diols studied by Kölbel *et al*. (**a**) and structure of the intercalated SmA phase and formation of the columnar phase (ribbons) on the addition of glycerol at elevated temperature (**b**).

Considering that the solvent-induced mesomorphism of compound *11*-16 in DMSO is not conventionally lyotropic, the tendency is to assign the induced mesophase as SmA rather than lamellar. The textures of the induced SmA phase are identical to those of the thermotropic SmA phases displayed by the shorter-chain homologues in the series. However, assignments of SmA and lamellar are used interchangeably throughout the discussion.

Another interesting comparison between the phase diagrams displayed by the silver(I) salt **4b** and *N*-phenylpyridinium ion **11**-*16* in DMSO is the significantly higher melting point of the latter across the whole phase diagram. Compound **4b** melts into crystal+cubic at roughly 45 °C, whereas **11**-*16* does not melt into crystal+SmA until around 100 °C. This behaviour is believed to be a feature of the mesogens in general owing to the more ionic nature of the *N*-phenylpyridinium materials, which thus require higher temperatures to overcome stronger electrostatic interactions. The triflate salts then display the highest melting temperature of any anion due to its small and spherical shape that can more easily be accommodated within the crystal structure. Compound **11**-*16* (with a triflate anion) melts at 125 °C as a thermotropic material,[25] whereas the melting point of silver(I) salt **4b** (with a tetradecylsulfate anion) is 50 °C as a dry compound.[26] So the addition of solvent to both compounds depresses the melting temperature to similar extents relative to the dry compounds.

The phase diagram constructed between compound **11**-*12* and dodecanol presented in Figure 4.8 shows that the SmA phase is significantly destabilised on the addition of 5 %wt dodecanol that corresponds to three solvent molecules per mesogen, after which point the mesomorphism shown is Col_h to 80 %wt **11**-*12*. At concentrations lower than 80 %wt **11**-*12*, only crystal and isotropic liquid phases are observed. Considering that the induced Col_h phase formed only across a narrow region of the phase diagram (and that this mesophase was observed only monotropically) suggests that the nature of this mesomorphism is different to that observed for **11**-*16* in DMSO.

3.3. Solvent-induced behaviour of the alkylsulfate salts

Compounds with alkylsulfate anions displayed the richest mesomorphism on the addition of external solvent. Much like the triflate salts, **11**-*12* and **11**-16, the alkylsulfate salts that formed cubic or Col_h phases as dry materials all formed induced SmA phases on the addition of DMSO and DMF. In one case, MeCN was also able to induce a SmA phase, albeit monotropically. Quite why only one case of induction was observed for MeCN is unclear, but the low boiling point of this solvent did limit the temperatures that could be accessed. The volatility and boiling point of the

solvent are hugely important factors for inducing mesomorphism in these compounds; in the many cases of SmA induction with DMSO, induction was observed at a temperature well above the boiling point of MeCN. The addition of alcohols upwards of propanol induced Col_h phases in the alkysulfate salts that displayed SmA and cubic mesophases as dry materials.

However, unlike the *N*-phenylpyridinium triflates, the addition of linear alkanes does induce lyomesomorphism in the alkysulfate compounds. Considering that linear alkanes did not induce lyomesomorphism in both the *N*-phenylpyridinium triflates and the silver(I) triflates, it is clearly a property inherent to the triflate anion that explains the lack of induction in these materials. A probable explanation for these findings is a chemical incompatibility between the hydrocarbon solvent and a fluorinated anion.

As mentioned in Section 2.2, compounds **27**-*10* and **28**-*10* (each with decyloxy chains and an octylsulfate and dodecylsulfate anion, respectively) formed induced Col_h phases on the addition of decane, dodecane and pentadecane. The addition of alkanes shorter than decane, however, did not induce lyomesomorphism presumably due to the volatility of these solvents. Compounds **27**-*8* and **28**-*8* with octyloxy chains, on the other hand, did not show induction with any linear alkane and the same mesophase(s) as the dry materials were observed. Compound **27**-*6*, on the other hand, with shorter hexyloxy chains formed a monotropic cubic phase on the addition of linear alkanes from octane to pentadecane. It would appear that compounds with hexyloxy and decylocy chains form induced mesophases on the addition of alkanes, but compounds with intermediate octyloxy chains did not. How can this behaviour be rationalised?

These results demonstrate well the balance between internal and external solvents in dictating the mesomorphism of a given system. Compound **27**-*6*, with the shortest terminal chains and an octylsulfate anion, forms a SmA phase as a dry compound. The addition of alkanes then induces the formation of a monotropic cubic phase, consistent with solvent location with the peripheral chains to influence curvature thereby. Compound **27**-*10*, with an octylsulfate anion and decyloxy chains, forms a SmA phase and a cubic phase as a dry compound, whereas dry **28**-*10* with a dodecylsulfate anion and decyloxy chains forms a cubic and a Col_h phase. The addition of alkanes to compounds **27**-*10* and **28**-*10* induces Col_h mesomorphism in both materials owing to the fact that solvent molecules locate preferentially with the aliphatic chains; the thermotropic cubic phase of **28**-*10* is totally supressed on the addition of alkanes consistent with the induction of a Col_h phase. However,

compounds **27**-*8* and **28**-*8*, with shorter terminal chains, each form a thermotropic SmA phase but an additional cubic phase is observed in **28**-*8* owing to the longer dodecylsulfate anion. However, only a cubic phase is observed when cooling both **27**-*8* and **28**-*8* from their isotropic liquids (as dry materials), which is the same mesomorphism observed in contact preparations with linear alkanes. An explanation consistent with these results is not that linear alkanes destroy mesomorphism in compounds **27**-*8* and **28**-*8*, but rather that they do not generate sufficient curvature to induce the formation of a new mesophase (a Col_h phase) and so the cubic phase persists. It is important to stress that the cubic phase is still observed in contact preparations with decane, dodecane and pentadecane and so these solvents are not destroying liquid-crystalline behaviour. Lengthening of the terminal chains covalently attached to the mesogen in compounds **27**-*10* and **28**-*10*, however, does then provide the necessary curvature to induce a Col_h phase on the addition of alkanes. Quite why the induction of a Col_h phase in compounds **27**-*8* and **28**-*8* is only observed on the addition of aliphatic alcohols (and not with linear alkanes) is still unclear.

3.4. Structural parameters of the thermotropic and induced Col_h phases

In Section 2.2, X-ray diffraction patterns of the thermotropic Col_h phase formed by compound **28**-*10* and the induced Col_h phase in a mixture of 30 %wt decanol and **28**-*10* were presented (Table 4.7 and Figure 4.12). Interestingly, the lattice parameter, *a*, was 4.3 Å smaller in the solvent-induced phase compared to that of the dry material. This was surprising as the nature of the induced mesophase formed on the addition of higher alcohols would suggest that the solvent swells the aliphatic chains of the mesogen to increase curvature established at the core-chain interface. Thus, one would expect an increase in the lattice parameter consistent with increasing the diameter of the columnar cross-section.

However, considering the generalised model for the structure of columnar phases formed by polycatenar mesogens,[27] a number of molecules (often between three and five depending on the material) can be considered as forming a repeat motif, being aligned at some angle in the column with respect to the columnar long axis (Figure 4.21). The transition from lamellar to columnar organisation is regarded as taking place by undulation of the layers on increasing chain length, with the undulations eventually becoming so large that discrete packs of molecules can be identified,[28] representing the columnar cross-section. Two models are consistent with a decrease in the lattice parameter on the addition of solvent. First, is that the alcohol solvent somehow induces greater tilting of the mesogens in the column, which would reduce the diameter of the columns and

consequently lead to reduction in the *a* parameter in the solvent-induced phase. Second, is that location of the solvent with the peripheral chains reduces the number of mesogens in the cross-section of the column so that if the solvent increases interfacial curvature by locating with the chains, then fewer mesogens may be found in the cross-section of a column, reducing the lattice parameter. With the data in hand, it is, however, not possible to discriminate between these two mechanisms and of course, the two mechanisms are not entirely discrete.
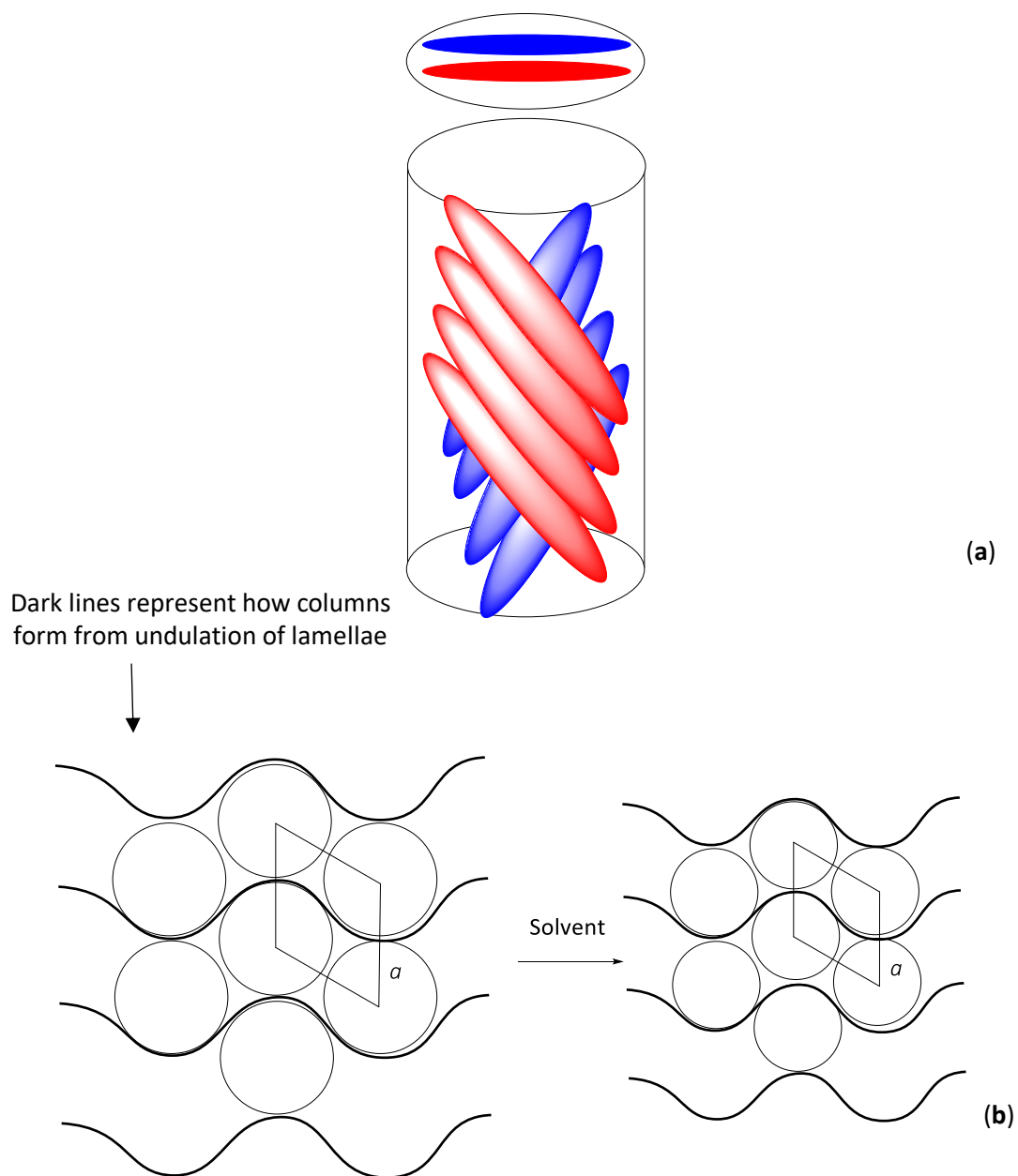
Figure 4.21. Model showing arrangement of polycatenar molecules in the columnar repeat units (**a**) and reduction in the *a* parameter on addition of decanol by reducing the cross-section of the columns (**b**).

3.5. Solvent-induced behaviour of the NTf$_2^-$ salts

Only polar aprotic solvents such as DMSO induced lyomesomorphism in the triflimide salts and a SmA phase was induced in all cases. An assignment of SmA is given rather than lamellar for this solvent-induced phase as the optical textures produced on the addition of DMSO were identical to the thermotropic SmA textures formed by the triflate salts (focal-conics and batonnets can be seen), and are considerably different to those formed by the dry material as shown in Figure 4.16. A diffraction pattern of the induced SmA phase formed by a mixture of compound **29**-*10* with 30 wt% DMSO was recorded and this is presented in Figure 4.17. A single reflection was observed in the small-angle regime consistent with a d_{001} reflection. Furthermore, the reflection observed at 10.9 Å in the Col$_r$ phase formed by the dry compound was absent, and so the diffraction data in general are consistent with the induction of a SmA phase on the addition of DMSO. The lamellar *d*-spacing is also similar in magnitude to the *d*-spacing observed in the thermotropic SmA phase formed by the triflate compound, **11**-*10*, also with decyloxy chains (32.9 Å *vs* 30.6 Å, respectively).

4. Conclusion

The solvent-induced mesomorphism of the newly prepared *N*-phenylpyridinium ions is broadly similar to that displayed by the stilbazole complexes of silver(I), demonstrating nicely their amphiphilic behaviour. The lyomesomorphism of these salts is controlled by a delicate balance between the internal solvent covalently attached to the mesogen and the external solvent added. Much like the silver(I) salts (and also the Group 10 metallomesogens studied by Usol'tseva *et al.*[18,20]) the chain length of apolar solvent molecules needed to be similar in length to the chains attached to the mesogen covalently if lyomesomorphism was to be induced. The nature of the anion was also important in controlling the induced mesomorphism and the alkylsulfate salts always showed richer mesomorphism than their triflate analogues; much the same behaviour was true for the silver(I) salts. One explanation consistent with these findings is the chemical incompatibility between a fluorinated anion and a hydrocarbon solvent and to test this hypothesis it would be possible to prepare analogous materials with a small, hydrocarbon-based anion that would mimic the spatial requirements of the triflate moiety. Some attempts were made during these studies to prepare methylsulfate salts as such an example, but the compounds could not be isolated in acceptable purity.

A crucial difference, however, between the lyomesomorphism of the silver(I) salts and the newly prepared *N*-phenylpyridinium ions was that observed on the addition of alcohols as a Col$_h$ mesophase was always induced in the latter materials, consistent with an increase in curvature at the core-chain interface. The silver(I) salts had behaved a little differently and the addition of alcohols could either increase or reduce interfacial curvature depending on the space available to the solvent molecules. The shortest alcohols (methanol and ethanol) also induced chromonic behaviour in the silver(I) salts where the nature of the mesogenic moiety was truly dependent on solvent concentration, a feature never observed in the *N*-phenylypridinium ions. The behaviour of the *N*-phenylpyridinium materials is then a little more predictable on the addition of alcohols.

The behaviour of the triflimide salts in response to solvent is certainly interesting and demonstrates the delicate competition between electrostatics and the relative core and chain volumes. Recall that the formation of the Col$_r$ phase by the dry materials was explained by the more charge disperse triflimide anion causing a break-up of the lamellae into ribbons, outweighing the competing increase in core volume imparted by the larger triflimide anion. The addition of DMSO to further

increase the core volume then causes volumetric arguments to dominate and a SmA phase is induced. The behaviour of the triflimide salts on the whole is a little different compared to their triflate and alkylsulfate analogues, and the preparation of a series of silver(I) triflimide salts would certainly make for an interesting comparison.

5. Experimental

5.1. Polarising optical microscopy

Mesophase identification on the addition of solvent was achieved through polarising optical microscopy, and in some cases by X-ray diffraction. Microscopy experiments were of the Lawrence penetration type, where the dry compound was placed on a microscope slide and covered with a coverslip. The sample was heated into the isotropic liquid to create an even thickness of the sample between the microscope slide and coverslip and cooled back to r.t. The solvent was then added to the edge of the sample and allowed to penetrate *via* capillary action, thus establishing a concentration gradient from the edge of the sample (highest solvent concentration) to the centre (no solvent). The sample was then heated at 10 °C min^{-1} and any induced mesophases observed. During this process, solvent was constantly added to the edge of the coverslip *via* a capillary tube to maintain a concentration gradient. Once in the isotropic liquid, the sample was cooled at 10 °C min^{-1} and mesophases identified by their characteristic optical textures. Establishing a concentration gradient provided a snapshot of the binary phase diagram at the temperature in question.

5.2. Binary phase diagrams

In two cases, a binary phase diagram was plotted. Requisite amounts of the mesogen and solvent were weighed onto a microscope slide and covered with a coverslip. The edges of the coverslip were then sealed with epoxy resin that was stable to 200 °C to prevent evaporation of the solvent. The sample was then heated on the polarising microscope to allow the two components to mix. Mesophases were identified from their characteristic optical textures when viewed between crossed polarisers.

5.3. X-Ray diffraction for solvent-induced mesophases

The required amounts of mesogen and solvent were weighed onto a microscope slide and mixed as best as possible using a spatula and needle. The resulting material was then added to a capillary

189

tube (0.9 mm in diameter) and pushed to the bottom using fine electrical wiring (care was taken not to smash the capillary tube). The top of the capillary tube was then sealed with epoxy resin to prevent evaporation of the solvent. Diffraction patterns were then recorded using a Bruker D8 Discover equipped with a temperature controlled, bored graphite rod furnace, custom built at the University of York. The radiation used was copper Kα (λ = 0.154056 nm) from a 1 µS microfocus source. Diffraction patterns were recorded on a 2048 x 2048 pixel Bruker VANTEC 500 area detector set at a distance of 127 mm from the sample. Two-dimensional diffraction patterns were collected every 10 °C on heating to the isotropic liquid and subsequent cooling to room temperature at a rate of 10 °C min^{-1}. The data were then processed using Origin.

5.4. DSC

Samples were prepared by weighing the requisite amounts of compound and solvent in a small vial and mixing as thoroughly as possible with a needle and spatula. The sample was then transferred to a 20 µL aluminium crucible and calorimetry scans were run on a Mettler Toledo DSC822e instrument (running on a Stare software) equipped with a TSO801R0 sample robot and calibrated using pure indium. Samples were run at heating/cooling rates of 5 °C min^{-1}.

6. References

1   A. I. Smirnova and D. W. Bruce, *J. Mater. Chem.*, 2006, **16**, 4299–4306.

2   A. I. Smirnova and D. W. Bruce, *Chem. Commun.*, 2002, **2**, 176–177.

3   A. Skoulios and V. Luzzati, *Nature*, 1959, **183**, 1310–1312.

4   T. K. Attwood, J. E. Lydon, C. Hall and G. J. T. Tiddy, *Liq. Cryst.*, 1990, **7**, 657–668.

5   J. Lydon, *J. Mater. Chem.*, 2010, **20**, 10071.

6   S.-W. Tam-Chang and L. Huang, *Chem. Commun.*, 2008, 1957.

7   L. Onsager, *Ann. N. Y. Acad. Sci.*, 1949, **51**, 627–659.

8   F. Livolant, S. Mangenot, A. Leforestier, A. Bertin, M. de Frutos, E. Raspaud and D. Durand, *Philos. Trans. R. Soc. A Math. Phys. Eng. Sci.*, 2006, **364**, 2615–2633.

9   J.-F. Revol, H. Bradford, J. Giasson, R. H. Marchessault and D. G. Gray, *Int. J. Biol. Macromol.*, 1992, **14**, 170–172.

10   J. Gregory and K. C. Holmes, *J. Mol. Biol.*, 1965, **13**, 796-IN15.

11   J. D. Bernal, *J. Gen. Physiol.*, 1941, **25**, 111–146.

12   T. E. Strzelecka, M. W. Davidson and R. L. Rill, *Nature*, 1988, **331**, 457–460.

13   F. Livolant, A. M. Levelut, J. Doucet and J. P. Benoit, *Nature*, 1989, **339**, 724–726.

14   J. N. Israelachvili, D. J. Mitchell and B. W. Ninham, *J. Chem. Soc. Faraday Trans. 2*, 1976, **72**, 1525.

15   N. Usol'tseva, K. Praefcke, D. Singer and B. Gündogan, *Liq. Cryst.*, 1994, **16**, 601–616.

16   N. Usoľtseva, P. Espinet, J. Buey, K. Praefcke and D. Blunk, *Mol. Cryst. Liq. Cryst.*, 1997, **299**, 457–465.

17   N. Usol'tseva, P. Espinet, J. Buey and J. L. Serrano, *J. Mater. Chem.*, 1997, **7**, 215–219.

18   N. Usol'tseva, K. Praefcke, A. Smirnova and D. Blunk, *Liq. Cryst.*, 1999, **26**, 1723–1734.

19   K. Praefcke, B. Bilgin, N. Usol'tseva, B. Heinrich and D. Guillon, *J. Mater. Chem.*, 1995, **5**, 2257.

20   K. Praefcke, J. D. Holbrey, N. Usol'tseva and D. Blunk, *Mol. Cryst. Liq. Cryst.*, 1997, **292**, 123–139.

21   J. Billard and B. K. Sadashiva, *Pramana*, 1979, **13**, 309–318.

22   V. Luzzati and F. Husson, *J. Cell Biol.*, 1962, **12**, 207–219.

23   F. Reiss-Husson and V. Luzzati, *J. Phys. Chem.*, 1964, **68**, 3504–3511.

24   M. Kölbel, T. Beyersdorff, C. Tschierske, S. Diele and J. Kain, *Chem. Eur. J.*, 2000, **6**, 3821–3837.

25   J. D. Herod, M. A. Bates, A. C. Whitwood and D. W. Bruce, *Soft Matter*, 2019, **15**, 4432–4436.

26   B. Donnio and D. W. Bruce, *J. Mater. Chem.*, 1998, **8**, 1993–1997.

27   D. W. Bruce, B. Donnio, B. Heinrich, D. Guillon, J. Kain, S. Diele and H. Allouchi, *J. Am. Chem. Soc.*, 2004, **126**, 15258–15268.

28   B. Donnio, B. Heinrich, T. Gulik-Krzywicki, H. Delacroix, D. Guillon and D. W. Bruce, *Chem. Mater.*, 1997, **9**, 2951–2965.

Chapter Five: Mesomorphism of an Homologous Series of Tetracatenar Complexes of Silver(I) Triflate and Silver(I) Dodecylsulfate Bearing 3,4-Dialkoxyphenylpyridine Ligands: A Comparison to the 3,4-Dialkoxystilbazole Complexes of Silver(I) and the *N*-Phenylpyridinium Ions.

1. Introduction

One point of interest in this work has been to compare the tetracatenar *N*-phenylpyridinium salts with the silver(I) stilbazole complexes made earlier in the group. The preparation of the *N*-phenylpyridinium materials goes through a 3,4-dialkoxyphenylpyridine intermediate, which itself can coordinate to silver(I). Therefore, the preparation of these new silver salts would allow a more precise comparison with the *N*-phenylpyridinium salts and so the synthesis of 3,4-dialkoxyphenylpyridine silver(I) complexes with triflate and dodecylsulfate anions, **31**-*n* and **32**-*n*, respectively, was undertaken. The structure of these newly prepared silver complexes is shown in Figure 5.1.

31-*n*: X = OTf
32-*n*: X = $O_3SOC_{12}H_{25}$
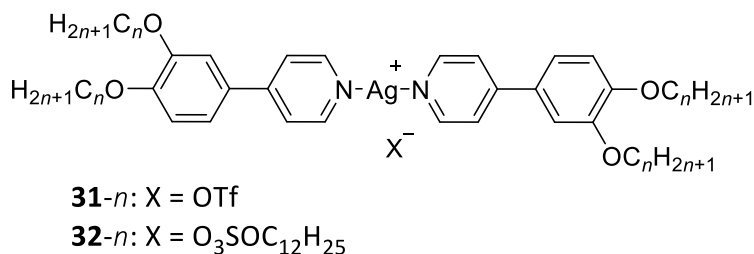
Figure 5.1. Structure of the 3,4-dialkoxyphenylpyridine complexes of silver(I) triflate and silver(I) dodecylsulfate.

2. Results

2.1. Thermal behaviour of the dodecylsulfate salts

The silver(I) complexes of the dialkoxyphenylpyridines were prepared following procedures outlined by Donnio *et al.*[1] and two molar equivalents of the phenylpyridine were stirred in dichloromethane along with silver(I) dodecylsulfate in a vessel protected from light. The silver(I) dodecylsulfate was prepared in house following literature procedures.[2,3] After 24 hours of stirring the ligand and silver(I) dodecylsulfate, the reaction mixture was filtered through a plug of celite and the filtrate evaporated to dryness. The residue was then crystallised from hot acetone and the resulting solid triturated with diethyl ether to afford the phenylpyridine complexes of silver(I) dodecylsulfate in analytical purity. Yields typically varied from 50-65% depending on the terminal chain length. ^{1}H NMR spectroscopy was able to differentiate the complexes from the free ligand, showing a downfield shift of 0.15 ppm in the resonances corresponding to the hydrogens *ortho* to the nitrogen atom of the pyridine ring. Thermal data from DSC are presented in Table 5.1 and the phase diagram in Figure 5.2.
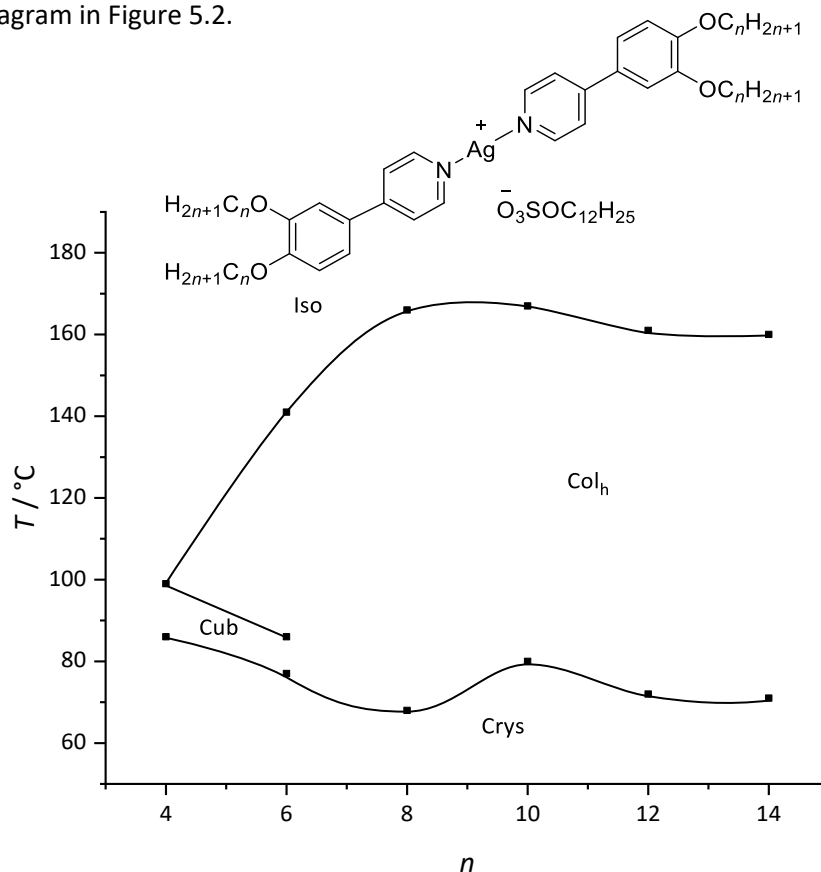
Figure 5.2. Phase diagram of 3,4-dialkoxyphenylpyridine complexes of silver(I) dodecylsulfate from polarising optical microscopy on heating.

Table 5.1. Thermal data from DSC; temperatures reported are onset temperatures on heating.

n	Transition	T / °C	ΔH / kJ mol^{-1}
4	Crys - Cub	86	6.9
	Cub-Iso	99	0.7
6	Crys-Crys'	40	2.6
	Crys'-Crys''	61	7.5
	Crys'' - Cub	77	11.8
	Cub-Col$_h$	86	1.7
	Col-Iso	141	1.5
8	Crys-Col$_h$	68	38.1
	Col$_h$-Iso	166	2.5
10	Crys-Col$_h$	80	22.6
	Col$_h$-Iso	167	1.9
12	Crys-Crys'	49	14.7
	Crys'-Crys''	63	11.3
	Crys''-Col$_h$	74	7.9
	Col$_h$-Iso	134	1.0
14	Crys-Col$_h$	83	54.6
	Col$_h$-Iso	154	2.7

The homologues with the shortest terminal chains displayed a cubic mesophase, whereas those with longer terminal chains displayed a columnar hexagonal mesophase. All homologues studied were mesomorphic and the butoxy derivative melted into a cubic phase at 86 °C (assigned on the basis of its high viscosity and optical isotropy) and cleared into the isotropic liquid at 99 °C. The hexyloxy derivative melted into a cubic mesophase at 77 °C, but then formed a Col$_h$ phase at 86 °C before clearing into the isotropic liquid at 141 °C; note also the significant increase in the clearing point on moving from the cubic mesophase formed by compound **32**-*4* to the Col$_h$ phase formed by **32**-*6*. Complex **32**-*8* then showed only a Col$_h$ phase between 68 and 166 °C and both the melting and clearing points were relatively invariant for the higher homologues studied.

On cooling from the isotropic liquid on the polarising microscope, the Col$_h$ phase formed by compound **32**-*6* grows in from the isotropic liquid as large pseudo focal-conic defects after which

the cubic phase grows in slowly and supercooled as sharp edges at 67 °C as shown in Figure 5.3. Homologues upwards of **32**-*8* displayed only an enantiotropic Col_h mesophase with pseudo focal-conic optical textures seen on cooling from the isotropic liquid. All homologues that formed Col_h mesophases initially formed glasses on cooling to room temperature, crystallising only with time, sometimes over the course of several days.

Assignment as columnar hexagonal mesophases was confirmed by SAXS, where all derivatives with the exception of compound **32**-*6* displayed clear d_{10}, d_{11} and d_{20} reflections with relative spacings of $1 : 1/\sqrt{3} : 1/\sqrt{4}$; complete diffraction data for series **32**-*n* are presented in Table 5.2. The lack of a d_{11} reflection for **32**-*6* implies less well-developed two-dimensional order in this material and may reflect the presence of the underlying cubic phase. In order to confirm that the columnar mesophase displayed by the hexyloxy homologue was in fact hexagonal, contact preparations were performed between this material and **32**-*8* (which is hexagonal from a clear d_{11} reflection). The two were found to be co-miscible in their liquid-crystalline states, proving the assignment of **32**-*6* as Col_h (Figure 5.4 (**c**)).
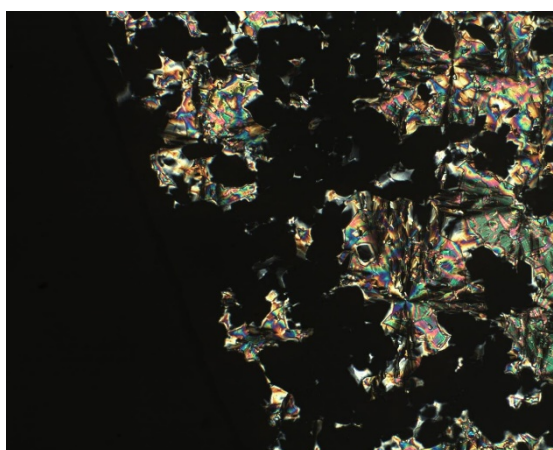
Figure 5.3. Photomicrograph of the cubic phase growing in from the Col_h phase on cooling compound **32**-*6* from the isotropic liquid. Texture is at x10 magnification.

All compounds also displayed a diffuse scattering in the wide-angle region of their diffraction patterns at a spacing of 4.5 Å corresponding to the liquid-like behaviour of the terminal alkoxy chains; a typical diffraction pattern is shown in Figure 5.6. Another diffuse reflection is seen at 10.5 Å, which currently cannot be assigned. It may be that this reflection arises from the silver-silver distances; this reflection was also observed in the diffraction patterns of the silver(I) stilbazole materials and were also not assigned.

A steady increase in the columnar *a* parameter was observed on increasing terminal chain length due to an increase in the width of the columns (Table 5.2 and Figure 5.5). However, the *a* parameter is significantly smaller than the molecular length estimated from single-crystal structure fragments (being 82% smaller at **32**-8 and falling to 73% by **32**-*12*). This is consistent with the model proposed by Bruce and co-workers for the revised mode of packing in the Col_h phase formed by polycatenar liquid crystals in which the molecules are tilted within the columns.[4]

Table 5.2. Observed and calculated d spacings from SAXS of the dodecylsulfate salts forming Col_h phases: the calculated molecular length of each cation assumes chains are in their all *trans* conformation.

n	d_{obs} / Å	*hk*	*Parameter* / Å	Calculated molecular length / Å
8	28.9	*10*	*a* = 33.4	40.5
	16.9	*11*		
	14.4	*20*		
	4.5	*halo*		
10	30.9	*10*	*a* = 35.7	45.9
	17.9	*11*		
	15.4	*20*		
	4.5	*halo*		
12	32.4	*10*	*a* = 37.4	51.0
	18.8	*11*		
	16.2	*20*		
	4.5	*halo*		
14	34.2	*10*	*a* = 39.5	55.1
	19.8	*11*		
	17.0	*20*		
	4.5	*halo*		

31-*8*

31-*6*

(a)

(b)

(c)
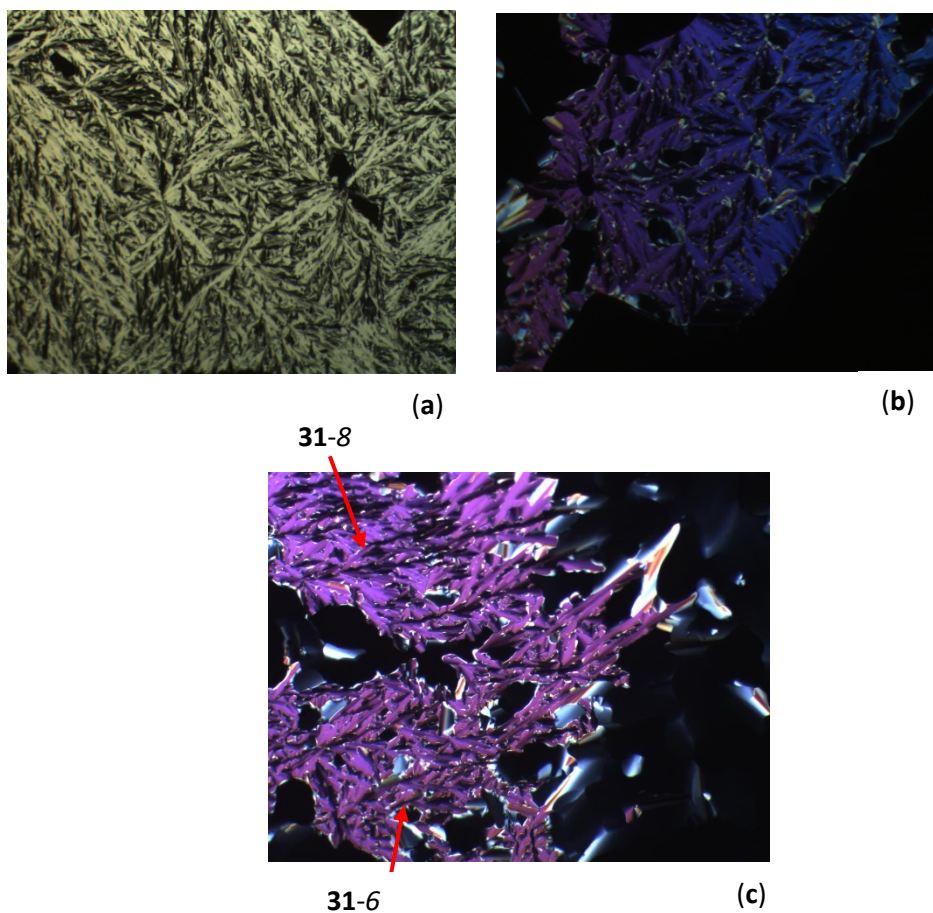
Figure 5.4. Polarising optical textures of (**a**) the Col$_h$ mesophase formed by **32**-*6*, (**b**) the Col$_h$ mesophase formed by **32**-*8* and (**c**) their co-miscibility to prove the symmetry of the former as hexagonal. Textures are at x10 magnification.
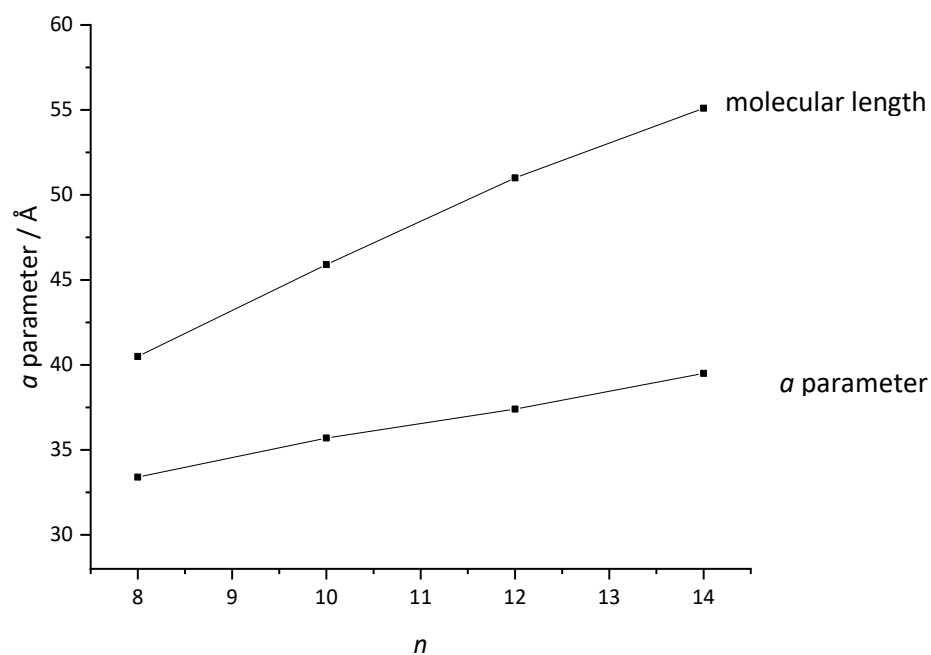
Figure 5.5. Plot of the *a* parameter *vs* chain length and calculated molecular length *vs* chain lengt for the series **32**-*n*.
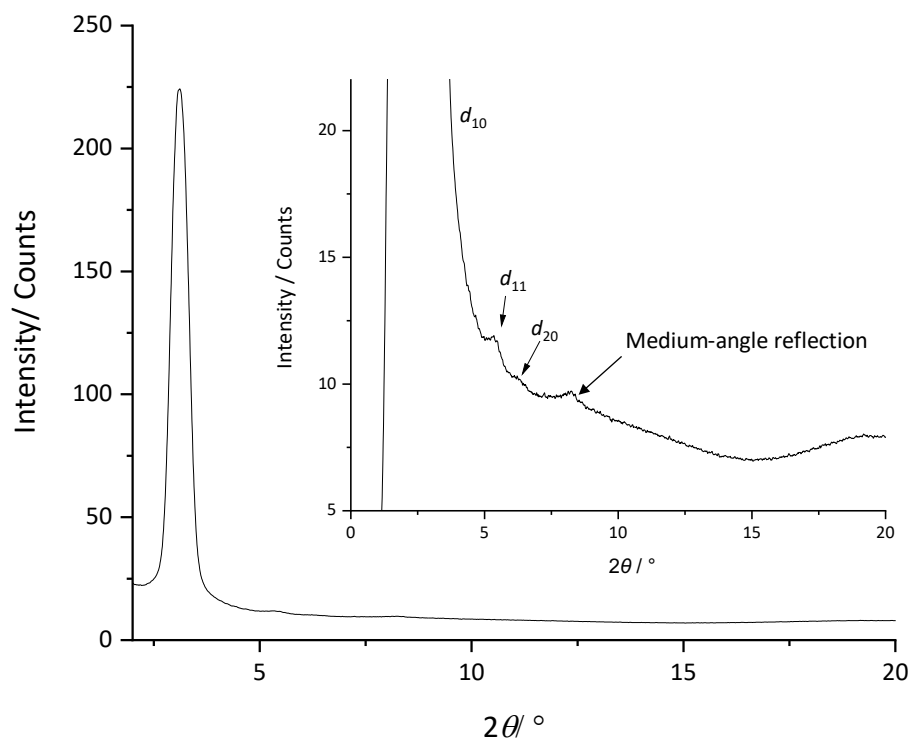
Figure 5.6. Diffraction pattern of **32**-8; inset shows clearly the d_{11}, d_{20} and unassigned medium-angle reflections.

2.2. Thermal behaviour of the triflate salts

The phenylpyridine complexes of silver(I) triflate were also prepared according to the procedure outlined by Donnio *et al.*[1] that involved stirring the phenylpyridine and silver(I) triflate in acetone in a vessel protected from light. After a minimum of 4 hours, the reaction mixture was cooled to -18 °C and the resulting precipitate isolated *via* filtration, washing with multiple portions of cold acetone and drying. Yields typically varied from 50-80% depending on the terminal chain length. Elemental analysis proved the analytical purity of each homologue prepared. The thermal data from DSC are reported in Table 5.3 and the phase diagram is shown in Figure 5.7.
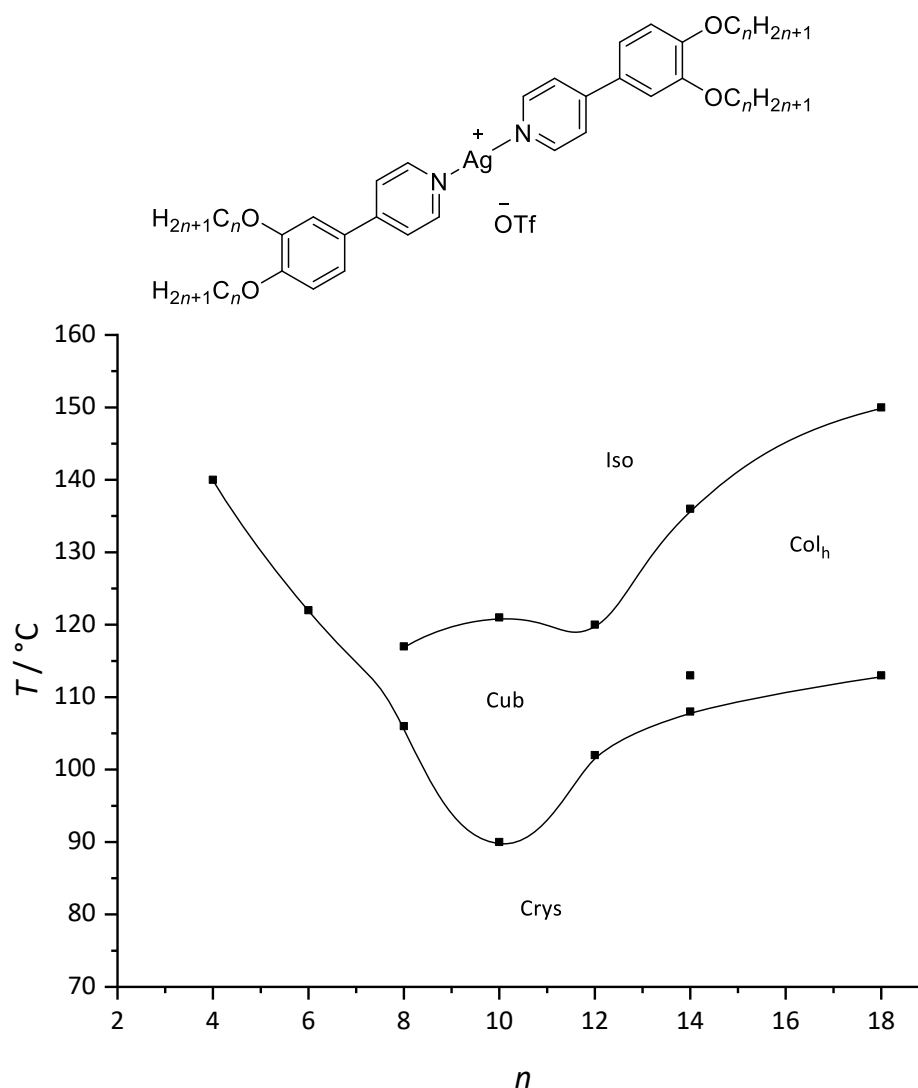
Figure 5.7. Phase diagram of the 3,4-dialkoxyphenylpyridines of silver(I) triflate, **31**-*n*; temperatures are from microscopy on heating.

Evident from Figure 5.7 is the steep decrease in the melting point from **31**-*4* to **31**-*10*, which then recovers to increase slowly for **31**-*12* to **31**-*18*. This behaviour is in contrast to that displayed by the dodecylsulfate series, **32**-*n*, where no appreciable difference in the melting point was observed on increasing chain length. Melting of the triflate salts is, therefore, dependent on the terminal chain length. Furthermore, the melting points of the triflate salts are consistantly higher than the dodecylsulfate salts, presumably due to the flexible alkylsulfate anion in series **32**-*n* that destabilises the crystal phase.

Table 5.3. Thermal data of the triflate salts, **31**-*n*, from DSC; transition temperatures reported here are onset temperatures on heating.

n	Transition	T / °C	ΔH/ kJ mol^{-1}
4	Crys-Iso	140	65.3
6	Crys-Iso	122	25.6
8	Crys-Crys'	65	14.8
	Crys'-Cub	102	9.9
	Cub-Iso	112	1.9
10	Crys-Cub	83	27.2
	Cub-Iso	117	1.4
12	Crys-Crys'	85	34.4
	Crys'-Cub	96	73.3
	Cub-Iso	116	3.2
14	Crys-Cub	102	27.8
	Cub-Col	111	0.8
	Col$_h$-Iso	129	0.3
18	Crys-Col$_h$	114	152
	Col$_h$-Iso	153	1.9

In the triflate salts, the butoxy and hexyloxy homologues are non-mesomorphic and melt directly into the isotropic liquid at 140 and 122 °C, respectively. Complexes **31**-*8* to **31**-*12* all form only a cubic phase as evidenced by the loss of birefringence on melting and formation of a viscous, optically extinct fluid when viewed on the polarising microscope. The clearing point was relatively constant, but variation in the melting point gave a narrow phase range of 10 °C for **31**-*8* and a wider

range of 34 °C for **31**-*10*. Complex **31**-*14* also showed a cubic phase with slightly reduced stability above which was a Col$_h$ phase, which increased in stability with chain length.

(**a**) (**b**)
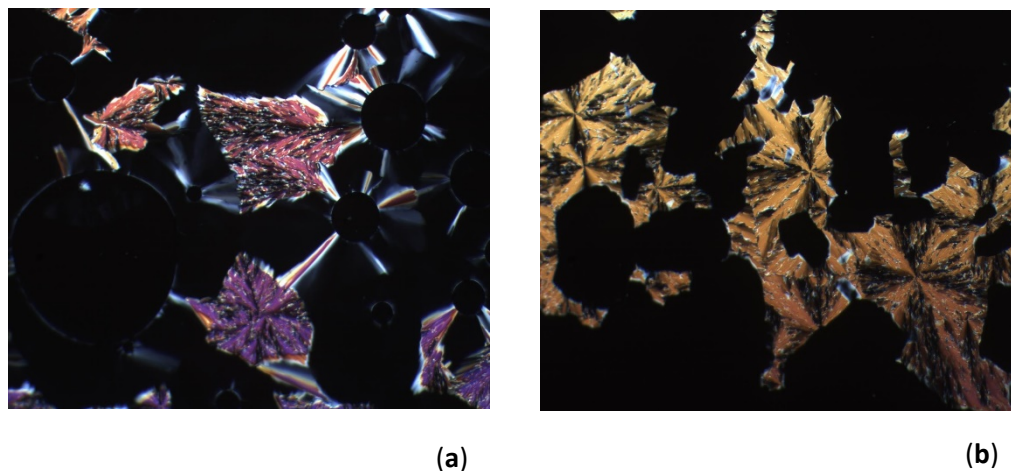
Figure 5.8. Optical texture of the Col$_h$ phase formed by compound **31**-*14* at 120 °C (**a**) and the cubic phase growing in from the Col$_h$ phase of **31**-*14* at 102 °C (**b**). Textures are at x10 magnification.

The d_{11} reflection of the columnar hexagonal phase formed by compound **31**-*14* cannot be seen *via* SAXS, and so to assign this phase as hexagonal columnar required contact preparations to be performed between this material and compound **32**-*12*, a compound which did show both d_{11} and d_{20} reflections. The co-miscibility of the two columnar mesophases proved the assignment of the former as hexagonal. Again, the lack of a clear d_{11} structure factor may well be down to the less well-developed two-dimensional order in this material with the underlying cubic phase (much like the *n* = 6 dodecylsulfate salt).

On cooling compounds **31**-*8*, **31**-*10* and **31**-*12* from the cubic phase, crystallisation occurred slowly when held at room temperature (or close to room temperature) with the exact temperature at which crystallisation occurred being dependent on the cooling rate. DSC was able to detect this crystallisation process, which often occurred on subsequent heating cycles due to the slow kinetics of crystallisation from cubic phases; these are observed clearly as exothermic peaks on subsequent heating cycles. These crystallisation peaks do appear at temperatures where the crystal phase is thermodynamically stable, despite being seen on a heating cycle. The columnar hexagonal phase of **31**-*14* crystallised repeatedly at 67 °C on cooling cycles *via* DSC, although, crystallisation was not observed until 56 °C *via* microscopy.

In addition, cooling compound **31**-*6* from the isotropic liquid sometimes results in the formation of a monotropic mesophase that exists only for a short period of time (sometimes several seconds), with the temperature at which it forms being very dependent on the cooling rate. This metastable phase is mostly homeotropic in nature, but some regions of a fan-like texture can be seen around the edges of the sample. These observations are consistent both with a metastable SmA or Col_h phase; however, as no lamellar phase was formed by any other homologue in this series the tendency is to assign this monotropic phase as Col_h.
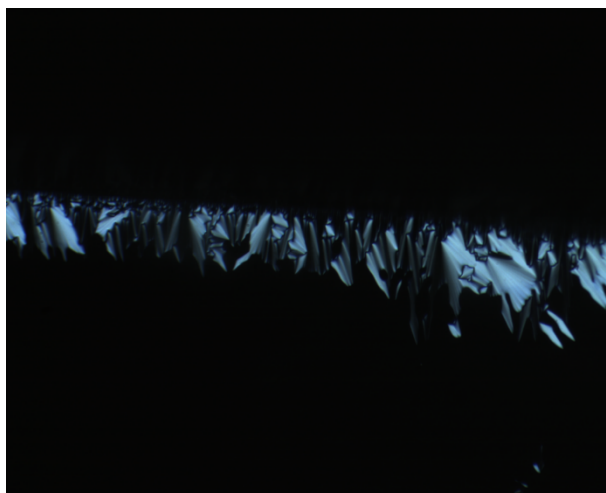
Figure 5.9. Optical texture of the metastable Col_h phase formed by the hexyloxy homologue, **31**-*6*. Texture is at x10 magnification.

3.   Discussion

3.1.   Comparison with the stilbazole complexes of silver(I)

The 3,4-dialkoxyphenylpyridine complexes of silver(I) triflate, **31**-*n*, and silver(I) dodecylsulfate, **32**-*n*, both behave largely in a similar fashion to the stilbazole complexes of silver(I). Clearly, the length of the terminal alkoxy chains has a strong influence over their mesomorphism, and in both cases, increasing the terminal chain length leads to a change from cubic to Col_h mesomorphases.[5,6]

A comparison between the mesomorphism displayed by the phenylpyridine complexes of silver(I) triflate and silver(I) dodecylsulfate reveals that the change from cubic to Col_h mesomorphism occurs at a shorter terminal chain length in the dodecylsulfate series, **32**-*n*, compared to the triflate series, **31**-*n*. The same general observation was made by Donnio *et al.*[1,5] who explained that it was due to the long alkylsulfate chain extending past the aromatic core to contribute to the terminal chain volume, thus increasing the curvature established at the core-chain interface. The smaller,

spherical, triflate anion locates next to the silver centre and cannot contribute to the chain volume; this behaviour is well understood and has been discussed extensively in Chapter Three.

Much like the stilbazole complexes of silver(I), the SmC phase is still absent at short terminal chain lengths. The steric hindrance of the anion coupled with weaker electrostatic attractions from the tightly bound nature of these salts is clearly sufficient to destabilise self-organisation into layers. The effect of the core size is observed when a comparison is made between the form of the phase diagrams formed by the phenylpyridine and stilbazole complexes (Figure 5.10 and 5.11). Thus, the cubic phase is significantly destabilised in the phenylpyridine complexes both in terms of its thermal stability and the chain length at which it is seen and this is particularly clear from Figure 5.10. This observation is entirely consistent with the proposal that the dodecylsulfate chain extends beyond the rigid cation core to contribute to the terminal chain volume, which it is able to do to a greater extent given the shorter length of phenylpyridine compared to stilbazole (9.4 Å *vs* 7.1 Å).
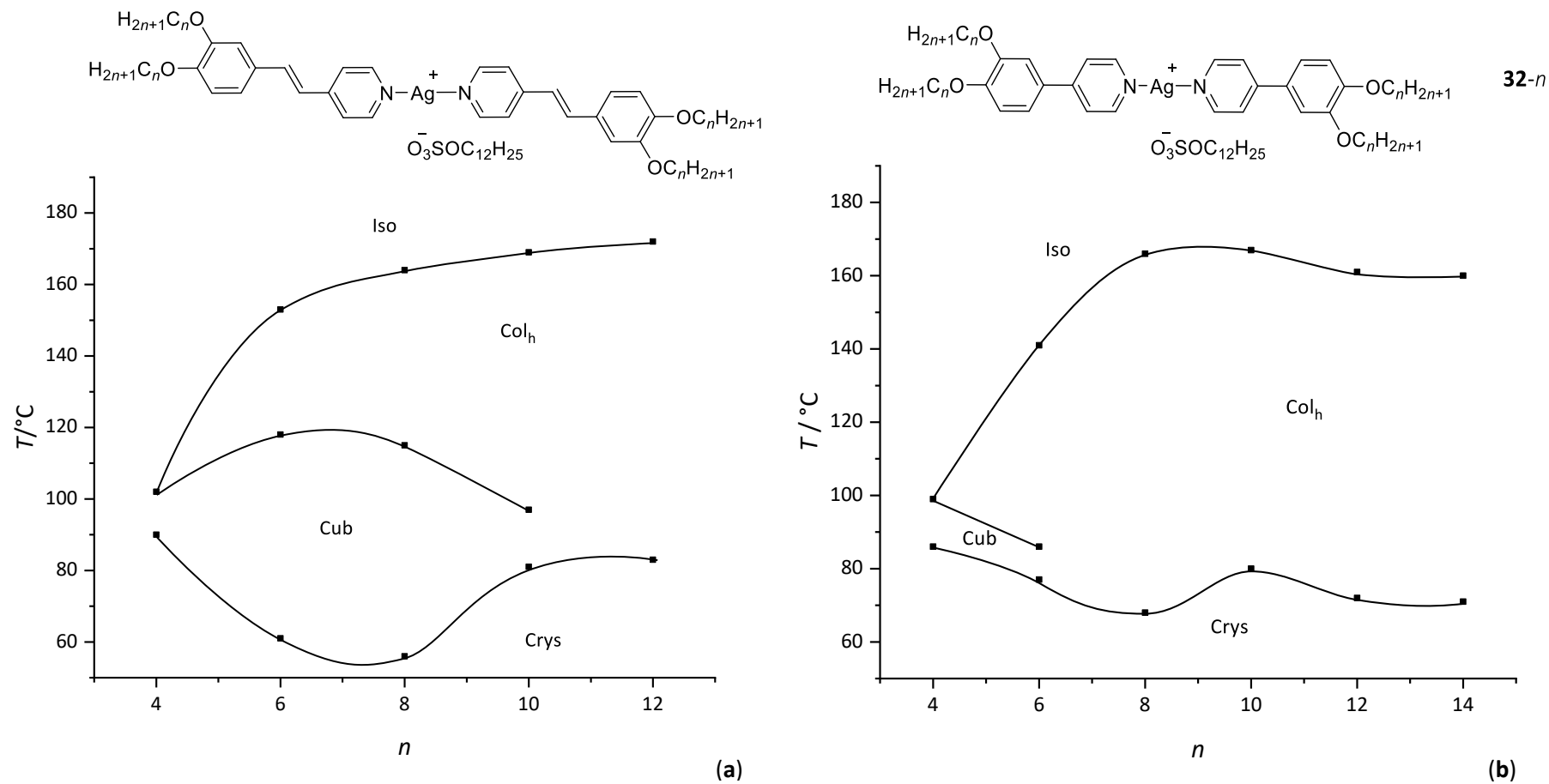
Figure 5.10. Comparison of phase diagrams of (**a**) the stilbazole complexes of silver(I) dodecylsulfate and (**b**) the analogous phenylpyridine complexes of silver(I) dodecylsulfate, **32**-n.
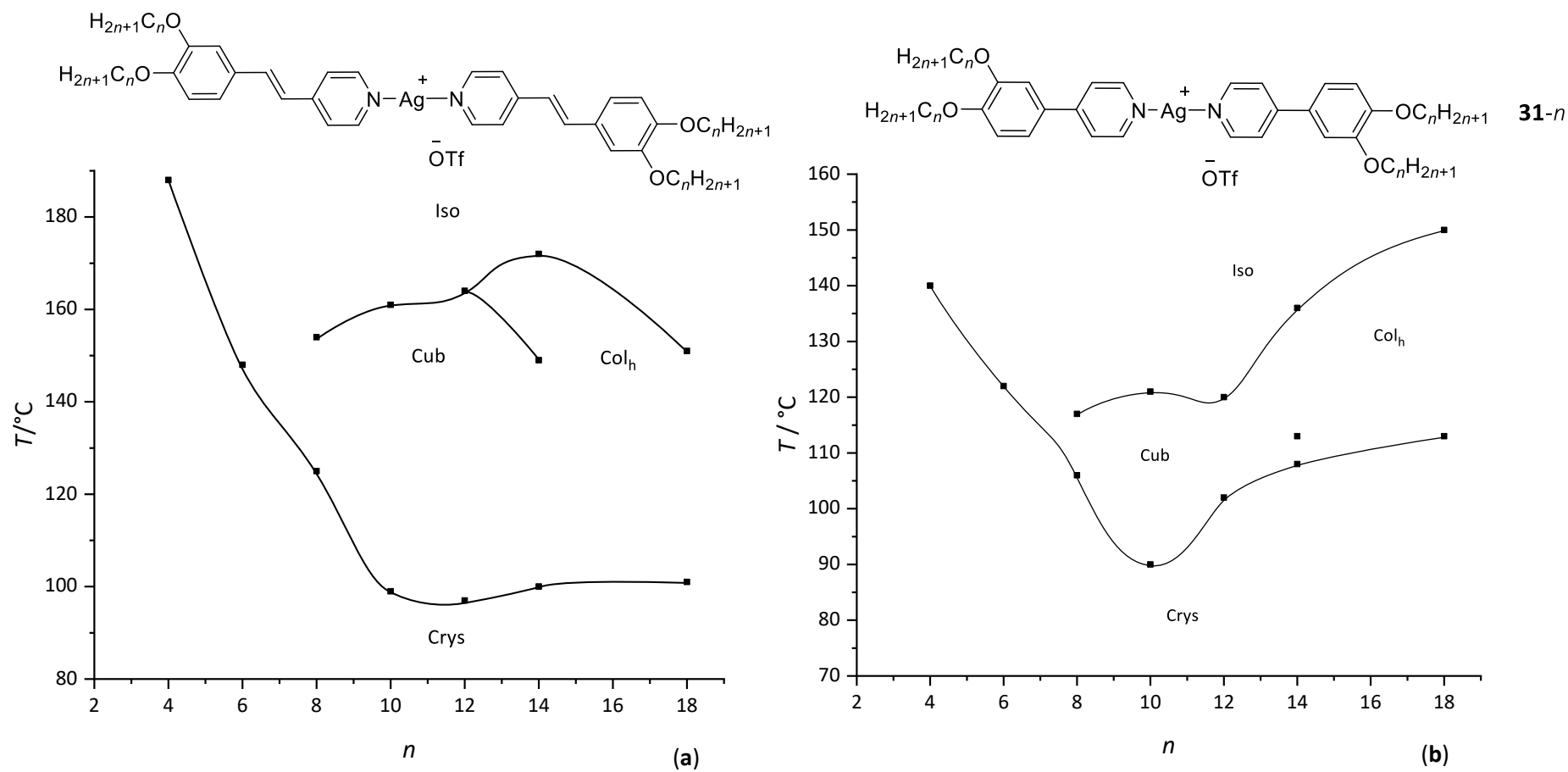
Figure 5.11. Comparison of the phase diagrams of (**a**) the stilbazole complexes of silver(I) triflate and (**b**) the analogous phenylpyridine complexes of silver(I) triflate, **31**-*n*.

A more significant difference, however, is the quite different form of the two phase diagrams with the triflate anion both in terms of cubic phase stability and the evolution of Col$_h$ phase stability (Figure 5.11). Thus, the clearing temperatures of the cubic phases formed by the phenylpyridine complexes are, on average, 40 °C lower than those formed by the stilbazole complexes.

This effect may arise due to the overall shape of the salt imparted by the different ligands. A schematic of the two different salts is shown in Figure 5.12 and those with stilbazole ligands have a core that runs diagonally through the silver centre due to the overall wedge-shape of the stilbazole moiety. The phenylpyridine ligand, on the other hand, generates a core that runs linearly through the silver centre due to the lack of *trans* vinyl bonds. The spatial requirements of the triflate anion can, therefore, be better accommodated by the stilbazole ligands so that the overall shape of the salt is more anisometric. The anion represents a greater perturbation from the core in the phenylpyridine complexes to behave as a lateral substituent and reduce the anisotropy of the phenylpyridine salts, which is consistent with reduced mesophase stability. A single crystal structure of the related 3,4-alkoxy-3'-stilbazole complex of silver(I) triflate[7] shown in Figure 5.13 reveals association of the triflate anion with the silver(I) cation and it can be assumed that a similar disposition of anion and cation exists in the phenylpyridine complexes (no single crystal structure could be obtained for the phenylpyridine materials). Although the single crystal structure may well not reflect precisely what is found in the mesophase, one can assume a similar arrangement of the anion and cation exits.

The Col$_h$ phase formed by the phenylpyridine complexes is then stabilised significantly when the mode of self-organisation changes and this could be a result of the added curvature of this mesophase being better able to accommodate the spatial requirements of the anion, akin to the stabilisation of the Col$_h$ phase formed by the *N*-phenylpyridinium salts.[8] After all, the shape of the cores of the phenylpyridine complexes of silver(I) and the *N*-phenylpyridinium ions are similar and so both may be able to accommodate the anion more readily on entering the Col$_h$ phase.
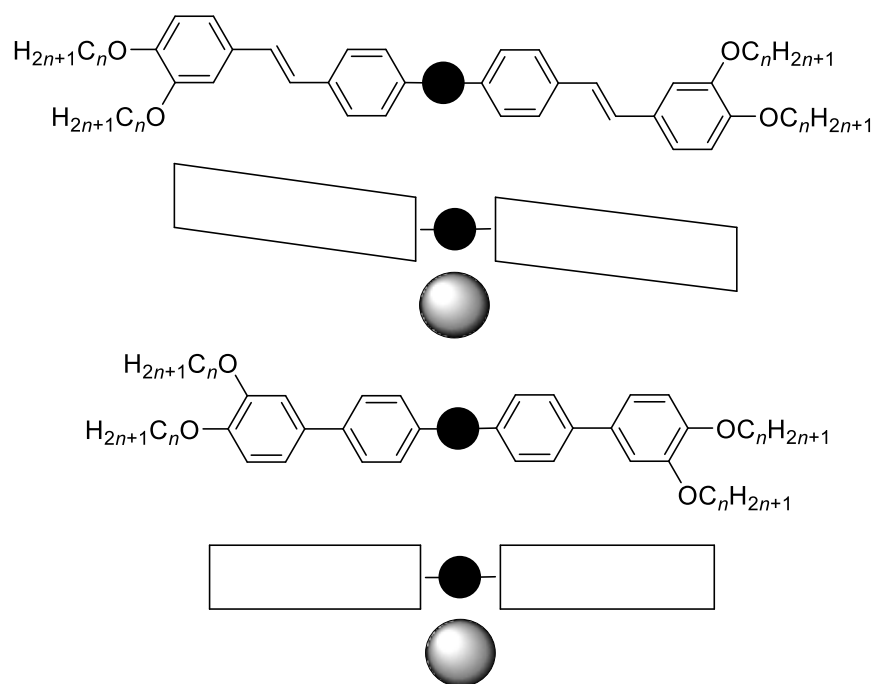
Figure 5.12. Schematic to show how the different ligands lead to better accommodation of the triflate anion into the mesophases generated by the stilbazole complexes.
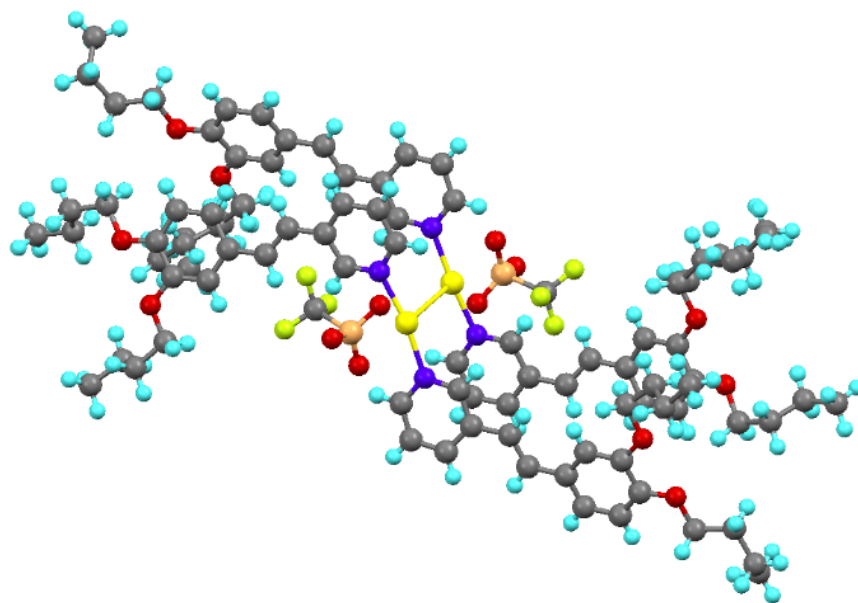
Figure 5.13. Single-crystal X-ray structure of a stilbazole complex of silver(I) triflate.[7]

3.2.   Comparison with the *N*-phenylpyridinium salts

A significant difference exists in the form of the two phase diagrams formed by the phenylpyridine complexes of silver(I) and the *N*-phenylpyridinium ions as evidenced by Figures 5.14 and 5.15. As noted earlier, the melting point of the silver(I) triflates (Figure 5.14 (**a**)) decreases rapidly to **31**-*10* and increases gradually thereafter, which implies that the melting temperature is controlled by the terminal chain length. Extrapolation of the clearing point from compound **31**-*8* reveals that the mesophase is not stable thermodynamically at short terminal chain lengths and compounds **31**-*4* and **31**-*6* melt directly into the isotropic liquid. The melting points of the *N*-phenylpyridinium salts (Figure 5.14 (**b**) and Figure 5.15 (**b**)) remain relatively constant across the series and, with the melting point controlled by the terminal chain length, would appear to be driven predominatly by a breakdown of the intermolecular ionic interactions.[8]

However, a more significant difference between the phase diagrams is evidenced by the type of mesophase formed at short terminal chain lengths, being SmA in the case of the *N*-phenylpyridinium salts and cubic in the phenylpyridine complexes. The formation of the SmA phase in the former materials is well understood and occurs due to space-filling effects of the anion coupled with strong electrostatic attractions between neighbouring anions and cations that stabilises self-organisation into layers. The SmA phase formed by the *N*-phenylpyridinium ions is destabilised on increasing chain length from compound **11**-*8* to **11**-*13*, whereas the stability of the cubic phase formed by the phenylpyridine complexes remains constant from **31**-*8* to **31**-*12*. All compounds (with both triflate and dodecylsulfate anions) then show significant stabilisation of the Col$_h$ phase when the mesomorphism changes at long terminal chain lengths. The *N*-phenylpyridinium dodecylsulfate salts (Figure 5.15 (**b**)) do, however, form an intermediate cubic phase between the SmA and Col$_h$ phases and this phase has a similar stability to the preceding SmA phase, albeit with a slight increase in the cubic-to-Col$_h$ transition temperature at **28**-*10*. It is also evident that a gradual increase in the clearing point of the Col$_h$ phase formed by the phenylpyridine complexes is observed from **31**-*14* to **31**-*18* (Figure 5.14 (**a**)), whereas the clearing temperature of the Col$_h$ phase formed by the *N*-phenylpyridinium salts decreases steadily from **11**-*14* to **11**-*18* (Figure 5.14 (**b**)). However, this is not a true reflection of the stability of the Col$_h$ phases formed by the pyridinium ions as decomposition occurs in the upper reaches of the mesophase.

It seems overall that the lamellar phase is destabilised strongly on increasing chain length, probably because the spatial requirements of the anion disrupts self-organisation of the cations into layers much like a lateral substituent attached to the core of a calamitic mesogen promotes nematic mesomorphism in place of smectic.[9,10] Then, on entering the cubic phase, a plateau of the clearing point is observed and the added curvature of this mesophase can better accommodate the spatial requirements of the anion. The most significant stabilisation in every case occurs when the mode of packing changes to Col$_h$ at long terminal chain lengths, and, as discussed in Chapter Three, this mesophase is evidently the most stable mode of self-organisation of ionic polycatenar liquid crystals due to the added curvature of this phase being best able to accommodate the anion.

A significant observation from the single-crystal structure of a stilbazole complexes of silver(I) was the formation of dimers[11] in the solid state as evidenced by Figure 5.13. Using EXAFs, Guillon *et al.*[12] had shown that the dimeric structure found in the solid state in a series of alkoxydithiobenzoate complexes of Zn(II) was retained in the mesophase, but similar studies of the silver(I) complexes was not possible given their instability to X-rays. The formation of dimers is ruled out from the monomeric solid state structure of the *N*-phenylpyridinium ions,[8] yet the same cannot be said for the phenylpyridine complexes of silver(I) owing to a lack of single crystals suitable for X-ray diffraction. However, it is not impossible for a dimeric mesogenic moiety of the silver(I) salts to contribute to their different mesomorphism when compared to the *N*-phenylpyridinium ions.
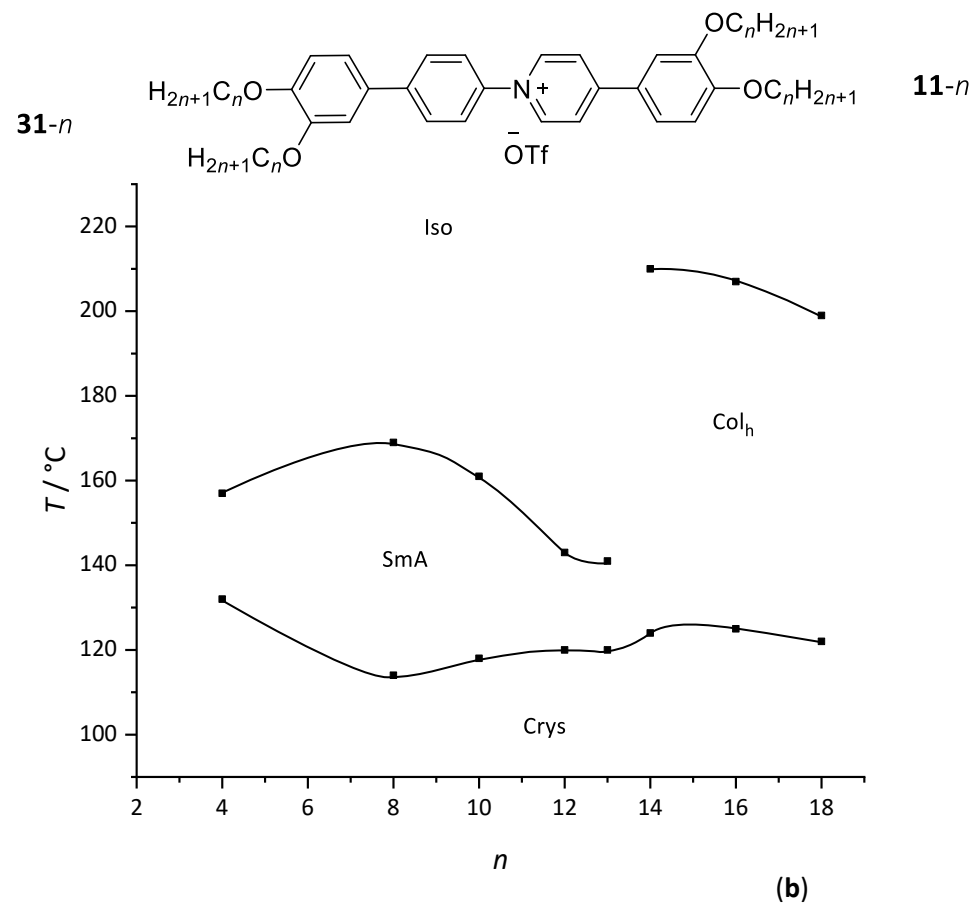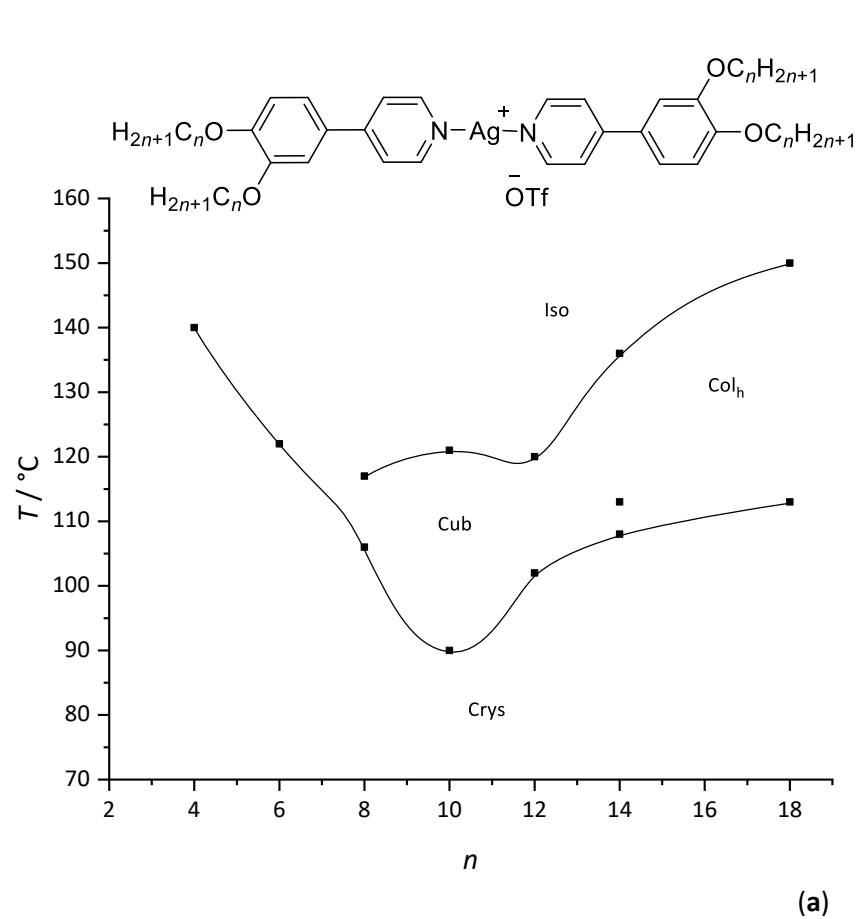
Figure 5.14. A comparison of the phase diagrams displayed by (**a**) the phenylpyridine complexes of silver(I) triflate and (**b**) the *N*-phenylpyridinium triflate salts.
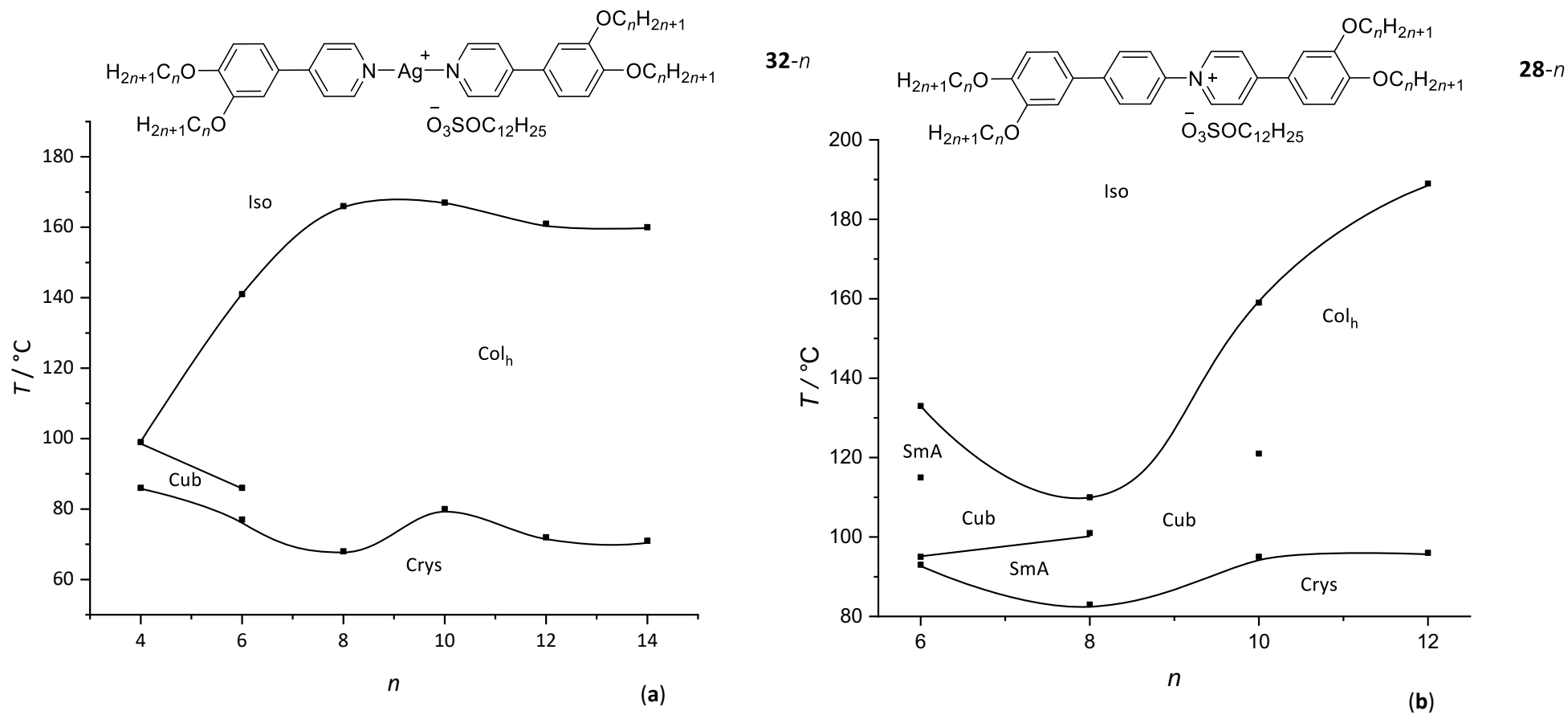
Figure 5.15. A comparison between the phase diagrams of (**a**) the phenylpyridine complexes of silver(I) dodecylsulfate and (**b**) the *N*-phenylpyridinium dodecylsulfate salts.

4. Conclusion

Given the extensive work carried out previously with the alkoxystilbazole complexes of silver(I), which, as formally ionic liquid crystals, formed the intellectual starting point for this work. The preparation of the related phenylpyridine complexes of silver(I) were then sought out to refine the comparison with the N-phenylpyridinium salts described in the main part of this thesis. Their preparation also allowed a comparison with the stilbazole complexes of silver(I), and, surprisingly, quite different forms of the phase diagram were observed given the relatively small structural modification. It seems that the spatial requirements of the anion dictate many of the behavioural differences (with respect to both the N-phenylpyridinium ions and the stilbazole complexes) with mesophase stability being enhanced if the anion is better accommodated structurally as this leads to more efficient space filling. As a general trend in ionic polycatenar liquid crystals, lamellar phases are the most severely destabilised by the anion, and, in combination with increasing terminal chain length, they are further destabilised as self-organisation into layers cannot accommodate the added volume of the terminal chains coupled with the steric perturbation of the anion. When the mesomorphism changes to cubic on lengthening of the terminal chains, the extra curvature present at the aromatic-aliphatic interface leads to a plateau in the clearing point and the anion appears to be better tolerated. Then, on entering the Col_h phase at the longest terminal chain lengths, a significant increase in mesophase stability is observed and this remarkable feature is observed in the phase diagram formed by every ionic polycatenar liquid crystal. It seems that the formation of columns can best accommodate the steric requirements of the anion as such stabilisation of the columnar mesophase was never observed for any neutral polycatenar material.

5. References

1   B. Donnio and D. W. Bruce, *New J. Chem.*, 1999, **23**, 275–286.

2   D. W. Bruce, B. Donnio, D. Guillon, B. Heinrich and M. Ibn-Elhaj, *Liq. Cryst.*, 1995, **19**, 537–539.

3   B. Donnio and D. W. Bruce, *J. Mater. Chem.*, 1998, **8**, 1993–1997.

4   D. W. Bruce, B. Donnio, B. Heinrich, D. Guillon, J. Kain, S. Diele and H. Allouchi, *J. Am. Chem. Soc.*, 2004, **126**, 15258–15268.

5   D. W. Bruce, *Acc. Chem. Res.*, 2000, **33**, 831–840.

6   M. Gharbia, A. Gharbi, H. T. Nguyen and J. Malthête, *Curr. Opin. Coll. Interfac. Sci.*, 2002, **7**, 312–325.

7   D. M. Huck, H. L. Nguyen, P. N. Horton, M. B. Hursthouse, D. Guillon, B. Donnio and D. W. Bruce, *Polyhedron*, 2006, **25**, 307–324.

8   J. D. Herod, M. A. Bates, A. C. Whitwood and D. W. Bruce, *Soft Matter*, 2019, **15**, 4432–4436.

9   M. Hird and K. J. Toyne, *Mol. Cryst. Liq. Cryst.*, 1998, **323**, 1–67.

10   A. I. Smirnova, B. Heinrich, B. Donnio and D. W. Bruce, *RSC Adv.*, 2015, **5**, 75149–75159.

11   H. Adams, N. A. Bailey, D. W. Bruce, S. C. Davis, D. A. Dunmur, P. D. Hempstead, S. A. Hudson and S. Thorpe, *J. Mater. Chem.*, 1992, **2**, 395.

12   D. Guillon, D. W. Bruce, P. Maldivi, M. Ibn-Elhaj and R. Dhillon, *Chem. Mater.*, 1994, **6**, 182–189.